

The Surface Chemistry of Adatom Mediated Oligomers of Aromatic Diisocyanides and Dithiols on Au(111) and Granular Films

by

John D. Kestell

A dissertation submitted in partial
fulfillment of the requirements for the
degree of
Doctor of Philosophy
in Chemistry
at
The University of Wisconsin-Milwaukee
May 2014

Abstract

The Surface Chemistry of Adatom Mediated Oligomers of Aromatic Diisocyanides and Dithiols on Au(111) and Granular Films

by

John D. Kestell

The University of Wisconsin-Milwaukee
Under the supervision of Professor W. T. Tysoe

Two seminal events are thought by many to be the birth of nanotechnology and molecular electronics. In 1959, Nobel Laureate Richard Feynman gave his famous “There's Plenty of Room at the Bottom” lecture to an American Physical Society meeting at Caltech. The transistor had been invented by Bell Laboratories in 1947, and already the race was on for device miniaturization. Feynman's lecture focused on some of the more serious technological problems of reading and writing on the atomic scale, and in particular, how one manipulates *single* atoms and molecules to build useful nano-architectures. His radical new paradigm was that rather than work from the top down, literally carving devices out of bulk silicon (an approach that still dominates today), perhaps we could take a lesson from Mother Nature. By intelligent design of molecules, he argues, it might be possible to allow them to assemble themselves.

Later, in 1974, Avarim and Ratner proposed a radical idea. Silicon devices such as transistors rely

on modulating *bands* in semiconductors to modulate charge through them. Avarim and Ratner proposed that with proper design, it might be possible to synthesize discreet molecules with essentially the same functionality. Analogous to band modulation in semiconductors, they argued that perhaps HOMO and LUMO orbitals could be modulated in a similar way to produce a sort of “molecular rectifier”.

In an effort to understand new paradigms in fabrication and molecular electronics, approaches to *self-assembly* will be presented in this dissertation. The research picks up with the observation that when single-crystal Au(111) was exposed to 1,4-phenylene diisocyanide, long, oligomeric structures spontaneously formed. 1,4-phenylene diisocyanide is a well studied and published molecule which has been subjected to a range of *single molecule* conductivity measurements. The structures are composed of alternating $-(\text{Au}-\text{PDI})_n$ - subunits, where “Au” is actually an adatom resting in a hollow site on the metal surface.

In this dissertation the structure of the 1,4-PDI oligomers will be discussed at length along with a proposed growth mechanism for the chains. To extend the chemistry further, another system was investigated. 1,4-benzene dithiol (1,4-BDT) is another well studied molecule. However there are large holes in the existing literature, and we report here for the first time that on Au(111), 1,4-BDT undergoes oligomerization chemistry as well. Similarly to 1,4-PDI, 1,4-BDT generates gold adatoms that seem critical in the growth of the oligomers, where either end of the molecule is covalently secured into the chain *via* RS-Au-SR type linkages.

To examine the electrical properties of these oligomers, granular gold films were prepared using thermal evaporation, and upon exposure to the “molecular wire materials”, a dramatic reduction in sheet resistance across the film was observed. It will be demonstrated that this reduction is a result of the oligomers bridging the gap between the particles and not a morphological change in the particles

themselves.

To further explore the requirements for the proposed self-assembly chemistry, other molecules were explored. 1,3-phenylene diisocyanide was shown to oligomerize, but due to the 120° angle between -NC groups, the chains assembled into “zigzag” structures. Curiously, 1,3-BDT was not shown to self assemble and instead is seen as di-adatom monomers at all coverages. Finally, to extend the chemistry further, 1,3,5-phenylene triisocyanide was prepared. The predicted “honeycomb” structures were shown to spontaneously form on Au(111) and represents a viable strategy for the fables fabrication of a well-defined array of small nanopores, once again templated by gold adatoms in linear -NC-Au-CN- configurations.

The self-assembly chemistry appears to be a rather general phenomenon, and with suitable synthetic modification a wide range of functional hybrid nanomaterials could be envisaged. Adatoms, particularly gold adatoms, are interesting in their own right as they possess higher reactivity than bulk or surface atoms do (a consequence of their low coordination number).

© Copyright John D. Kestell, 2014

All Rights Reserved

In memory of my father and my grandparents.
You always understood, and I miss you terribly.

Gouge Away.

You can gouge away.

Stay all day, if you want to.

“Gouge Away”, the Pixies

Table of Contents

Chapter 1: Introduction	1
Chapter 2: Methods and Materials	9
<i>Why UHV?</i>	9
<i>UHV Chambers</i>	11
<i>Vacuum Pumps</i>	13
<i>Mechanical (Rotary) Pumps</i>	14
<i>Turbomolecular Pumps</i>	15
<i>Oil Diffusion Pumps</i>	16
<i>Ion Pumps</i>	17
<i>Ultra-High Vacuum Systems</i>	19
<i>RAIRS System</i>	20
<i>Conductivity Measurement Chamber</i>	21
<i>STM System</i>	23
<i>Metal Evaporator</i>	25
<i>STM Theory and Instrumentation</i>	26
<i>STM History</i>	27
<i>STM Theory</i>	28
<i>STM Instrumentation</i>	32
<i>RAIRS Theory</i>	37
<i>Herringbone Reconstruction on Au(111)</i>	40
Chapter 3: Determination of Adsorbate Structures from 1,4-Phenylene Diisocyanobenzene on	
Gold	45

<i>Experimental Methods</i>	47
<i>Density Functional Theory Calculations</i>	47
<i>Results</i>	47
<i>Discussion</i>	52
<i>Conclusions</i>	55

Chapter 4: Understanding and Controlling the 1,4-Phenylene Diisocyanobenzene-Gold

Oligomer Formation Pathways.....57

<i>Introduction</i>	57
<i>Theoretical Methods</i>	59
<i>Results</i>	59
<i>Oligomerization</i>	61
<i>Chain Mobility</i>	66
<i>Discussion</i>	66
<i>Potential Utility</i>	67
<i>Conclusions</i>	70

Chapter 5: Electrical and Structural Properties of 1,4-Phenylene Diisocyanide Oligomers

Bridging Between Gold Nanoparticles on Mica.....73

<i>Introduction</i>	73
<i>Experimental</i>	76
<i>Results</i>	77
<i>Structure and Mobility</i>	78
<i>Bridging Gold Nanoparticles</i>	80
<i>Conductivity and Morphology</i>	81

<i>Discussion</i>	8
<i>Abeles Theory</i>	86
<i>Conclusions</i>	89
Chapter 6: Gas Adsorption on $-(\text{Au}-\text{PDI})_n$ - Oligomers on Au(111) and Gold Nanoparticle	
Films on Mica	92
<i>Adsorption of CO on Au/PDI Oligomers</i>	94
<i>Granular Thin Film Based CO Sensor</i>	98
<i>cis and trans-2-Butene on Au/PDI Oligomers</i>	100
<i>Conclusions</i>	104
Chapter 7: Adsorption of 1,3-Phenylene Diisocyanide on Au(111)	112
<i>Introduction</i>	112
<i>Experimental Methods</i>	112
<i>Results</i>	112
<i>Discussion</i>	116
<i>Conclusions</i>	118
Chapter 8: Self-assembled Structures of 1,4-Benzenedithiol on Au(111) and Formation of	
Conductive Oligomers Between Gold Nanoparticles on Mica	121
<i>Introduction</i>	121
<i>Experimental Methods</i>	122
<i>Results</i>	122
<i>STM Results</i>	122
<i>Electrical Studies</i>	128
<i>Discussion</i>	130

<i>Field emission tip cleaning</i>	179
<i>Ion bombardment</i>	185
<i>Controlled crashing or “dipping”</i>	186
<i>Other “tricks”</i>	187
<i>Conclusions</i>	188
Curriculum vitae:	198

List of Figures:

Chapter 1.....1

Figure 1: At left is the classic Aviram and Ratner diode. X is an electron donor group ($-\text{CH}_3$, $-\text{OH}$) and Y is an acceptor group ($-\text{F}$, $-\text{NO}_2$) [1]. The two halves are separated by a sigma-bonded bridge (R) which serves as a tunneling junction between them. At right is another example of a molecule with rectifying behavior, as measured in a Langmuir-Blodgett film configuration.....2

Chapter 2.....9

Figure 1: A typical stainless-steel UHV chamber. A variety of ports are installed which allow the chamber to be reconfigured if the need arises. UHV conditions are achieved by *baking* at temperatures of around 120°C while pumping. At these temperatures, water and other contaminants desorb from the inner walls and are pumped away.....12

Figure 1: Rotary-Mechanical Vacuum Pump The heart of the mechanical pump is a set of spring loaded vanes that rotate eccentrically within an oil containing cylinder. Since the vanes are off-axis, one half of the rotation results in an increase of the entrapped volume while the second phase results in a decrease of the volume (compression). The oil both seals and lubricates the vanes.....14

Figure 2: Cutaway view of a turbomolecular pump. Turbomolecular pumps operate on the principle of *momentum transfer*. A stack of turbine blades rotate at very high speed with respect to stator blades. A compression gradient is set up which causes gas molecules entering the front of the pump to be directed to the rear where they are pumped away by a mechanical pump.15

Figure 3: Oil Diffusion Pump The diffusion pump operates by heating low vapor pressure oil (formerly mercury) to vaporization and allowing it to travel up a series of concentric cones. The abrupt change in direction produces a super-sonic jet of oil which propels gas molecules from the chamber into the base of the diffusion pump where they are pumped away by a mechanical pump.....18

Figure 4: Ion Pump Ion pumps function by generating ions from molecules in the presence of a strong electric field. The resulting ions are then accelerated towards the cathodes with sufficient kinetic energy that they become embedded in them. The process also sputters a small amount of the cathode material (typically a titanium alloy). The reactive metal serves to help pump the system by generating unreactive solids from gasses in a process known as *gettering*.....19

Figure 5: Top view of RAIRS system. Some components not shown for clarity. In this configuration, crystal is moved into

main chamber for cleaning or Auger analysis, and back to IR (high pressure) cell for surface infrared studies.....21

Figure 6: Typical configuration of I/V chamber. In the configuration shown, molecular wire (precursor) materials can be dosed from a Knudsen source. Not shown is a leak valve which was used for gas sensor experiments. Details of instrumentation are found in Fig. 7.....22

Figure 7: Block diagram of I-V curve instrumentation. An A/D card under PC control was used to ramp a voltage (typically $\pm 4V$) through the sample or *device under test*. A picoammeter placed in series collects the resulting current which is fed back in to the A/D card. This allows for the collection of I/V data directly. The Labview program allows for increasing integration time and changing the voltage step as needed. High-quality shielded wire and careful grounding are critical for proper functioning of such a system.....23

Figure 8: Details of Cooke Vacuum Products CVE 301 thermal evaporator. B) details the inner workings—simple tungsten baskets pre-wetted with high purity gold. Samples are mounted above them (face down) during preparation, and the filament is heated by passing an AC current through it. Resistance was measured via the measurement feedthroughs and a hand-held Fluke multimeter.....25

Figure 9: Schematic of tunneling (from left to right) through a rectangular barrier of height Φ . Before and after the barrier, the wave-function takes the form of a sine wave. Within the barrier it takes the form of an exponential decay.....30

Figure 10: Distortion of tunneling barrier in the presence of a small bias between sample and scanning-probe.....31

Figure 11: Schematic of a scanning-tunneling microscope. A bias is placed between a surface and a sharp (ideally *atomically sharp*) tip which is rastered over it. A *tunneling current* is measured, amplified, and feedback electronics move the tip closer or further away to maintain a constant tunneling current. This extraordinary x, y, and z resolution was not possible until the advent of high quality piezoelectric materials.....33

Figure 12: RHK sample holder (image used with permission, RHK). Crystal (12) is cut in *top-hat* configuration and held under spring pressure between sapphire washers. This keeps it electrically and thermally isolated from the rest of the sample holder. The ramps are TiN coated tungsten and the base is ultra-pure copper.....35

Figure 13: STM head sitting on sample holder. In this head, coarse motions are carried out by three tubular piezo legs and tip rastering functions are performed by the central Z-piezo which is controlled independently of the other 3. (Adapted with permission, RHK Technologies).....37

Figure 14: The origins of the surface selection rule—the *image dipole effect*. For vibrations parallel to the (conductive) surface, the mirror charge is anti-parallel and exactly cancels the dynamic dipole of the adsorbate.39

Figure 15: Reflection geometry showing s and p polarized components of incident and reflected radiation.....39

Figure 16: A) Gold has the *face centered cubic* structure diagrammed. B) In the *Miller Index* crystallographic notation, the (111) planes intersects opposite corners of a cube. C) In *hexagonal close-packed* structures, atoms in the third layer fall directly on top of atoms in the first layer. Thus *hcp* packing is also called *ABA* packing. In *face-centered cubic* structures, atoms in the third layer reside directly on top of vacancies (octahedral “holes”) in the first layer. *Fcc* is sometimes called *ABC* packing.....40

Figure 17: For a hexagonal lattice, The “close-packed directions” are indicated in A). The *root 3* directions are indicated in B).....41

Figure 18: A) A large scan area image of a perfectly formed herringbone reconstruction of Au(111). Inset shows a typical line profile across solitons. The red ellipse shows the “pinched in” elbow, and the magenta ellipse shows the “pinched out” elbow. $V = -1.0V$ $I = 0.89nA$. B) Atomically resolved herringbone reconstruction highlighting the *hcp* and *fcc* domains (red and green lines, respectively), and the solitons that result from a stacking fault between the two. $V = -0.50V$, $I = 342pA$...42

Chapter 3.....45

Figure 1: (A) $-(Au-PDI)_n$ - oligomers on an Au(111) single crystal. An eroded step edge runs diagonally through image. $V = -1.2 V$, $I = 328 pA$. (B) Line profile along indicated segment.....46

Figure 2: The structure of (Au-PDI) oligomers on gold calculated using density functional theory showing (A) an angled view and (B) a top views of the oligomer chains.....49

Figure 3: A series of reflection-absorption infrared spectra of PDI adsorbed on Au(111) as a function of exposure time, where the exposure times are indicated adjacent to the corresponding spectrum. Data acquired at room temperature.....50

Figure 4: (A) Experimental high-resolution STM images of PDI on Au(111) collected as a function of tip bias voltage for negative biases, where the bias voltages are indicated in the images. The corresponding simulated images (B), using the Bardeen method, for the Au-PDI oligomeric structures depicted in Figure 2 are shown in the bottom panels along with the locations of the gold adatoms and the aryl rings.....51

Figure 5: Plot of the conductivity of gold nanoparticles deposited onto a mica substrate after exposure to solutions of PDI in benzene as a function of the solution dose. (Experiment performed by Rasha Abuflaha).....51

Chapter 4.....57

Figure 1: The structure of (Au-PDI) oligomers on gold calculated using density functional theory shown (A) an angled view and (B) a top views of the oligomer chains.....58

Figure 2: A) The structure of the most stable, vertical Au-PDI adatom complex on a Au(111) substrate. B) Shown also is the energy profile for diffusion of the complex from the most stable, face-centered cubic (fcc) three-fold hollow site to the adjacent hexagonal-close packed (hcp) site.....60

Figure 3: The calculated structure of a PDI molecule bound to a gold step, with a second PDI molecule placed close to it as an initial configuration for calculating the reaction barrier (top and side views).....63

Figure 4: The final structure of a gold-PDI adatoms complex bound to an isocyanide molecule on a gold step edge.....63

Figure 5: The energy profile for the binding of a gold adatom complex to a PDI molecule attached to a gold step edge.

Figure 6: The calculated structure of a PDI molecule bound to a gold step, with a second PDI molecule placed close to it and an initial configuration for calculating the reaction barrier, now including Van der Waals' interactions.....64

Figure 7: The final structure of a gold-PDI adatoms complex bound to an isocyanide molecule on a gold step edge, now including Van der Waals' interactions. Terminal CN is drawn significantly closer to the surface than was showing in Fig. 4, in the absence of VdW corrections.....65

Figure 8: The energy profile for the binding of a gold adatom complex to a PDI molecule attached to a gold step edge, now including Van der Waals' interactions.....66

Figure 10: The classic Aviram and Ratner molecular diode. X=(methyl, amino, hydroxyl) and Y=(nitro, cyano, fluoro). A donor and acceptor separated by a methylene tunneling bridge. The groups, in theory, could serve as *intramolecular* n or p dopants respectively.....68

Figure 11: Plot of the orientational excess, *versus* electric field in V/m for molecules with dipole moments of 0.5, 1, 2 and 3 Debye.....70

Chapter 5.....73

Figure 1: The regimes of granular thin films. (A) represents the *dielectric* regime where discrete particles exist isolated by a dielectric matrix. Here the Temperature Correlation of Resistance (TCR) is negative. (C) represents the *metallic* regime where particles are mostly touching but with dielectric inclusions. Here the TCR is positive. (B) is the *transition* regime and is defined by the coverage through which the TCR changes sign [7-9].....75

Figure 2: Configuration of granular thin film samples. First ~200nm thick electrode pads are deposited (fully metallic), then the granular thin film is evaporated over the top.....76

Figure 3: Typical curve showing dramatic enhancement in conductivity across a granular film as a function of PDI dosing time. One critical parameter for a film, R_0 is the sheet resistance of the clean film, prior to dosing.....77

Figure 4: Sequential images of $-(\text{Au-PDI})_n$ - oligomers on Au(111). The chain above the white line appears to “unzip” from one chain and hop down to interact with the one below it. Room temperature, $V = -1.5 \text{ V}$, $I = 55 \text{ pA}$78

Figure 5: Sequence of images showing $-(\text{Au-PDI})_n$ - oligomers linking nanoparticles on an Au(111) surface. The location of the nanoparticles are given by A, B, and C. Also see movie in supplement to reference [10]. $V = -2.00 \text{ V}$, $I = 198 \text{ pA}$79

Figure 6: Depiction of $-(\text{Au-PDI})_n$ - oligomers on an Au(111) surface. Chains A and B run along hexagonal close packed (hcp) sites while chains D and E run along face-centered cubic (fcc) sites. Chain C can reside in two possible sites of nearly equal energy and it is possible for the chain to “hop” between them.....80

Figure 7: $1 \mu\text{m} \times 1 \mu\text{m}$ tapping mode AFM images of granular gold films on mica. In film (A), $R_0 = 312 \text{ M}\Omega$ and particle density is $3.3 \pm 0.1 \times 10^{15} / \text{m}^2$. For film (B), $R_0 = 48 \text{ M}\Omega$ and particle density is $3.2 \pm 0.1 \times 10^{15} / \text{m}^2$81

Figure 8: STM images of a granular, thermally evaporated gold film before dosing 1,4-PDI (A), and after (2 mM in benzene) (B). Images were acquired in air at room temperature. $V = -1.0 \text{ V}$, $I = 8.85 \text{ pA}$. The film did not undergo a statistically relevant change in morphology.....82

Figure 9: Plots of $\ln(R)$ vs. $T^{-1/2}$ for two films of differing initial sheet resistances, R_c . The slope of such a plot yields a parameter designated α which can yield information about the nature of the tunneling barrier between adjacent nanoparticles.....83

Figure 10: Plot of α values vs. $\ln(R_c)$ for the 12 films studied in this chapter. The linear dependence of such a plot is in agreement with the theory of activated tunneling in granular materials put forth by Abeles and Sheng.....84

Figure 11: A series of control experiments. Curves A, B, and C correspond to the uptake of phenylisocyanide on film with initial conductivities of 17.12nS, 8.20nS, and 5.86nS respectively. The dosing pressure of phenylisocyanide (an oil with considerable vapor pressure) is estimated to be $\sim 600X$ as that for 1,4-PDI. Curve D is the dosing curve for a clean mica film exposed to 1,4-PDI. To achieve the dramatic enhancement in conductivity as shown in Figure 3 a bifunctional linker molecule is needed, as are gold nanoparticles (as a sink of gold adatoms required for oligomerization).....85

Figure 12: Energy level diagram for gold nanoparticles linked by 1,4-PDI oligomers where ϕ_c corresponds to the work function of the 1,4-PDI covered nanoparticles (4.08 eV) and ϕ_f is the tunneling barrier through the linker molecule measured to be $0.10 \pm 0.02 \text{ eV}$89

Chapter 6.....92

Figure 1: Results of a CO dosing experiment on $-(\text{Au-PDI})_n$ - oligomers at low temperature. The CO peaks are circled in

gray (dosed at 2×10^{-7} Torr, 5 minutes): CO is stable to $\sim 150\text{K}$, then desorbed. However, further heating is required to regenerate the original CN peak.....95

Figure 2: -CN mode of $-(\text{Au}-\text{PDI})_n$ - saturated surface exposed to 2×10^{-7} Torr of CO for 5 minutes. Spectra acquired at $\sim 95\text{K}$. The peaks at 2166, 2153, and 2128 cm^{-1} (found in this 3-mode fit) are in good accord with the anchored, flat-lying and free modes reported at 2172, 2153, and 2121 cm^{-1} [14,15].....95

Figure 3: Results of a CO on $-(\text{Au}-\text{PDI})_n$ - isotope study. Both the ^{13}CO (upper) and CO spectra show two peaks.

The literature suggests that even for clean (un-PDI functionalized) Au(111), CO adsorption can occur with associated step edge roughening and terrace restructuring. [18].....95

Figure 4: STM image of 1,4-PDI saturated surface, exposed to 2×10^{-7} Torr, 5 minute CO dose. Note the formerly long, straight chains have been distorted, and there is evidence for gas adsorption between them.....96

Figure 5: STM image of $-(\text{Au}-\text{PDI})_n$ - oligomer exposed to CO at $\sim 110\text{K}$. The pronounced tall/short (oval/circle) structure of the chain suggests that this is direct microscopic evidence for CO adsorption on low-coordination adatom-like gold in the oligomers.....96

Figure 6: Granular film based gas-sensors. Film was prepared as in Chapter 5 and dosed with 1,4-PDI. A) Shows the result of a CO back-filling experiment. The bend in the curve is reproducible, but its origin is unknown. B) Resistance vs. CO pressure response is reversible, at least out to 5 Torr.....97

Figure 7: A) and B) depict *cis* and *trans*-2-butene impinging upon an adatom. Based on steric arguments, one would expect *cis*-2-butene to allow for better π -overlap with the adatom via “head on” attack.....98

Figure 8: A) High-frequency, and B) low-frequency regions of $-(\text{Au}-\text{PDI})_n$ - oligomers, dosed for the time and pressure shown with *cis*-2-butene.....100

Figure 9: High (A) and low (B) frequency regions of *trans*-2-butene dosed onto 1,4-PDI saturated Au(111). In contrast to the *cis*-2-butene data presented above, no evidence of CN decoordination was observed.....101

Figure 10: PDI CN mode of Au(111) crystal exposed to *cis* and *trans*-2-butene. Both exposures were 2×10^{-10} Torr for 120 seconds.....102

Figure 11: Current map of 110K $-(\text{Au}-\text{PDI})_n$ - surface exposed to 3L of *cis*-2-butene. The oval features terminated by ball-like structures appear to be *cis*-2-butene molecule adsorbed in ordered rows on the surface.....103

Figure 12: 110K STM image of *cis*-2-butene exposed $-(\text{Au}-\text{PDI})_n$ - surface. There is a high degree of mobility in the

chains, as evidenced by arch-like structures. The chains appear anchored on one end, and free to move on the other. Some of the straight segments show similar behavior—evidence of hopping laterally, and imaging as kind of “ghost” image.....104

Chapter 7.....112

Figure 1: A series of Auger spectra after dosing 1,3-PDI on Au(111) at 300 K for up to 8 minutes and the effect of subsequent heating to 900 K.....113

Figure 2: Uptake of 1,3-PDI on Au(111) at 300 K from the peak-to-peak intensity of the carbon KLL Auger features in the spectra shown in Fig.1.....113

Figure 4: A) An STM image of a saturated overlayer of 1,3-PDI adsorbed on Au(111) at 300 K ($I_t = 132$ pA, $V_b = -0.5$ V). B) Shows long, straight segments of “zigzag chains” in addition to closed and hair-pin structures.....114

Figure 5: Reflection-adsorption infrared spectra of 1,3-PDI adsorbed on Au(111) at 300 K as a function of exposure. The top spectrum shows the effect of heating the sample to 373 K.....115

Figure 6: A depiction of the top and side views of 1,3-PDI adsorbed on gold adatoms on a Au(111) substrate calculated using density functional theory.....115

Figure 6: A) Represents 3 1,3-PDI monomers on a (111) surface. Note that the monomeric units are mediated by gold adatoms, as supported by DFT and STM studies. B) Represents a model for the commonly found hexagonal structures on the surface.....119

Figure 7: STM images indicate chains are often found with their long axis parallel with each other. A) is a representation of an “in phase” pair of chains while B) represents an “out of phase” pair.....119

Chapter 8.....121

Figure 1: A) Intermediate coverage of 1,4-BDT on Au(111) at room temperature ($V = -0.5$ V, $I = 102$ pA) B) Intermediate coverage, 1,4-BDT dosed at room temperature, image acquired at ~ 110 K. ($V = -0.5$ V, $I = 112$ pA).....124

Figure 2: A) Line profile of 1,4-BDT chains shows pronounced bright/dim structure and differences in apparent height. This appears to be a direct observation of gold adatoms between 1,4-BDT phenyl rings. ($V = -0.4$ V $I = 96$ pA) B) Higher resolution image showing lateral packing and resolution of the phenyl rings themselves. C) Illustrates straight segments of “all-trans” S-Au-S “zig-zag” bonding, and 120° cis-bends (the second S- on the ring omitted for clarity).....124

Figure 3: STM images of 1,4-BDT adsorbed on Au(111) at a temperature of ~ 110 K. The crystal was warmed briefly to ~ 250 K, and cooled back to 110K for imaging. B) was cropped from A) (indicated in red). The structures show three bright lobes and appear to be a 1,4-BDT trimer. ($V = -0.5$ V, $I = 114$ pA).....125

Figure 4: Wide area STM image of 1,4-BDT on Au(111) (room temperature) . Dark regions between chains image at $\sim 1 \text{ \AA}$ deep (inset) and are presumably one source for the gold adatoms required for oligomer growth, with step edges being the other. ($V = -0.5\text{V}$, $I = 142\text{pA}$).....126

Figure 5: A reasonable model for a gold-dithiol unit. In this model the sulfur occupies a $\text{Au}_{\text{adatom}}\text{-Au}_{\text{atop}}$ bridge site. The direct interaction with the substrate might explain the total lack of mobility observed for Au/1,4-BDT oligomers. This type of bonding is in contrast to the so called “standard model” where the sulfur occupies a bridge or hollow site on the surface. [7].....127

Figure 6: As was the case for 1,4-PDI on granular gold (Chapter 5), 1,4-BDT on similarly prepared films shows a linear $\ln(R)$ vs. $T^{1/2}$ dependence, a behavior which is predicted by the model of Abeles and Sheng. R_0 sheet resistance of the film prior to dosing, and scales with gold coverage. The slope the plot (α) provides insights into the height of the tunneling barrier between the particles.....129

Chapter 9.....134

Figure 1: A) top view of η^1 adatom complex of 1,3-benzene dithiol (1,3-BDT) without consideration for van der Waals forces. $E_{\text{ads}} = -180 \text{ kJ/mol}$. B) When van der Waals forces are considered, $E_{\text{ads}} = -205 \text{ kJ/mol}$. This η^1 state was not observed experimentally, but may represent a short-lived precursor state in the formation of the monomeric 1,3-BDT species imaged *via* STM studies.....136

Figure 2: Structures of three η^2 1,3-BDT monomers on Au(111), corrected for van der Waals forces. A) is a “di-atop” complex with a calculated heat of adsorption of $E_{\text{ads}} = -342 \text{ kJ/mol}$. B) is a “di-bridge” complex, with a heat of adsorption of $E_{\text{ads}} = -351 \text{ kJ/mol}$. C) is a “di-adatom” complex with a heat of adsorption of $E_{\text{ads}} = -444 \text{ kJ/mol}$. While bonding directly to the surface is stable, the di-adatom complex is more stable by $\sim 100 \text{ kJ/mol}$137

Figure 3: Saturation dose of 1,3-BDT on Au(111). The crystal was dosed and imaged at room temperature. No sign of ordered structures were observed under these conditions. Another striking feature is that the phenyl rings are clearly resolved including the central “pore” in the ring.....138

Figure 4: A) A clean but incompletely reconstructed Au(111) crystal. “Missing rows” of gold atoms, and black spots (missing surface atoms) image at $\sim 50 \text{ pm}$ deep. B) Properly annealed Au(111) crystal exposed to 3s 1,3-BDT dose. Adsorbates image as white features while black features suggest that significant *etch pitting* has occurred.....139

Figure 5: High resolution STM image of step edge and terraces. Clearly resolved are hexagonal phenyl ring (lower terrace

especially clear) and an interesting super-lattice structure. The structure appears to be a “missing row” reconstruction. The origins of this structure are unknown, but was observed reproducibly with 1,3-BDT on

Au(111).....140

Figure 6: A) 3-sulfhydrylphenyl-methylthioether B) The steric bulk (dotted cone) can be modulated by the identity of of the alkyl group (shaded cone), and this should tune the kinetics of dealkylation upon adsorption onto a metal surface. In theory, the sulfhydryl group should react much more readily than the the thioether functionality.....144

Figure 8: A postulated, mobile η^1 complex. Alkylating the second sulfur group (to generate a thioether) should significantly slow adatom sequestration for this group. For the methylthioether, methane should be produced be expelled *via* reductive elimination.....145

Chapter 10.....147

Figure 1: A 3-step route to 1,3,5-phenylenetriisocyanide.....149

Figure 2: Room temperature 1,3,5-PTI uptake on Au(111). Note single peak corresponding to CN stretching mode. Also note red-shift in this frequency with increasing exposure.....151

Figure 3: 1 minute 1,3,5-phenylenediisocyanide dose on Au(111). Note 2 dimensional, hexagonal lattice and eroded step edge. $V=-1.0$ V, $I= 103$ pA. B) Some well formed hexagonal structures. Some, like the one circled show a protrusion inside the “nanopore” which could correspond to a low-coordination gold atom slightly proud of the surface.....152

Figure 4: Structural model of 1,3,5-phenylenetriisocyanide “honeycomb” network. The structure is in accordance with simple geometric arguments—the 3-fold symmetry of the molecule and 180° NC-Au-CN bonding.....153

Figure 5: Small scan area image of well formed honeycomb and typical line scan along edge. All line scans show a protrusion in the center of the edge which is completely consistent with a gold adatom. Similar results were obtained in the Au(111)/1,4-PDI system. The vertex to vertex distance (averaged over 6 edges) was found to be 1.17 nm. $V= -1.0$ V, $I= 121$ pA.....154

Figure 6: A) Etch pits and step edge erosion imply that 1,3,5-PTI is abstracting gold atoms from the bulk. B) Shows pits imaging at ~ 550 pm which is slightly less than would be expected for an atomic step of gold. Closer examination, however, shows that more honeycomb structures exist in the bottom of the pit and could easily account for the discrepancy.154

Figure 7: 3s 1,3,5-PTI dose on Au(111). The molecules are reacting first with the “pinched out” elbows of the herringbone reconstruction. B) Closeup of elbows, and “waviness” in the solitons of the reconstruction. $V= -0.5$ V, $I= 95$ pA.....155

Figure 8: 30 second 1,3,5-PTI dose on Au(111). The herringbone reconstruction is lifted, and replaced with extended

hairpin turn features. $V = -0.5V$, $I = 102$ pA.....156

Figure 9: A and B show signs of long range structure induced by a low exposure of 1,3,5-PTI (2 minute dose). These features are $\sim 20X$ larger than the molecules themselves and appear to be a distortion of the herringbone reconstruction (rather than the adatom templated structures described above). In A) the directions of the original herringbone are given in red, and the directions of the long segments of the new reconstruction are given in purple. The new reconstruction is rotated 60° from the original.....156

Appendix A166

Figure A-1: Photo taken through view-port of tungsten wire recrystallization. The circular object in the center is a 2 kg weight which keeps the wire under considerable tension. (image used with permission Boscoboinik).....169

Figure A-2: Double lamellae tip-etching setup. Unlike the traditional drop-off method, in the setup pictured the tungsten wire serves as it's own switch. Once the lower portion drops free, the circuit is broken and etching is halted.....173

Figure A-3: One-step (A) and two-step (B) wet etching of tungsten STM tips. In the one-step process, resulting tips are frequently mechanically weak and wiry. In a 2-step process the wire is first *necked down* to about $\frac{1}{2}$ it's original diameter, then carefully cut through. The aspect ratio of the tip is controlled by lamella thickness and placement.....176

Figure A-4; SEM image of electrochemically etched tungsten probe at 258X magification. Note flawless, perfectly symmetric etch zone. The tip is extremely sharp but mechanically rugged. (Image used with permission Joanna Millunchick, University of Michigan).....177

Figure A-5: A highly localized *tip-state* investigating the atomic corrugation of localized *surface-states*. For a tungsten tip, perhaps the tip-state is dz^2 in character. For a silicon surface, the states might be sp^3 . The key to good imaging is a stable and clean tunneling junction between the two.....179

Figure A-6: An *electron wind-force* can be used to draw low-coordination atoms (A) to a sharp and stable tip (B).....181

Figure A-7: A) Side and B) front view of Fowler-Nordheim tip conditioning system. Tips are mounted to nichrome filament. Tip conditioning and testing is performed by cycles of heating and field emission.....182

Figure A-8: Construction detail of the tip mounting system and copper disk. Heating is accomplished by passing a current through the nichrome filament. Field emission is carried out by placing a large bias between the tip and the copper disk. A Keithley picoammeter is placed in series to measure field-emission current as a function of applied voltage.....183

Figure A-9: Typical results of a field-emission tip conditioning. The tip was flashed to dull red (~ 1200 K) prior to each field-emission run. Then a high-voltage supply was placed between the tip and the copper collector with a picoammeter in

series. Bias was increased in arbitrary steps until a final current of $\sim 10\text{nA}$ was arrived at, then brought back down. Notice dramatic reduction in slope and shift to lower voltage with run number.....184

Appendix B.....190

Figure B-1: A representation a metal/vacuum interface. μ is the Fermi level and ϕ is the work function. Both quantities are typically expressed in units of electron-volts (eV).....190

Figure B-2: Distortion of a barrier at a metal/vacuum interface as the result of an applied external field. The effective width and height decrease with field strength making tunneling through it more probable.....193

Figure B-3: Probability densities for A) an un-perturbed and B) a system perturbed by an external electric field.....194

Acknowledgments

Kurt Vonnegut, in Cat's Cradle, describes a (fictitious) religion called *Bokonism*. The religion is presented in the form of *foma*—harmless untruths that can be useful if implemented carefully. Among these untruths is the idea of the *karass*—groups of people that are cosmically linked, even when no superficial connection appears to exist. I have worn many hats over the years, and my *karass* encompasses a strange and wonderful cross-section of humanity. I will make the statement that I owe each and every one of you an unpayable debt. Every one of you—the good, the bad, and the ugly—is an object of my gratitude.

Several specific acknowledgments are in order, as the completion of this undertaking would have been impossible without a great deal of assistance. First, my adviser Prof. W.T. Tysoe. I have never worked under another person who *truly* led by example. He expected a lot out of me, and out of the other group members—but he was always out in front leading the charge. He is an excellent and quite brilliant scientist, and a genuinely kind and good man, and I have no idea where his boundless energy comes from. I'll be proud to count myself as one of yours, Professor, and place my champagne bottle on the shelf of honor. I would also like to thank Prof. D. Bennett. Prof. Bennett is largely responsible for recruiting me to UWM. I was sitting at my desk one Saturday at my “real world” job, bored to tears. On a whim I performed an internet search for “inorganic chemistry university of Wisconsin”. I went through a few pages, and Prof. Bennett's page on “molecular wires” came up. My former graduate studies were in inorganic chemistry/photophysics, and so I was immediately intrigued, and a few minutes later I emailed him. A few weeks later I met him, Prof. Schwabacher and Prof. Pacheco. I was immediately impressed with my conversations with them, and the caliber of the research being performed here.

I would like to thank Prof. Schwabacher. I consider it an honor that we had several long, convoluted conversations. Prof. Schwabacher is a true asset to this department and is much appreciated by students and faculty alike. I would also like to thank Prof. Woehl and Prof. Lyman for providing several insightful comments on my research and extensive commentary on my dissertation.

Dr. Juan Pablo Claude, years ago, was the professor at my alma mater who asked one day during my final semester of my B.S. studies “did you ever think of going to graduate school?” The honest answer was “no, I haven't”. I joined his lab shortly thereafter on an REU grant and from him I learned everything I know about spectroscopy and photophysics. This has been a long time in the works, Juan Pablo, but here is!

I can't forget the Tysoe group. Anibal Boscoboinik was the first friend I made upon returning to school. He was part of the group we affectionately refer to as “The Argentinians”. Anibal is an excellent microscopist, and with his help we hammered out the ground work for much of what is presented in this dissertation. Also, Octavio Furlong and Luke Burkholder who taught me (and I think all of the group members) UHV technique and a great deal about surface science.

More recently, I would like to thank Dr. Mike Garvey who not only performed much of the computational work presented here, but also did much to keep the group functioning more or less properly. Mike and I both possessed the same working class upbringing and work ethics—I like people like that—smart but down to Earth. Heather Adams filled the roll of helping me negotiate academics—the landscape, in my mind sometimes felt like walking through a mine-field. Sometimes when my patience was running a little thin, or my temperament was running a little hot, I was glad (perhaps to her chagrin) that Heather was around. Rasha Abuflaha was the first new student I was personally charged with training. I was extraordinarily busy with other things, but Rasha was able to figure it out in spite of this. You've grown immensely as a scientist and we are all very proud of you. And finally Mausumi Mahapatra. I think only once in the past 5 years have I heard her say anything disparaging about anyone. She's an example of patience and dedication—silent professionalism. The patience, especially, is a quality I find enviable. I can't count how many days in the basement where the best thing that happened all day was Mausumi's arrival in the morning, like a rare bird flew in to the lab.

I would like to thank my family, and in particular my mother and step father, and my dad and stepmother, and my brother and sister. I've put all of you through a lot over the years. Even when I decided to go back to school and finish my Ph.D., and you questioned my sanity, you still supported me. My sister Molly deserves special mention—she helped me through some very dark times (but that's story for another time). Regrettably my father and stepmother, and my grandparents are not here to see this. My grandparents offered unconditional support and taught me good, working class, values. My dad used to tell me when I was a kid “you march to your own drummer.” I think he was amused by my healthy disregard for authority. Perhaps he's watching this chapter of my life with pride. I like to think so. For my mom—I know my past looks like a junk-yard full of false starts, but finally this chapter of my life is coming to a close. I guess a lot of life had to happen first. And you have to admit, this past 25 years has been something they could write movies about. (maybe the memoirs will be my second book?) I came into this with the conviction that I will literally work myself to death before I have it ripped out of my hands again. Perhaps not the healthiest approach to life, but you have to admire the fortitude.

Finally, I have to thank Ruth who was behind this from the very beginning. When I came home from work and announced “I think I'm going back to finish my Ph.D.” I think I was hoping she would talk me out of it. Instead, she encouraged me to take a GRE, loaned me the funds for a security deposit on an apartment, funds for books and a laptop.... She watched, sometimes with real concern for my health, as I struggled and clawed my way through a degree. Ruth is one of the few influences in my life that I can set my watch to (in fact, Ruth's watch is set 10 minutes fast!) and has been a source of much needed stability (“stability” is a commodity in short supply as a graduate student). She always helped me slow down for a minute and not act out of haste. Ruth has faced trials of her own, and has emerged very strong, very logical and very organized. She is also extremely charitable, and is an absolute warrior when it comes to causes she believes in. She has been the most positive influence in my adult life and she has helped me immeasurably through my various highs and lows. The world could use more people like her, and I'm certain her influence has extended much further than she appreciates. Because she doesn't care about reward or recognition. She simply does good things because they are the right thing to do. That's a philosophy I can really get behind.

This has been one of the most difficult and certainly the most demanding undertaking of my life. I can't express the gratitude I feel for everyone who supported me—the financial, emotional, and intellectual resources were put to good use and I can honestly say this dissertation represents my maximum effort and highest intellectual, scientific, and aesthetic standards. I hope I did you proud.

Chapter 1

Introduction

In this work, the surface chemistry of isocyanide and thiolate ligands on gold substrates will be explored. While the chemistry of these functional groups had been explored extensively for many years, it wasn't until quite recently that 1,4-phenylene diisocyanide was found to *self assemble* on single-crystal Au(111) substrates to generate long, linear oligomers of alternating Au/PDI units. The result was curious as earlier literature suggests that when dosed from solution, 1,4-PDI coordinates gold in an upright η^1 configuration, yet scanning-tunneling microscope (STM) studies (which were amply confirmed by DFT calculations) indicated that the flat lying η^2 state was stable. This offers intriguing opportunities for study in several areas. One is potential applications to the growing field of *molecular electronics*. The second is the chemistry of the adatoms themselves, and how they might be used to take an extremely unreactive metal like gold, and tune it's reactivity through surface functionalization.

The term “molecular electronics” was coined in a visionary 1974 paper by Avarim and Ratner. [1] The modern silicon based transistor (the basic component of a vast number of integrated circuits) was invented by Bell Laboratories in 1947. Since that time, a staggering effort has been made to decrease the size of these devices. In 1974, Avarim and Ratner proposed an intriguing idea. It should be possible to build a *molecular* diode in a similar fashion to building a standard silicon P/N-junction based diode, simply swapping out the silicon for molecular level components. To this end, an N-type half of the molecule could be built by substituting half of the molecule with electron donating groups, and the P-type half could be substituted with electron withdrawing groups. The two would be connected through a sigma-bond (a *methylene bridge*) to provide weak electronic coupling between the

two. By applying a forward bias, the HOMO and LUMO orbitals can be brought into a resonant condition, allowing for conduction of charge carriers, while if the bias is reversed the orbitals are pushed further out of resonance. Since the time of Aviram and Ratner's seminal work, great strides have been made in the field. Theoretical studies have complimented some very elegant experiments in an effort to understand, on the quantum level, the dynamics of passing charge through discreet molecules.

From a more practical view, we are rapidly reaching the limits standard lithographic techniques. If

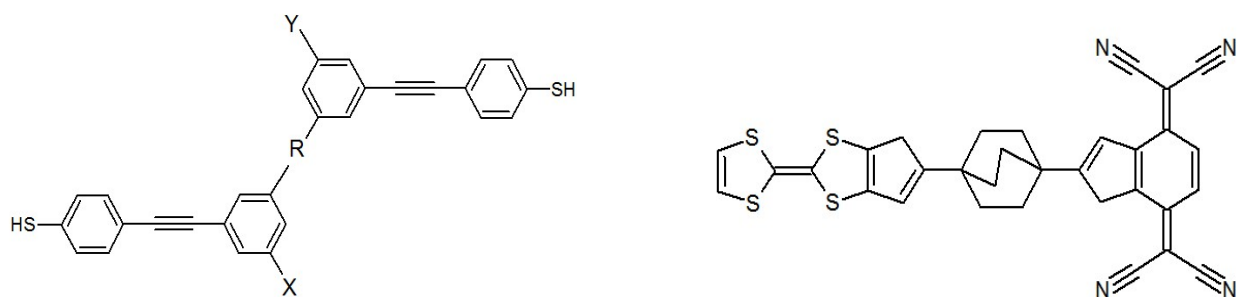


Figure 1: At left is the classic Aviram and Ratner diode. X is an electron donor group ($-\text{CH}_3$, $-\text{OH}$) and Y is an acceptor group ($-\text{F}$, $-\text{NO}_2$) [1]. The two halves are separated by a sigma-bonded bridge (R) which serves as a tunneling junction between them. At right is another example of a molecule with rectifying behavior, as measure in a Langmuir-Blodgett film configuration [2].

the rate of miniaturization of electronic devices is to continue a method to increase the packing density of devices on a chip must be increased. Unfortunately modern techniques rely of some form of optical lithography and as such the smallest absolute size becomes a function of the wavelength of light used for the lithography.

The lithographic techniques represent a *top-down* method of fabricating devices. In some sequence of masking, etching, implanting, etc., devices are, in a sense, carved out of a bulk semiconductor. In his famous “There's Plenty of Room at the Bottom” lecture, Nobel Laureate Richard Feynman suggested another philosophy—a *bottom-up* approach to the problem [3]. He holds up nature as a

model of what is possible (information storage in DNA for example), and envisioned a world where devices could be fabricated where conductors were wires perhaps 10 atoms wide, or bits of information could be encoded in clusters or other assemblies as small as a couple dozen atoms. According to Feynman, it was a matter of “arranging atoms the way we want”—of building useful nanostructures, literally, from the bottom up. He obviously understood that one great challenge would be the manipulation of objects on the *truly* small scale. Feynman's 1959 lecture is considered by many to be the seminal event in the history of nanotechnology.

Presented in this work is largely an effort to understand the rules of adatom templated molecular self assembly, and demonstrate that this chemistry is a viable paradigm for manipulating objects on the atomic scale. The resulting nano-architectures of the thiolate and isocyanide systems have in common a gold adatom to which two functional groups are coordinated (in structures broadly termed *metal-organic coordination networks*—a surface analog of 3-dimensional *metal-organic frameworks* or *MOFs*).

This dissertation will focus on molecules functionalized with either thiolate (-SH) or isocyanide (-NC) “anchor groups”, and their chemistry on gold will be presented. This volume begins with Chapter 2, where the requirement for working in ultra-high vacuum conditions will be discussed, along with much of the hardware require to achieve and maintain these pressures ($\sim 2 \times 10^{-10}$ Torr or less). As scanning tunneling microscopy (STM) and reflection-absorbtion infrared spectroscopy (RAIRS) were used extensively in this work, the theory behind these instruments and details of the specific instruments used in this work will be discussed.

In Chapter 3, the structure of self-assembled oligomers of 1,4-phenylene diisocyanide on Au(111) will be discussed in detail. STM measurements indicated that that oligomers image as a series of bright spots of equal size, “brightness”, and apparent height. The structure of the oligomers was interrogated by bias dependence studies and comparison with density functional theory (DFT) calculations and

STM simulations.

Chapter 4 proposes a mechanism for the initiation and propagation of the 1,4-PDI/Au oligomeric chains presented in Chapter 3. DFT calculations support the hypothesis that the chains propagate from step edges, where η^1 1,4-PDI/adatom species are rapidly formed by reaction of 1 -NC group with the low coordination atoms of the step. Then, mobile 1,4-PDI on gold adatom species diffuse into position and “click” into place, generating the next monomeric link in the chain.

The field of *molecular electronics* is dominated by elegant but exceedingly difficult experiments designed to probe transmission through *single molecules* or small ensembles of them. One clever approach relies on a mechanically controlled break junction (MCBJ), where molecules are installed between electrodes which are moved in and out of contact while I-V measurements are carried out [4-6]. Another common approach involves scanning a surface with a conductive atomic-force microscope probe (C-AFM) [7,8]. Chapter 5 is an effort to examine whether the self-assembly chemistry demonstrated in Chapter 3 can be extended from single crystal Au(111) to an insulating substrate, muscovite mica. If the approach to *bottom up* fabrication presented in this dissertation is to have a chance at real-world implementation, growing the architectures on insulating substrates would be a critical first step toward integration with existing CMOS technologies. Thermally evaporated granular gold films were prepared, and the films dosed with 1,4-PDI which caused a dramatic drop in sheet resistance. It was found that plots of $\ln(R_0)$ vs. $T^{-1/2}$ (where R_0 is the resistance of the clean film) are linear. This suggests that the model of activated tunneling proposed by Abeles and Sheng is appropriate [9], rather than a simple Arrhenius model where it would vary with $1/T$.

Gold was long thought of as chemically “uninteresting” [11]. In fact, investor Warren Buffett is claimed to have said gold is “without utility” [10]. This view changed in the mid-1980's when it was reported by Haruta [12] that gold served as an efficient CO oxidation catalyst, and by Hutchings that it

could also serve as a hydrochlorination catalyst for acetylene [13]. The literature suggests that the interesting chemistry on gold occurs on atoms with low-coordination such as are found on step edges or defect sites [14]. Chapter 6 explores the idea that the adatoms generated and stabilized by 1,4-PDI molecules on Au(111), having a coordination number of only 5 (*vs.* 7 on the surface), could be harnessed. It will be demonstrated that 1,4-PDI saturated surfaces are indeed activated towards gas adsorption. Carbon monoxide, for example, is shown to be stable to $\sim 150\text{K}$, *vs.* $\sim 80\text{K}$ for unfunctionalized, annealed Au(111). Interestingly, the surface was observed to adsorb *cis*-2-butene but not *trans*-2-butene—an effect that is most certainly a matter of steric hinderance. The most intriguing observation of this chapter is the finding that 1,4-PDI is shown shown to undergo a process of “decoordination” upon gas adsorption. The adsorbates induce a change in state from flat-lying 1,4-PDI to an upright, pendant η^1 moiety. If the oligomers are molecular wires, the “decoordination hypothesis” suggest that the individual units can function as gas-driven chemical switches. Indeed, it will be shown that 1,4-PDI functionalized granular gold films can serve as sensors for CO.

As 1,4-PDI was shown to self-assemble on Au(111), a logical direction was to investigate if the phenomenon was general. To this end, 1,3-phenylene diisocyanide on Au(111) was studied in Chapter 7. STM data suggests that indeed 1,3-PDI oligomerizes. However, the 120° angle between the -NC groups imposes structural constrains on the system such that the chains formed by 1,3-PDI are assembled with a pronounced “zigzag” structure, or occasionally forming closed, hexagonal features.

Dithiols, in the field of molecular electronics, have been exhaustively studied [15]. Curiously, only one report involving the surface science of these molecules was found after an exhaustive search of the literature, a surface-enhanced raman (SERS) study [16]. A recent STM report of thiophenol on Au(111) indicated that the monofunctional molecule participates in adatom templated RS-Au-SR bonding [17]. As a consequence of the sp^3 nature of the sulfurs (or more appropriately, *sulphydryls*), the thiophenol dimers were shown to form adatom structures in a *cis* or *trans* configuration. This is

impossible in 1,4-PDI as the sp nature of the bonding imposes the -NC-Au-CN- bonds to be strictly linear. Chapter 8 reports the observation that 1,4-benzene dithiol participates in adatom templated bonding, in perfect agreement with the reports for thiophenol. It seems as though the two functional groups (either “end” of the molecule) participate in this bonding independently. Thus 1,4-BDT is capable of similar oligomerization chemistry as 1,4-PDI. Finally, results of electrical studies on granular films indicate that 1,4-BDT is capable of modulating the height of the tunneling barrier in a similar manner to the observations for 1,4-PDI (in Chapter 5).

In Chapter 9, the surface chemistry of 1,3-benzene dithiol (1,3-BDT) will be investigated. STM data suggests that the bonding to the surface is mediated by gold adatoms. However, no evidence for oligomerization was observed. Instead, rather mobile 1,3-BDT monomers were observed. 1,3-BDT was among the molecules reported fraudulently in the Schön scandal [18]. 1,3-BDT, however, has been reported to show a legitimate gate effect [19], although only 3 out of 256 devices exhibited this property (non-linear I-V curves as a function of gate bias). A hypothesis as to why 1,3-BDT does not participate in RS-Au-SR bonding will be discussed, as well as a possible strategy for inducing oligomerization by modifying adsorption kinetics.

In an effort to investigate further the relationship between molecular geometry and self-assembly, 1,3,5-phenylene triisocyanide was synthesized and investigated by RAIRS and STM. The molecule, as one might predict, generated adatom-mediated structures in the form of well ordered two-dimensional hexagonal “honeycombs”. Structures of this form represent a sort of 2-dimensional metal-organic framework, and Chapter 10 presents a molecular (rather than lithographic) approach to forming well ordered arrays of nanopores.

Appendix A presents techniques for fabricating atomically sharp STM probes. Anodic dissolution, factors effecting aspect ratio, and extensive troubleshooting are presented, along with several strategies for cleaning and sharpening the as-fabricated tips. Clean, stable probes are absolutely critical for STM

performance, and this appendix offers some of the essential skills for this aspect of scanning-tunneling microscopy.

In Appendix B, some of the quantum mechanics behind phenomenon such as the work function of a metal, and the emission of electrons from metals under the influence of a strong electric field will be presented. *Field emission* or *Fowler-Nordheim tunneling* refers to electrons “escaping” a metal surface, and being emitted from a sharp tip (and tunneling into vacuum). The results of a *Fowler Nordheim Plot* (linear plots of $\ln(I V^{-2})$ vs. I/V) can allow for estimates of the radius of an emitter—for our purposes, the sharpness of an STM probe.

The common thread running through this research is the significance of adatom mediation in the self-assembly of various structures on metal and mica surfaces. Also included, where appropriate, are propositions for future research, and in some cases, for overcoming various experimental challenges that were experienced. It is our conclusion that the oligomerization chemistry presented here is a more or less general phenomenon, and if that is the case, there are a great number of systems which could be investigated (assuming, of course, the molecules could be synthesized). With suitable functionalization, hybrid nanomaterials with a range of interesting properties could be envisaged.

References:

- 1) Avarim, A.; Ratner, M.; *Chem. Phys. Lett.* **1974**. 29. 277-83.
- 2) Jenny, N.; Single molecules which show a rectification behavior. **2009**. Powerpoint presentation, Calame research group.
- 3) Feynman, R.; Transcript of 1959 American Physical Society talk available at www.zyvex.com/nanotech/feynman.html
- 4) Jortner, J.; Nitzan, A.; Ratner, M.; *Lecture Notes in Physics*. **2005**. Vol. 680, 13-54.
- 5) Li, C.; et. al. *J. Amer. Chem. Soc.* **2008**. 130. 318-326.
- 6) Bruot, C.; Hihath, J.; Tao, N.; *Nature Nanotechnology*. **2012**. 7. 35-41.
- 7) Kim, C.; Bechhoefer, J.; *J. Chem. Phys.* **2013**. 138 (1).
- 8) Tivanski, A.; et. al.; *J. Phys. Chem. B*. **2005**. 109 (12). 5398-5402.
- 9) Abeles reference
- 10) 2003 July 21, The Times (UK), Section: Business, “Demand for Global Listing Helps to put New Gloss on Gold”
- 11) Häkkinen, H.; The gold-sulfur interface at the nanoscale; *Nature Chemistry*. **2012**, (4), 443-455.

- 12) Haruta, M.; Kobayashi, T.; Sano, H.; Yamada, N.; Novel gold catalyst for the oxidation of carbon monoxide at temperatures far below 0°C. *Chem. Lett.* **1987**, *405*. 405-408.
- 13) Hutchings, G.J.; Vapor phase hydrochlorination of acetylene: Correlation of catalytic activity of supported metal chloride catalysts. *J. Catal.* **1985**, *96*, 292-295.
- 14) Haruta, M.; Kobayashi, T.; Sano, H.; Yamada, N.; Novel gold catalyst for the oxidation of carbon monoxide at temperatures far below 0°C. *Chem. Lett.* **1987**, *405*. 405-408.
- 15) Song, H.; Reed, M.; Lee, T.; *Adv. Mater.* **2011**. XX 1-26.
- 16) Joo, S.; Han, S.; Kim, K.; *Journal of Colloid and Interface Science.* **2001**. *240* (2). 391-9.
- 17) Maksymovych, P.; Yates, J.; *JACS* **2008** *120* (24). 7518-9
- 18) Schön, J. H.; Meng, H.; Bao, Z. *Nature* (London). **2001**, *413*, 713.
- 19) Lee, J.; Lienstchnig, G.; Wiertz, F.; Janssen, R.; Egberink, R.; Reinhoudt, D.; Hadley, P.; Dekker, C.; *Nano Letters.* **2003**. (3). 2. 113-117.

Chapter 2

Materials and Methods

Vacuum Systems

The majority of the research carried out during the course of the studies contained in this work were performed under conditions of reduced pressure. In the case of scanning-tunneling microscopy (STM) and reflectance-absorbance infrared (RAIRS) studies, the experiments were carried out exclusively in the *ultra-high vacuum* regime where the pressures were maintained in the range of 10^{-10} Torr. The electrical studies on granular films could not be performed at these pressures as the sample integrity would not be preserved during the *bake out* of the system which would be required to achieve them. The experiments were still carried out in the *high vacuum* regime, at pressures in the 10^{-7} - 10^{-8} Torr range. This section will include details on the necessity for such conditions and the hardware required achieve them.

Why UHV?

It has been stated “nature abhors a vacuum” [1]. The phrase *horror vacui* is often attributed to Aristotle who held the belief that there were no true voids in nature—that as soon as one were created, the more dense surroundings would move in and fill it. Anyone who has undertaken research requiring reduced vacuum, and particularly ultra high vacuum (UHV) would certainly agree. Creating and maintaining pressures lower than deep space, here on Earth, is fraught with difficulty. The obvious question then is, why do it?

There are two major reasons why it is desirable to work in reduced pressures. The first one is cleanliness. The *flux* of particles on a surface can be calculated according to Equation 1 which is also known as the Hertz-Knudsen equation.

$$F = \frac{P}{\sqrt{2 \pi k_b T m}} \quad 1)$$

Here the flux, F is a function of the gas pressure P , the temperature T , the mass of the gas molecules m . A crystal with an area of 1 cm^2 has approximately 10^{15} atoms at the surface. If $T=300\text{K}$ and $P=10^{-6}$ Torr, the resultant flux would be $F = \frac{10^{15} \text{ molecules}}{\text{cm}^2 \text{ s}}$ [2,3]. For a reactive gas and metal (say palladium exposed to CO), one would expect every collision to result in the molecule sticking (ie, the *sticking coefficient*, $S=1$). In this case, a perfectly clean crystal would become saturated with an adsorbate in 1s at 10^{-6} Torr. In fact this is the basis for the common unit of gas exposure, the Langmuir, L ($1L=10^{-6}$ Torr . s).

If one goes through a difficult and complicated process of getting a surface atomically clean, if the surface is reactive it could be completely saturated with contamination within one second at a pressure of only 1×10^{-6} Torr. In order to lengthen the time the sample stays clean, the only solution is to make the *impingement rate* of adsorbates (from the vacuum chamber's *background pressure*) as small as possible. This makes it possible to exclude extraneous molecules and carefully expose the sample to known amounts of adsorbates.

The second reason one might want to work in ultra high vacuum is that there are a range of techniques that require a large *mean free path*. The mean free path is a measure of the average distance a molecule (or other species such as electrons) in the gas phase can travel before colliding with another molecule. This allows several powerful techniques to be utilized that would not work in an atmosphere. Specifically, surface scientists work with many electron and ion based techniques such as low-energy electron diffraction (LEED) and Auger spectroscopy. A large mean free path is also needed for many methods of fabrication where metals, ceramics, and other materials are evaporated and travel large distances before landing on a target. Using the *hard sphere approximation*, the mean free path (λ) can be calculated according to Equation 2 where d is the effective diameter of the molecule, P is the

pressure, and T is the absolute temperature [2].

$$\lambda = \frac{k_b T}{\sqrt{2\pi} d^2 P} \quad 2)$$

The research discussed in this volume was carried out in the ultra high vacuum regime, except in the case of I-V measurements where thermal instability precluded baking the vacuum chamber. Even in this case background pressures were in the 10^{-8} Torr (or less) range.

UHV Chambers:

Traditionally UHV chambers were made of glass, but in the past several decades they have been all but replaced with welded stainless-steel. Stainless steel is a suitable material for UHV chambers as, in order to achieve pristine UHV it is necessary to *bake* the chamber to a temperature of ~ 150 - 200°C for 24-36 hours to remove the vast majority of adsorbed contamination from interior surfaces. Stainless-steel can easily withstand these temperatures, is easy to fabricate with standard techniques, and offers a very low outgassing rate and a high barrier to diffusion of lighter gasses such as hydrogen and helium. Many of the techniques used in surface science rely on accelerating ions or electrons. For this reason, non-magnetic stainless steel (typically 304 series) is used. This material is easy to fabricate, has a low-outgassing rate, and will not induce extraneous magnetic fields inside the chamber [4].

Generally the vacuum chamber has a round cross section and is fabricated with a number of *ports* which allow for the installation of instrumentation, windows, etc. The ports have flanges which have been machined to a knife-edge that is designed to be used with a high-purity copper gasket. Upon torquing the bolts in a *torque sequence*, the knife-edge cuts in to the copper (which is much softer) and forms a seal that is UHV compatible, and also capable of withstanding the high temperature bakeout. *Conflat*® type knife hardware was used throughout. These offer excellent UHV performance, but care must be taken to avoid damaging the edge. Even very small nicks in the edge can create micron sized leaks, and for good UHV performance this is totally unacceptable.

The use of flanged ports allows a chamber to be configured in a number of different ways. The ports are typically aligned towards the central axis of the vacuum chamber so that a manipulator or transfer arm can be used to position the sample for such tasks as cleaning, annealing, or analysis—any apparatus required for these operations is also mounted radially on the chamber body. Any unused

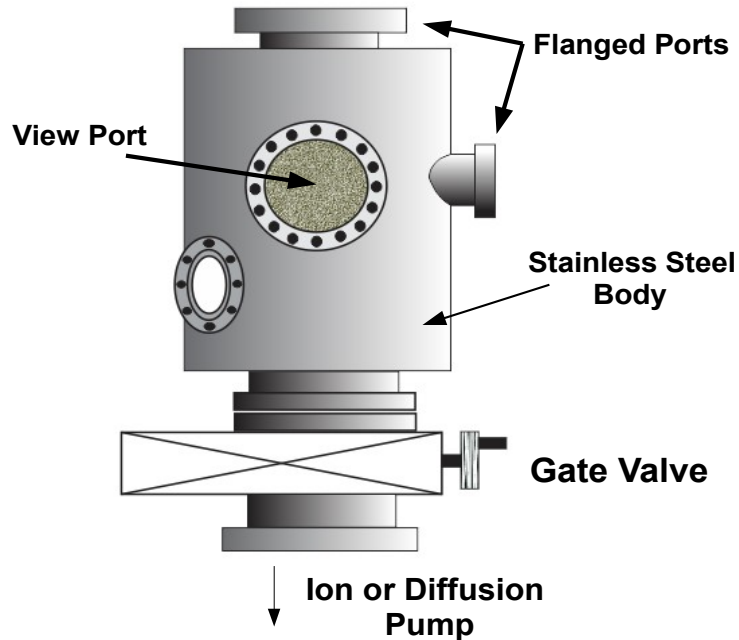


Figure 1: A typical stainless-steel UHV chamber. A variety of ports are installed which allow the chamber to be reconfigured if the need arises. UHV conditions are achieved by *baking* at temperatures of around 120⁰C while pumping. At these temperatures, water and other contaminants desorb from the inner walls and are pumped away. ports can be covered in blank flanges to simply cap them off.

The *bakeout* is performed by wrapping the chamber tightly with resistive heating wire and then a layer of close fitting aluminum foil to help distribute the heat (aluminum is a much better thermal conductor than stainless). Finally the entire chamber is covered by a loose fitting “tent” of aluminum foil to help contain the heat and keep drafts away from the body while it is heating. The temperature is then increased by using a variable AC transformer such as a Variac to pass a current through the heating wires and monitoring the temperature and pressure. It is critical during the bakeout to have uniform

and sufficiently high temperature to desorb contaminants. The temperature (and pressure) are monitored periodically with a thermocouple probe and ionization gauge installed in the chamber. From time to time the heating wires burn out or short, and this can leave large sections of the chamber well below proper temperature. Cold spots will act to condense the contamination which was desorbed elsewhere in the chamber and strong temperature gradients have been known to slightly deform flanges and cause leaks.

The entire point of baking a chamber is to remove as many molecules from the inner volume as possible. While it is rather easy to desorb molecules from clean stainless steel, it can be a little more troublesome to desorb them from components such as filaments or heating wires. Some of these filaments are coated with materials such as iridium to modify their work functions and can be quite gassy. For this reason it is common practice to *degas* as many components as possible prior to baking. This process involves simply heating the component (i.e. running a higher than normal current through a filament), monitoring the pressure, and discontinuing heating when the pressure begins to drop. It is solid vacuum practice to degas the components prior to baking (if pressures are low enough that it can be safely done) to rid the chamber of the bulk of the contamination, and once again after turning off the bake but while the chamber is still fairly warm.

Vacuum Pumps

Vacuum pumps are perhaps the most critical component when working in UHV conditions. In order to achieve good UHV conditions (5×10^{-10} Torr or less) obviously the most minute of leaks must be eliminated and a pump must be installed that is capable of pumping faster than the outgassing rate of the chamber. To achieve this, pumps are normally installed in stages as they operate best over narrow pressure ranges. In this section the basic functions of the mechanical oil pump, the oil diffusion pump, the turbomolecular pump, and finally the ionization pump will be discussed. Each has there place along with their own particular strengths and weaknesses.

Mechanical (rotary) Pumps

A mechanical pump is in a class called the *positive-displacement pumps* [5]. In a mechanical pump, a set of rotating vanes are moving off-axis within an oil-containing cylinder. The vanes are spring loaded and as such are moving in constant contact with the cylindrical *stator*. The principle behind its operation is simple and clever. As the vanes rotate eccentrically within a cylinder, on one half of the cylinder the volume of the container is increasing as the rotor spins. This expansion causes a decrease in pressure which is what is creating the “pull” of the vacuum. On the other half of the cylinder, the volume is being reduced and the entrained gas molecules are being compressed until they finally are exhausted through a one-way valve. These pumps, with clean oil and in proper working condition can attain pressures in the low-millitorr range. While this is not nearly sufficient for UHV work, we will see that the mechanical pumps are an indispensable part of vacuum science. The advantage of a mechanical pump, often referred to as a *roughing pump* is that they are the only one in the arsenal that can be started at atmospheric pressure. They are mechanically rugged and will function literally for

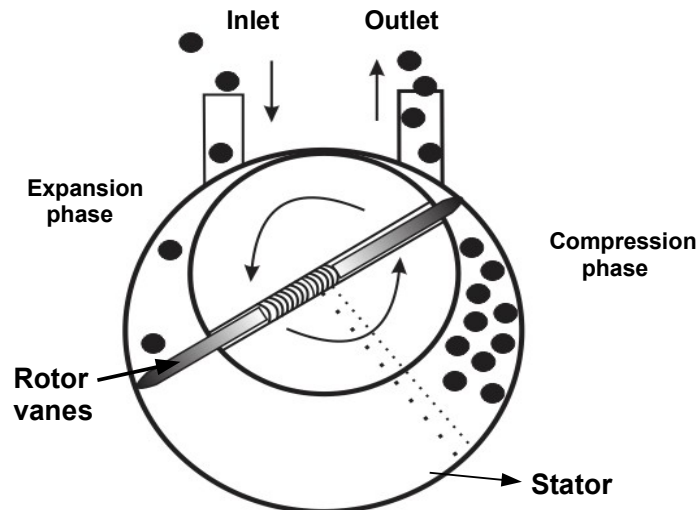


Figure 1: Rotary-Mechanical Vacuum Pump The heart of the mechanical pump is a set of spring loaded vanes that rotate eccentrically within an oil containing cylinder. Since the vanes are off-axis, one half of the rotation results in an increase of the entrapped volume while the second phase results in a decrease of the volume (compression). The oil both seals and lubricates the vanes.

months with only minor maintenance. The disadvantages are that they do use oil, so backstreaming can be a problem. Also, they are noisy and generate significant mechanical vibrations—they must not be running when one is imaging with an STM for example. Finally, in at least one case an electrical motor was responsible for inducing noise into a low-current measurement. This is not a problem with mechanical pumps specifically, but with electric motors in general.

Turbomolecular pumps

Turbomolecular pumps fall into a class referred to as the *momentum transfer* pumps [6]. Turbomolecular pumps function in a manner not unlike a jet-aircraft engine. A series of blades rotate at very high speed (thousands of RPMs) in very close proximity to a set of stationary *stators*. As the blades spin, in a sense they “hit” the gas molecules, giving them momentum in a given direction. The blades are configured so that blades closest to the chamber are at a more aggressive angle than the one furthest away. As a result, the compression is highest in the front and gets progressively smaller towards the rear. As the blades rotate there is a higher probability of the gas molecule colliding with the surface facing to the back and thus most often the momentum is transferred in such a way that the molecules are propelled away from the vacuum chamber. In this way a compression gradient is set up that moves molecules from the front of the pump to the back of it. For a turbomolecular pump to work properly, the gap between the rotor and stator (the moving and non-moving pairs of parts) must be smaller than the mean free path of the gas molecules in the pump. At atmospheric pressures the mean free path is ~70 nm and building a pump with these tolerances would be virtually impossible. Instead, the pump is operated with a *backing pump*. This reduces pressures to the milliTorr range and increases the mean free path to several centimeters. The rotor/stator tolerance is typically ~1 mm, and so the pump functions perfectly backed by a mechanical rotary pump [7].

Turbomolecular pumps have the advantage of high pumping speed for the heavier gasses (momentum transfer is not a great strategy for removing light molecules). They are very clean, and

also can be started and stopped in a few minutes. While the pumps work extremely well, they are expensive and great care must be used while operating them. Accidentally exposing one to high pressure while it is up to full speed can cause severe damage. The blades are extremely thin and moving with incredible angular velocity. Still, the turbomolecular pump is extremely versatile and can be operated from intermediate to UHV pressures.

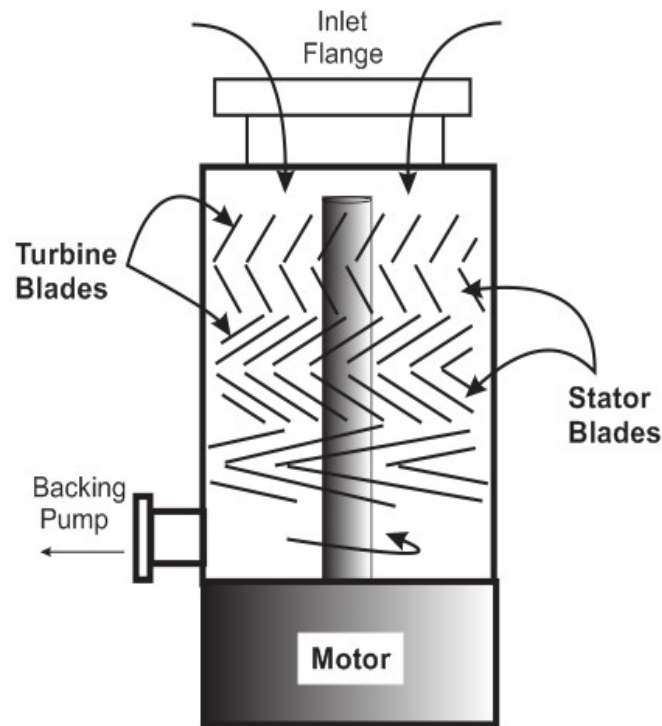


Figure 2: Cutaway view of a turbomolecular pump. Turbomolecular pumps operate on the principle of *momentum transfer*. A stack of turbine blades rotate at very high speed with respect to stator blades. A compression gradient is set up which causes gas molecules entering the front of the pump to be directed to the rear where they are pumped away by a mechanical pump.

Oil Diffusion Pumps

Another momentum transfer pump is the *diffusion pump* [8,9]. Diffusion pumps use a special oil with very low vapor pressure, and rely on a very clever mechanism to generate UHV conditions. The oil is heated in the base of the pump under rough vacuum. At some temperature the oil begins to vaporize and climb up the central portion of the pump. Here, a series of nested cones (often called the

Christmas tree) force the rising oil to make an abrupt change in direction—back down. The clearance between the nested cones is quite small, and if the pump is functioning properly, this change in direction actually generates a *shock wave* as the oil changes from the laminar to the supersonic flow regimes. In operation, gas molecules that are being pumped from the vacuum chamber find their way in to the diffusion pump where they encounter this shock wave. As a result they get propelled to the bottom of the pump housing where the mechanical pump removes them from the system. Any gas molecules that try to escape have a very low probability of doing so, as to escape they would have to overcome a series of 3 or 4 shock waves directing them in the opposite direction.

The diffusion pump has several advantages. It is very capable of achieving UHV conditions. There are no moving parts, or at most require a small cooling fan. However, since the pump relies on hot oil, there can be some backstreaming of oil into the UHV chamber. This is often mitigated with a liquid nitrogen cold trap, which serves the dual purpose of reducing oil from streaming up in to the chamber, and also soaking up energy from the molecules in the UHV chamber, which makes them pump more readily. Finally, diffusion pumps are sensitive to oil contamination. Even small amounts of water or solvents can ruin the operation—the ultimate pressure is a function of the vapor pressure of the oil. Oil diffusion pumps seem to be on the way out in recent years as there are cleaner options. Still, they provide a viable method for achieving high and ultra high vacuum conditions.

Ion Pumps

Also referred to as *sputter-ion pumps*, these are the modern choice for achieving pristine UHV conditions. The pumps are capable of reaching vacuums into the 10^{-11} Torr range, and they do not require the use of any oil or moving parts so there are no associated problems with vibration or oil backstreaming. An ion pump works on by applying a high DC bias between anodes (normally stainless-steel tubes) and cathodes which are often made of a titanium alloy. There are strong permanent magnets installed which induce a field along the axis of the hollow anodes, and this forces

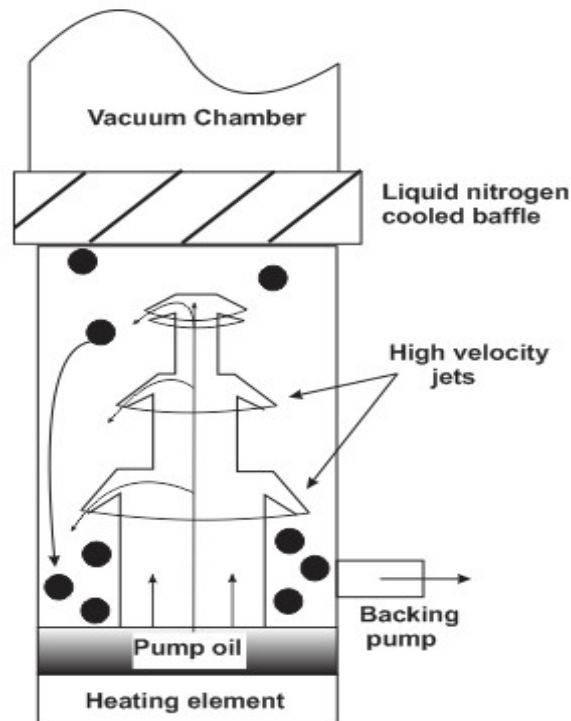


Figure 3: Oil Diffusion Pump The diffusion pump operates by heating low vapor pressure oil (formerly mercury) to vaporization and allowing it to travel up a series of concentric cones. The abrupt change in direction produces a super-sonic jet of oil which propel gas molecules from the chamber in to the base of the diffusion pump where they are pumped away by a mechanical pump.

electrons within them to move with a cylindrical or helical trajectory (a *Penning trap*). This trajectory enhances the probability of a collision with incoming gas molecules.

As gas molecules are ionized, they are accelerated towards the cathodes with enough kinetic energy to be buried in it, effectively trapping them there. When heavy atoms and molecules are pumped, they often have enough kinetic energy to *sputter* some of the cathode material away which leaves a fresh, clean film of reactive metal. Titanium readily forms stable complexes with reactive gasses such as CO, oxygen, and water so these offenders are quickly and permanently removed from the system in the form of non-volatile oxides, hydroxides, and carbonyls [10]. It should be noted that *inert* gasses such as argon do not form complexes with titanium and so pumping these species with an ion pump is painfully slow.

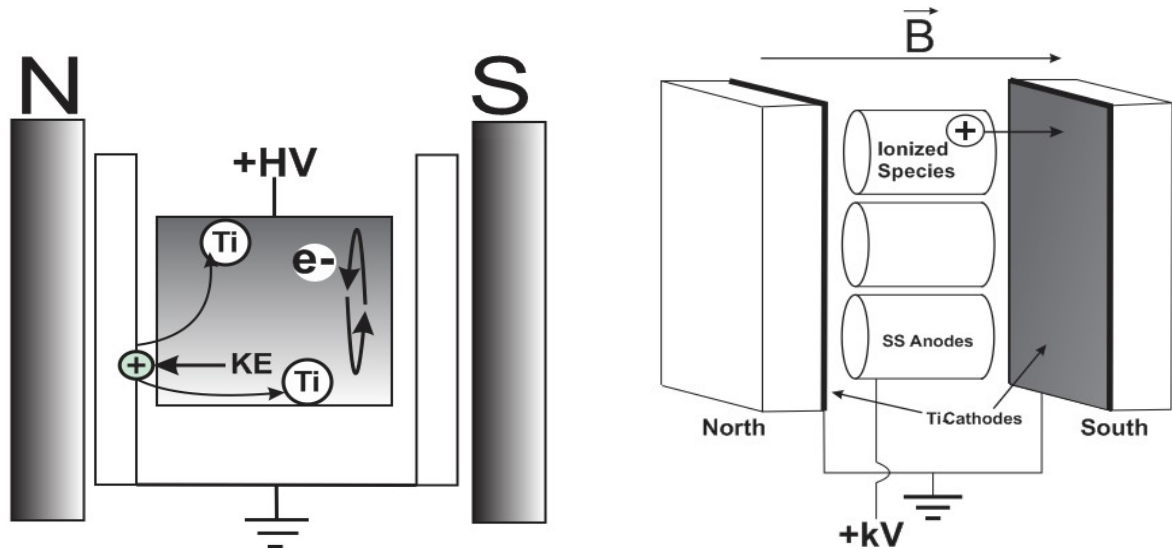


Figure 4: Ion Pump Ion pumps function by generating ions from molecules in the presence of a strong electric field. The resulting ions are then accelerated towards the cathodes with sufficient kinetic energy that they become embedded in them. The process also sputters a small amount of the cathode material (typically a titanium alloy). The reactive metal serves to help pump the system by generating unreactive solids from gasses in a process known as *gettering*.

Since ion pumps work by taking gasses and either chemisorbing or physisorbing (a process often called *gettering*) them into the electrodes of the pump, they do not require backing pumps. If used properly (i.e. not pumping on leaks) they require very little maintenance. The lack of mechanical backing and moving parts make ion-pumps ideal for vibration sensitive applications like STM chambers. Recent literature suggests that under some conditions ion pumps can back stream free radicals [11]. While we have not experienced this problem, it should be noted as being within the realm of possibility.

Ultrahigh Vacuum Systems

When we discuss a UHV *system* we are generally concerned with the entire chamber with its associated vacuum pumps, instrumentation, windows, ports, manipulators, etc. In the course of this research, two UHV systems were used, and another system was operated under high vacuum conditions ($\sim 1 \times 10^{-8}$ Torr): These systems will be discussed in the following sections.

RAIRS system:

The reflectance absorption infrared spectroscopy (RAIRS) chamber used in this work comprises a 12” diameter main body to which a number of flanges are available for mounting vacuum hardware. A screw-drive rotatable manipulator allow a crystal to be mounted on rods connected to vacuum-compatible feedthroughs. The chamber is pumped by a Varian ion pump as well as a 10” turbomolecular pump. The sample can be moved in to the main chamber for cleaning (oxygen roasting and/or argon ion bombardment). The main chamber also features Auger spectroscopy capabilities, an ion gun for sample cleaning, and several available flanges for other hardware such as evaporation or dosing sources.

To perform measurements, the RAIRS chamber is combined with a commercial Bruker Vertex FT-IR spectrometer. A diagram of the system is shown in Figure 5. The spectrometer has been configured to direct infrared radiation from the glow bar through a port in the side of the body. The infrared beam is reflected from a series of gold-coated mirrors and through a KBr window, and on to a single-crystal (the “sample”). In this configuration, the crystal itself is acting as one of the optical elements. The beam is reflected off the crystal, out of the cell, and finally in to a nitrogen cooled mercury-cadmium telluride detector. The entire external optical path is enclosed under polycarbonate boxes which allow the IR beam to be maintained under a purge of scrubbed air (passed through CO₂ and H₂O columns) or liquid nitrogen boil off. This *purge path* is critical as there is over 1m of optical path outside of the commercial instrument. If the purge path becomes compromised with leaks, it becomes exceedingly difficult to acquire a good, stable background. A small concentration of these gasses multiplied by a 1m path length can result in signals that obscure the experiment entirely.

Another extremely useful feature of the RAIRS system is the capability for performing low-temperature spectroscopy. To facilitate this a long, thin stainless steel tube can be inserted into the

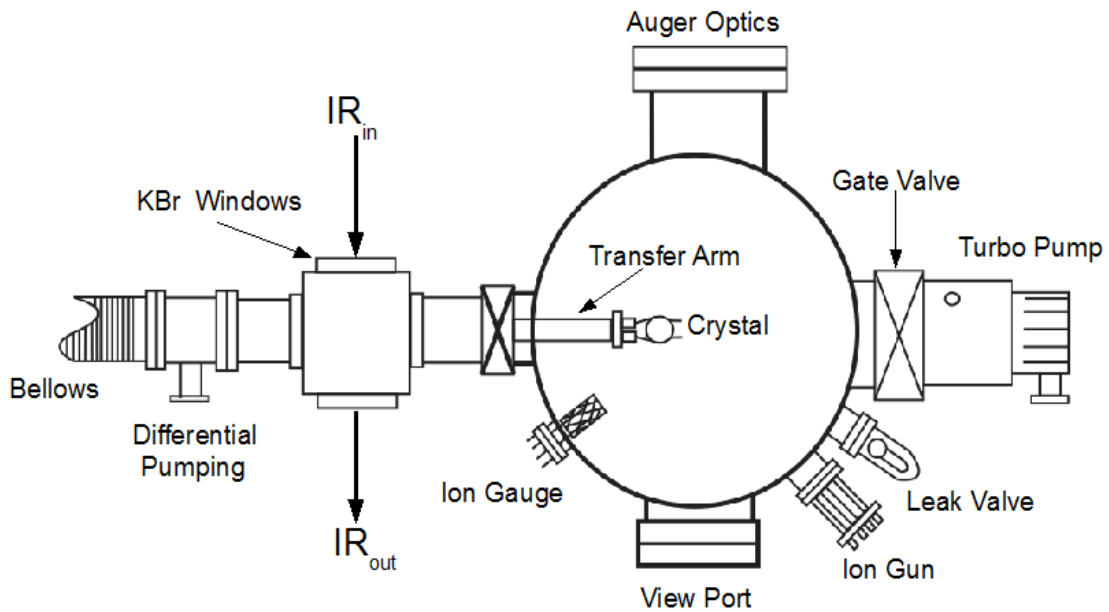


Figure 5: Top view of RAIRS system. Some components not shown for clarity. In this configuration, crystal is moved into main chamber for cleaning or Auger analysis, and back to IR (high pressure) cell for surface infrared studies.

transfer arm and a gentle stream of liquid nitrogen introduced onto the non-vacuum side of the flange.

The sample is in excellent thermal contact with the heating wire feedthroughs, so by cooling the feedthroughs to 77 K, the sample can typically be cooled to a temperature of ~ 90 K. Since the sample can be resistively heated while it is under liquid nitrogen cooling, often times RAIRS can provide direct spectroscopic measurements of thermodynamic properties such as desorption temperature.

Further discussion of the theory behind surface infrared can be found later in this chapter.

Conductivity Measurement Chamber:

The chamber used for sample conductivity measurements (I/V measurements) consists of a main body built from a 10" 6-way cross. The chamber is pumped with a turbomolecular pump as well as a rather oversized ion pump. The sample holder is fitted to high vacuum feedthroughs which are installed in an X, Y, Z, Theta manipulator as in Figure 6. These samples are not thermally stable, so the chamber is operated un-baked. As such it's not truly a "UHV chamber". Still, the chamber routinely achieves pressures below 10^{-8} Torr after several hours of pumping at room temperature. The

chamber can be reconfigured easily to include leak valves, ion guns, or other hardware as needed.

The manipulator was configured so that a copper plate was mounted to both current feedthroughs. However, in this configuration the feedthroughs were simply used to couple the copper plate to the liquid nitrogen reservoir (on the non-vacuum side of the system). Electrical connections to the sample as well as a thermocouple were connected through a secondary feedthrough. Electrical measurements were carried out under PC control. Briefly, a Labview program was implemented (O. Furlong) such that a data card ramps a voltage (specified by the experimenter) across the *device under test*. The resulting current was measured through a Keithley picoammeter placed in series. The Keithley converted the current to a voltage signal which was sent back to the data acquisition card and a

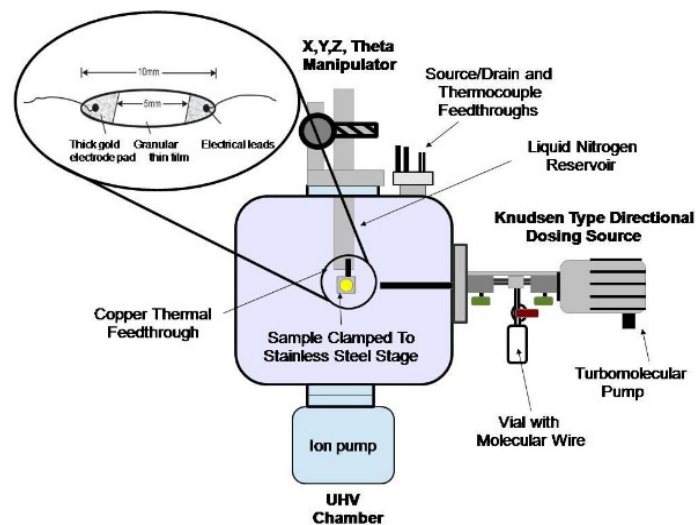


Figure 6: Typical configuration of I/V chamber. In the configuration shown, molecular wire (precursor) materials can be dosed from a Knudsen source. Not shown is a leak valve which was used for gas sensor experiments. Details of instrumentation are found in Fig. 7.

simple X,Y data table was created of current vs. voltage. To enhance signal to noise, the Labview program allowed for time integration and also for taking multiple measurements and averaging the results. These last two features became important with very high resistance samples (ie, low-current measurement). To further lower noise levels, it became critical to keep measurement leads as short as

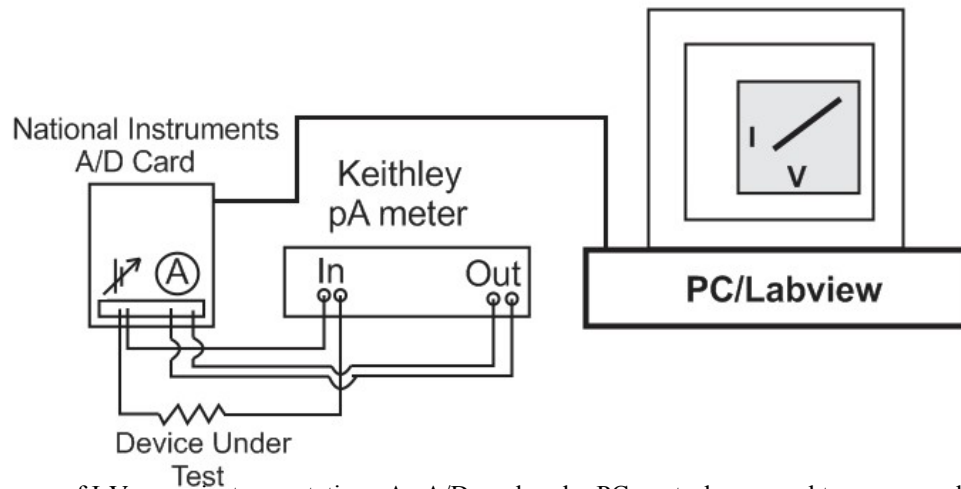


Figure 7: Block diagram of I-V curve instrumentation. An A/D card under PC control was used to ramp a voltage (typically $\pm 4\text{V}$) through the sample or *device under test*. A picoammeter placed in series collects the resulting current which is fed back in to the A/D card. This allows for the collection of I/V data directly. The Labview program allows for increasing integration time and changing the voltage step as needed. High-quality shielded wire and careful grounding are critical for proper functioning of such a system.

possible. The leads were constructed of high quality shielded wire (with the shield grounded to the chamber). The data card was placed in a metal box which was grounded to the Keithley chassis ground, and both of these were also grounded to the chamber. In this configuration, extraneous electrical noise and ground loops are minimized as the entire system (except for the measurement path) is floating at the potential of the chamber itself and the chamber and wire braids of the shields function as a suitable Faraday shield.

The actual electrical connection to the samples was made using smooth micro-alligator clips. The half of the clip that comes into contact with the sample was polished with fine sand paper to prevent damage to the delicate mica substrate. To account for the thickness of the sample stage ($\sim 3\text{ mm}$), the clips were carefully bent in such a way that upon clamping them down on the mica substrate a plane on plane connection was formed. Then the other jaw (the one that would be in contact with the sample stage itself) was covered with UHV compatible fiberglass tubing. Samples were installed carefully to prevent damage to the mica or granular gold film.

Scanning Tunneling Microscope (STM) System:

The STM system is composed of 2 chamber connected by vacuum-compatible gate valve, with a transfer arm system that allows the sample holder or scanning tips to be moved between them. On one side of the gate valve is the *preparation chamber* or simply *prep chamber*. The prep chamber is fitted with an ion-gun pointing towards the central axis of the chamber. The chamber is also fitted with two leak valves connected to a glass gas handling manifold. Finally, the chamber is fitted with a turbo-molecular pump used both for bakeout and for routine operations such as cleaning. In this way, the preparation chamber is where samples can be ion bombarded, oxygen roasted, or annealed. The high gas pressures required for these steps means that pressures can take considerable time to recover. However, these steps are carried out with the gate valve between the preparation and SPM chamber closed. This allows the high pressure (dirty) work to be carried out without undue contamination of the microscope chamber. The preparation chamber is also fitted with a LEED system.

The *SPM* chamber is the other half of the STM system. The SPM chamber is constructed of 12” diameter stainless steel and also pumped by a Varian ion pump. The chamber is fitted with a leak valve, a Knudsen source, and of course a scanning-probe microscope (and sample stage). Two commercial scanning tunneling microscopes were used in this research. Both were designed and built by RHK Technologies. One of the microscopes is capable of AFM or STM operation, while the other one features STM only capability. The microscopes are mounted to 6” flanges which contain the required electrical and (in the case of the AFM system) fiber optic connections. Both can operate in air or UHV, and the system is rated for low-temperature operation using liquid nitrogen or helium as the cryogen (although the helium capability remains, at the moment, untested). The cryogenes cool a sample stage that features extensive vibration isolation measures. The SPM chamber has a set of shelves with allow for storage of 3 sample holders and 3 tip exchangers. Another very useful feature of the SPM chamber is a *load lock* system which allows for transferring samples and tips in and out of the

chamber without breaking UHV. The load lock is pumped by a turbomolecular pump, which is also used to pump the system during bake out. The load-lock has saved considerable time as minor repairs to the sample holders or changing out tips can be performed after just a few hours of pumping rather than breaking vacuum, performing the repair, and baking the entire chamber for several days.

The chambers are mounted on a very solidly built, massive steel frame fitted with air legs. While imaging, great care is taken to isolate the chamber from the rest of the laboratory. Nothing is allowed to contact the chamber or frame that is not absolutely required for operation (ion pump and microscope cables). The sheer mass of the system (estimated at over 1000 pounds) and the air legs act as a low-pass filter and is the first line of defense against extraneous vibrations--a serious issue for high-resolution STM work. Also, the microscope is installed in the basement where presumably building vibrations, building movements and acoustic noise are at a minimum.

Metal Evaporator:

The metal evaporation carried out as part of this work was performed in a Cooke Vacuum Products CVE 301. Figure 8 shows the important features of this device. Samples were prepared by clamping them to microscope slides and suspending them over tungsten filaments. The filaments were pre-wetted with an excess of 99.995% purity gold (metals basis, Alfa Aesar). Smooth micro-alligator clips were attached to the pads of the sample so that resistance could be measured as gold was deposited on the mica substrates. The bell jar was pumped down using a mechanical pump, then with an oil diffusion pump (cooled with a nitrogen baffle between it and the bell jar) to a final pressure of $\sim 10^{-8}$ Torr. The evaporation rate could be controlled simply as a function of the current passing through the filament (which determines the temperature of the filament). Samples were allowed to age in the bell jar, monitoring the resistance across the film periodically. At the appropriate time, the jar was let up to atmospheric pressure with nitrogen and the samples were removed. This evaporator also allows for the use of 2 filaments, which in some cases was used if an adhesion layer was to be deposited prior to the

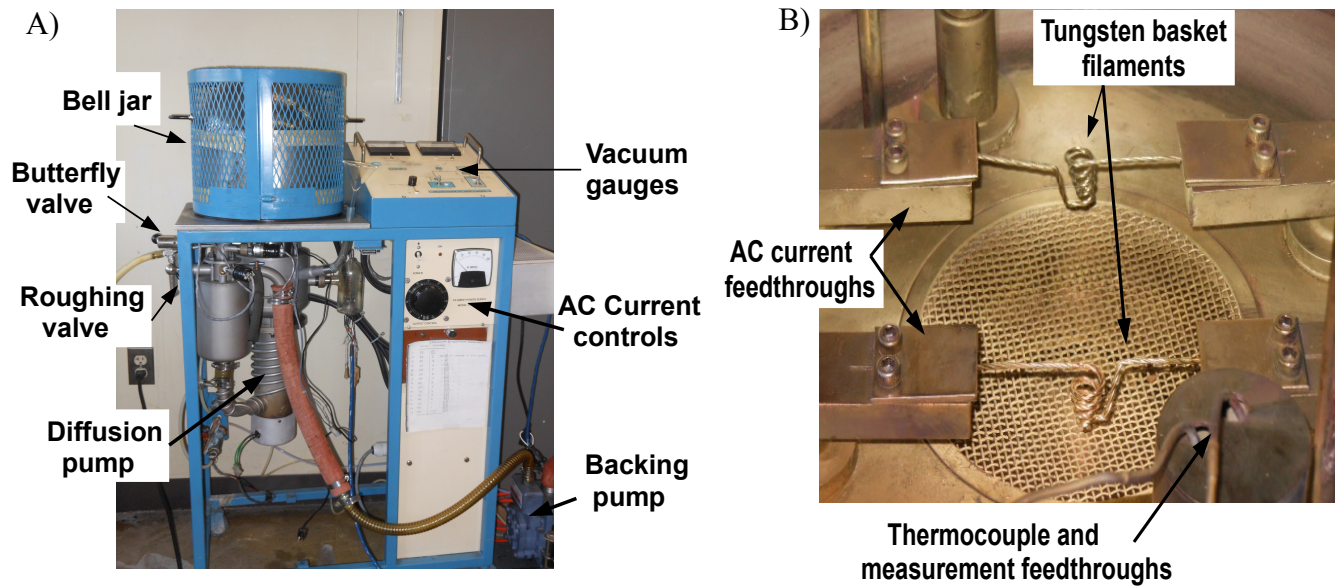


Figure 8: Details of Cooke Vacuum Products CVE 301 thermal evaporator. B) details the inner workings—simple tungsten baskets pre-wetted with high purity gold. Samples are mounted above them (face down) during preparation, and the filament is heated by passing an AC current through it. Resistance was measured via the measurement feedthroughs and a hand-held Fluke multimeter.

gold.

STM Instrumentation and Theory

The theory and technical challenges of scanning-probe microscopy will be discussed in the following. Details of tungsten probe (tip) fabrication and conditioning can be found in Appendix A. The microscopes used in the course of the research presented in this dissertation along with the controller were manufactured by RHK Technologies. These microscope heads are mounted on flanges are designed to function in UHV.

Briefly, STM is a technique where a sharp metal tip is rastered over a conductive (or semi-conductor) surface. The tip moves by supplying voltages to piezo legs which change dimension in proportion to the magnitude of the voltage. A bias is placed between the tip and the surface under interrogation. Interestingly, the technique relies on the purely quantum-mechanical phenomenon of *tunneling*. While the tip is extraordinarily close to the sample, it never actually touches it. The history,

instrumentation, and theory of this powerful technique will now be discussed.

STM History:

The 1986 Nobel Prize in physics was awarded to Gerd Binnig and Heinrich Rohrer for developing the scanning-tunneling microscope, a contribution which they perfected while working at IBM in Zurich, Switzerland [12,13]. For an STM to collect truly mind-blowing, atomically resolved images at surfaces, a tip of extreme sharpness must be rastered over the surface. Not only that, but “good” lateral resolution involves moving it with an X/Y precision of ~ 0.1 nm, and acceptable Z resolution requires the tip be controlled within ~ 0.01 nm.

This amazing technological feat was not possible until the advent of high quality piezoelectric materials which can change their dimensions in direct proportion to an applied voltage. As an interesting side note, neither Binnig nor Rohrer were trained as microscopists, and in fact had their roots in magnetism and superconductivity. As such they “brought along some experience in tunneling and Angstroms, but none in microscopy or surface science.” They stated that this lack of experience was perhaps what gave them the “courage and light-heartedness to attempt something that should not have worked in principle” [14]. It seems the developers at IBM started with little more than an interest in the quantum phenomenon of tunneling, and an awareness that piezoelectric materials might provide the needed spatial control over a scanning tip. This latter possibility was first exploited by a device called a *topografiner* which was developed by Russell Young, John Ward, and Fredric Scire [15]. While the hardware required for this device is similar to that of an STM (i.e., a sharp tip rastered over a sample by way of piezoelectric materials), the Z-distance was substantially longer. In fact it operated outside the metal-vacuum-metal range an STM operates within, and instead functioned in the Fowler-Nordheim tunneling regime as a sort of field-emission microscope.

The original STM experiments involved not only learning how to manipulate a scanning tip with extraordinary precision, but also how to surmount other technological problems. Obviously, if one is trying to control a tip with sub-nanometer resolution, any and all mechanical vibrations can easily couple to the tip causing at the very least high-level noise. At worst it can cause tip crashes or other damage. The section on the RHK microscope used by our group is included detailing its vibration isolation system, but for a fascinating historical perspective the reader is urged to read Binnig and Rohrer's Nobel lecture [14]. The first functional attempt at vibration isolation involved hanging a stage which was floating on superconducting magnets from rubber bands, and then only scanning at night when building noises were at a minimum. It truly was remarkable that the technique worked at all, much less that they were able to atomically resolve silicon. It was this work which largely led to their nomination for the Nobel Prize.

STM Theory:

Recall from classical mechanics that if an object is to reach the other side of an obstacle, it must in some way gain enough energy to surmount the obstacle. If, for example, a person on a motorcycle is trying to reach the other side of a hill, he must provide enough throttle to give enough mechanical (kinetic) energy in order to climb over it. We would not expect to ever observe the rider going directly through the barrier, or at any point finding himself inside of it. The area under the barrier is said to be *classically forbidden* [3,16,17]. This can be shown mathematically according to Equation 3. The total energy of the object (in this case the motorcycle and rider) is nothing more than the sum of their kinetic and potential energies:

$$\frac{p^2}{2m} + U(z) = E \quad 3)$$

where p is the momentum, m is the mass, and U is the potential energy as a function of distance. Classically, this expression only makes physical sense when $E \geq U(z)$ as if this inequality is not satisfied, the rider would have negative kinetic energy.

A direct consequence of the wave-particle nature of electrons, and the uncertainty involved in knowing both their position and momentum simultaneously, quantum mechanics tells us that if a small enough object encounters a sufficiently narrow barrier, there is some probability that object arriving at the other side, even if it has insufficient energy to surmount the barrier. This purely quantum mechanical event is called *tunneling* and is the physical basis upon which STM operates. Specifically, STM operate in a regime called *metal-vacuum-metal* tunneling and achieves extraordinarily high resolution as a consequence of the scanning tip being closer to the surface than the de Broglie wavelength of the tunneling electrons (for a 1 eV electron, $\lambda = 1.23$ nm). As we shall see, this can allow tunneling between a highly localized *tip state* and localized *surface states*. Tunneling current between the tip and sample decreases exponentially with separation between the two. In vacuum, this results an attenuation of tunneling current by a factor of about 1decade / Angstrom. It is this exponential dependence which gives rise to the extraordinarily high resolution an STM is capable of.

Figure 9 shows a depiction of an electron incident upon barrier of finite width and height (traveling from left to right). Recall from quantum mechanics, the Schrödinger equation for a particle of mass m in a region where the potential energy is U is given by Equation 4 where the first term is the kinetic energy operator.

$$\frac{-\hbar^2}{2m} \frac{d^2 \psi}{dz^2} + U \psi = E \psi \quad 4)$$

Taking a trial solution to Equation 2.4 as $\psi = A e^{\alpha z}$ yields the following solution:

$$\alpha = \pm i \sqrt{\frac{8\pi^2 m (E - U)}{\hbar^2}} \quad 5)$$

In the classically allowed region where $E > V$ and the solution has the form of a sine or cosine wave which are represented on the right and left side of the barrier in Figure 2-9. In the classically forbidden region, the wavefunction takes the form of an exponential as a result of Equation 6.

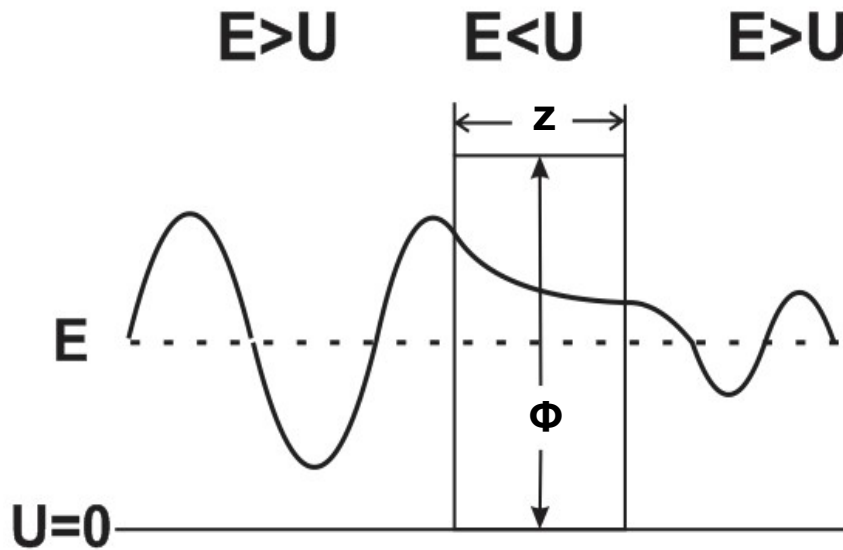


Figure 9: Schematic of tunneling (from left to right) through a rectangular barrier of height Φ . Before and after the barrier, the wave-function takes the form of a sine wave. Within the barrier it takes the form of an exponential decay.

$$\alpha = \pm \sqrt{\frac{8\pi^2 m(E-U)}{\hbar^2}} \quad 6)$$

The positive solution would represent an exponential increase in probability with increasing energy and distance is not physically meaningful. The negative solution which represents an exponential decay of the wavefunction with height and z -distance, however, makes perfect physical sense.

The wavefunction Ψ therefore attenuates according to Equation 7. Recall that the square of the wave function represents the probability function, and the result is perfectly consistent—one would expect the probability to decrease the more forbidden (the larger the energy deficit) and also the greater the distance between the origin and destination of the electron.

$$\psi \sim e^{-\sqrt{\frac{8\pi^2 m(U-E)}{\hbar^2}} z} \quad 7)$$

Which is sometimes written according to Equation 9 which more clearly demonstrates the exponentially decaying wave function as a function of distance z and in terms of the *decay constant*

κ .

$$\psi(z) = \psi(0)e^{-\kappa z} \quad 8)$$

where:

$$\kappa = \frac{\sqrt{2m(U - E_t)}}{\hbar} \quad 9)$$

The quantum mechanics described above are for the classic particle in a 1-dimensional box with a rectangular barrier. While an excellent starting point for discussing STM, the equations above do not include the one critical parameter STM relies on—the *bias*. A typical image is acquired by placing a small bias between the tip and sample, and (for “constant current mode” experiments) a *tunneling current*—literally the electron flow through a quantum mechanical barrier is set. Figure 10 shows a depiction of the barrier resulting from placing a bias between the tip and sample. The typical assumptions made are that the work functions of the sample and tip are roughly equal, and that

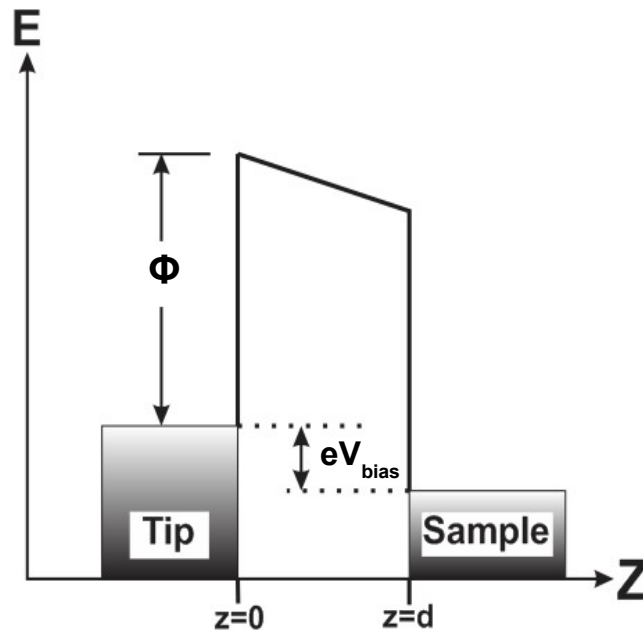


Figure 10: Distortion of tunneling barrier in the presence of a small bias between sample and scanning-probe.

$eV_{\text{bias}} \ll \Phi$ and if that is true the following simplification can be used:

$$\kappa \approx \frac{\sqrt{2m\phi}}{\hbar} \text{ when } eV \ll \phi \quad 10)$$

Here Φ (the barrier height) is often replaced by a simple average of the work function of the sample and tip as very rarely are these two made of the same material. The tunneling current which passes from one electrode to the other (from the tip to the sample in Figure 10) can be calculated directly from

the *probability* of electrons tunneling through the barrier. An Ampere is defined as a current of 1 Coulomb/second. A Coulomb of charge contains $\sim 6.25 \times 10^{18}$ electrons, and so even though a typical current setpoint in STM might be ~ 100 pA there are still on the order of 10^8 electrons/second tunnelling through the barrier.

It should follow that the tunneling current can then be phrased in terms of the probability of electrons to tunnel through the barrier (recall that it is the square of the wavefunction that represents the probability). We will also invoke the idea of *local density of states* as this is what STM is truly interrogating—the density of states near the Fermi level of the sample and tip.

The current is proportional to the probability of electrons tunneling through the barrier:

$$I \propto \sum_{E_n=E_F-eV}^{E_F} |\Psi_n(0)|^2 e^{-2\kappa d} \quad (11)$$

Using the definition for the local density of states for $\varepsilon \rightarrow 0$:

$$\rho(z, E) \equiv \frac{1}{\varepsilon} \sum_{E_n=E-\varepsilon}^E |\Psi_n(z)|^2 \quad (12)$$

the current density can be approximated according to:

$$I \propto V \rho_s(0, E_F) e^{-2\kappa d} \quad (13)$$

or substituting in to previous equations, it can be further approximated by:

$$I \approx V \rho_s(0, E_F) e^{-1.025d\sqrt{\Phi}} \quad (14)$$

Where d is in Angstroms and Φ is in eV. It is this last equation that is perhaps most useful when examining the the extremely good vertical resolution an STM instrument is capable of. A typical metal might have $\Phi=5$ eV. From Equation 2.14, one would expect a change in current of an order of magnitude for a 1 \AA change in vertical distance of the tip, and the extraordinary vertical resolution a well functioning STM is capable of is a direct consequence of it.

STM Instrumentation:

We have just examined the quantum mechanical foundations behind the *theory* of STM operation. On it's most basic level, the experiment requires a small bias be placed between a conducting sample

and sharp tip, and for the tip to be rastered over the surface. In this section we will discuss in finer detail the actual hardware required to perform such imaging experiment because while conceptually the experiment is straightforward, the implementation of the theory is not necessarily. Figure 11 shows a greatly simplified diagram of the required components.

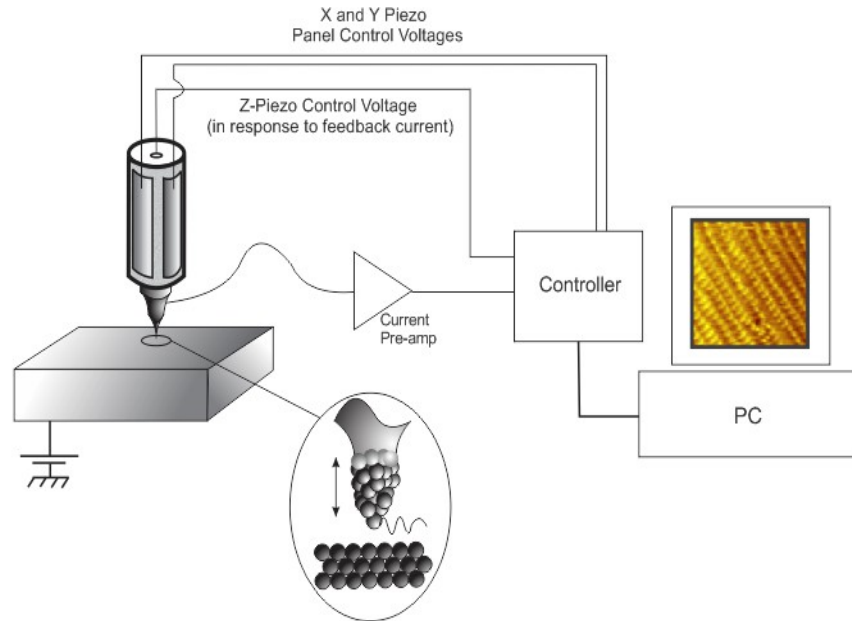


Figure 11: Schematic of a scanning-tunneling microscope. A bias is placed between a surface and a sharp (ideally *atomically* sharp) tip which is rastered over it. A *tunneling current* is measured, amplified, and feedback electronics move the tip closer or further away to maintain a constant tunneling current. This extraordinary x, y, and z resolution was not possible until the advent of high quality piezoelectric materials.

Vibration Isolation:

STM experiments are typically conducted with the scanning tip moving less than 1 nm above a surface (often far less than that). The tip is *atomically sharp* under ideal conditions, and as such is extremely delicate. A *tip crash*—an event where the tip (for a host of reasons) comes into physical contact with the surface, will very likely damage the tip beyond repair. Extraneous vibrations and acoustic noise are capable of inducing such an event. Even if the tip does not crash, the most minor mechanical vibrations will show up as high level noise in an STM image (which typically have a Z-

scale on the order of tens of picometers). For this reason, a four-tiered approach to vibration isolation is utilized in our microscope as outlined below.

The first tier is the shear mass of the system. The frame was fabricated from heavily braced 1/4” thick, 2”x2” structural square steel tubing and topped with a steel optics table. The mass of this combined with the microscope and preparation chamber and the ion pumps hanging from them yields a system with an estimated weight of over 1000 pounds. This, combined with the location of the microscope in the basement of the building gives a very stable platform for the rest of the vibration system.

The second tier of the vibration dampening system are the pneumatic *air legs* which the system floats on. The pneumatic legs suspend the microscope chamber a few centimeters from the floor. The combination of high mass and pneumatic cushioning act as a *low pass filter* for the system, where if it is properly functioning, high frequency noise cannot efficiently couple into the system. This noise could come from other activities in the building—slamming doors, foot traffic, construction projects, etc.

When one is getting ready to image, one first has to *drop* the stage. The stage (and sample/sample holder which is installed upon it) is suspended from a system of springs with weak spring constants. Since the springs are weak they have a low natural resonant frequency and provide a high degree of mechanical decoupling between the sample/stage and the chamber itself. This part of the system helps to attenuate mechanical vibrations as well as acoustic noise. Presumably, sound waves incident upon the chamber would propagate through the stainless steel components readily (but obviously, not the vacuum itself). However, the sample stage would be coupled to the rest of the system only very poorly through the weak springs suspending it.

The final stage of vibration isolation comes from an eddy current dampening system built in to the stage. When a magnetic field (a magnet) moves through a conductor, an *eddy current* is induced in the

conductor that generates a field opposing that of the magnet. This eddy current generates heat, so briefly, the eddy current dampening is a method to take an oscillation (like a vibration of the sample/scan head) and dissipate it's energy thermally.

STM Sample Holder:

Figure 2-12 shows the sample holder utilized by the RHK microscope. Unlike the RAIRS system, which heats the sample resistively, the STM crystals are heated by *electron-beam heating*. Crystals are cut in a *top-hat* configuration. The narrow portion of the sample fits through a hole in sapphire washer and is resting on another sapphire washer. This keeps the crystal electrically isolated from the rest of

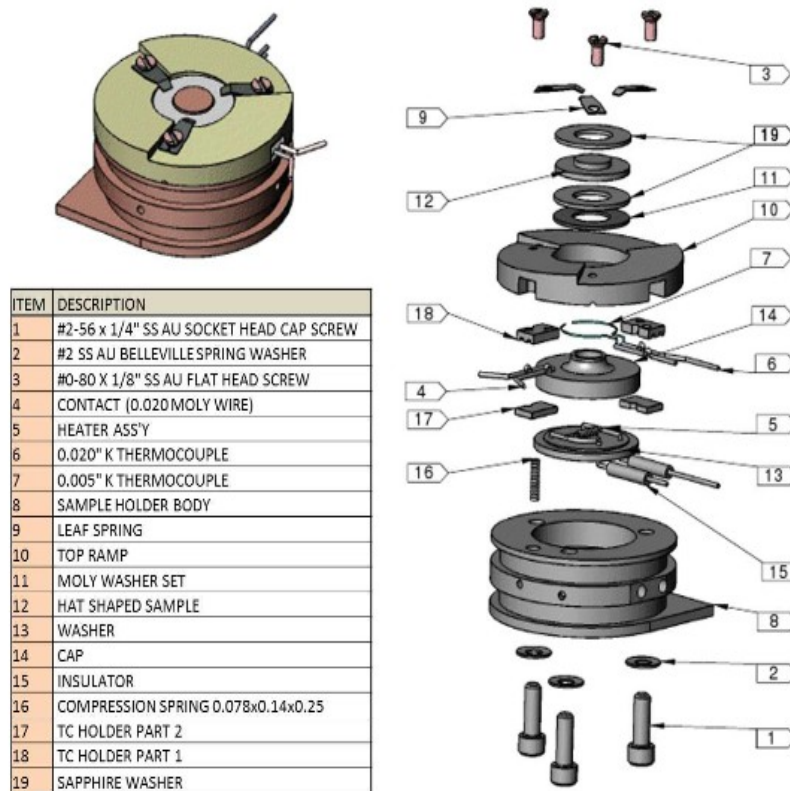


Figure 12: RHK sample holder (image used with permission, RHK). Crystal (12) is cut in *top-hat* configuration and held under spring pressure between sapphire washers. This keeps it electrically and thermally isolated from the rest of the sample holder. The ramps are TiN coated tungsten and the base is ultra-pure copper.

the system. In fact, the only electrical conduit between the sample and the rest of the system is through the thermocouple which is mounted below the crystal and held in place by spring pressure. Sample

heating is carried out by connecting the two filament wires into an Oxford Scientific e-beam heating supply (model OS-Beam). This device functions by passing an AC current through the filament. However, this AC current is floated on a large DC voltage. The system is configured so that the thermocouple runs from the crystal, through a Fluke multimeter, to ground. Electrons emitted from the filament as a result of the AC current passing through it and are accelerated towards the crystal due to the DC field. This provides rapid and efficient heating, particularly since the crystal is thermally well isolated from the sample holder. Alternatively, if temperature requirements are low, the power supply can be operated without a bias between the filament and crystal. Here, the crystal is warmed through simple radiative heating as a result of being a few millimeters from a hot filament.

Scan Head:

Two STM instruments (both from RHK Technologies) were utilized in the course of this research. One microscope was an AFM/STM system and the other an STM only system. Figure 13 shows a diagram of the STM only head. In this system, coarse motions of the tip (such as approaching the sample or coarse lateral motions) are carried out by the concerted motions of the three legs upon which the head rests. The STM control unit supplies a wave-form to the tubular piezo legs (or *piezo motors* as they are sometimes called). The feet at the bottom of the legs are simple glass balls which rest on top of the *ramps* which are constructed of titanium nitride coated tungsten. Friction between the glass feet and ramp keeps the head stationary in the absence of a wave form, but when required the head can move in the X or Y directions, or up or down the ramp via *stick-slip* motion.

In this head, the actual tip-rastering is carried out by a fourth piezo tube which is controlled completely independently of the legs. In this system, the scanning tip is mounted concentrically within the scanning tube. Upon tip approach, the instrument retracts the tip with the central *Z-piezo*, then advances the entire scan head forward a step with the three legs. On each step the instrument then extends the *Z-piezo* (and tip), and determines if the current is within a set value. If a tunneling current

is measured the coarse approach is halted and the tip released for scanning. If no tunneling current is measured, another coarse step is taken. Other (faster) tip-approach methods are available, but the one described has proven itself safe (from accidental tip crashes).

The AFM/STM scan head works in a similar fashion except that there is no dedicated Z-piezo to control the tip. Instead, the three piezo legs carry out both the coarse motions of the head as well as tip-rastering functions.

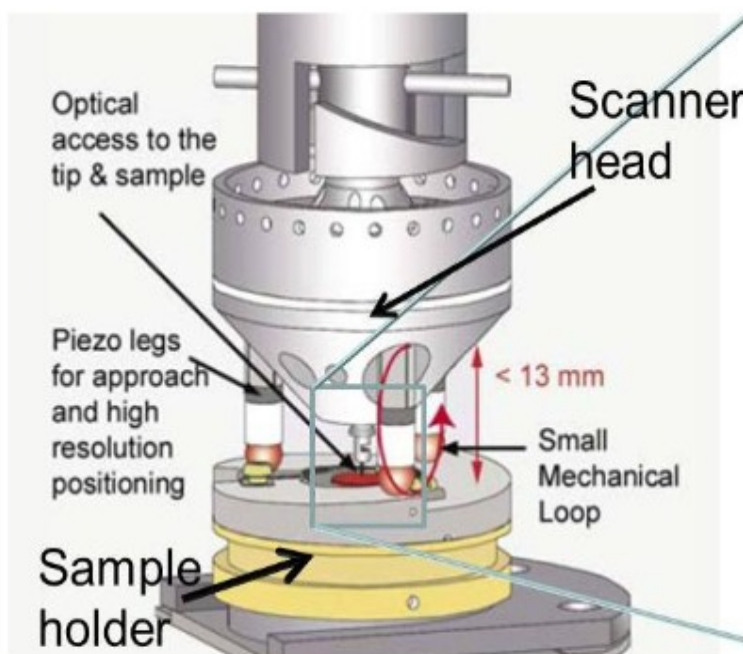


Figure 13: STM head sitting on sample holder. In this head, coarse motions are carried out by three tubular piezo legs and tip rastering functions are performed by the central Z-piezo which is controlled independently of the other 3. (Adapted with permission, RHK Technologies)

RAIRS Theory:

Earlier in this chapter the basic setup of the reflectance-absorbance infrared (RAIRS) instrument was discussed. As stated, our system is based on a commercial Bruker FT-IR, but rather than transmitting infrared radiation *through* a sample, in a RAIRS experiment the infrared radiation is reflected *from* it. In a transmission IR experiment (a KBr pellet or mull for example) the molecules under investigation are found randomly oriented in the matrix. In theory this allows one to observe all

the allowed vibrational modes of the molecule. RAIRS spectroscopy is different in that typically the sample thickness is only a monolayer or perhaps a few layers of an organic material chemisorbed or physisorbed onto (typically) a metal surface.

The technique is not without difficulties. Perhaps the greatest problem that must be overcome is one of sensitivity. In standard infrared spectroscopy, one can adjust the absorption of the sample simply by varying the path length or the concentration of the analyte. Just as in UV-visible spectroscopy, the intensity of peaks in transmission IR are subject to the Beers-Lambert law. In the case of RAIRS, one is examining a sample that is often a mere monolayer thick. A crystal might have a surface area of 1 cm^2 and this active area might have $\sim 10^{15}$ adsorbed molecules—less than a nanomole. Fortunately there is no interference from background (Nujol, solvent, etc.). In addition, modern instruments are capable of measuring absorbances down to $\sim 0.01\%$ which is sufficient if adequate signal to noise is maintained.

The origin of the *surface dipole selection rule* can be understood in terms of a dipole/induced dipole interaction between the adsorbates and the underlying, highly polarizable metal substrate [18,19]. The adsorbates induce an image charge in the metal. As shown in Figure 14, the charge is equal in magnitude to the dynamic dipole moment of the adsorbate, but antiparallel with it. If the vibration is parallel with the surface, the induced dipole will be canceled by the mirror charge of the substrate. Conversely, if the vibration is perpendicular to the surface the induced dipole creates an effective dynamic dipole that is additive.

RAIRS instruments are normally configured using *grazing incidence*. The incident infrared beam strikes the sample at a high angle of incidence (i.e. nearly parallel with the surface), and is reflected at the same angle. Fresnel's condition tell us that only p-polarized light can be reflected from a surface. For a vibrational excitation to occur (i.e. for a molecule to absorb a photon) the molecule must be

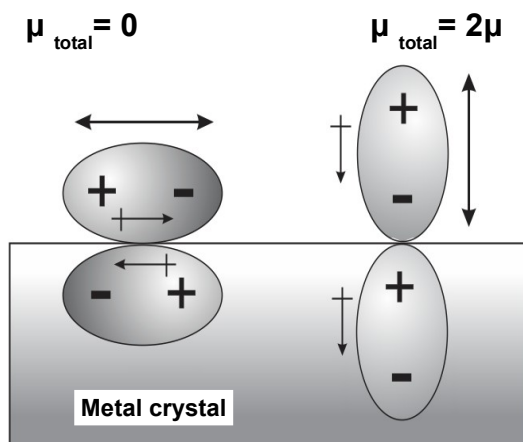


Figure 14: The origins of the surface selection rule—the *image dipole effect*. For vibrations parallel to the (conductive) surface, the mirror charge is anti-parallel and exactly cancels the dynamic dipole of the adsorbate.

oriented in such a way that the mode in question is in-plane with the oscillating electric field. In the case of molecules adsorbed on a surface, this condition is only met when the vibrations are normal to the surface, or at least have some component normal to it. As illustrated in Figure 14, for a dipole parallel with the (metal) surface, the image dipole exactly cancels it.

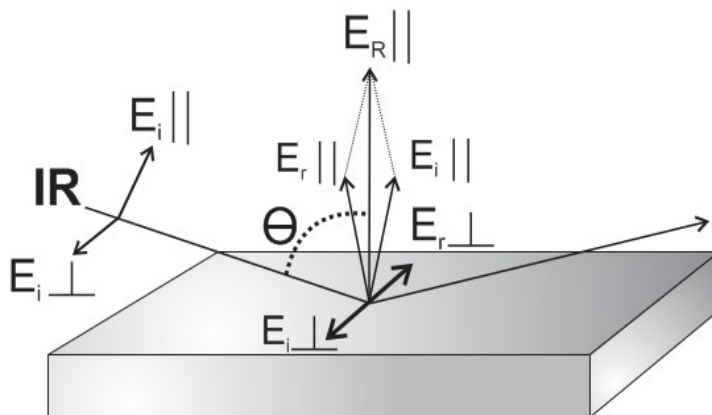


Figure 15: Reflection geometry showing s and p polarized components of incident and reflected radiation.

We have seen in this section that while RAIRS is a technique not without difficulties (particularly in terms of sensitivity), the *selection rules* imposed by the image dipole allow for a unique and powerful glimpse into the metal-vacuum interface. By careful consideration of both the intensity of peaks and the vibrational frequency, it is often possible to gain information on the specifics of bonding with respect to a surface or with adsorbates with respect to each other.

Herringbone Reconstruction of Au(111):

As single crystal Au(111) was used for a large part of the research presented in this work, attention will be given to some unique properties of this surface. Figure 16 shows a depiction of the (111) plane as defined within a cube where the numbers $1\ 1\ 1$ correspond to the *lattice vectors* according to the *Miller Index* system for crystalline solids [20].

The crystal structure of metallic gold is *face centered cubic*, *fcc* (Figure 16 B)) where gold atoms occupy the vertices of a cube in addition to center of each face [21].

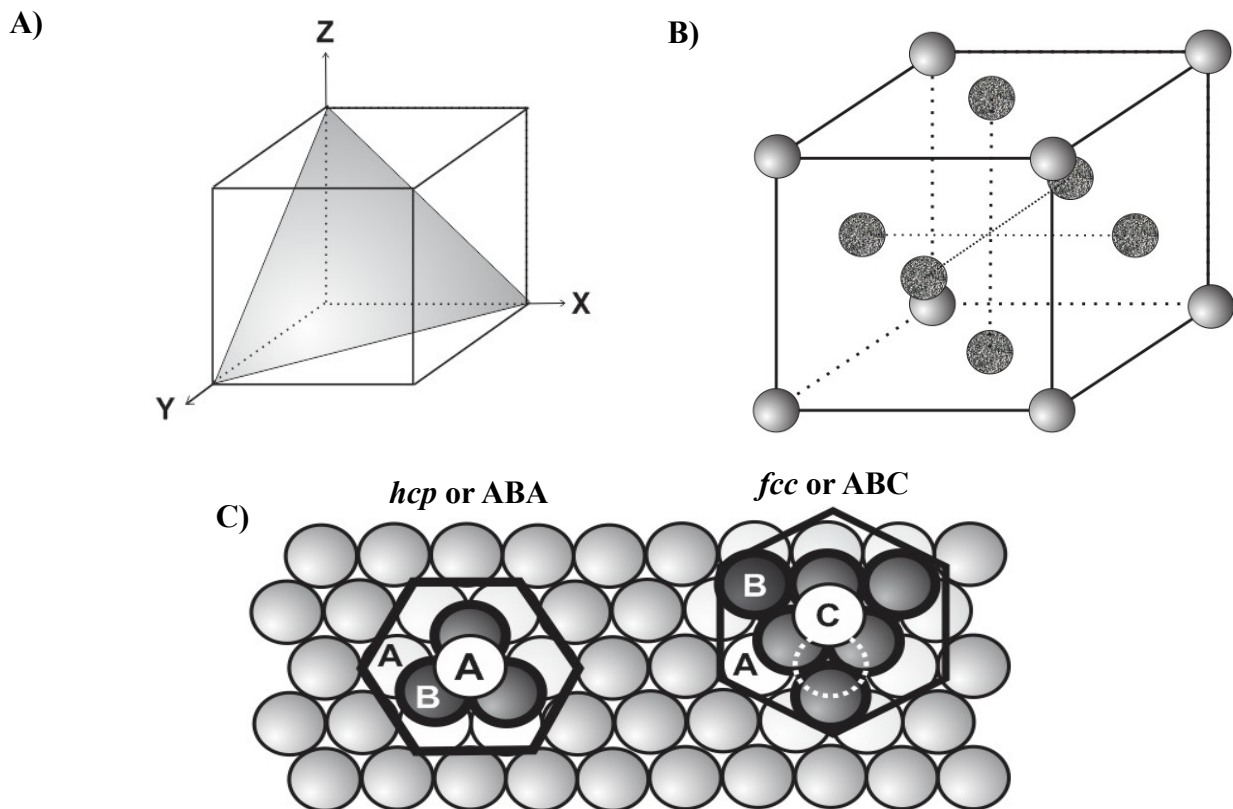


Figure 16: A) Gold has the *face centered cubic* structure diagrammed. B) In the *Miller Index* crystallographic notation, the (111) planes intersects opposite corners of a cube. C) In *hexagonal close-packed* structures, atoms in the third layer fall directly on top of atoms in the first layer. Thus *hcp* packing is also called *ABA* packing. In *face-centered cubic* structures, atoms in the third layer reside directly on top of vacancies (octahedral “holes”) in the first layer. *Fcc* is sometimes called *ABC* packing.

In a *close-packing of equal spheres* model, there are 2 nonequivalent ways which the spheres can be

packed, but which result in the same packing density (i.e., the same void space between the spheres). Figure 16 C) demonstrates that plane A can be arranged with hexagonal symmetry (which maximizes the density of the layer). Then plane B can be placed on top of it, with the spheres resting in the *holes* in the first layer. When the third layer is placed on top, the spheres can either occupy holes with a sphere directly under them (in plane A)--this system is called *ABA* packing or hexagonal close-packed, *hcp*. Alternatively, the third plane of atoms can occupy holes that are directly on top of octahedral holes in layer A. This type of packing is called *ABC* packing or face-centered cubic, *fcc*.

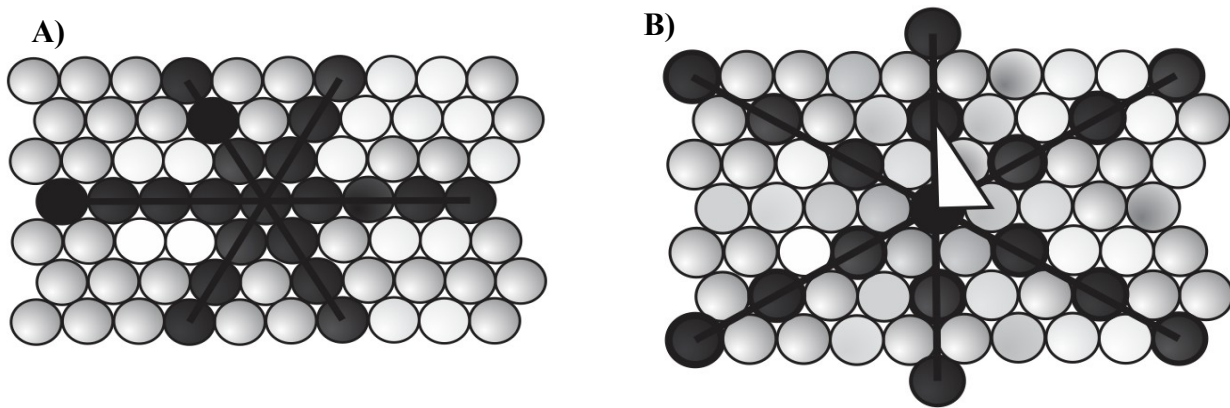


Figure 17: For a hexagonal lattice, The “close-packed directions” are indicated in A). The $\sqrt{3}$ directions are indicated in B).

Figure 17 shows two directions (defined with respect to the central atom) that are commonly discussed for crystals of hexagonal symmetry.

What makes a Au(111) surface unique is not, in fact, its hexagonal symmetry. Rather the lattice of clean Au(111) undergoes a characteristic *herringbone reconstruction* which results from tensile stresses present in the surface [Frenkel-Konterova solitons, 22]. The tensile strain causes a uniaxial contraction along the close-pack $\langle 110 \rangle$ directions, and allows for the incorporation of 4% more gold atoms in the surface than would be expected for the un-reconstructed surface [23, 24]. To accommodate the “extra” atoms, in the herringbone reconstruction 23 gold atoms are fit into a space that should only allow for 22 (as would be in a hexagonal lattice), then the lattice puckers out slightly, and changes direction by

120°. This herringbone reconstruction is shown clearly in Figure 18 A), with an inset that shows a line scan perpendicular to the perfectly reconstructed surface. Figure 18 B) shows an atomically resolved image of the herringbone reconstruction and reflects more clearly the origin of the features on the surface (the ridges are called *soliton walls*). There are *fcc* and *hcp* regions which exist parallel to each other. The solitons represent an area where a *stacking fault* exists and the surface atoms are shown to protrude ~10 pm from the *fcc* and *hcp* regions. The gold atoms composing the solitons reside on top of bridge sites in the layer beneath. The formation of these rotationally degenerate domains allows for more isotropic distribution of stresses in the lattice. While the herringbone reconstruction is the most stable surface state (of Au(111)) at temperatures below ~600 K, the forces holding it together are rather

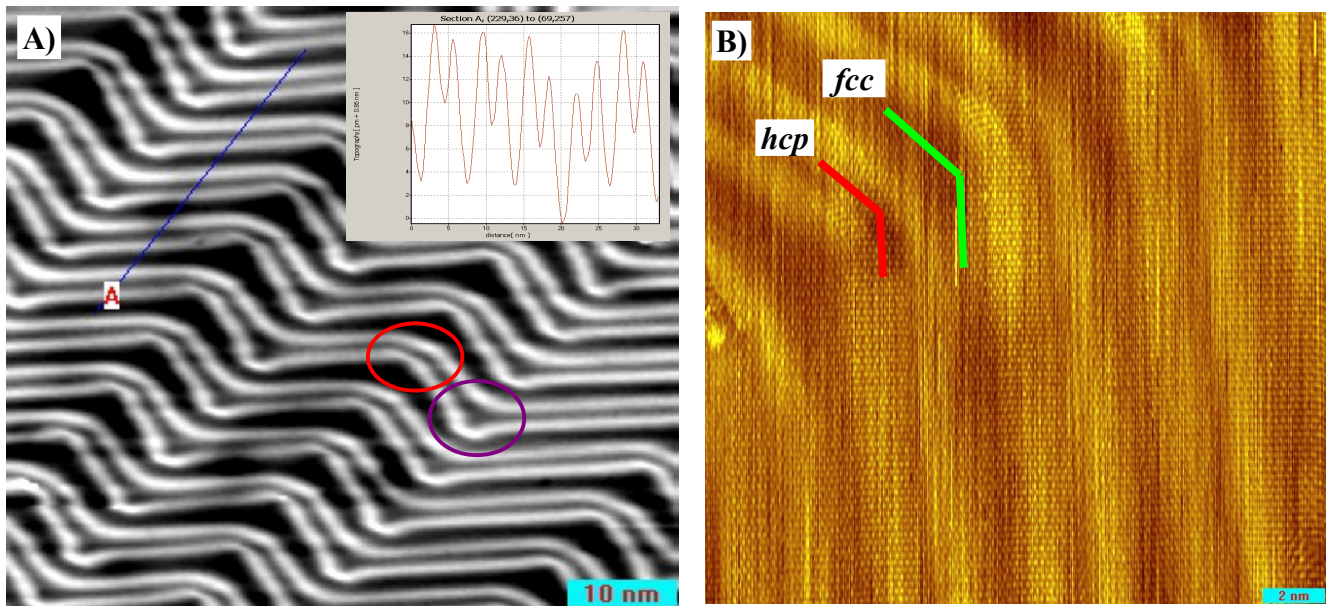


Figure 18: A) A large scan area image of a perfectly formed herringbone reconstruction of Au(111). Inset shows a typical line profile across solitons. The red ellipse shows the “pinched in” elbow, and the magenta ellipse shows the “pinched out” elbow. $V = -1.0\text{V}$, $I = 0.89\text{nA}$. B) Atomically resolved herringbone reconstruction highlighting the *hcp* and *fcc* domains (red and green lines, respectively), and the solitons that result from a stacking fault between the two. $V = -0.50\text{V}$, $I = 342\text{pA}$. subtle. It is not uncommon for the reconstruction to become distorted or *lifted* entirely through the adsorption of certain molecules, particularly with adsorbates that can abstract gold atoms from the

surface (such as thiolates) and upset the delicate tensile stresses holding the reconstruction together.

References:

- 1) Aristotle. Physics ca. **330BCE** available at <http://ebooks.adelaide.edu.au/a/aristotle/physics/book4.html#section32>
- 2) Burkholder, L.; The Surface Chemistry of Enantioselectively Modified Palladium(111) Systems. **2009**. Ph.D. dissertation, University of Wisconsin-Milwaukee
- 3) Boscoboinik, J.A.; Small Organic Molecules on Transition Metals Surfaces and Monte Carlo Simulations of Surface Alloys. **2010**. Ph.D. dissertation, University of Wisconsin-Milwaukee.
- 4) Furlong, O.; Tribological and Tribochemical Processes in Sliding Metal Interfaces. **2010**. Ph.D. dissertation, University of Wisconsin-Milwaukee.
- 5) Gast Mfg.; “Rotary Vane Compressors and Vacuum Pumps”. **2012**. Available for download at http://www.gastmfg.com/catalogs/F-5_Rotary_Vane_Feb17-2012_lores.pdf
- 6) Pfeiffer Vacuum; “Working with turbopumps”. **2003**. Technical document *PT 0053* available for download at <http://mmrc.caltech.edu/Vacuum/Pfeiffer%20Turbo/Turbos.pdf>
- 7) Roth, A.; Vacuum Technology, 3rd ed. **1986**. Elsevier Publishing. 121-4.
- 8) Mattox, D.; Educational Guide to Vacuum Coating Procedures. **2001**. Society of Vacuum Coaters technical document available at <http://www.svc.org/assets/file/English4.pdf>
- 9) Westinghouse Electric; Vacuum Pump Setup, Operation and Maintenance. **1944**. Instruction book 5669-168 available for download at http://loen.ucolick.org/Telescope_Operations_Manual/Telescope_Ops_Manuals/Volume_3/Coating%20Facilities%20Operation/Oil%20Diffusion%20Vacuum%20Pump/Oil%20Diffusion%20Vacuum%20Pump.pdf
- 10) Chambers, A.; Modern Vacuum Physics, **2005**. CRC Press.
- 11) Zikovsky, J.; Dogel, S.; Dickie, A.; Pitters, J.; Wolkow, R.; Reaction of a hydrogen-terminated Si(100) surface in UHV with ion-pump generated radicals. *Journal of Vacuum Science and Technology A*. **2009** 27 (2): 248
- 12) Binnig, G.; Rohrer, H.; Scanning tunneling microscopy. *IBM Journal of Research and Development* **1986**. 30: 4.
- 13) Royal Swedish Academy of Sciences. “The Nobel Prizes in Physics 1986”. press release available at http://www.nobelprize.org/nobel_prizes/physics/laureates/1986/press.html
- 14) Binnig, G.; Roehrer, H.; Scanning Tunneling Microscopy—From Birth to Adolescence. Nobel lecture **1986**. Available at http://www.nobelprize.org/nobel_prizes/physics/laureates/1986/binnig-lecture.pdf
- 15) Young, R.; Ward, J.; Scrie, F.; *Rev. Sci. Instrum.* **1972**. 43, 999.
- 16) Strocio, J.; Kaiser, W.; Scanning Tunneling Microscopy **1993**. Academic Press, 17-23.
- 17) Tysoe, W.T.; Physical Chemistry Laboratory Manual Dept. of Chemistry and Biochemistry UW-Milwaukee 224-563-801. **2013** University of Wisconsin-Milwaukee
- 18) Eischens, R.P.; Pliskin, W.A.; Francis, S. A.; *J. Chem. Phys.*, **1954**, 22, 1786
- 19) Terenin, A.N.; *Zh. Fiz. Khim.*, **1940**, 14, 1362.
- 20) Academic Resource Center; “Miller Indices” download available at https://www.iit.edu/arc/workshops/pdfs/Miller_Indices.pdf

- 21) Murphy, C.; “Herringbone” **2012**, Powerpoint presentation under supervision of Prof. C. Sykes, Tufts University.
Available for download at <http://ase.tufts.edu/chemistry/sykes/Sykes%20Lab%20Research%20Group.html>
- 22) Harten, U.; Lahee, A.; Toennies, J.P.; Woll, C.; *Phys. Rev. Lett.* **1985**, *54*, 2619.
- 23) Woll, C.; Chiang, S.; Wilson, R.; Lippel, P.; *Phys. Rev. B.* **1989**, *39*, 7988
- 24) Barth, J.; Brune, H.; Ertl, G.; Behm, R.; *Phys. Rev. B.* **1990**, *42*, 9307.

Chapter 3

Determination of Adsorbate Structures from 1,4-Phenylene Diisocyanobenzene on Gold

Introduction

Adsorbing 1,4-phenylene diisocyanobenzene (PDI) on Au(111) at room temperature results in the spontaneous formation of one-dimensional chains which are observed when the surface is imaged using scanning tunneling microscopy (STM). These one-dimensional, self-assemblies have been ascribed to the formation of oligomeric chains comprising alternating gold and PDI units, [1-3] suggesting that they form by extracting gold atoms from low-coordination sites on the gold substrate. Adatom structures formed on coinage metals are relatively common [4-7]. This structure was proposed by excluding other possible structures that did not involve gold-adatom/linker molecule bonding [2]. More recent theoretical work has confirmed that formation of the $-(\text{Au}-\text{PDI})_n-$ oligomer chain is energetically feasible [8].

In contrast to these observations, the results of previous work to explore the structures formed following PDI adsorption onto planar gold surfaces and nanoparticles from solution proposed structures in which the PDI adsorbed in an η^1 configuration leaving a pendant, isolated isocyanide [9-14]. Compelling evidence for this structure comes from the detection of a vibrational stretching mode due to an unbound isocyanide. It appears, therefore that there is a discrepancy between the STM results obtained under ultrahigh vacuum conditions and those found when dosing from solution.

These issues are addressed here by measuring the reflection-absorption infrared spectra

(RAIRS) to determine the structure and orientation of 1,4-PDI adsorbed on a Au(111) single crystal

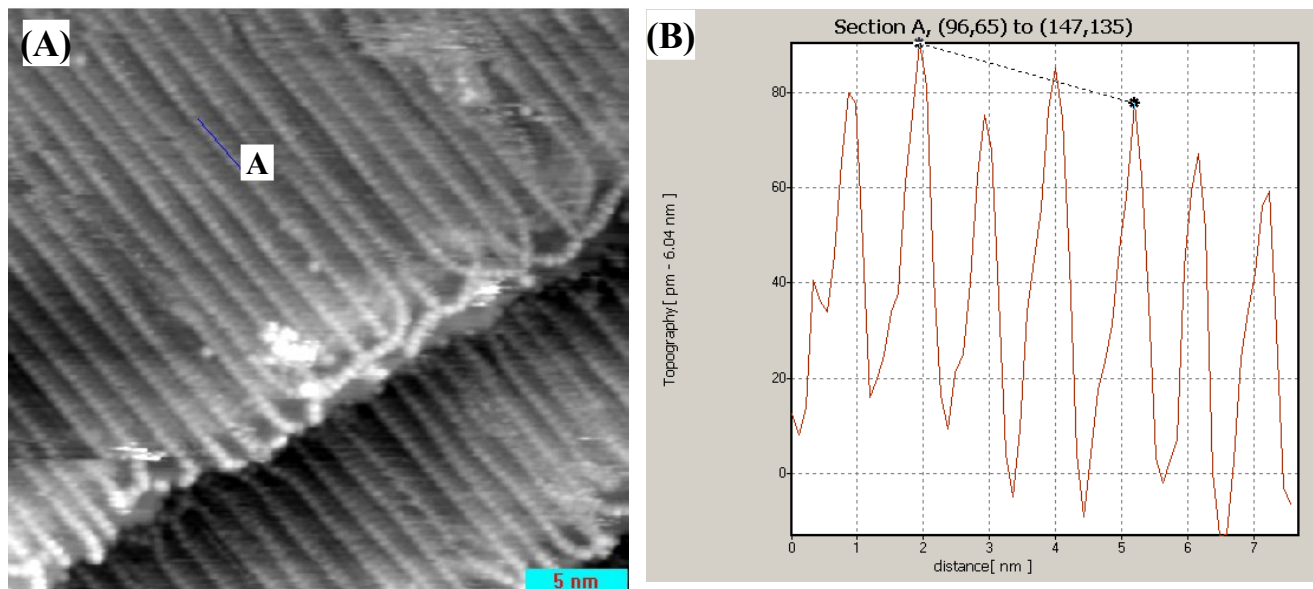


Figure 1: (A) $-(\text{Au-PDI})_n$ oligomers on an Au(111) single crystal. An eroded step edge runs diagonally through image.

$V = -1.2$ V, $I = 328$ pA. (B) Line profile along indicated segment.

surface. This orientation is established using the surface selection rules, [15-17] combined with comparison of the experimental vibrational frequencies with those calculated for the most stable $-(\text{Au-PDI})_n$ oligomer chain structure obtained using density functional theory (DFT). To further confirm that the self-assembled oligomer chains incorporate gold atoms, the STM images for the most stable structures from DFT are simulated as a function of tip bias using the Bardeen method [18] and compared with the experimental images.

In order to explore the difference between solution and vacuum dosing of PDI, the conductivity of a gold-nanoparticle array grown on an insulating mica support is measured after exposing it to PDI solutions. It has been shown previously and will be discussed again in Chapter 5 that dosing such mica-supported gold nanoparticles with 1,4-PDI *in vacuo* results in the formation of $-(\text{Au-PDI})_n$ oligomeric molecular bridges between the gold nanoparticles [19]. Here, the gold metal atoms are again proposed to originate from low-coordination sites on the gold nanoparticles. This results in a

substantial increase in conductivity of the gold-nanoparticle covered mica sample due to the presence of molecular conduction pathways between the nanoparticles. However, it is expected that if the PDI adsorbs in an η^1 -configuration *via* one isocyanide group, the conductive path should be interrupted, thereby lowering the conductivity thereby providing an *in situ* probe of any change in molecular configuration.

Experimental Methods

Scanning tunneling microscopy (STM) and RAIRS measurements were made in separate ultrahigh vacuum (UHV) chambers operating with base pressures of $\sim 2 \times 10^{-10}$ Torr after bakeout. The systems are described at length in Chapter 2 and the method of STM tip fabrication can be found in Appendix A. Standard methods of sample cleaning/annealing and adsorbate dosing were utilized.

The conductivity of PDI on nanoparticle-covered mica was measured as described elsewhere [19]. Briefly, gold nanoparticles were deposited by thermal evaporation onto a (freshly) cleaved mica substrate (Ted Pella, highest grade). 80 μl aliquots of serially diluted PDI solutions (with a 10 mM initial solution concentration) in benzene were deposited using an Eppendorf pipette on to the surface of the nanoparticle-covered sample and allowed to react for 10 s, after which the excess was washed away with benzene and the substrate allowed to dry in air. The samples were installed in the I/V chamber and electrically characterized as diagrammed in Chapter 2. 1,4-PDI was obtained commercially (Aldrich Chemicals, 99% purity).

Density Functional Theory Calculations

Density functional theory calculations were performed with the projector augmented wave (PAW) method [21] as implemented in the Vienna *ab initio* simulation package, VASP [22]. Geometric relaxations were considered to be converged when the force was less than 0.02 eV/Å on all unrestricted atoms. STM topography simulations were performed using the Bardeen[18] approach to tunneling using bSKAN 3.7.1 [24-27] Details of the DFT methods and implementation are found

elsewhere [34].

Results

A typical STM image of 1,4-PDI adsorbed on Au(111) is shown in Fig. 1(A), with Fig. 1(B) showing a line scan along the axis of one of the chains. The 1,4-PDI molecules and gold adatoms (at this scanning bias) show equal heights. DFT calculations of PDI-Au oligomer chains were performed by bridging gold adatoms placed on a Au(111) substrate aligned along the close-packed directions, corresponding to the orientations on the linear chains observed by STM on Au(111) [2,3,8]. The gold adatoms were separated by four-substrate lattice-translation distances, corresponding to the experimental repeat distance of ~ 1.1 nm. The PDI molecule was then placed between the gold adatoms and the structure allowed to relax. The resulting structures are displayed in Fig. 2, where Fig. 2(A) shows a angle view of the Au-PDI-Au bridging units and Fig. 2(B) illustrates a top view. As found previously, the isocyanide groups are angled slightly (at $\sim 18^\circ$) with respect to the surface and the molecule has local C_{2v} symmetry, with the aryl ring oriented parallel to the Au(111) plane. The binding energy, calculated from the difference between the energy of the final structure shown in Fig. 2, and the energy of the gold-adatom-covered surface plus the energy of gas-phase PDI is -177 kJ/mol. The energy for the formation of the chains on Au(111) will be somewhat lower than this because of the energy required to remove gold adatoms from the substrate to form the initial adatom-covered surface. The calculated $N\equiv C$ vibrational frequency for the oligomer chains (Fig. 2) is 2139 cm^{-1} , and the value for a free isocyanide group, calculated for the gas-phase molecule, is 2113 cm^{-1} . These results are in accord with previous work on 1,4-PDI on gold films [9] that suggested that the molecules adsorbed perpendicularly to the surface with the free isocyanide group exhibiting a vibrational frequency of 2120 cm^{-1} and the frequency due to the surface-bound group shifted to 2181 cm^{-1} . More recent work [10] showed similar frequencies of 2121 (free) and 2172 (surface-bound) cm^{-1} . Sum-frequency generation (SFG) results [28] provided corresponding vibrational frequencies of 2122 and 2195 cm^{-1} for the free

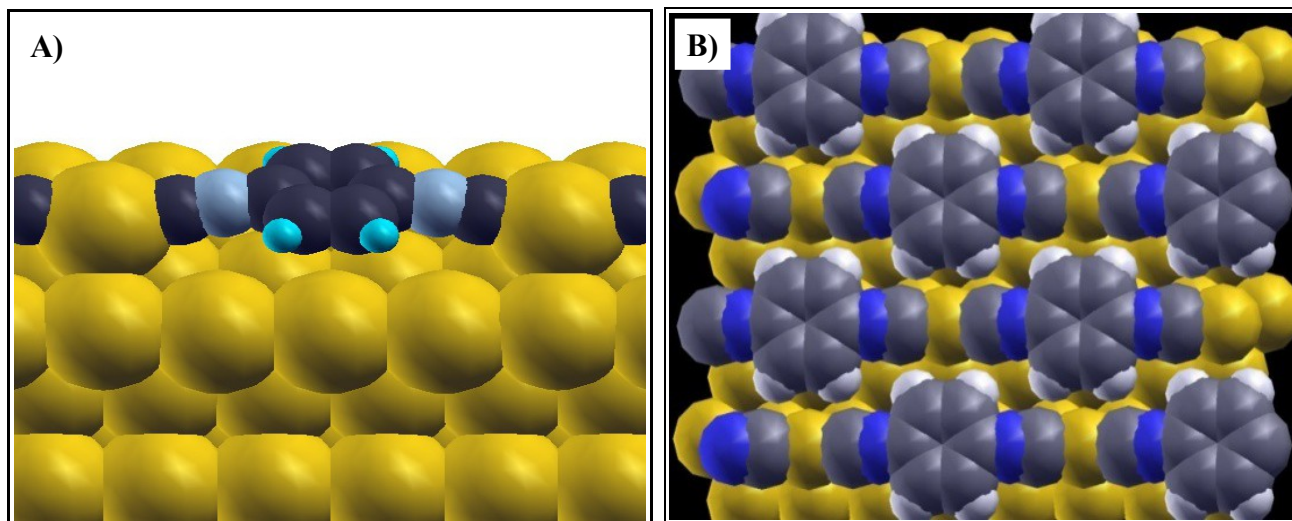


Figure 2: The structure of (Au-PDI) oligomers on gold calculated using density functional theory showing (A) an angled view and (B) a top views of the oligomer chains.

and bound isocyanide groups, respectively. An average of the values of the vibrational frequencies of isocyanide SAM's on gold from the literature (summarized in reference [28]) yields a value of $2123 \pm 1 \text{ cm}^{-1}$ for a free isocyanide group and $2181 \pm 4 \text{ cm}^{-1}$ for a surface-bound group.

The experimental infrared spectra for 1,4-PDI on Au(111) (at room temperature) as a function of dosing time are shown in Fig. 3. At low exposures (15 s dosing time), the spectrum displays two clearly visible features at ~ 2154 and 822 cm^{-1} . The modes red-shift with increasing dosing time, so that after a ~ 90 s dose, the 2154 cm^{-1} mode has shifted to $\sim 2136 \text{ cm}^{-1}$ and the 822 cm^{-1} feature to $\sim 813 \text{ cm}^{-1}$. These frequencies remain constant as additional PDI is dosed onto the surface, while a shoulder appears on the high-frequency peak at $\sim 2123 \text{ cm}^{-1}$.

The 2123 cm^{-1} shoulder presumably corresponds to a free CN mode which could result from the formation of a multilayer. As the intensity of the flat-lying peaks would scale with $\cos^2(18^\circ)$ of the fully allowed intensity, a multilayer would likely be built of 1,4-PDI molecules found in all possible orientations. A large number would be found more or less perpendicular to the surface and fully allowed. Because of the surface selection rules, the shoulder could correspond to a rather small number of molecules that absorb very strongly as a result of their perpendicular orientation with respect to the

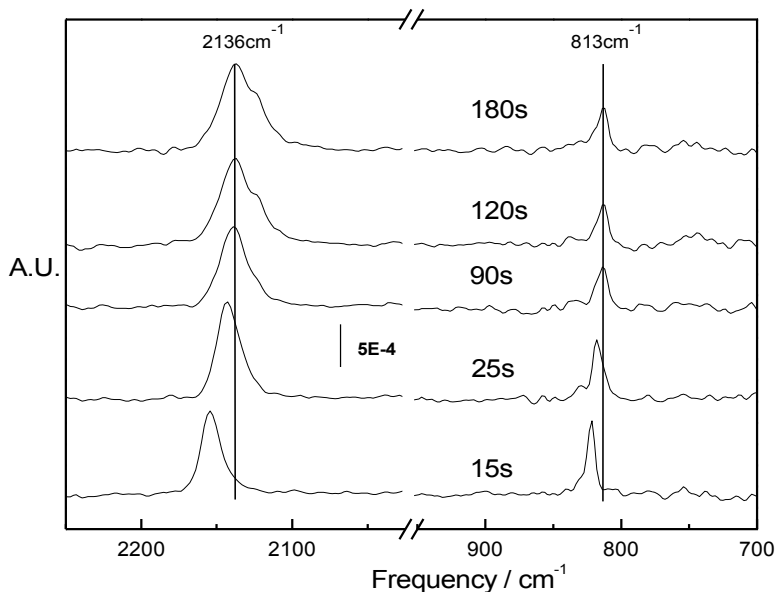


Figure 3: A series of reflection-absorption infrared spectra of PDI adsorbed on Au(111) as a function of exposure time, where the exposure times are indicated adjacent to the corresponding spectrum. Data acquired at room temperature.

Vibrational Frequency / cm⁻¹

PDI/Au(111) Low coverage-Expt.	PDI/Au(111) High Coverage-Expt.	DFT Calculation
822	813	–
2154	2136	2139
-	2123	2113

Table 1: Calculated and experimentally derived infrared frequencies for $-(\text{Au-PDI})_n-$ oligomers.

surface.

A series of high-resolution STM images of a PDI-saturated Au(111) surface is displayed in Fig. 4 (top panels) as a function of tip bias. Attempts were made to collect images with positive biases, but the resulting low image quality and lack of image stability suggested that molecules were being transferred to the tip under these conditions. The experimental images are in excellent agreement with the simulations (Fig. 4(B)).

Finally, the conductive properties of gold nanoparticles deposited onto a mica substrate exposed to 80 μl aliquots of serially diluted PDI solutions in benzene are summarized in Fig. 5. The clean sample, prior to 1,4-PDI dosing, had a conductivity of ~ 0.5 nS. The conductivity of the sample increases substantially as the 1,4-PDI concentration increases to reach a maximum value of ~ 18 nS

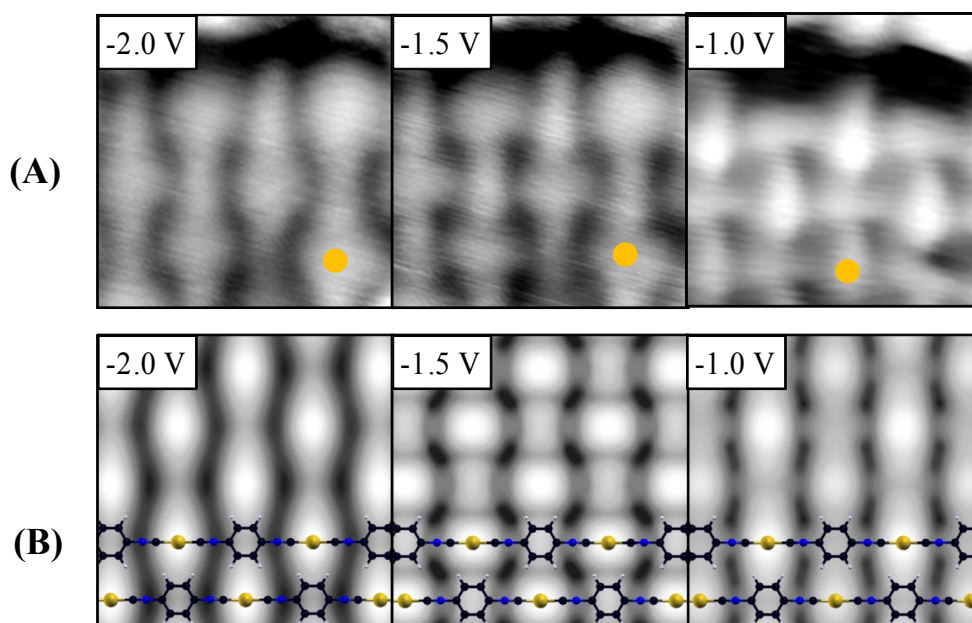


Figure 4: (A) Experimental high-resolution STM images of PDI on Au(111) collected as a function of tip bias voltage for negative biases, where the bias voltages are indicated in the images. The corresponding simulated images (B), using the Bardeen method, for the Au-PDI oligomeric structures depicted in Figure 2 are shown in the bottom panels along with the locations of the gold adatoms and the aryl rings.

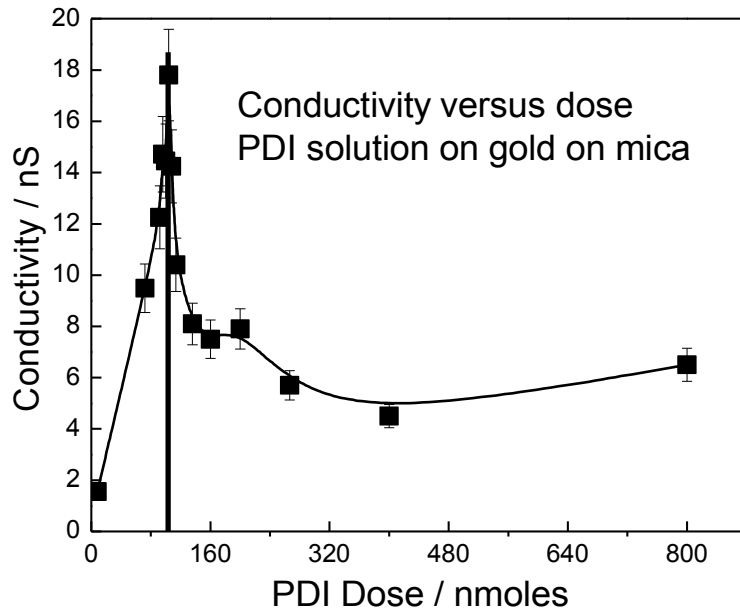


Figure 5: Plot of the conductivity of gold nanoparticles deposited onto a mica substrate after exposure to solutions of PDI in benzene as a function of the solution dose. (Experiment performed by Rasha Abuflaha)

after a PDI dose of ~ 100 nanomoles. At higher doses, the conductivity then decreases, initially quite rapidly, to a value of ~ 8 nS and then more slowly as the PDI dose exceeds ~ 160 nanomoles.

Discussion

The DFT calculations (Fig. 2) provide a basis for analyzing both the infrared and STM data. The calculations indicate that the formation of $-(\text{Au}-\text{PDI})_n$ oligomer chains is energetically feasible and are in accord with previous DFT results [8]. The experimental infrared data (Fig. 3) show the presence of two features at ~ 2136 and 813 cm^{-1} following a gas-phase PDI dosing time of $\sim 90 \text{ s}$. Lower exposures show slightly higher frequencies, presumably due to the formation of shorter chains on the surface and is ascribed to coupling between adjacent isocyanide species in the oligomer chain. Since the DFT calculations were performed for an infinite chain, it is appropriate to compare with the experimental data at higher exposures. As discussed above, the shoulder that appears at $\sim 2123 \text{ cm}^{-1}$ at higher PDI dosing times ($\sim 120 \text{ s}$ and greater) is assigned to a free isocyanide group and is in good agreement with the calculated value of 2113 cm^{-1} (Table 1).

The vibrational spectrum of gas-phase 1,4-PDI (D_{2h} symmetry) has been assigned with the aid of quantum calculations [29] and the strongest modes are at 850 (B_{1g} symmetry), 1505 (B_{1u}), 2127 (A_g) and 2132 cm^{-1} (B_{1u}). The first two modes are aryl ring modes while the last two are the symmetric and asymmetric $\text{N}\equiv\text{C}$ stretching modes, respectively. This indicates that the 2136 cm^{-1} feature is due to a bonded isocyanide stretching mode, in good agreement with the calculated value of 2139 cm^{-1} (Table 1), and the presence of a single $\text{N}\equiv\text{C}$ vibrational mode suggests that the isocyanides are symmetrically equivalent, in accord with the calculated structure (Fig. 2). The $\sim 833 \text{ cm}^{-1}$ feature is assigned to an out-of-plane C-H wagging mode and, according to the surface infrared surface selections rules, [30,31] its presence indicates that the plane of the aryl ring is parallel to the Au(111) surface, agreeing with the calculated structure (Fig. 2). The frequencies of out-of-plane CH modes in aryl rings depend strongly on the number and location of substituent groups on the ring, which affect the coupling between the C-H groups; [32] two adjacent hydrogen atoms in a 1,4-disubstituted molecule have in-phase, out-of-

plane vibrations at $817 \pm 17 \text{ cm}^{-1}$, in good agreement with the experimental value of $\sim 813 \text{ cm}^{-1}$. The infrared spectrum is in accord with the molecular structure predicted using DFT (Fig. 2) since both the $\text{N}\equiv\text{C}$ stretching ($\sim 2136 \text{ cm}^{-1}$) and out-of-plane C-H wagging ($\sim 849 \text{ cm}^{-1}$) are both evident.

Together, the infrared results provide clear evidence that the molecular structure shown in Fig. 2 is correct, but do not confirm that the molecule is bonded to gold adatoms, although the correspondence between the experimental and theoretical periodicities strongly suggests that it does. In order to explore this, the STM images were simulated using the Bardeen method, using a gold-covered tungsten tip [18]. This structure was selected since the tungsten wire used to make the tip is passivated by dipping it into the Au(111) surface resulting in the transfer of gold atoms to the end of the tip as discussed in Appendix A [33]. The simulated results (Fig. 4B) are compared with the experimental images (Fig. 4A) collected with tip biases of -2.0, -1.5 and -1.0 V. The locations of the gold adatoms and aryl rings are indicated in the bottom panels. In all cases, the intensity of the regions corresponding to the gold adatoms changes only slightly, while the image intensities corresponding to the aryl rings show a considerable bias dependence. The close correspondence between the experimental and simulated images indicates that the structure calculated by DFT is correct for the one-dimensional oligomer chains and, in particular, incorporates a gold adatom between the 1,4-PDI linker groups.

The results confirm the formation of one-dimensional oligomer chains on Au(111) by coupling between gold adatoms extracted from the substrate. However, analogous experiments in which gold films or nanoparticles are dosed with a 1,4-PDI solution present clear evidence for η^1 - species in which the PDI is bonded to gold *via* one isocyanide group, the uncoordinated group having a vibrational frequency close to the of a free isocyanide. The vibrational data for PDI on Au(111) at high dosing times (greater than $\sim 120 \text{ s}$, Fig. 3) suggests that such an η^1 geometry may form at high exposures from the appearance of the free isocyanide feature at $\sim 2123 \text{ cm}^{-1}$, either by adsorbing additional PDI or by

displacing one end of the PDI linking between gold adatoms.

In order to explore this effect, the conductivity of a gold-nanoparticle-covered mica surface was measured as a function of PDI dose. Analogous experiments in which the gold nanoparticles were exposed to PDI *in vacuo* showed that the conductivity increased from ~ 0.5 nS for the nanoparticle array prior to dosing, to a maximum value of ~ 23 nS when the sample was saturated with PDI (Chapter 5) [19]. This effect was ascribed to the linking of the nanoparticles by $-(\text{Au}-\text{PDI})_n-$ oligomers. A similar linkage of gold nanoparticles by dosing PDI from solution would be expected to yield a similar increase in conductivity. This is indeed found experimentally for solution dose up to ~ 100 nanomoles (Fig. 5) leading to a maximum conductivity of ~ 18 nS, in reasonable agreement with the results from gas-phase dosing (~ 23 nS). However, as the sample is exposed to higher PDI doses, the conductivity decreases substantially indicating that the conductive pathway is being disrupted, although there is some residual conductivity in the neighborhood of ~ 7 nS. This result is clearly consistent with the idea that the initial $-(\text{Au}-\text{PDI})_n-$ oligomer chains reorient at higher PDI concentrations. The results also indicate that it is possible to fabricate linked nanoparticle systems by simpler solution dosing as opposed to the more difficult process of depositing PDI *in vacuo*.

While the dosing times and solvents were different for earlier infrared experiments for PDI on gold films and nanoparticles from the ones used in this work, it is instructive to compare the conditions used to collect the data shown in Fig. 5 with those used to obtain the previous results. Work on PDI on gold films incorporated 15 mM solutions of PDI in DMSO in which the surface was exposed overnight, [10] clearly corresponding to the region in which additional PDI adsorbs on the surface (Fig. 4). Other work on gold films [9] used a 1 mM PDI solution in methylene chloride or THF for an exposure time of 12 hours likely also to result in additional PDI adsorption compared to the short time (10 s) used in this work. Interestingly, experiments on gold nanoparticles [11] that used PDI concentrations up to 1

mM in methanol in which the suspension was shaken for a relatively short time of ~30 s, also showed clear evidence for a free isocyanide group (at 2121 cm^{-1}). These conditions are similar to those used here for dosing the gold nanoparticles arrays on mica and would have suggested the formation of flat-lying species.

Conclusions

The proposed oligomeric structure of PDI adsorbed on Au(111) surface is confirmed using a combination of RAIRS and STM measurements combined with DFT calculations of -(Au-PDI)-oligomer chains on the surface. The first-principles quantum calculations confirm that the bonding of PDI between gold adatoms is thermodynamically feasible and the optimum spacing between the adatoms of ~1.1 nm is in good agreement with the experimental periodicity (Figure 1). The calculated structure is confirmed since the calculated vibrational frequencies and the nature of the simulated STM images are in agreement with experiment. It is found that the conductivity of gold nanoparticles deposited onto a mica substrate increases when dosed with PDI solutions up to a doses of ~ 100 nanomoles in agreement with the idea that the nanoparticles are linked by the oligomer chains. However, the conductivity decreases at higher doses, suggesting that the PDI is displaced to disrupt the oligomer chains in accord with the detection of vibrational modes due to free isocyanide groups.

Acknowledgements

We thank Professor Michael Weinert for advice on carrying out density functional theory calculations and Professor Werner Hofer for assistance with simulating STM images using bSKAN.

References

- 1) Boscoboinik, J.; Kestell, J.; Garvey, M.; Weinert, M.; Tysoe, W. *Top. Catal.* **2011**, *54*, 20.
- 2) Boscoboinik, J. A.; Calaza, F. C.; Habeeb, Z.; Bennett, D. W.; Stacchiola, D. J.; Purino, M. A.; Tysoe, W. T. *Physical Chemistry Chemical Physics* **2010**, *12*, 11624.
- 3) Zhou, J.; Acharya, D.; Camillone, N.; Sutter, P.; White, M. G. *The Journal of Physical Chemistry C* **2011**, *115*, 21151.
- 4) Maksymovych, P.; Sorescu, D. C.; Yates, J. T. *Phys. Rev. Lett.* **2006**, *97*.
- 5) Maksymovych, P.; Yates, J. T. *J. Am. Chem. Soc.* **2008**, *130*, 7518.

- 6) Lennartz, M.; Atodiresei, N.; Muller-Meskamp, L.; Karthaeuser, S.; Waser, R.; Blugel, S.; *Langmuir* **2008**, *25*, 856.
- 7) Voznyy, O.; Dubowski, J. J.; Yates, J. T.; Maksymovych, P. *Journal of the American Chemical Society* **2009**, *131*, 12989.
- 8) Boscoboinik, J.; Kestell, J.; Garvey, M.; Weinert, M.; Tysoe, W. *Topics in Catalysis* **2011**, *54*, 20.
- 9) Henderson, J. I.; Feng, S.; Bein, T.; Kubiak, C. P. *Langmuir* **2000**, *16*, 6183.
- 10) Swanson, S. A.; McClain, R.; Lovejoy, K. S.; Alamdari, N. B.; Hamilton, J. S.; Scott, J. C. *Langmuir* **2005**, *21*, 5034.
- 11) Robertson, M. J.; Angelici, R. J. *Langmuir* **1994**, *10*, 1488.
- 12) Shih, K.-C.; Angelici, R. J. *Langmuir* **1995**, *11*, 2539.
- 13) Angelici, R. J.; Lazar, M. *Inorganic Chemistry* **2008**, *47*, 9155.
- 14) Angelici, R. J. *J. Organomet. Chem.* **2008**, *693*, 847.
- 15) Greenler, R. G. *Journal of Chemical Physics* **1966**, *44*, 310.
- 16) Kottke, M. L.; Greenler, R. G.; Tompkins, H. G. *Surf. Sci.* **1972**, *32*, 231.
- 17) Xiao-Dong, W.; Tysoe, W. T.; Greenler, R. G.; Truszkowska, K. *Surface Science* **1991**, *257*, 335.
- 18) Bardeen, J. *Phys. Rev. Lett.* **1961**, *6*, 57.
- 19) Kestell, J.; Abuflaha, R.; Boscoboinik, J. A.; Bai, Y.; Bennett, D. W.; Tysoe, W. T. *Chem Commun* **2013**, *49*, 1422.
- 20) Kaltchev, M.; Thompson, A. W.; Tysoe, W. T. *Surface Science* **1997**, *391*, 145.
- 21) Kresse, G.; Joubert, D. *Physical Review B* **1999**, *59*, 1758.
- 22) Kresse, G.; Hafner, J. *Physical Review B* **1993**, *47*, 558.
- 23) Perdew, J. P.; Burke, K.; Ernzerhof, M. *Physical Review Letters* **1996**, *77*, 3865.
- 24) Hofer, W. A.; Redinger, J. *Surface Science* **2000**, *447*, 51.
- 25) Hofer, W. A.; Fisher, A. J.; Lopinski, G. P.; Wolkow, R. A. *Chemical Physics Letters* **2002**, *365*, 129.
- 26) W.A, H. *Progress in Surface Science* **2003**, *71*, 147.
- 27) Hofer, W. A.; Garcia-Lekue, A. *Physical Review B* **2005**, *71*, 085401.
- 28) Ito, M.; Noguchi, H.; Ikeda, K.; Uosaki, K. *Phys. Chem. Chem. Phys.* **2010**, *12*, 3156.
- 29) Han, H. S.; Han, S. W.; Joo, S. W.; Kim, K. *Langmuir* **1999**, *15*, 6868.
- 30) Greenler, R. G. *The Journal of Chemical Physics* **1966**, *44*, 310.
- 31) Greenler, R. G. *The Journal of Chemical Physics* **1969**, *50*, 1963.
- 32) Colthup, N. B.; Daly, L. H.; Wiberley, S. E. *Introduction to infrared and raman spectroscopy. 2.ed*; Academic Press: New York,N.Y., 1975.
- 33) Burkholder, L.; Garvey, M.; Weinert, M.; Tysoe, W. T. *Journal of Physical Chemistry C* **2011**, *115*, 8790.
- 34) Garvey, M.T.; Ph.D. dissertation, **2014**. University of Wisconsin-Milwaukee

Chapter 4

Understanding and Controlling the 1,4-Phenylene Diisocyanobenzene-Gold Oligomer Formation Pathways

Introduction

In Chapter 3 the structure of 1,4-phenylenediisocyanide/Au oligomers on Au(111) was investigated. The structure was elucidated through high-resolution STM which indicated that these structures form spontaneously at room temperature at all coverages under UHV conditions. These findings were confirmed via RAIRS which showed evidence of a single CN mode 2136 cm^{-1} which is in excellent agreement with the 2139 cm^{-1} calculated with high level DFT. The RAIRS spectra also showed an 813 cm^{-1} mode which for a *para*-substituted phenyl ring is consistent with an out of plane C-H wagging mode. For a ring lying parallel with the surface, this out of plane vibration would be fully allowed and visible in RAIRS. The system is of practical interest as PDI is a prototypical *molecular wire* material. The idea that not only will *single molecules* conduct charge, but that in fact extended, highly conjugated wire-like assemblies could form is most intriguing.

Further research on the system was therefore undertaken for two reasons. The first reason is that the flat-lying PDI/Au oligomeric structures are actually inconsistent with earlier findings that rather conclusively demonstrated that 1,4-PDI is found in an upright η^1 coordination motif. The system from which this conclusion was drawn is significantly different as the PDI was solution dosed on to thermally evaporated films (rather than sublimed onto single-crystal Au(111)). Still, it suggests that the

upright PDI covered surface is thermodynamically stable or meta-stable at least.

A second reason for our interest comes from the desire to build *functionality* into the oligomeric systems. While it is most exciting to have the capability of wiring two nanoelectrodes with a “wire” 1 molecule in diameter (discussed in chapter 5), it is perhaps not a stretch to envision wiring the nanoelectrodes with a “smart” material such as an Avrim and Ratner type molecular diode. Such a functional structure would first require building asymmetry into a molecule (a donor half and an acceptor half), and second it would require the ability to install the molecular component into the circuit directionally. Knowledge of the mechanics of the assembly of the oligomers could perhaps provide insights into realizing this goal. It could skirt the problem of *nanofabrication* and instead allow nanostructures to form spontaneously, driven by the laws of thermodynamics.

1,4-phenylene diisocyanobenzene (PDI) self-assembles on a Au(111) surface at room temperature results to form of one-dimensional chains that comprise alternating gold and PDI units, [1-3] suggesting that they form by extracting gold atoms from low-coordination sites on the gold substrate. Adatom structures formed on coinage metals are relatively common [4-7]. The formation of

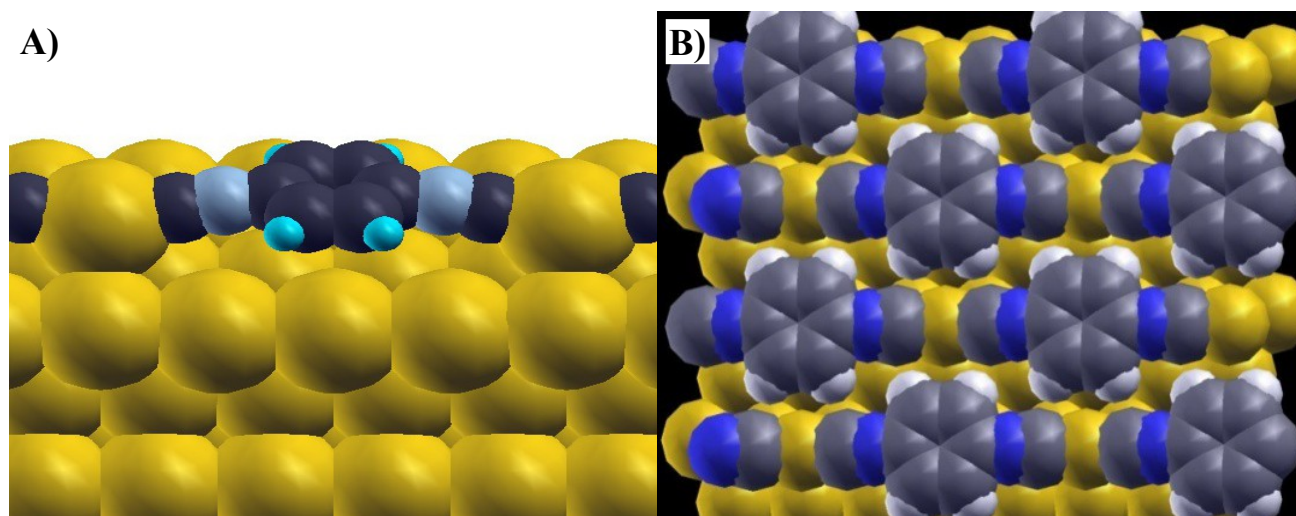


Figure 1: The structure of (Au-PDI) oligomers on gold calculated using density functional theory shown (A) an angled view and (B) a top views of the oligomer chains.

such one-dimensional units has been shown to be energetically favorable and the structure calculated

using density functional theory calculations are displayed in Fig. 1. The formation of this structure has been confirmed using reflection-absorption infrared spectroscopy and by comparing the simulated scanning tunneling microscopy (STM) images calculated for the structure should in Fig. 1 with experiment, where the two show good agreement. In addition to forming on a gold single crystal substrate, it has been found that the $-(\text{Au}-\text{PDI})_n-$ oligomers are capable of bridging between gold nanoparticles deposited onto an insulating mica substrate, thereby providing a conductive pathway between the nanoparticles.

In a later chapter, a process known as *decoordination* will be discussed. It will be demonstrated that while the flat-lying oligomeric chains form spontaneously from UHV dosing, under certain conditions it is indeed possible to generate upright η^1 from the flat lying species simply by exposing the surface to an adsorbate such as CO. The system has been shown to function as a sort of 2 state device or chemically driven switch. This chapter attempts to address the mechanistic aspect of the *formation* of the $-(\text{Au}-\text{PDI})_n-$ chains, based heavily on computational work.

Theoretical Methods

Density functional theory calculations were performed with the projector augmented wave (PAW) method [9] as implemented in the Vienna *ab initio* simulation package, VASP [10]. The exchange-correlation potential was described using the generalized gradient approximation (GGA) of Perdew, Burke and Ernzerhof [11]. A cutoff of 400 eV was used for the planewave basis set, and the wavefunctions and electron density were converged to within 1×10^{-5} eV. The first Brillouin zone was sampled with a $4 \times 4 \times 1$ Γ -centered k-point mesh. Geometric relaxations were considered to be converged when the force was less than $0.02 \text{ eV}/\text{\AA}$ on all unrestricted atoms. Since Van der Waals have been found to have a large contribution to the binding energies on coinage metals surfaces, [12-17] calculations were also performed by including Van der Waals corrections.

Results

The results of DFT calculations of PDI-Au oligomer chains are presented for reference and the surface structure was constructed by bridging gold adatoms placed on a Au(111) substrate aligned along the close-packed directions, corresponding to the orientations on the linear chains observed by STM on Au(111) [1-3]. The gold adatoms were separated by four-substrate lattice-translation distances, corresponding to the experimental repeat distance of ~ 1.1 nm. The PDI molecule was then placed between the gold adatoms and the structure allowed to relax. The resulting structures are displayed in

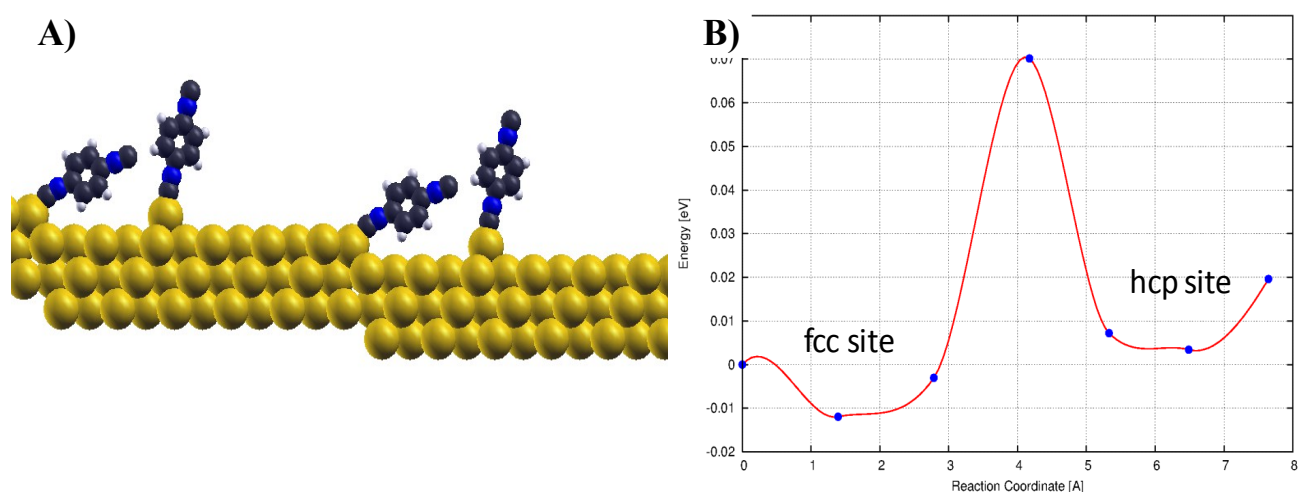


Figure 2: A) The structure of the most stable, vertical Au-PDI adatom complex on a Au(111) substrate. B) Shown also is the energy profile for diffusion of the complex from the most stable, face-centered cubic (fcc) three-fold hollow site to the adjacent hexagonal-close packed (hcp) site.

Fig. 1, where Fig. 1A) shows an angle view of the Au-PDI-Au bridging units and Fig. 1B) shows a top view. The isocyanide groups are angled slightly (at $\sim 18^\circ$) with respect to the surface and the molecule has local C_{2v} symmetry, with the aryl ring oriented parallel to the Au(111) plane. The binding energy, calculated from the difference between the energy of the final structure shown in Fig. 1, and the energy of the gold adatom covered surface plus the energy of gas-phase 1,4-PDI is 203 kJ/mol.

Since the oligomer consists of Au-PDI units, this is proposed to react by extracting gold atoms

from low-coordination sites. To explore the structure and mobility of this putative precursor, a PDI molecule was placed on a gold adatom on a Au(111) surface and the geometry optimized. It was found that the most stable site for the gold adatom in the complex was at a face-centered cubic (*fcc*), three-fold hollow site and the structure is depicted in Fig. 2. Similar structures for the Au-PDI adatom complex on gold have been found previously [18]. The binding energy of the PDI to the gold adatom was calculated from the difference between the energy of the isocyanide molecule bound to a gold adatom on the substrate and the energies of an isolated, gas-phase PDI molecule and a Au(111) surface with a gold adatom. While the most stable structure was found with the principal axis of the 1,4-PDI molecule perpendicular to the surface, the energy to tilt the molecule is fairly small. This is discussed in greater detail below. Since oligomerization of this adatom complex necessitates it being relatively mobile on the surface, the energy for it to diffuse from the most stable *fcc*, three-fold hollow site to the closed (*hcp*) three-fold-hollow site was calculated. The results of energy versus reaction coordinate are also displayed in Fig. 2B) along with selected structures along the reaction pathway. An animation of the motion is available in the Supplementary Materials section. The energy of the *hcp* site is almost degenerate with the *fcc* site, which is slightly less stable and the barrier for diffusion is relatively low at ~ 0.08 eV (~ 8 kJ/mol). Thus the adatom complex is mobile on the surface at 300 K.

Oligomerization:

Examination of a large number of STM images of 1,4-PDI dosed Au(111) have indicated that the resultant surfaces do not disturb the herringbone reconstruction. This is especially obvious in the lower-coverage where the clean substrate between the chains can be readily resolved. Also absent in STM images is evidence for *etch pits*—places where the isocyanides have abstracted gold atoms from terraces. What is quite evident is that the smooth, gently curved step-edges of the crystal become eroded. What has not been observed are oligomers where both termini are free-standing. These findings strongly imply that the mechanism of oligomer growth is a matter of the chains originating

at a step or other feature and propagating from there.

As described above, a critical feature of this system is the formation of an η^1 PDI/Au_{adatom} complex which is suggested to be the precursor state for chain growth. There are two possible ways in which the mobile adatom complex can oligomerize. In the first, the Au-PDI adatom complex can diffuse to a step edge or a gold adatom at the terminus of a growing $-(\text{Au-PDI})_n$ - oligomer chain, and tilt to coordinate the free isocyanide group to the gold terminus. This process creates a new terminus for subsequent oligomerization steps. The relatively low energies required to tilt the 1,4-PDI on the adatom complex suggests that this should be energetically feasible. However, when the gold-adatom complex is placed adjacent to a gold atom terminating the chain, the PDI molecule merely tilts and does not form a bond between the isocyanide group and the gold atom. Presumably this might be possible if the adatom complex tilted when located on a site an appropriate distance for the chain terminus (~ 4 lattice spacings), but the mobility of the adatom complex calculated above suggests that the residence time at that site would be too short for this step to occur with a high probability. We therefore explored the alternative possibility in which an isocyanide-terminated chain couples directly with the gold in the gold adatom complex. This was initially explored for a PDI molecule bound to a step edge. The structure of PDI bound to a step edge is shown in Fig. 3. This reveals that the PDI molecule is now substantially tilted (at $\sim 30^\circ$ to the surface), with the plane of the aryl ring perpendicular to it. Clearly, such a tilted geometry will facilitate coupling between the isocyanide terminus and a gold atom in the adatom complex. To illustrate this, a gold adatom complex was placed at a three-fold hollow site next to the tilted PDI molecule, which causes it to tilt somewhat. The final structure, when the isocyanide has bonded to gold adatom is shown in Fig. 4. This is stable by ~ 0.4 eV (~ 38 kJ/mol) with respect to the initial state shown in Fig. 3 and so is thermodynamically feasible. Interestingly, the PDI terminus is now even closer to the surface than when bound to a step edge,

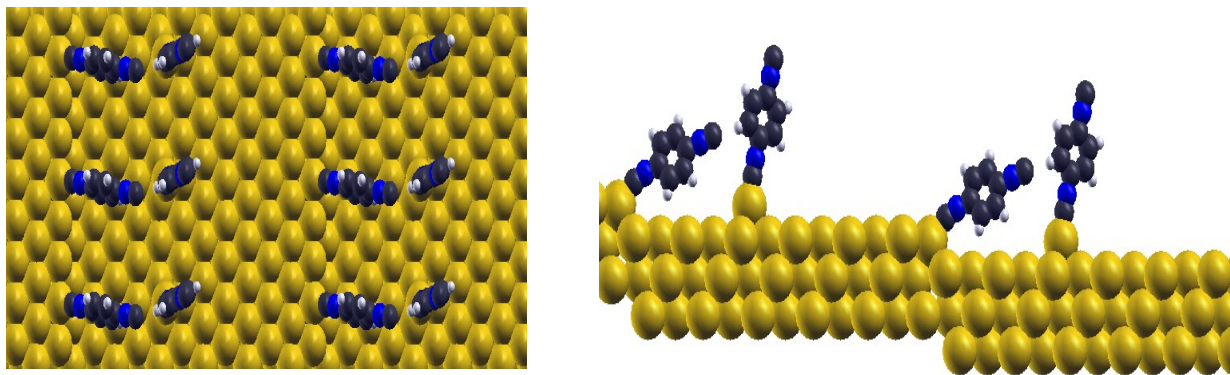


Figure 3: The calculated structure of a PDI molecule bound to a gold step, with a second PDI molecule placed close to it as an initial configuration for calculating the reaction barrier (top and side views).

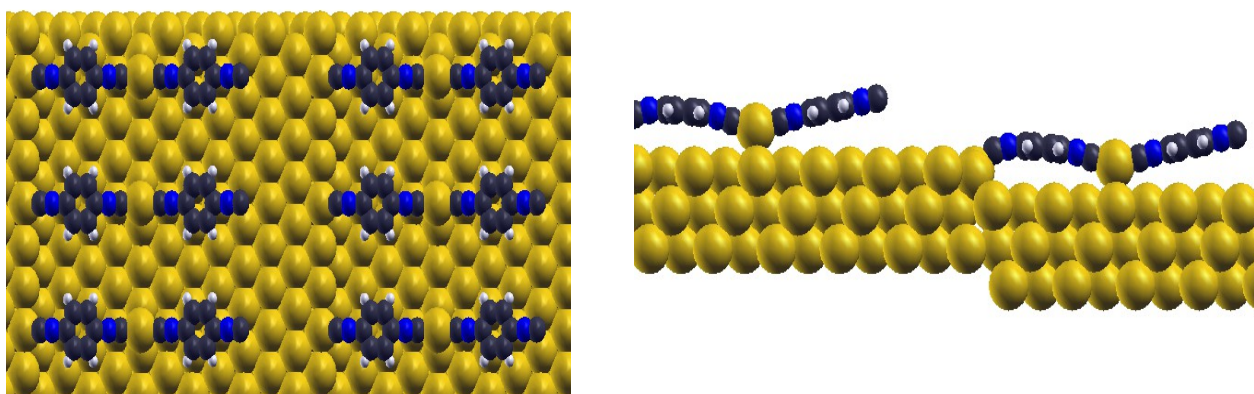


Figure 4: The final structure of a gold-PDI adatoms complex bound to an isocyanide molecule on a gold step edge.

thereby facilitating further oligomerization by Au-PDI adatom complex coupling. This *trans* effect is common in organometallic complexes and is consistent with the structure of isolated Au-PDI chains [2]. The energy profile for the transition from the initial (Fig 3) to the final (Fig. 4) states is shown in

Fig. 5, along with along with selected structures along the reaction pathway. As the reaction proceeds, both PDI molecules start to tilt, until the isocyanide group forms a bond with the gold adatom, when the gold adatom moves slightly to optimize the bonding to the isocyanide group. This is accompanied by additional tilting of the terminal PDI molecule, which is then oriented close to parallel to the surface. The energy profile shows an initial, metastable intermediate and a second, higher barrier, occurs when the gold-isocyanide bond is formed. The height of the barrier is ~ 0.28 eV (~ 27 kJ/mol), indicating that this step is relatively rapid at room temperature. Since Van der Waals'

interactions have been found to affect the energetic and, in some cases, the structure of adsorbate on gold, similar calculations were performed by including these interactions. The resulting initial structure (analogous to that shown in Fig. 3) is displayed in Fig. 6. The addition of Van der Waals

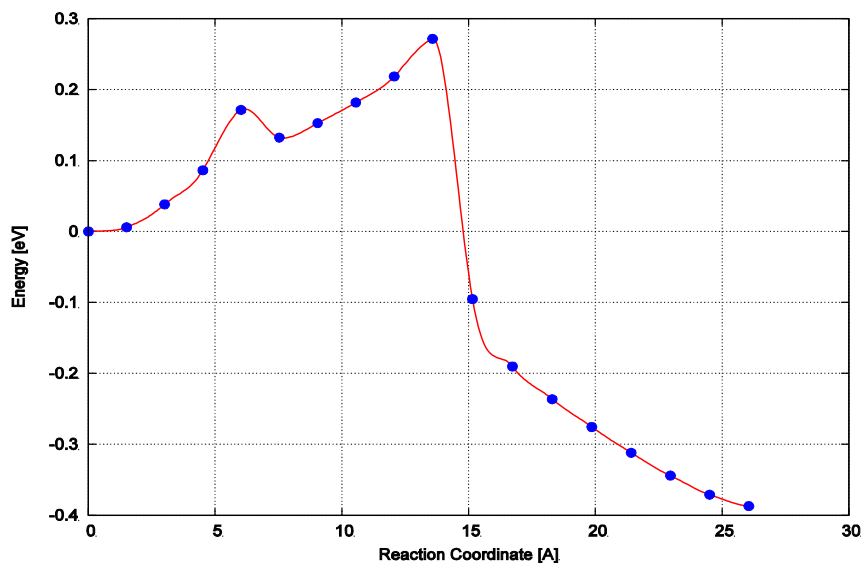


Figure 5: The energy profile for the binding of a gold adatom complex to a PDI molecule attached to a gold step edge.

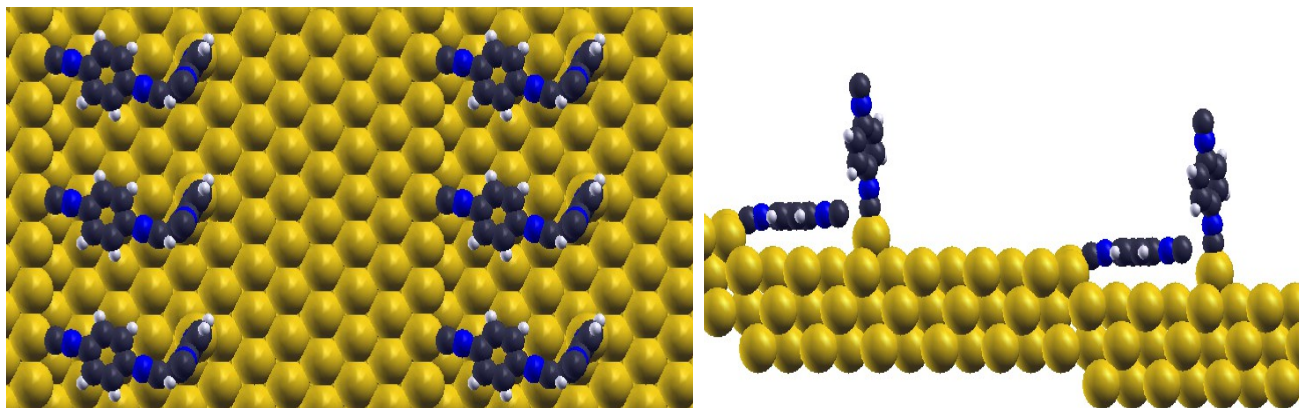


Figure 6: The calculated structure of a PDI molecule bound to a gold step, with a second PDI molecule placed close to it and an initial configuration for calculating the reaction barrier, now including Van der Waals' interactions.

interactions has a profound effect on the initial state structure. Now the PDI molecule at the step edge is parallel and much closer to the surface because of the Van der Waals' interactions. This minimizes the interaction with the Au-PDI adatom complex, which now has a structure that is closer to the isolated species (Fig. 2). The structure of the final state is similarly affected (Fig. 7), where the PDI molecule at the terminus of the growing oligomer is also parallel and close to the surface. The

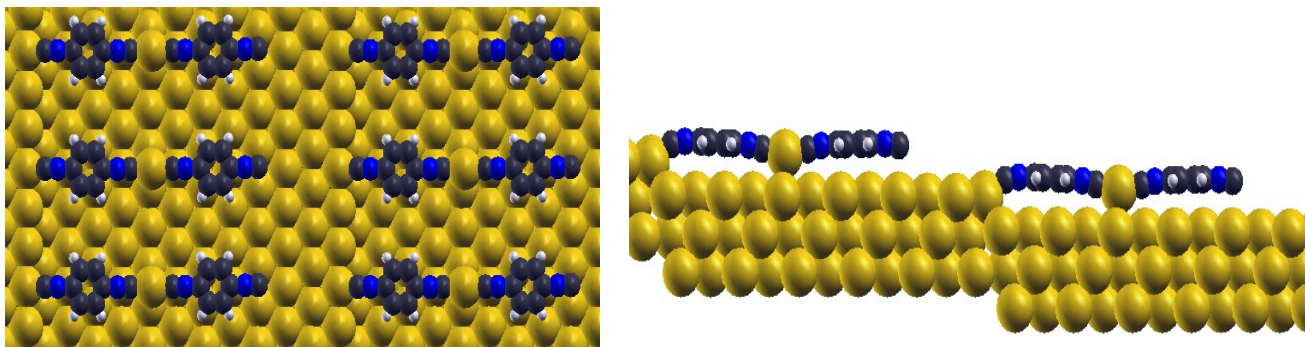


Figure 7: The final structure of a gold-PDI adatoms complex bound to an isocyanide molecule on a gold step edge, now including Van der Waals' interactions. Terminal CN is drawn significantly closer to the surface than was showing in Fig. 4, in the absence of VdW corrections.

oligomerization reaction is now significantly more exothermic (by ~ 1.2 eV, ~ 115 kJ/mol). The corresponding energy profile calculated by including Van der Waals interactions is shown in Fig. 8. Now, in spite of the increased exothermicity, the barrier height is only very minimally affected, but is still a relatively low ~ 0.3 eV. This is consistent with the structural evolution indicating that the reaction occurs with a relatively early transition state [19-23].

These results suggest that PDI oligomerizes on the surface by a mobile Au-PDI adatom complex approaching a tilted, bound PDI molecule, either on a step edge or at the end of a growing $(\text{Au-PDI})_n$ - oligomer chain to form a gold-isocyanide bond. However, rapid diffusion of the gold-adatom complex, while facilitating its access to the end of a growing chain, may now reside for a sufficient time for the bond to form. To explore this, the energy of a gold-adatom complex was calculated as a function of its distance from a chain terminus. In this case, the location of the gold adatom was fixed at a particular site, while the rest of the system was allowed to relax to its minimum energy and the calculation were performed without using Van der Waals' corrections. It is clear that there appears to be a significant, relatively long-range interaction between the adatom complex and the growing terminus of several kJ/mol. This will have the effect of funneling the diffusing gold-adatom complex towards the isocyanide group and stabilizing it, thereby enhancing the reaction probability

Finally, in order to isolated adatom monomers to diffuse to interact with isocyanide termini, they must remain isolated. One might a priori expect that low-coordination gold adatoms might

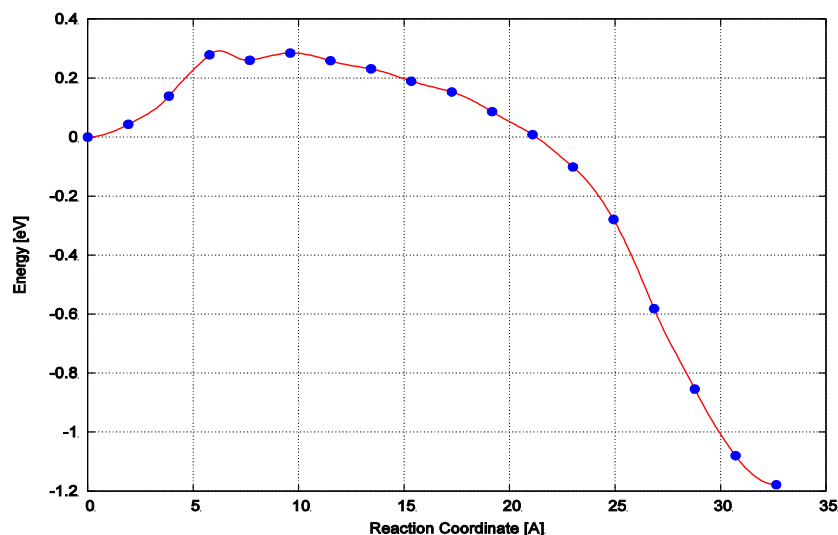


Figure 8: The energy profile for the binding of a gold adatom complex to a PDI molecule attached to a gold step edge, now including Van der Waals' interactions.

agglomerate to form clusters that are consequently less mobile. In order to investigate this effect, the energy of two adjacent adatom complexes on Au(111) was calculated to compare with the energies of isolated species. It was found that the adjacent dimers were repulsive by ~ 0.3 eV (~ 28 kJ/mol) and will therefore remain apart when diffusing on the surface. There are two possible origins for this effect. The first is that isocyanide binding to gold causes a charge transfer that leads to electrostatic repulsion between adatom complexes. An alternative possibility is that the gold adatom complex forms because of the reactivity of the isolated gold adatom [24]. Thus, forming gold dimers leads to weakening of the gold-isocyanide bond resulting in a net repulsive interaction between the adatom complexes.

CHAIN MOBILITY:

Discussion

The DFT calculations described above provide evidence for a plausible $-(\text{Au}-\text{PDI})_n-$ oligomerization pathway found following PDI adsorption on Au(111) and linking between gold

nanoparticles. The propagating monomer is proposed to comprise a vertical gold adatom complex, which remains isolated but is rather mobile on the surface. They are, however, attracted to the terminus of a growing $-(\text{Au}-\text{PDI})_n-$ chain or a PDI molecule coordinated to a step edge and can bind to the isocyanide group of the terminal PDI with a relatively low activation barrier (~ 28 kJ/mol) to rapidly propagate the chain. It is anticipated that such an oligomerization pathway is available to any bifunctional molecule that can form strong bonds with gold to form a mobile adatom complex. This requires that the second, uncoordinated group be sterically isolated from the surface to prevent it forming η^2- complexes that would not be able to propagate. This condition is clearly fulfilled in 1,4-phenylene diisocyanobenzene, where the isocyanide groups are located para to each other and the molecule is rigid. For example thiols have also been shown to form thiolates on gold that also bind to gold adatoms [4,5,7] so that it is anticipated that dithiols would form similar oligomeric chains as long as the second thiolate was constrained so as not to bind to the surface. It is therefore expected that this lateral self-assembly pathway should be available to a range of bifunctionalized molecules, as long as the molecular structure prevented the second functional group from accessing the surface.

Potential Utility of Chain Propagation Mechanism:

The field of “molecular electronics” stemmed from the 1974 thought experiment of Avrim and Ratner who proposed a molecular with rectifying behavior [8]. The idea was presented by way of comparison with silicon based devices and standard p-n junctions. They hypothesized that it should be possible to create a molecule, properly functionalized, to behave in a similar fashion. To this end, they envisioned a structure along the lines of figure 10. A π -system functionalized with electron donating groups (methyl, amino or hydroxyl) would be covalently bonded to another π -system functionalized with electron accepting groups (fluoro, nitro or nitrile), the two systems separated by a methylene bridge which would act as a tunneling junction between them.

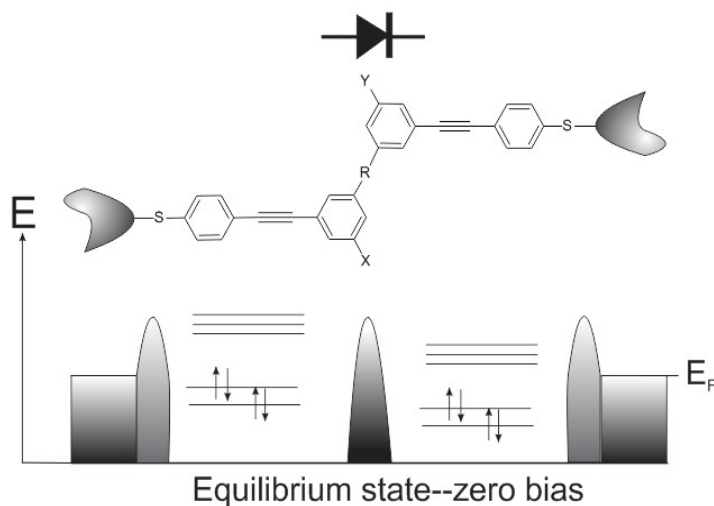


Figure 10: The classic Aviram and Ratner molecular diode. X=(methyl, amino, hydroxyl) and Y=(nitro, cyano, fluoro). A donor and acceptor separated by a methylene tunneling bridge. The groups, in theory, could serve as *intramolecular* n or p dopants respectively.

The synthetic methodologies to create such molecules certainly exist, as do the instrumentation which would be required to test such devices (break junctions for example). What seriously complicates the issue is that the devices would need to be installed in a molecular circuit in a *directional* way. If two of the above molecular diodes bridge an electrode in parallel, the device might work as planned. However, if they install themselves in an *anti*-parallel arrangement, the effect of one would negate the effect of the other.

What we propose is that given a bifunctional *polar* molecule, it might be possible to put the above assembly mechanism to good use. If a molecule is polar, it should experience a substantial torque in the presence of an applied electric field. As we are proposing the molecules assemble into wires through stepwise coordination of tilted PDI-Au_{adatom}, we are suggesting that under the influence of an applied field, it should therefore be possible to assemble polar molecules *preferentially* in one orientation over the other. This is assuming of course, that the self assembly presented here is general for similar diisocyanides.

While this could not be achieved with the nanoparticle arrays on mica that have been used to explore the electron transport properties of bridged nanoparticles (discussed in Chapter 5), it should be possible for systems with discrete nanogaps, such as those fabricated using techniques such as electromigration. The effect of an external force on the rate of a chemical reaction has been modeled using Bell theory [25-27] where the reaction rate constant under the influence of an external force is given by: $k_{\pm}(\tau) = k_0 \exp\left(\frac{\pm \mu E \cos(\Delta\theta^{\ddagger})}{k_B T}\right)$. Here k_0 is the thermal rate constant, μ is the external force exerted on the molecule and $\Delta\theta^{\ddagger}$ is a vector from the reactant to the transition state. In the case of PDI on gold, reaction from the initial to the transition state involves a rotation of the coordinating PDI molecule as the molecule on the step edge forms a bond with the gold. Since the reaction coordinate in this case involves the rotation of the molecule, a torque τ exerted to rotate the molecule through an angle $\Delta\theta^{\ddagger}$ will lead to a modified equation:

$$k_{\pm}(\tau) = k_0 \exp\left(\frac{\pm \mu E \cos(\Delta\theta^{\ddagger})}{k_B T}\right), \quad 1)$$

On order to estimate the value of $\Delta\theta^{\ddagger}$, it is assumed that a molecule analogous to PDI has a dipole moment μ and is similarly oriented perpendicular to the surface (Fig. 6), and that oligomerization proceeds *via* a similar pathway. The torque exerted on the polar molecule will depend on the alignment of the dipole moment with respect to the field, where one alignment will lower the barrier, while the other will increase it. For an electric field of magnitude E parallel to the surface, where the + and – indicate the orientation of the polar molecule with respect to the electric field. Note that this enhancement will be identical irrespective of which side of the nanogap the oligomerization is initiated. Thus:

$$\frac{k_+(E, \mu)}{k_-(E, \mu)} = \exp\left(\frac{2\mu E \cos(\Delta\theta^{\ddagger})}{k_B T}\right)$$

The relative propagation rates will lead to a preferential orientation in one direction is direct proportion to the rate constants. The resulting values of $\Delta\theta^{\ddagger}$ are estimated by assuming that the value of $\sim 30^\circ$ seen for the tilt from the initial to the transition state in Fig. 7 is typical. The values of orientational excess, calculated from:

$$\begin{aligned} & \frac{(N_+(E, \mu) - N_-(E, \mu)) / ((N_+(E, \mu) + N_-(E, \mu)))}{= \left(\frac{N_+(E, \mu)}{N_-(E, \mu)} - 1\right) / \left(\frac{N_+(E, \mu)}{N_-(E, \mu)} + 1\right)} \end{aligned} \quad 2)$$

are estimated for electric fields between 10^7 and 10^9 V/m for dipole moments between 0.5 and 3 Debye at $T=300\text{K}$. In this case, completely random orientations yield a value of zero, while perfect alignment results in a value of unity. The results are plotted *versus* electric field in Fig. 11. This reveals that significant orientation occurs with applied electric fields of $\sim 10^8$ V/m, and that almost complete

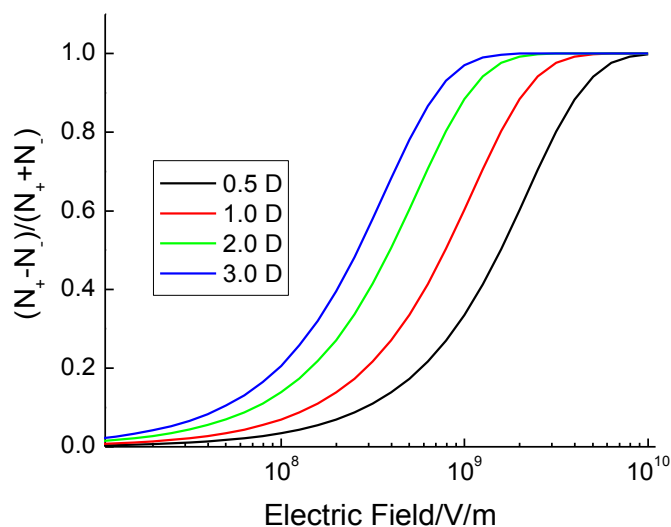


Figure 11: Plot of the orientational excess, *versus* electric field in V/m for molecules with dipole moments of 0.5, 1, 2 and 3 Debye.

alignment can occur if the fields reach $\sim 10^9$ V/m. Such fields can easily be attained by the application of ~ 1 V across a 10 nm gap.

Conclusions

In this chapter a mechanism for the growth of the $-(\text{Au}-\text{PDI})_n$ - oligomers described in Chapter 3 was put forth. The hypothesis begins with the formation of an η^1 PDI / Au_{step} complex. As low-coordination gold atoms are more reactive, it is not unlikely that the oligomers would propagate from or be terminated by a feature such as a step or crystal defect rather than an atomically flat terrace. As indicated by DFT (Figure 6), when Van der Waals corrections are incorporated, this precursor/anchoring PDI group is found lying nearly parallel with the gold surface. This leaves the

terminal isocyanide group in an optimal orientation to coordinate another gold atom. It has been demonstrated elsewhere that PDI found on gold adatoms yield a moiety that is far more mobile on the surface than adatoms alone would be. It is not unlikely that the surface, upon exposure to 1,4-PDI, is capable of abstracting gold atoms from the steps and allowing them to diffuse away. As the η^1 PDI / Au_{adatom} complexes are diffusing about the surface, they would simply be required to lean over slightly to leave them in perfect configuration to coordinate the anchored PDI (the one tied to the step or defect). This now leaves a terminal CN group, analagous to the first, ready to receive another η^1 PDI / Au_{adatom} complex. The process continues until the surface is either saturated or the impingement of PDI is stopped.

We also propose in this chapter the potential utility of such a mechanism as it pertains to the field of molecular electronics and specifically to the so called *bottom up* approach to molecular self-assembly. Demonstrated here and in the previous chapter, PDI/Au based molecular wires do indeed form spontaneously on Au(111) surfaces. However, to build truly *useful* molecular devices it will become necessary to extend this chemistry. First, functionality must be built into the molecule (as in the Aviram and Ratner system) typically through some well reasoned asymmetry. The synthetic strategies for this step already exist. Secondly, the molecules must be inserted between electrodes in a directional way—something which eludes researchers still. We propose here that perhaps PDI could be altered in some way to leave it polar, it should be possible to grow the oligomers in the presence of an electric field and have the electric field exert a torque on the growing (dipolar) molecules. This should enhance the growth kinetics of the molecules growing *with* the field and retard those trying to oppose it.

References:

- 1) Boscoboinik, J.; Kestell, J.; Garvey, M.; Weinert, M.; Tysoe, W. *Top. Catal.* **2011**, *54*, 20.
- 2) Boscoboinik, J. A.; Calaza, F. C.; Habeeb, Z.; Bennett, D. W.; Stacchiola, D. J.;

- Purino, M. A.; Tysoe, W. T. *Physical Chemistry Chemical Physics* **2010**, *12*, 11624.
- 3) Zhou, J.; Acharya, D.; Camillone, N.; Sutter, P.; White, M. G. *The Journal of Physical Chemistry C* **2011**, *115*, 21151.
 - 4) Maksymovych, P.; Sorescu, D. C.; Yates, J. T. *Phys. Rev. Lett.* **2006**, *97*.
 - 5) Maksymovych, P.; Yates, J. T. *Journal of the American Chemical Society* **2008**, *130*, 7518.
 - 6) Lennartz, M.C.; Atrodiresi, N.; Muller-Meskamp, L.; Karthaus, S.; Waser, R.; Blugel, S.; *Langmuir* **2008**, *25*, 856.
 - 7) Voznyy, O.; Dubowski, J. J.; Yates, J. T.; Maksymovych, P. *Journal of the American Chemical Society* **2009**, *131*, 12989.
 - 8) Aviram, A.; Ratner, M. A. *Chem. Phys. Lett.* **1974**, *29*, 277.
 - 9) Kresse, G.; Joubert, D. *Phys. Rev. B* **1999**, *59*, 1758.
 - 10) Kresse, G.; Hafner, J. *Phys. Rev. B* **1993**, *47*, 558.
 - 11) Perdew, J. P.; Burke, K.; Ernzerhof, M. *Phys. Rev. Lett.* **1996**, *77*, 3865.
 - 12) Ramalho, J. P. P.; Gomes, J. R. B.; Illas, F. *RSC Advances* **2013**, *3*, 13085.
 - 13) Li, G.; Tamblyn, I.; Cooper, V. R.; Gao, H.-J.; Neaton, J. B. *Phys. Rev. B* **2012**, *85*, 121409.
 - 14) Liu, W.; Carrasco, J.; Santra, B.; Michaelides, A.; Scheffler, M.; Tkatchenko, A. *Phys. Rev. B* **2012**, *86*, 245405.
 - 15) Mura, M.; Gulans, A.; Thonhauser, T.; Kantorovich, L. *Phys. Chem. Chem. Phys.* **2010**, *12*, 4759.
 - 16) Kelkkanen, A. K.; Lundqvist, B. I.; Nørskov, J. K. *Phys. Rev. B* **2011**, *83*, 113401.
 - 17) Duy, L.; Maral, A.; Adam, K.; Talat, S. R. *Journal of Physics: Condensed Matter* **2012**, *24*, 222001.
 - 18) Li, Y.; Lu, D.; Swanson, S. A.; Scott, J. C.; Galli, G. *The Journal of Physical Chemistry C* **2008**, *112*, 6413.
 - 19) Santen, R. A. v.; Neurock, M. *Molecular heterogeneous catalysis : a conceptual and computational approach*; Wiley-VCH: Weinheim; Cambridge, 2006.
 - 20) Evans, M. G.; Polanyi, M. *Transactions of the Faraday Society* **1938**, *34*, 11.
 - 21) Logadottir, A.; Rod, T. H.; Nørskov, J. K.; Hammer, B.; Dahl, S.; Jacobsen, C. J. H. *Journal of Catalysis* **2001**, *197*, 229.
 - 22) Santen, R. A. v.; Neurock, M.; Shetty, S. G. *Chemical Reviews* **2009**, *110*, 2005.
 - 23) Cushing, G. W.; Navin, J. K.; Donald, S. B.; Valadez, L.; Johánek, V.; Harrison, I. *The Journal of Physical Chemistry C* **2010**, *114*, 17222.
 - 24) Janssens, T. V. W.; Clausen, B. S.; Hvolbaek, B.; Falsig, H.; Christensen, C. H.; Bligaard, T.; Nørskov, J. K. *Top. Catal.* **2007**, *44*, 15.
 - 25) Kauzmann, W.; Eyring, H. *Journal of the American Chemical Society* **1940**, *62*, 3113.
 - 26) Bell, G. *Science* **1978**, *200*, 618.
 - 27) Ribas-Arino, J.; Marx, D. *Chemical Reviews* **2012**, *112*, 5412.

Chapter 5

Electrical and Structural Properties of 1,4-Phenylene Diisocyanide Oligomers Bridging Between Gold Nanoparticles on Mica

Introduction:

The field of molecular electronics, where molecules serve as putative electronic components, has grown rapidly since the idea was first proposed in the early 1970's by Aviram and Ratner [1]. A large amount of work has been carried out to explore the conduction mechanisms through molecules using break junctions or by using scanning-probe microscope tips [2-6]. Several excellent reviews have recently emerged.

To complement measurements of single-molecule circuits between fixed electrodes, reports have been published on transport in systems containing conductive (usually metallic) nodes linked together by molecules or molecular chains. Examples include systems with nodes comprising single transition-metal atoms, gold clusters, and semiconductor nanocrystals. One substantial advantage of such systems is that the geometries can evolve or adjust: ligation can change, the nodes can move, and the film can adjust dynamically to a favorable geometry—and that geometry may continue to evolve when charge is introduced to and moves around in this dynamically disordered medium. Measurements and models of particular examples of the dynamically adjusted molecule/node conjugates reveal both dynamical structure evolution and conduction patterns that can be described by dynamical disorder around multiple thermodynamic minima.

Another feature of these dynamically-disordered media that again contrasts sharply with single-molecule conductance junctions is that the transport can vary from simple hopping on a fixed lattice to dynamically-disordered hopping. Indeed percolation models may be relevant—both static percolation (in the case of minimal motion of the nodes) and dynamical percolation (in systems in which the ligation between nodes fluctuates as the nodes themselves move).

Here, we provide an example of dynamically linked gold nanoparticles based on the self-assembly chemistry of 1,4-phenylene diisocyanide on gold surfaces. This chemistry was discussed at length in Chapters 3 and 4. It was our desire to explore the feasibility of extending the system from Au(111) to an insulating substrate such as mica. PDI has previously been proposed as a prototypical molecular electronic component since it has two isocyanide groups (in *para* configuration), something which (at least to first order) would be a technical requirement for such a component to function.

In Chapter 3, the structure of $-(\text{Au}-\text{PDI})_n-$ oligomers were discussed. STM images indicate that these assemblies routinely span microns—distances that are enormous on the atomic scale. The individual units are on the order of ~ 1.1 nm. However, it seems likely that if the distance between nanoelectrodes is greater than this, the system would be able to *adapt* by installing more monomers as needed until the gap spanned. This would be especially valuable if one were trying to synthesize hybrid nanomaterials from granular or other other ambiguous materials.

This idea is explored in this chapter by measuring the conductivity of PDI-dosed granular gold films. These films were grown on cleaved mica substrates using simple and straight forward thermal evaporation of high purity gold. The structure of evaporated films on mica (and other insulating substrates such as silica) has been investigated extensively [7-9]. It is found that below a critical nominal thickness, the gold forms isolated particles which ripen in such a way that the sheet resistance of the film increases with time until the sheet resistances reaches a stable value. Conversely, at coverages above this critical coverage the sheet resistance is observed to decrease during this ripening

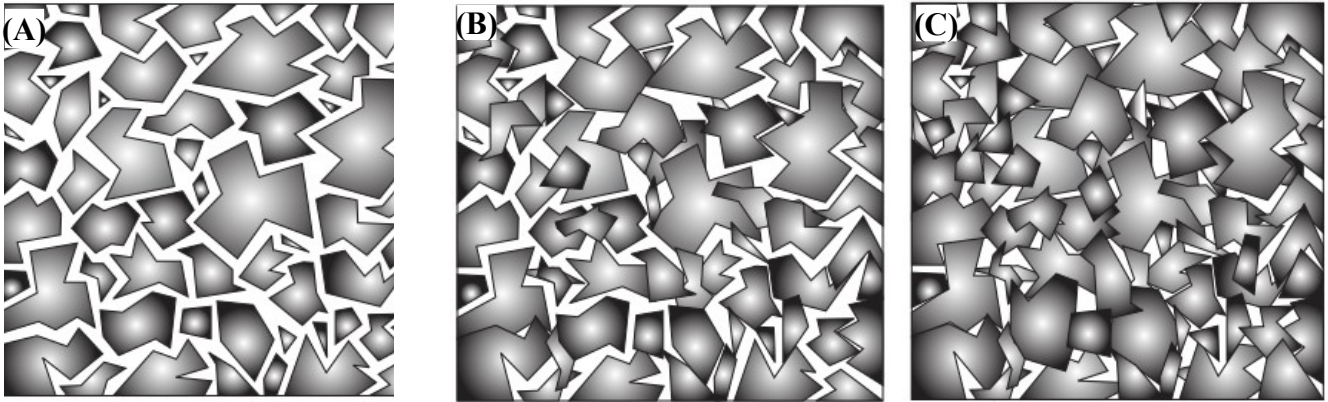


Figure 1: The regimes of granular thin films. (A) represents the *dielectric* regime where discrete particles exist isolated by a dielectric matrix. Here the Temperature Correlation of Resistance (TCR) is negative. (C) represents the *metallic* regime where particles are mostly touching but with dielectric inclusions. Here the TCR is positive. (B) is the *transition* regime and is defined by the coverage through which the TCR changes sign [7-9].

period. As shown in Fig. 1, these are the *granular* and *continuous* granular regimes, separated by the *transition* regime.

In this chapter experiments were carried out exclusively in the dielectric regime with discrete gold nanoparticles supported on mica, with vacuum separating them. The sheet resistance of a granular film decreases with increasing nominal thickness which makes intuitive sense. If the particles are not actually *touching* each other, charge is being transferred instead through processes such as tunneling or hopping, one would certainly expect the barrier to conduction (whatever that mechanism might be in the dielectric regime) to decrease as the particles become closer. In a granular film, there are two ways in which this can happen. The particles may simply grow in size, and therefore they leave a larger “foot print” on the support. As the particles grow larger, they also grow closer together. The second way the particle separation can decrease is by keeping the particle size constant, but increasing the number-density of the particles. This second effect has been observed if a low coverage film is evaporated, allowed to age, and more metal evaporated on top of it. The new particles preferentially grow in the gaps between the older (ripened) ones. The *particle density* has been shown to be a

function of the deposition rate of the metal and in thermal evaporation this is mostly a function of the current passing through the evaporation filament (the current, I , dictates the power, P dissipated by the filament by $P=I^2 R$, where R is the resistance). For that reason, care was taken to prepare samples at a set current and in one evaporation step—an effort to maintain constant particle density and modulate sheet resistance by changing particle size alone. The self-assembly chemistry of $-(\text{Au}-\text{PDI})_n-$ was then used to bridge these particles and electrical studies were performed on them.

Experimental:

AFM: Atomic force microscopy (AFM) of gold nanoparticle covered mica surfaces were collected in air using a Pacific Nanotechnology instrument operating in tapping mode. The mica samples (1 cm x 1 cm Ted Pella, Highest Grade) were affixed to glass microscope slides with double-stick tape. Silicon close contact probes were used (ultra-sharp, μMasch) and measurements taken with the following parameters: Q-factor of 620-710, drive amplitude of $\sim 130\text{mV}$, and phase shift $\sim -15^\circ$. This allowed for imaging using light intermittent contact, minimizing potential damage to the very delicate samples.

STM imaging, electrical measurements, and gold film preparation were carried as described in Chapter 2. The test samples were configured according to Figure 2.

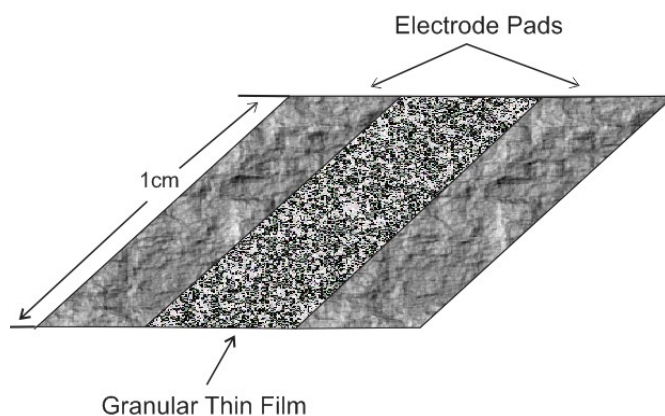


Figure 2: Configuration of granular thin film samples. First $\sim 200\text{nm}$ thick electrode pads are deposited (fully metallic), then the granular thin film is evaporated over the top.

Preparation and Electrical Measurements of PDI Dosed Films: Films were prepared for electrical studies by dosing PDI from the gas phase via a directional dosing source. Prior to being mounted on the sample holder, the granular films were carefully rinsed in 2 or 3 drops of anhydrous benzene (99%, Aldrich). They were clipped in place on the sample stage both to hold them in thermal contact and also to provide electrical contact to the vacuum feedthroughs. After the chamber was evacuated ($\sim 10^{-8}$ Torr), the PDI dosing was commenced. Plots of conductivity vs. PDI dosing time were prepared real time, and when two consecutive points were within 1-3% of each other, the sample was assumed to be saturated. (Figure 3 is a typical PDI uptake curve).

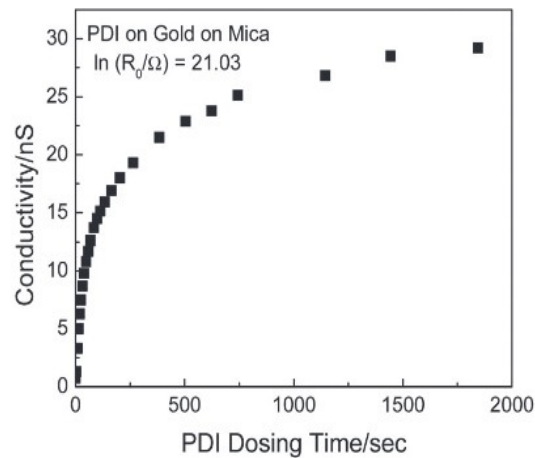


Figure 3: Typical curve showing dramatic enhancement in conductivity across a granular film as a function of PDI dosing time. One critical parameter for a film, R_0 is the sheet resistance of the clean film, prior to dosing.

Electrical measurements were carried out in the I/V chamber using the PC-controlled A/D system described in Chapter 2. Resistance vs. temperature data was collected by cooling the sample manipulator (and sample holder) to liquid nitrogen temperature. The liquid nitrogen was allowed to boil off, at which point the temperature of the sample began to rise (under ambient heating), back to room temperature, over the course of about 1 hour. As the collection of an I/V curve takes on the order of 30 seconds, each data point corresponds to a narrow temperature range (~ 2 K)

Results:

Structure and Mobility of $-(\text{Au}-\text{PDI})_n$ - Oligomers: In Chapter 3 the structure of $-(\text{Au}-\text{PDI})_n$ oligomers was discussed at length. We have so far considered the oligomeric self-assemblies in a *static* way. At this point it would be advantageous to extend the findings. Shown in Figure 4 are two consecutive images of $-(\text{Au}-\text{PDI})_n$ on Au(111) taken at room temperature. The first feature that is immediately apparent is that the chains are very frequently found clustered in pairs or in groups of three or four. There are spaces between the clusters, but not sufficient space for another chain to grow. The pairing and clustering of chains has also been observed at lower coverages which suggests that this effect is a consequence of lateral attractive interactions between chains rather than a result of crowding.

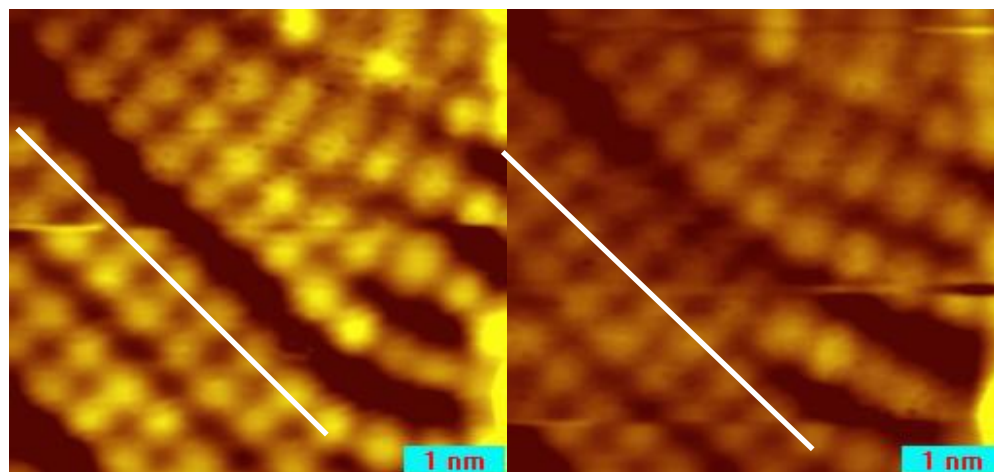


Figure 4: Sequential images of $-(\text{Au}-\text{PDI})_n$ oligomers on Au(111). The chain above the white line appears to “unzip” from one chain and hop down to interact with the one below it. Room temperature, $V = -1.5$ V, $I = 55$ pA

In previous work it has been shown that the gold adatoms that template the oligomers are located either *fcc* or *hcp* three-fold hollow sites, which are virtually isoenergetic. Within a group of adjacent chains, the inter-row spacing is 0.485 nm and this corresponds to chains in the same type of three-fold site. A smaller spacing of 0.44 nm has been observed less frequently corresponding to adjacent chains with gold adatoms occupying different types of three-fold hollow sites.

The stability of the chains is investigated in Figure 5 (and more clearly in the movie supplement of reference [6]). A series of 15 consecutive images taken 53 seconds apart show the repeated lateral

motion of the entire chain. The motion of the chains could be either thermal or tip-induced. It is reasonable to assume that such motion is likely occurring in the absence of the scanning tip however as the chains have spontaneously organized themselves into compact structures prior to scanning. It is proposed that the chains migrate between different types of three-fold sites as illustrated in Figure 6. Here *hcp* and *fcc* sites have been arbitrarily labeled with different colors. Chains *A* and *B* run along *hcp*-sites while chains *D* and *E* run along *fcc*-sites. Considering that the chains with gold adatoms located at both kinds of sites have nearly equivalent energies, chain *C* (nestled between the other two sets) can be located in two equivalent configurations and it is possible that it can hop between these two states. The *hopping* event would presumably correspond to the gold adatoms traversing the *bridge*-site that resides between the *fcc* and *hcp* site. Careful examination of the frames in Figure 5 show that over the course of imaging, 9 hopping events were observed. This corresponds to a maximum hopping rate of 1 hop every 82 seconds. A maximum activation energy for this process was

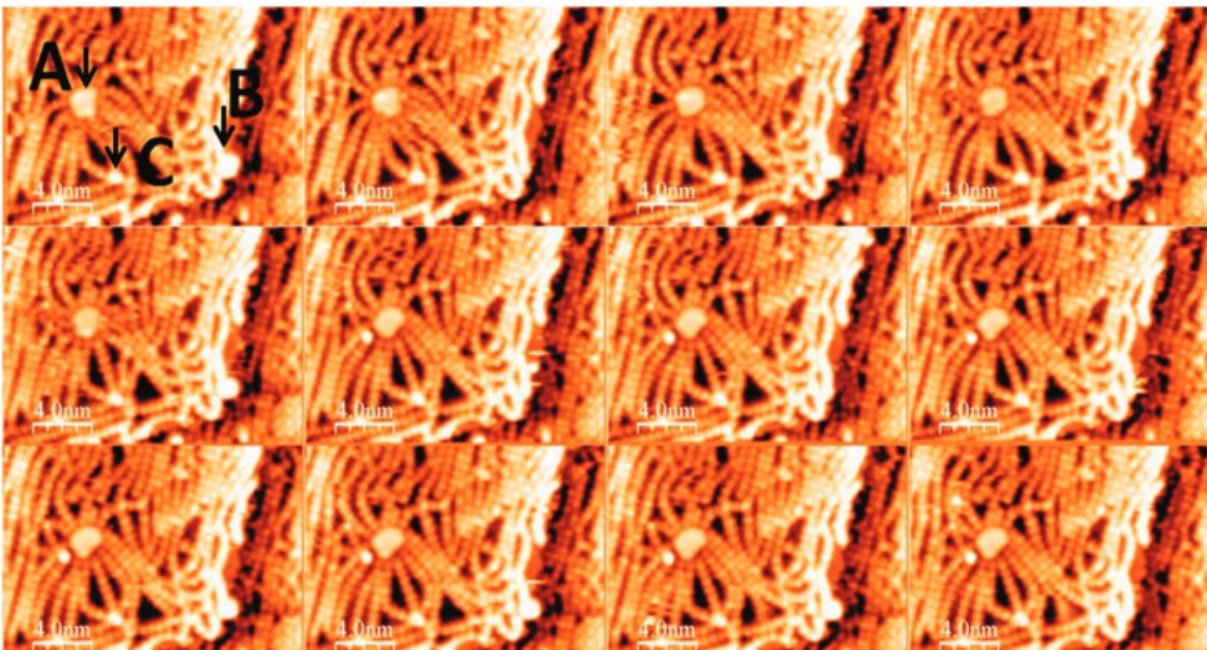


Figure 5: Sequence of images showing $-(\text{Au-PDI})_n-$ oligomers linking nanoparticles on an Au(111) surface. The location of the nanoparticles are given by A, B, and C. Also see movie in supplement to reference [10]. $V = -2.00$ V, $I = 198$ pA.

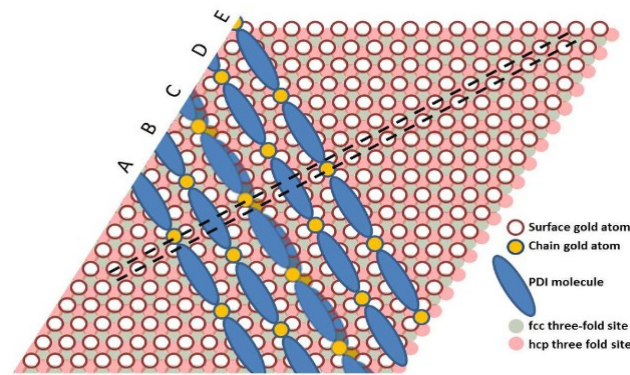


Figure 6: Depiction of $-(\text{Au—PDI})_n$ oligomers on an Au(111) surface. Chains A and B run along hexagonal close packed (*hcp*) sites while chains D and E run along face-centered cubic (*fcc*) sites. Chain C can reside in two possible sites of nearly equal energy and it is possible for the chain to “hop” between them.

estimated to be ~ 0.8 eV, derived if we assume Arrhenius behavior and a frequency factor of $A \sim 10^{13} \text{ s}^{-1}$.

It is in fact likely that the hopping rate is higher than observed (image collection is on the order of 1 image per minute). If this is so, it would lead to a lower activation energy.

Bridging Gold Nanoparticles with $-(\text{Au—PDI})_n$ Oligomers: In Chapter 3 it was stated that the $-(\text{Au—PDI})_n$ oligomers are observed to propagate from defects such as step edges. This became the starting point for the DFT calculations described in Chapter 4 where the propagation of the chains was modeled as growing from a fixed PDI molecule found at an atomic step.

Figure 5 allows us to make the reasonable statement that if two (or three in the figure) nanoparticles are involved, the chains propagate *from* and are terminated *by* defects on a surface. The surface described so far has been Au(111). Of practical consideration, particularly if one were to attempt to integrate this chemistry into existing CMOS technologies, is whether this bridging of gold nanoparticles could occur on an *insulating* substrate. For these studies freshly cleaved mica (prepared as in the experimental section) was selected. It offers one of the highest dielectric breakdown voltages available, an extremely low thermal expansion and contraction coefficients, and atomically flat surfaces can be produced simply through careful delamination of the mica along the basal planes.

Conductivity and Morphology of Bridged Gold Nanoparticles on Mica. Gold nanoparticles were prepared on mica, and PDI dosed onto the films as described above. Figure 3 shows a typical conductivity vs. PDI dosing time curve. Similar behavior was obtained for all films. The films studied here had initial sheet resistances (R_0) spanning the range from $\sim 30 \text{ M}\Omega$ to $990 \text{ M}\Omega$, and in all cases these values dropped dramatically on PDI dosing (orders of magnitude in some cases). It is tempting to attribute this outright to the formation of $-(\text{Au}-\text{PDI})_n-$ oligomers between the gold nanoparticles. Another possibility is that it is the morphology of the nanoparticles themselves which is altered through the coordination of isocyanide functional groups. If the isocyanides modified the surface energy of the particles, it is possible that the contact angle of the particles could increase to the point where they begin to touch each other, and that the conductivity enhancement is a simple consequence of a shift in morphology from the *dielectric* to the *transition* regimes.

In order to investigate the surface morphology more closely, tapping mode AFM was employed. Figure 7 displays the results of performed on two of the films (A= $312 \text{ M}\Omega$ and B= $48 \text{ M}\Omega$), although similar results were obtained for the other films.

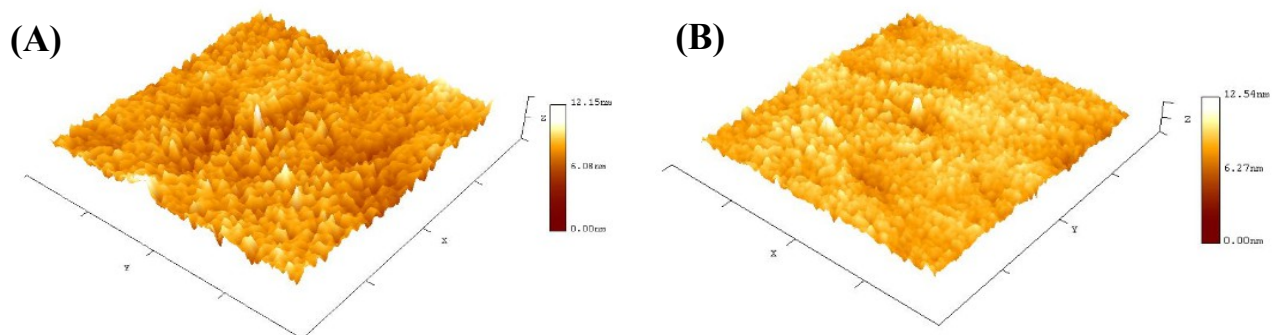


Figure 7: $1 \mu\text{m} \times 1 \mu\text{m}$ tapping mode AFM images of granular gold films on mica. In film (A), $R_0 = 312 \text{ M}\Omega$ and particle density is $3.3 \pm 0.1 \times 10^{15} / \text{m}^2$. For film (B), $R_0 = 48 \text{ M}\Omega$ and particle density is $3.2 \pm 0.1 \times 10^{15} / \text{m}^2$.

An important conclusion can be drawn from this data. As was discussed earlier, the initial film resistance (in the dielectric regime) is modulated by the distance between particles. This distance is a

function of the particle size and separation. Figure 7 (and other films, data not shown) have a particle density of $\sim 3 \times 10^{15} / \text{m}^2$ so the resistance seems to be modulated (in this case) by the size of the particles.

While STM is typically unavailable for imaging insulating substrates such as mica, Figure 8 shows the result of a successful attempt. To facilitate the experiment, a film substantially thicker than the highest coverage interrogated in the electrical measurements was prepared. The lower sheet resistance was required for the feedback and tip approach of the STM to function properly. Figure 8A) is an image of a high-coverage film prior to dosing PDI, while Figure 8B) is an image of the same film after dosing PDI (2 mM in benzene solution). The images illustrate with higher resolution than the AFM images presented in Figure 7 that PDI dosed from benzene solution does not appreciably alter the particle morphology. The particle size histograms included for the pre- and post-PDI dosed film indicate, in both cases, that the films show a high degree of monodispersity. In fact for the undosed film, the average particle size is 8.3 ± 2.2 nm while after dosing the average particle size was 7.2 ± 2.2 nm. While the images were collected on the *same* film, the film was removed from the microscope for dosing. Thus the images were not collected in the same *area* of the film. The ~ 1.1 nm difference in average particle size likely is a reflection of local particle morphology on the mica substrate.

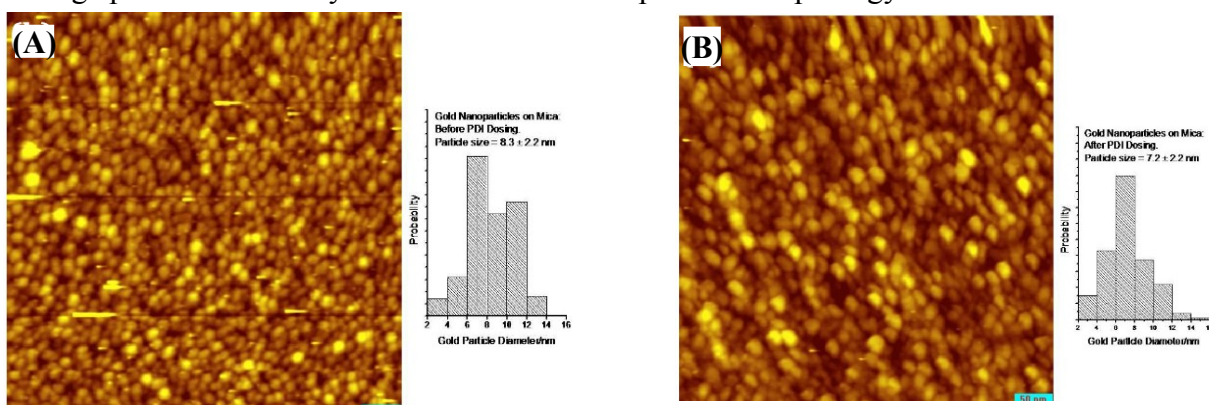


Figure 8: STM images of a granular, thermally evaporated gold film before dosing 1,4-PDI (A), and after (2 mM in benzene) (B). Images were acquired in air at room temperature. $V = -1.0$ V, $I = 8.85$ pA. The film did not undergo a statistically relevant change in morphology.

I/V curves were measured as a function of temperature for all of the samples. Ohmic behavior was found for all films to a bias of ± 4 V, enabling precise sheet resistances to be measured for each film. Arrhenius plots of $\ln(R)$ vs. T^{-1} were constructed and showed pronounced nonlinearity. Plots of $\ln(R)$ vs. $T^{-1/2}$, however, were remarkably linear (illustrated for a few select data sets in figure 9). Arrhenius behavior is predicted by the theory of activated tunneling in granular materials as formulated by Nuegbauer and Webb [11]. However, the excellent linear fits from the $\ln(R)$ vs. $T^{-1/2}$ plots suggest that, at least for our system, the model proposed by Abeles and Sheng is more appropriate.

The slopes of the plots of $\ln(R)$ vs. $T^{-1/2}$ were obtained for films spanning a wide range of initial (undoped) resistances, R_0 . The slopes of these plots, designated α was found to vary linearly with $\ln(R_0)$ (Figure 10). The slope of this plot was found to be 3.7 ± 0.2 with an intercept of -52 ± 3 . The significance of this finding will be discussed next, framed in terms of *Abeles Theory*.

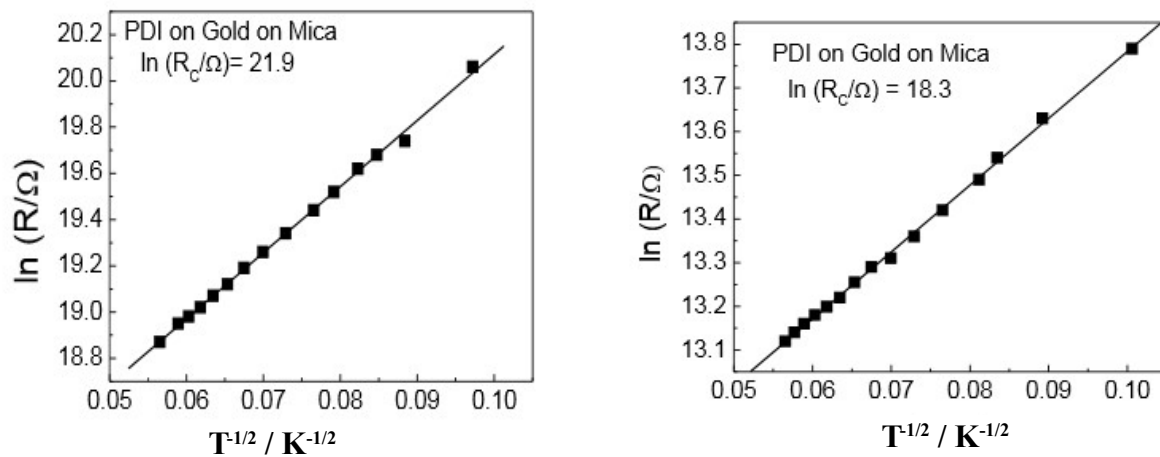


Figure 9: Plots of $\ln(R)$ vs. $T^{-1/2}$ for two films of differing initial sheet resistances, R_c . The slope of such a plot yields a parameter designated α which can yield information about the nature of the tunneling barrier between adjacent nanoparticles.

Finally, Figure 11 shows the results of several control experiments. While the linear plots of α vs. R_c give weight to the argument that $-(\text{Au}-\text{PDI})_n$ oligomers are bridging gold nanoparticles, the dramatic

reduction in sheet resistance of the films upon 1,4-PDI dosing could potentially be the result

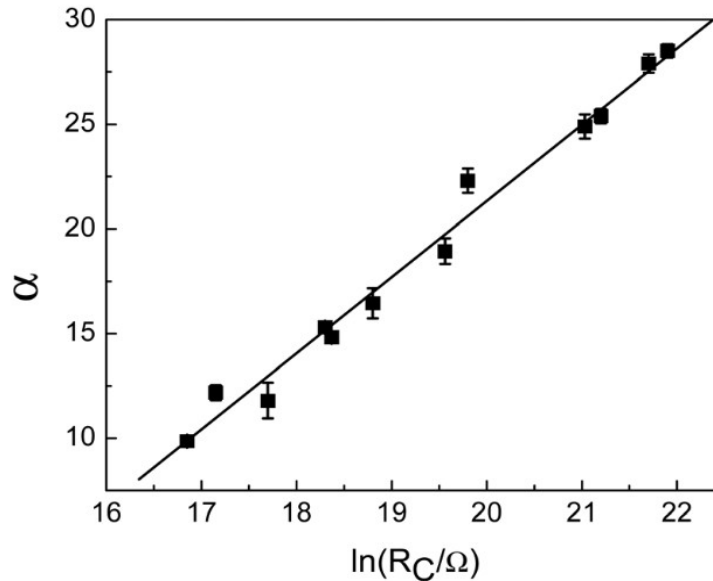


Figure 10: Plot of α values vs. $\ln(R_C/\Omega)$ for the 12 films studied in this chapter. The linear dependence of such a plot is in agreement with the theory of activated tunneling in granular materials put forth by Abeles and Sheng.

of other effect. One such effect is that saturating a gold nanoparticle with R-NC: functional groups is modifying the work function of the gold, and thus reducing the barrier. If this were the case, one would expect that dosing the films with phenylisocyanide would produce a similar reduction in sheet resistance, even though this molecule (being mono-functional) is incapable of bridging. Fig. 11 A), B), and C) show conductivity vs. phenylisocyanide dosing time. Conductivity is enhanced slightly (a few percent, regardless of gold coverage), but the enhancement is orders of magnitude less than was observed for bifunctional 1,4-PDI. Figure 11 D) shows a 1,4-PDI uptake curve for a mica substrate for which no gold nanoparticles have been evaporated. This experiment was meant to demonstrate that the mechanism of conductivity enhancement between gold nanoparticles is *via* gold-adatom mediated oligomeric species. The results of these experiments indicate that for the self assembly chemistry to work, a sink from which gold adatoms can be sequestered is required (i.e. gold nanoparticles), and also, bifunctional molecular wire materials are required (such as 1,4-PDI). These findings are entirely

consistent with the structure and proposed mechanism of oligomer growth presented earlier.

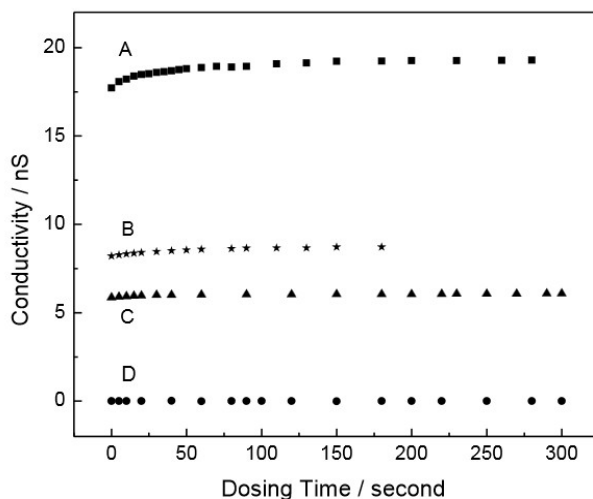


Figure 11: A series of control experiments. Curves A, B, and C correspond to the uptake of phenylisocyanide on film with initial conductivities of 17.12nS, 8.20nS, and 5.86nS respectively. The dosing pressure of phenylisocyanide (an oil with considerable vapor pressure) is estimated to be $\sim 600X$ as that for 1,4-PDI. Curve D is the dosing curve for a clean mica film exposed to 1,4-PDI. To achieve the dramatic enhancement in conductivity as shown in Figure 3 a *bifunctional* linker molecule is needed, as are gold nanoparticles (as a sink of gold adatoms required for oligomerization).

Discussion:

Figures 4 and 5 reveal that $-(\text{Au}-\text{PDI})_n-$ oligomers are quite mobile on Au(111) surfaces. Figure 5 also demonstrates the propensity for the oligomers to spontaneously bridge between nanoparticles separated by a considerable distance. The work presented in this chapter is an effort to extend this chemistry to *insulating* substrates as the long-term goal of this research is to develop methods towards integrating the PDI/Au self-assembly chemistry with standard fabrication techniques which are currently typically based on silicon (or other) oxides. Direct observation of the oligomers on insulating surfaces is hindered by the *insulating* nature of the substrate. The STM images acquired in Figure 8 could only be acquired as the film was prepared at the extreme high-coverage end of the dielectric regime which left the film of sufficiently low-resistance to pass a feedback current and allow for imaging. While the STM tip is very sharp, it is not sharp enough to resolve the substrate in the area

between the particles.

It was proposed and discussed in Chapters 3 and 4 that oligomeric $-(\text{Au-PDI})_n-$ propagates from defects such as step edges or other features with low-coordination gold atoms. Low-coordination atoms would be abundantly present on a nanoparticle covered surface. The electrical studies were performed to examine more closely the nature of the barrier between the particles, and to exclude the possibility that the dramatic enhancement in conductivity was a result of a morphological change in the nanoparticles themselves.

Characteristic of electrical conduction in the granular regime, all of the films studied showed a *decrease* of resistance with *increasing* temperature. This negative *temperature correlation of resistance* (TCR) implies that the mechanism of electrical resistance is fundamentally different than it would be for a thicker, metallic film (where the mechanism is largely electron back-scattering across grain boundaries) [7,8,11].

The linear $\ln(R)$ vs. $T^{-1/2}$ is predicted by Abeles theory for thermally assisted tunneling through granular materials. Unlike the model of Nuegbauer and Webb, the Abeles model provides an explicit dependence of the conductivity on the size as well as the separation of the nanoparticles, something which has been experimentally verified elsewhere (a more thorough derivation can be found in the supplement to ref. [10]). While the I-V curves were acquired by ramping a voltage through ± 4 V, recall that the particle density of the films is on the order of $10^{15} / \text{m}^2$. If the film is treated as a *percolation network* of interconnected resistors, the voltage drop across any two of the nanoparticles would be exceedingly small. The use of the *low-field limit* is therefore warranted. In the Abeles model, the resistance of a two-dimensional film is given by Equation 1:

$$R = R_0 e^{(2\sqrt{\frac{C}{kT}})} \quad 1)$$

Where $C = \chi s E_c^0$, s is the average spacing between particles, $\chi = \left(\frac{2m\phi}{\hbar^2}\right)^{1/2}$, ϕ is the height of the

tunneling barrier, E_c^0 is the Coulomb charging energy, and R_0 is the pre-dosed sheet resistance of the film. The Coulomb charging energy can be understood by considering a pair of neutral, adjacent nanoparticles. These particles have some small capacitance associated with them (which is a function of the size of the particles and the distance between them). The charging energy is the energy cost associated with generating a positively and negatively charged pair of nanoparticles from a pair of neutral nanoparticles. In neutral metals, the charging energy has the form $E_c = (e^2/d)F(s,d)$ and can be thought of as the energy associated with charging a (nano)capacitor. When $\Delta V \ll \frac{kT}{e}$ (the voltage drop between adjacent particles), the density of charge carriers $\propto e^{\left[-\frac{E_c^0}{2kT}\right]}$, thus it is the Coulomb charging energy that gives rise to the *thermally assisted* nature of tunneling in granular materials.

The variable C can be written as $f(s,d) = \frac{\left(\frac{s}{d}\right)^2}{\left(\frac{1}{2} + \left(\frac{s}{d}\right)\right)}$ [7,8]. The value of $f(s,d)$ is unaffected by PDI

dosing (Figure 8—the morphology does not change), but it does vary with initial gold thickness producing different resistances for each of the films. Thus R_c of the film—the clean resistance, provides a convenient parameter to describe its properties and from Equation 2 is:

$$\ln(R_c) = \ln(R_c^0) + 2\sqrt{\frac{C_c}{300k}} \quad 2)$$

Where $T = 300$ K, the temperature at which the initial resistance was measured. Taking $\epsilon = 1$ for a vacuum yields:

$$\ln(R_c) = \ln(R_c^0) + \left(\sqrt{\frac{e^2 f(s,d)}{k}}\right) \times \sqrt{\frac{4}{75}} \times \sqrt{\chi_c} \quad 3)$$

In the case of PDI-saturated films, the slope of the plots of $\ln(R)$ vs. $T^{-1/2}$ (α , Figure 9) are shown to vary

linearly with $\ln(R_c)$ (Figure 10). From Equation 1, $\alpha = 2\sqrt{\frac{C_F}{k}}$ and $C_F = \frac{4\chi_F e^2 f(s,d)}{\epsilon_F}$ thus α is given

by:

$$\alpha = \sqrt{\frac{16\chi_F e^2 f(s, d)}{\epsilon_F}} \quad 4)$$

Since $f(s, d)$ is identical for a particular clean and PDI covered film (the morphology does not change upon PDI dosing), rearranging Equation 4 and substituting from Equation 3 gives a relationship between α (the slope of the *Abeles plot* of $\ln(R)$ vs. $T^{1/2}$) and the resistance of the clean film R_C as given in Equation 5:

$$\alpha = 17.32 \sqrt{\frac{\chi_F}{\epsilon_F \chi_C}} \times \ln(R_C) - 17.32 \sqrt{\frac{\chi_F}{\epsilon_F \chi_C}} \times \ln(R_C^0) \quad 5)$$

Such a linearity confirms that the function $f(s, d)$ is unaffected by PDI dosing. Thus the slope of the graph in Figure 10 (α vs. $\ln(R_C)$) is 3.7 ± 0.2 and yields $\frac{\chi_F}{\epsilon_F \chi_C} = 0.045 \pm 0.005$. A value of 3.5 has

been suggested for the dielectric constant of PDI and since $\chi = \left(\frac{2m\phi}{\hbar^2}\right)^{(1/2)}$ where ϕ is the height of the tunneling barrier, then $(\phi_F/\phi_C) = 0.025 \pm 0.005$, where ϕ_F and ϕ_C are the barrier heights for the PDI dosed and clean films respectively.

There have been several measurements of transport through Au—PDI—Au contacts [6 and references therein]. In particular, the tunneling barrier height was measured for a number of phenyl-based isocyanides and diisocyanides by STM and related to the difference between the Fermi energy of the metal and the energy of the highest occupied molecular orbital (HOMO) of the linker [4]. For 1,4-PDI this value ($E_F - E_H$) was measured to be 0.38 ± 0.1 eV. In this case, therefore, $\phi_F = E_F - E_{H(Au-PDI)}$ where $E_{H(Au-PDI)}$ is the HOMO energy of the $-(Au-PDI)_n$ - oligomer. In the case of the clean surface, the corresponding energy is the difference between the Fermi energy of the metal and a free electron which by definition is the work function of the metal (here, the gold nanoparticle). The work function for clean gold varies between 5.1–5.5 eV which would lead to values of $E_F - E_H \sim 0.10$ to 0.11 eV, a value somewhat larger than the STM value. More recent measurements for a single PDI molecule

bridging nano-electrodes gave a value of 0.19 ± 0.02 eV where the difference was ascribed to differences in the number of PDI molecules in the contact [12]. Finally, break junction studies measured a thermionic barrier height of 0.22 eV. These values are all somewhat higher than the value of ~ 0.1 eV reported here for $-(\text{Au}-\text{PDI})_n$ oligomers. Direct spectroscopic measurements of the oligomers on Au(111) show the HOMO lies ~ 0.88 eV below the Fermi level of gold, with the LUMO ~ 3.32 eV above it, in full accord with the general picture of that the tunneling barrier is dictated by the location of the HOMO with respect to the Fermi level and is summarized in Figure 12.

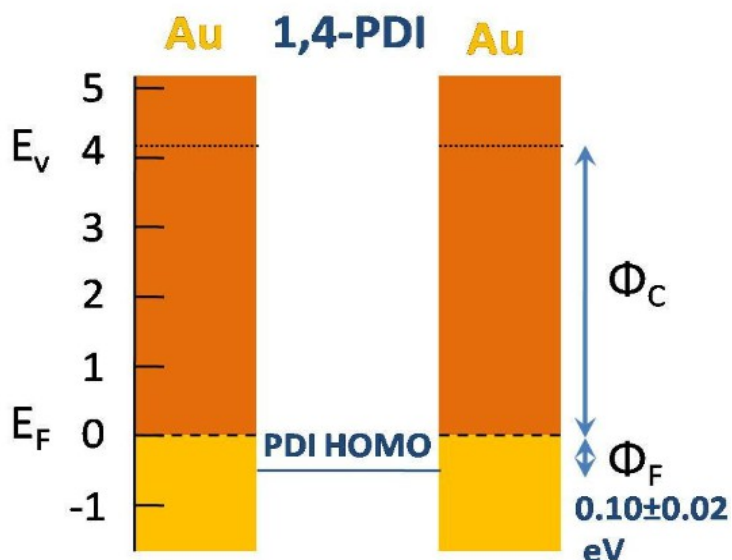


Figure 12: Energy level diagram for gold nanoparticles linked by 1,4-PDI oligomers where ϕ_C corresponds to the work function of the 1,4-PDI covered nanoparticles (4.08 eV) and ϕ_F is the tunneling barrier through the linker molecule measured to be 0.10 ± 0.02 eV.

Conclusions:

In Chapter 2 the structure of $-(\text{Au}-\text{PDI})_n$ oligomers on Au(111) was presented. This chapter was an effort to investigate whether this self-assembly chemistry could be extended to insulating substrates—something that would be required for integrating the oligomeric structures with existing semiconductor fabrication technologies such as CMOS. The electrical properties of PDI have been studied *via* STM and break-junction techniques elsewhere. Those experiments, while elegant, are

exceedingly difficult to implement. We present here an alternative method for measuring the barrier height between an array of nano-electrodes. In the studies presented here, granular gold films were prepared using the straight forward technique of thermal evaporation. The nominal thickness of these films was kept low enough that they were in the *dielectric regime*. As such, the granular films act as a *percolation network* of closely spaced but isolated particles, through which charge can transfer.

In the case of all films studied here, plots of $\ln(R)$ vs. $T^{-1/2}$, where R is the resistance of the dosed film, showed remarkable linearity. The slope of such plots is a parameter designated α and the linearity is in good accord with the theory of Abeles and Sheng for activated tunneling in granular materials. For the film presented here, a plot of α vs. $\ln(R_0)$, where R_0 is the resistance of the clean (pre-PDI dosing) film was also linear. AFM measurements indicate that the particle *density* does not vary with R_0 so the effect is a result of the particle size.

A thermionic barrier height of 0.22 eV has been suggested [4], obtained through break junction experiments. This value is somewhat higher than, but within the same range of the value of ~ 0.1 eV presented here. The somewhat lower value obtained in the work presented here might be expected for the extended conjugation of the oligomers bridging the nano-particles versus the single 1,4-PDI molecules studied in the break junction experiments.

Finally, the effect of a non-bridging isocyanide (phenylisocyanide) was studied. It might be expected that simply coordinating isocyanide functional groups to gold nanoparticles could change their work function and hence the barrier height. Curves A, B, and C in Figure 12 show only a very slight enhancement of conductivity with phenylisocyanide dosing which could be a result of a lowering in the gold work function or perhaps some small enhancement due to π - π interactions between the phenyl rings. The conductivity enhancement is orders of magnitude less than was found for gold films of similar coverage exposed to the *bi*-functional 1,4-PDI. Figure 12 D) shows the effect of exposing a

clean mica film to 1,4-PDI. The conductivity across the mica was (as would be expected) immeasurably low and did not increase with dosing. This precludes the mechanism of conductivity enhancement for the granular thin films as being the result of some purely organic film. A bifunctional linker molecule and gold nanoparticles are a both requisites for the self assembly of oligomeric molecular wires.

References:

- 1) Avarim, A.; Ratner, M.; *Chem. Phys. Lett.* **1974**, *29*, 277-83.
- 2) Martin, S.; Grace, M.; Bryce, M.; Wang, C.; Jitcharti, R.; Batsonov, S.; Higgins, C.; Lambert, C.; Nichols, R.; *JACS*, **2010**, *132*, 9157-64.
- 3) Reed, M.; Zhou, C.; Muller, T.; Burgin, T.; Tour, J.M.; *Science*, **1997**, *132*, 252-4.
- 4) Chen, J.; Wang, W.; Klemic, M.; Reed, M.; Axelrod, B.; Kaschak, A.; Rawlett, D.; Price, D.; Dirk, S.; Tour, J.; Grubisha, D.; Bennett, D.W.; *Ann. N. Y. Acad. Sci.* **2002**, *960*, 69-99.
- 5) Song, H.; Kim, Y.; Jang, Y.; Jeong, H.; Reed, M.; Lee, T.; *Nature*, **2009**, *462*, 1039-43.
- 6) Kim, B.; Beebe, Y.; Jun, Y.; Zhu, X.; Frisbie, C.; *JACS*, **2006**, *128*, 4970-1.
- 7) Abeles, B.; Sheng, P.; Coutts, M.; Arie, Y.; *Adv. Phys.* **1975**, *24*, 407-61.
- 8) Sheng, P.; Abeles, B.; Arie, Y.; *Phys. Rev. Lett.* **1973**, *31*, 44-7.
- 9) Kolek, A.; *J. Phys. Cond. Mat.* **6** **1994**, 469-80.
- 10) Kestell, J.; Abuflaha, R.; Boscoboinik, J.; Bai, Y.; Bennett, D.; Tysoe, W.T.; *Chem. Comm.* **2012**, *49*, 1422-4.
- 11) Neugebauer, C.; Webb, M.; **1962**, *J. App. Phys.* **33**, (74).
- 12) Lortscher, E.; Cho, C.; Mayor, M.; Tschudy, M.; Rettner, C.; Riel, H.; *ChemPhysChem* **2011**, *12*, 1677.

Chapter 6

Gas Adsorption on $-(\text{Au}-\text{PDI})_n$ - Oligomers on Au(111)

and Gold Nanoparticle Films on Mica

Financial expert and super-investor Warren Buffet is claimed to have said “Gold gets dug out of the ground in Africa, or some place. Then we melt it down, dig another hole, bury it again and pay people to stand around guarding it. It has no utility. Anyone watching from Mars would be scratching their head” [1]. Gold's “lack of utility” –its chemical inertness in its bulk form—is precisely the quality that makes it useful as a currency or decorative material. However, it is not a quality one seeks when looking for a catalyst. As we will see, the statement is a rather pedestrian view of the subject. Gold does have rich organometallic chemistry and complexes have been isolated with oxidation states ranging from -I to +V, most commonly in the form of linear ligand-Au(I)-ligand or square planar Au(III) [2].

Until quite recently, gold has been ignored as a catalyst being regarded too inert to perform interesting chemistry. This belief was dispelled in the mid-1980's when the work of Haruta [3] and Hutchings [4] demonstrated that gold functions efficiently as a catalyst for CO oxidation and ethylene hydrochlorination. Surprisingly, gold has also been demonstrated to be ~1000 times more active than platinum in the electrochemical oxidation of CO under basic (but not acidic) conditions [5, 6].

There has been a great deal of progress in the field of gold-based catalysts, particularly with regards to supported nanoparticle systems, where the support is often a metal oxide. While the role of the support in the CO oxidation chemistry continues to be a matter of debate, as is the exact method of producing the nanoparticles, consensus can be found when it comes to the *size* of the particles [7,8].

Particles in the 2-4 nm range seem to show optimal activity, while particles much larger than 15-20 nm behave as bulk gold and are (catalytically) of little interest. If we neglect for a moment any support effects (Au(I) dissolved in the support, for example), the literature has amply suggested that reactivity of gold atoms in nanoparticles scales inversely with coordination number. [9, 10]. If, as is often seen, the nanoparticle is *cuboctahedral*, one would expect that the atoms composing the faces would have the highest coordination number and would be least reactive. Atoms at the edges (the intersection between the square and triangular faces) would have an intermediate number, and the vertices would have the lowest coordination number and would therefore be the most reactive.

Low Miller index gold surfaces (such as Au(111)) are known to be very unreactive towards CO adsorption. In fact, carbon monoxide only adsorbs on low-Miller-index surfaces below 80 K, or under high CO pressures at higher temperatures. Thus, significant CO adsorption is found on Au(111) at 300 K only if the CO pressure exceeds ~10 Torr [11]. Two thermal desorption peaks (of carbon monoxide) have been observed for single crystal gold and attributed to CO adsorbing on defect sites containing gold atoms with coordination numbers of 7 and 6 [12]. Gottfried observed a third, higher temperature peak on ion-sputtered Au(110), but the exact nature of defects giving rise to the peak are not well known (due to the poorly characterized nature of a bombarded surface) [13]. The important point is that for low Miller index gold, CO (and presumably other adsorbates) coordinate gold surfaces more strongly at low-coordination sites such as defects, steps, dislocations, or areas roughened in some way (chemically, or through ion bombarding). What these sites all have in common is a coordination number <7.

In Chapters 3 and 4, the chemistry of 1,4-phenylene diisocyanide on Au(111) was investigated. High resolution STM images indicated that at room temperature, oligomeric $-(\text{Au}-\text{PDI})_n-$ chains form on the surface. The system was modeled as 1,4-PDI coordinating gold adatoms that are resting in either

fcc or *hcp* sites (the two schemes are virtually isoenergetic). In this case, the coordination number of the gold is 5—three from the 3-fold hollow site, and one from each of the PDI molecules. This suggests that 1,4-PDI could be used to “emboss” or template a large number of low-coordination gold atoms at a surface, and that perhaps the catalytic activity of the metal could be tuned. In the $-(\text{Au}-\text{PDI})_n-$ system, the gold adatoms are covalently bonded into a stable matrix—a situation which would be advantageous over the roughened surfaces discussed above, these surfaces being only meta-stable.

Adsorption of CO on $-(\text{Au}-\text{PDI})_n-$:

Figure 1 shows the results of a CO uptake on 1,4-PDI saturated Au(111) experiment. The background was acquired at a temperature of ~ 95 K. The crystal was then warmed to 300 K and exposed to a 30s 1,4-PDI dose (source 0°C), and the crystal was cooled back to 95 K.

The reported frequencies for the anchored, flat-lying, and free CN modes are reported to be 2172, 2153 and 2121 cm^{-1} [14, 15]. Figure 2 shows a 3-mode fit to the -NC stretch of a similarly prepared CO exposed $-(\text{Au}-\text{PDI})_n-$ surface. The fits were to a Gaussian-Lorentzian as implemented in the Origin 7.0 software package [15].

The stretching frequency of carbon monoxide on a metal is sensitive to the environment. In the CO dosing experiments described so far, in fact two CO modes were observed. This implies that CO is found in at least two states on the surface. To confirm this finding, and rule out the second “peak” being merely a background subtraction problem, a similar CO dosing experiment was performed with ^{13}CO . The sensitivity of the peaks with coordination environment is a consequence of ability of the metal to which the CO is coordinated to donate “extra” electron density back into the $2\pi^*$ orbital and weaken the formally triple bond (thereby lowering its vibrational frequency). The difference in vibrational frequency, as calculated by DFT (gas phase, data not shown) is $\sim 47\text{ cm}^{-1}$ but without

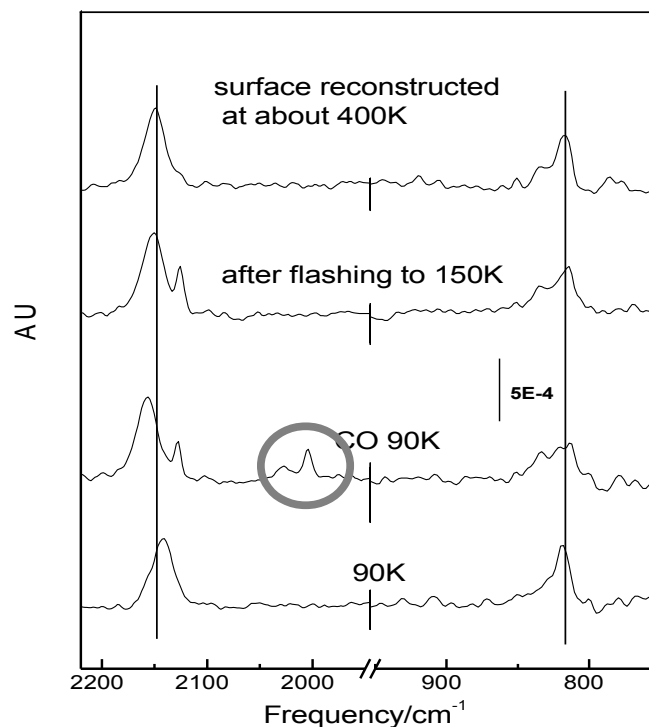


Figure 1: Results of a CO dosing experiment on $-(\text{Au-PDI})_n$ oligomers at low temperature. The CO peaks are circled in gray (dosed at 2×10^{-7} Torr, 5 minutes): CO is stable to $\sim 150\text{K}$, then desorbed. However, further heating is required to regenerate the original CN peak.

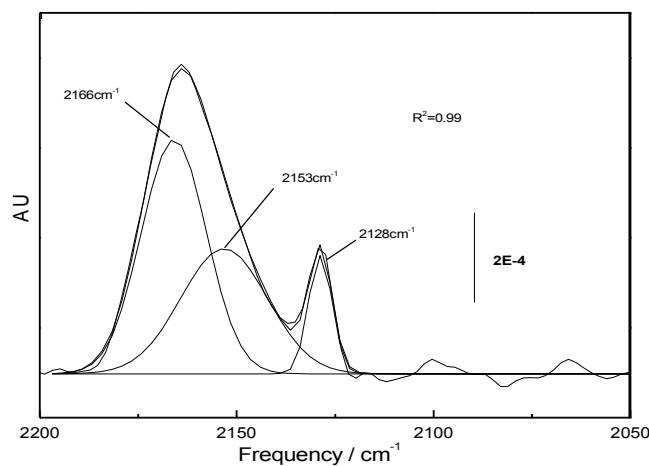


Figure 2: -CN mode of $-(\text{Au-PDI})_n$ saturated surface exposed to 2×10^{-7} Torr of CO for 5 minutes. Spectra acquired at $\sim 95\text{K}$. The peaks at 2166, 2153, and 2128 cm^{-1} (found in this 3-mode fit) are in good accord with the anchored, flat-lying and free modes reported at 2172, 2153, and 2121 cm^{-1} [14,15].

knowledge of the degree of pi-backbonding it is difficult to predict the exact frequency of the

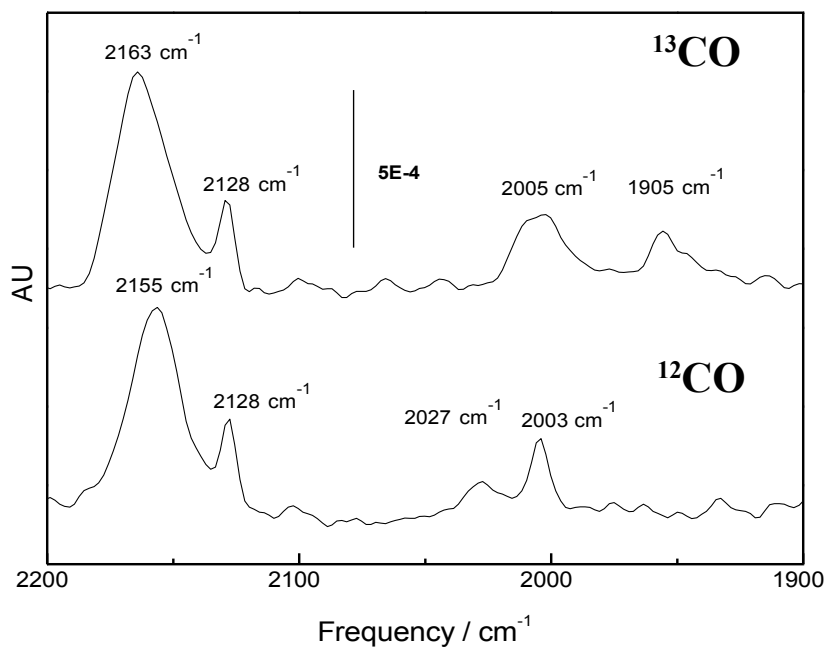


Figure 3: Results of a CO on $-(\text{Au-PDI})_n$ - isotope study. Both the ^{13}CO (upper) and ^{12}CO spectra show two peaks.

The literature suggests that even for clean (un-PDI functionalized) Au(111), CO adsorption can occur with associated step edge roughening and terrace restructuring. [18]

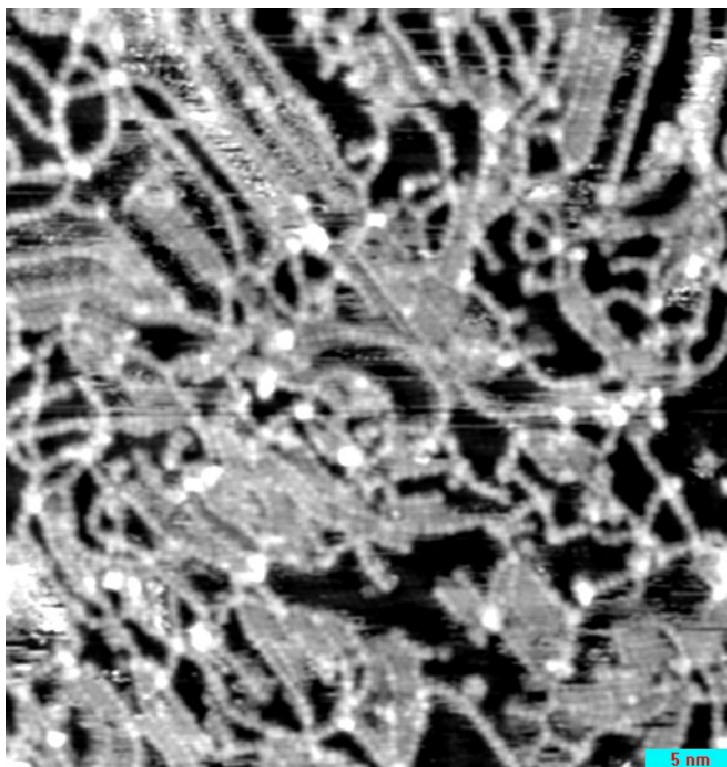


Figure 4: STM image of 1,4-PDI saturated surface, exposed to 2×10^{-7} Torr, 5 minute CO dose. Note the formerly long, straight chains have been distorted, and there is evidence for gas adsorption between them.

Figure 4 shows an STM image of an Au(111) surface exposed to a saturation dose of 1,4-PDI and exposed (at $\sim 110\text{K}$) to a 2×10^{-7} Torr (5 minute) CO dose. An interesting observation is that the long, straight chains typically present in 1,4-PDI covered Au(111) have given way to curved chains which possess little order. The surface has a large number of closed “cell” like structures, and there is evidence for CO residing on the surface (the crystal surface). It is not unlikely that this finding represents CO's ability to chemically roughen the surface at high gas pressures [18]. Figure 5 is an image of a smaller area, collected at $\sim 110\text{ K}$ and appears to provide direct microscopic evidence for gas adsorption. Recall from Chapter 3 that the $-(\text{Au}-\text{PDI})_n$ chains image as bright spots of the same height ($\sim 50\text{ pm}$), with a periodicity of 1.13 nm .

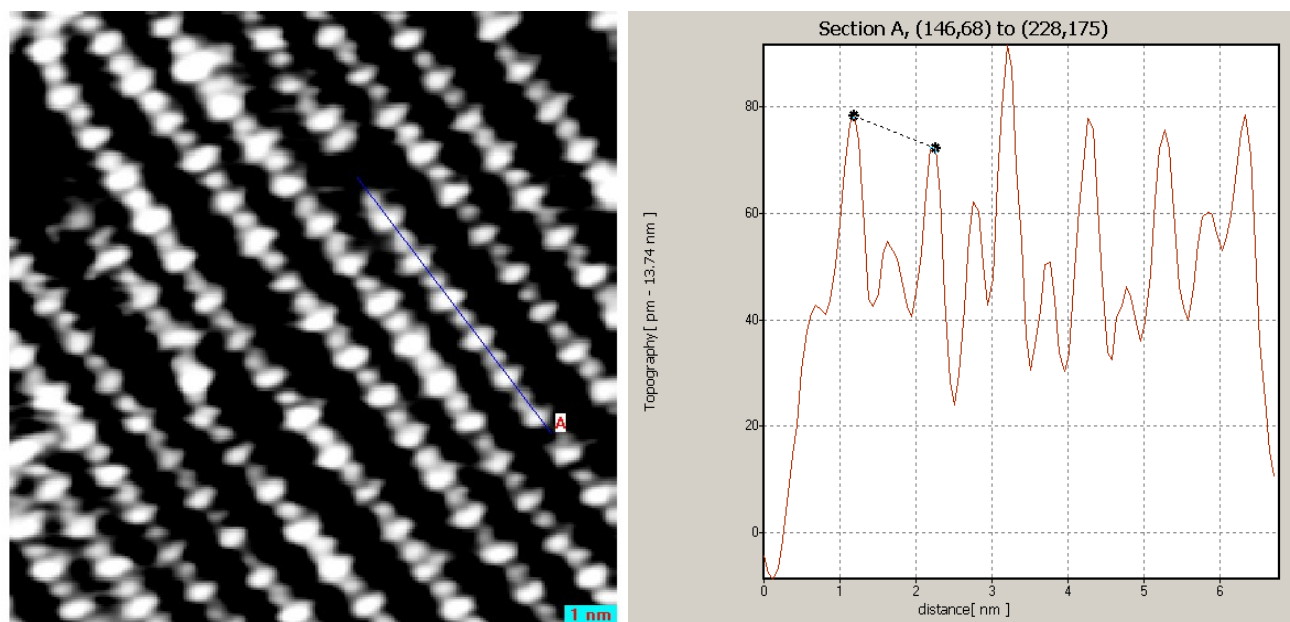


Figure 5: STM image of $-(\text{Au}-\text{PDI})_n$ oligomer exposed to CO at $\sim 110\text{K}$. The pronounced tall/short (oval/circle) structure of the chain suggests that this is direct microscopic evidence for CO adsorption on low-coordination adatom-like gold in the oligomers.

To further investigate the decooordination hypothesis (suggested by the RAIRS data), a model gas-sensor was constructed along the lines of the granular films described in Chapter 5. In Chapter 5, it

was concluded that indeed $-(\text{Au}-\text{PDI})_n$ - oligomers can bridge the gap between gold nanoparticles of a granular film. The dramatic reduction in sheet resistance across these films was attributed to exactly this process. If this is the case, and if CO adsorption does indeed cause decoordination of PDI from gold upon adsorption, measuring the sheet resistance of a granular film as a function of CO pressure should provide confirmation that such a process is occurring. Figure 6 shows the results of one such study.

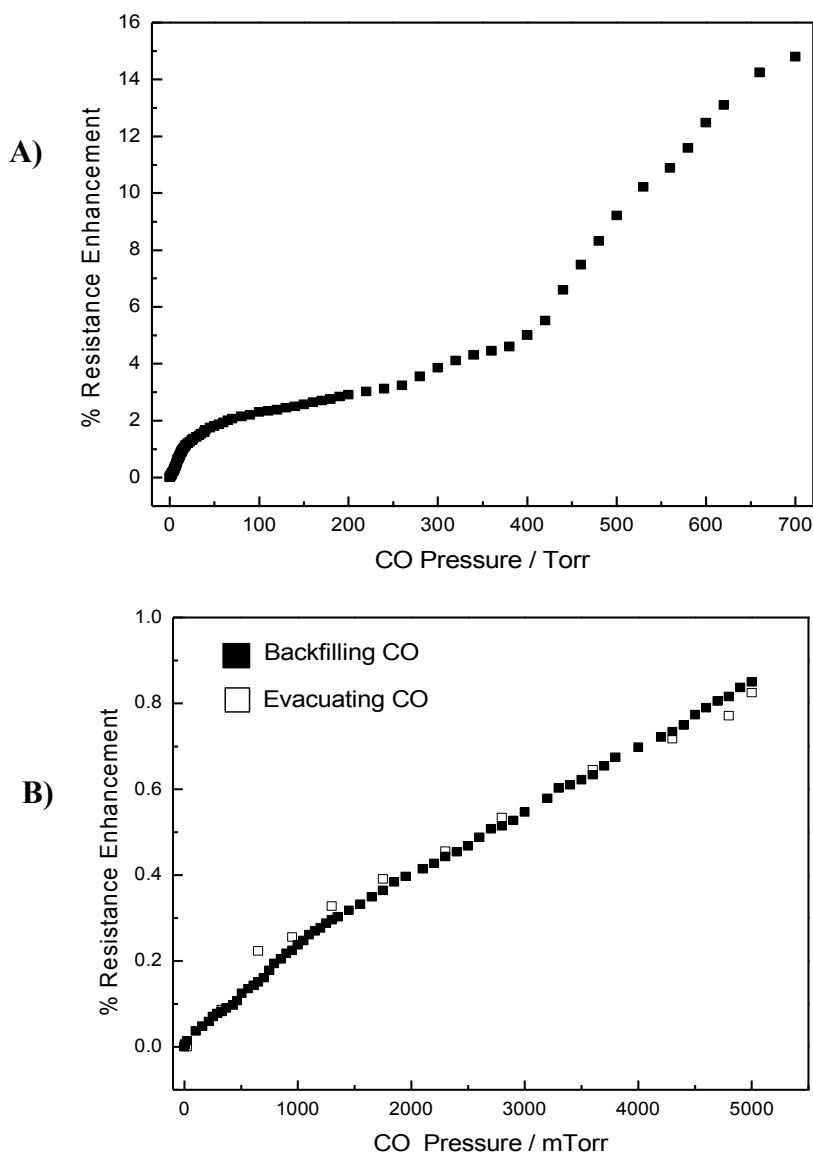


Figure 6: Granular film based gas-sensors. Film was prepared as in Chapter 5 and dosed with 1,4-PDI. A) Shows the result of a CO back-filling experiment. The bend in the curve is reproducible, but its origin is unknown. B) Resistance vs. CO pressure response is reversible, at least out to 5 Torr.

cis and *trans*-2-butene on $-(\text{Au}-\text{PDI})_n-$

As described in the introduction to this chapter, one of the primary goals of the research presented in this work has been investigating the unique properties of the adatom-like gold atoms that are generated by the self-assembly of 1,4-PDI on Au(111). The adsorption of carbon monoxide on 1,4-PDI templated surfaces led to the conclusion that CO is capable of “decoordinating” one end of a 1,4-PDI unit which leaves the gold adatom available for the gas adsorption. To further probe the decooordination hypothesis, other chemically (and catalytically) relevant species were investigated. In this chapter the adsorption characteristics of two prototypical alkenes (*cis* and *trans*-2-butene) will be discussed.

Figure 7 shows a schematic of *cis* and *trans*-2-butene impinging upon an adatom. The models were created in Avagadro, minimized using the MMFF94s level of theory, and shown here using Van der Waals spheres to give some indication of the steric bulk associated with the two isomers of 2-butene.

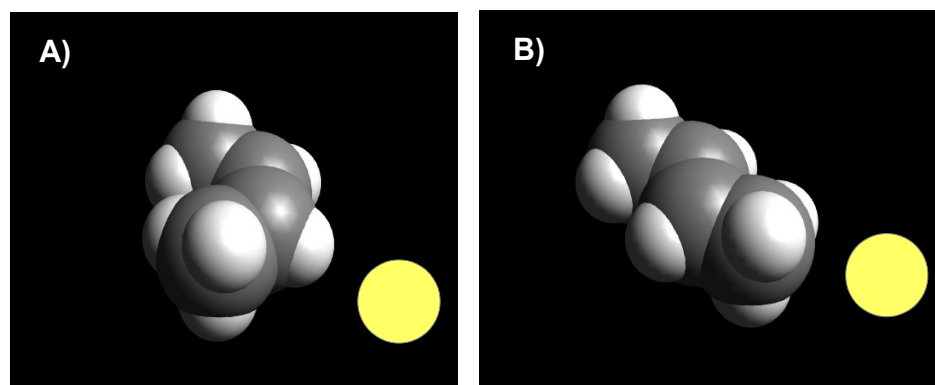


Figure 7: A) and B) depict *cis* and *trans*-2-butene impinging upon an adatom. Based on steric arguments, one would expect *cis*-2-butene to allow for better π -overlap with the adatom via “head on” attack.

Figure 8 shows a *cis*-2-butene uptake experiment. Interestingly, the CN monolayer mode is shown to undergo decooordination resulting in a very similar peak shape as was described for a similar experiment dosing CO. In fact the decooordination appears to be complete at an exposure of 2×10^{-10} Torr (vs. 9.2×10^{-11} Torr base pressure) for only 90s. At this exposure, the coverage is low enough that

the *cis*-2-butene modes themselves are just starting to emerge from baseline noise. The dosing was carried out at a temperature of approximately 95K, and upon flashing to ~110K *cis*-2-butene is shown to have desorbed. However, the split CN mode of PDI is shown to persist after the

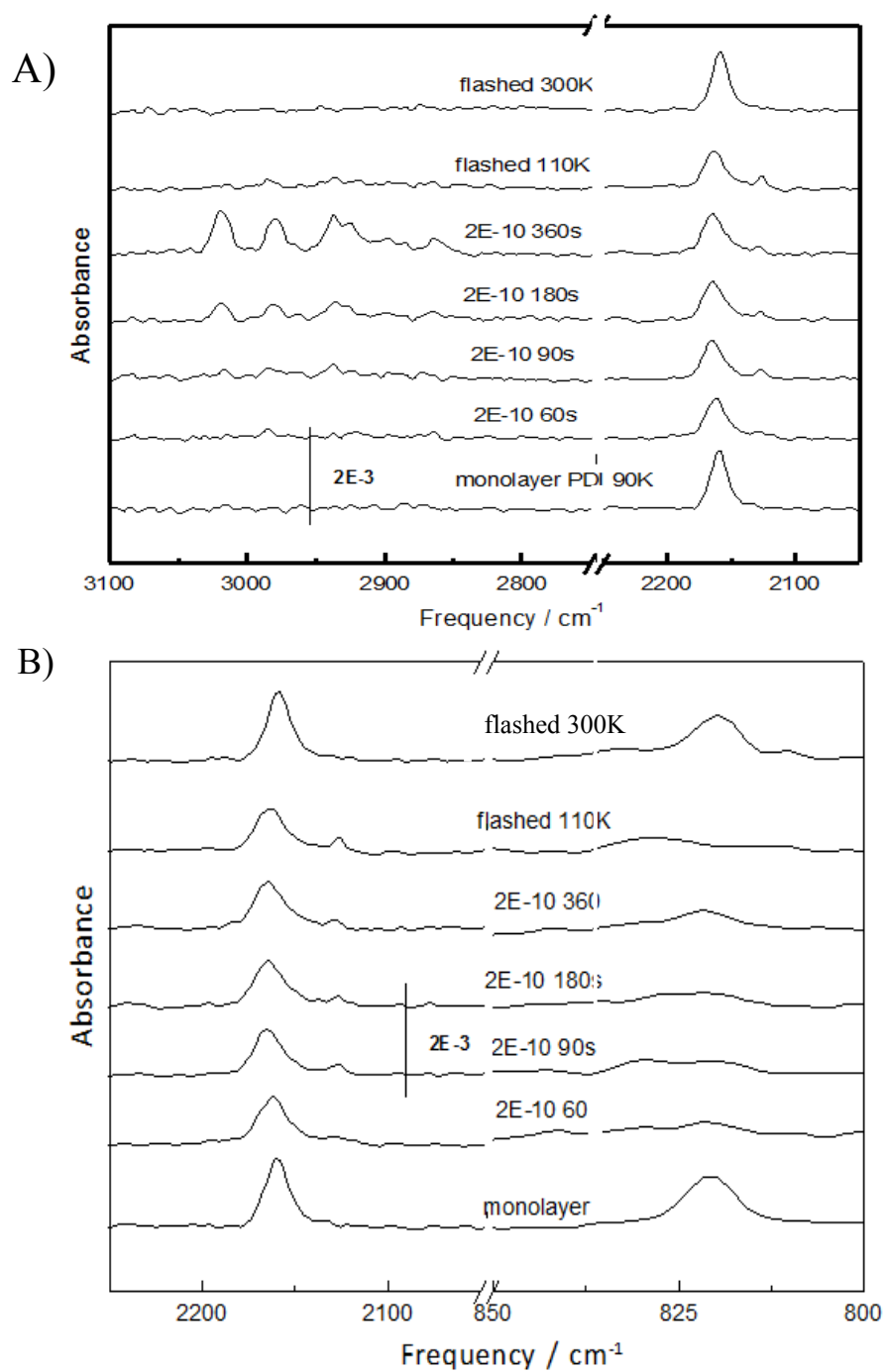


Figure 8: A) High-frequency, and B) low-frequency regions of $-(\text{Au-PDI})_n$ oligomers, dosed for the time and pressure shown with *cis*-2-butene.

desorption—a situation identical to that observed in the CO uptake experiments described earlier in this chapter. Also similar to the CO uptake studies, heating the crystal briefly to slightly above room temperature results in the regeneration of a single CN 1,4-PDI peak. This suggests once again that the formation of η^2 1,4-PDI from the upright η^1 moiety is a weakly activated process.

Figure 9 shows the results of a RAIRS uptake study of *trans*-2-butene on a 1,4-PDI saturated Au(111) surface. Cleaning and dosing protocols were exactly as described above for *cis*-2-butene (above). The spectra do not show any sign of decooordination, as the CN modes of PDI remain perfectly intact with exposure. This implies that *trans*-2-butene is not capable of coordinating the gold adatoms present in the Au/PDI oligomer system. The frequencies corresponding to *trans*-2-butene (between about 2900 and 3100 cm^{-1}) are then simply a multilayer of the molecule frozen out on the surface of the crystal.

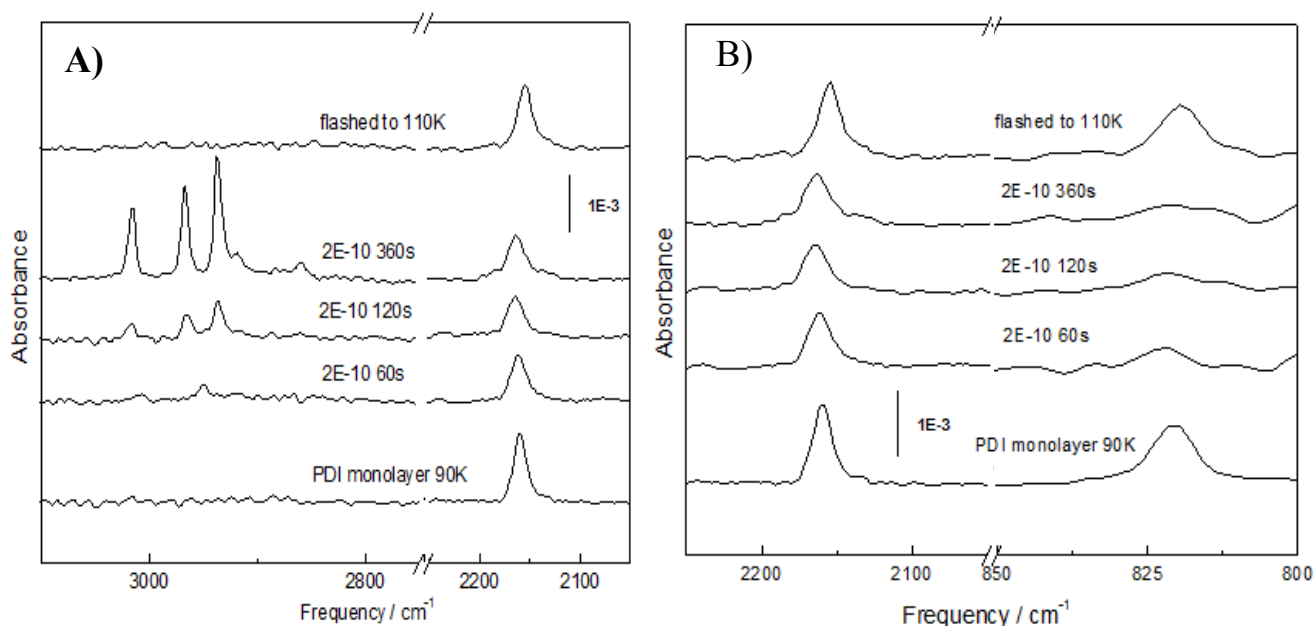


Figure 9: High (A) and low (B) frequency regions of *trans*-2-butene dosed onto 1,4-PDI saturated Au(111). In contrast to the *cis*-2-butene data presented above, no evidence of CN decooordination was observed.

experiments, a final experiment was performed. Figure 10 shows the result. A 1,4-PDI saturated monolayer was prepared as above, and cooled to $\sim 95\text{K}$ as before. The top spectra shows the results of

dosing with *trans*-2-butene while the lower one shows the CN region of the surface after exposure to *cis*-2-butene.

The butene overlayer observed in this experiment could also account for the attenuation of the CN and also the ring mode (at $\sim 821\text{cm}^{-1}$). The decrease in intensity suggests that the vibrations are being damped, but they are not changing in energy suggesting that the chemical environment with respect to their coordination motif (*vs.* gold adatoms) remains unchanged. In an effort to confirm the above two The *trans*-2-butene experiment was performed first as this adsorbate was shown not to induce morphological changes to the surface (STM data, not shown). Then the sample was warmed to 200K

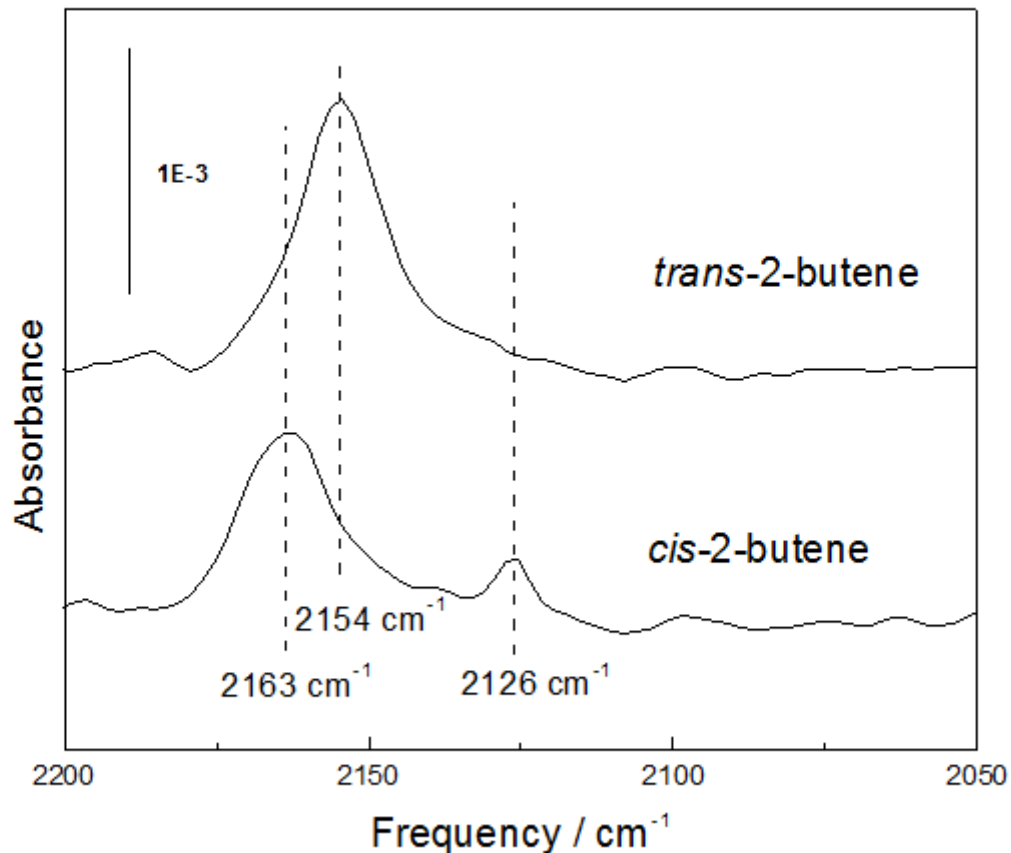


Figure 10: PDI CN mode of Au(111) crystal exposed to *cis* and *trans*-2-butene. Both exposures were 2×10^{-10} Torr for 120 seconds.

to desorb *trans*-2-butene and the other isomer was dosed under identical conditions. This allowed both

data sets to be collected with the same background, identical dosing conditions, and with an identical surface (assuming that the *trans* isomer is indeed totally inert towards CN decoordination). The resultant CN peak observed in the *cis*-2-butene dosing experiment is strikingly similar to the peak observed in the CO dosing experiments earlier in this chapter.

Figure 11 is an STM current map of a $-(\text{Au}-\text{PDI})_n$ -saturated surface, which had been exposed to $\sim 3\text{L}$ of *cis*-2-butene (crystal at 100 K). The image clearly shows periodic structures, which are resolved as oval features with ball-like protrusions. The width of the features is approximately 2 nm. These appear to be direct evidence for the existence of *cis*-2-butene on the surface, preferentially sticking to the PDI oligomers, presumably to the adatoms generated thereby.

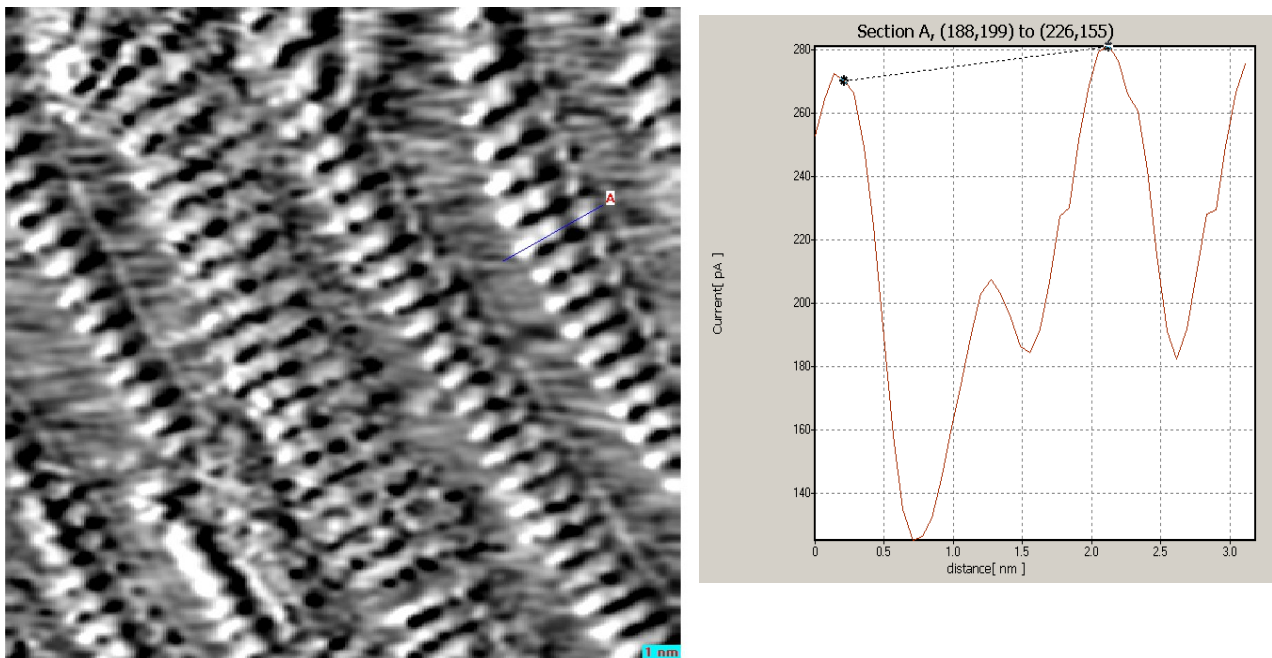


Figure 11: Current map of 110K $-(\text{Au}-\text{PDI})_n$ - surface exposed to 3L of *cis*-2-butene. The oval features terminated by ball-like structures appear to be *cis*-2-butene molecule adsorbed in ordered rows on the surface.

Figure 12 shows a larger area image of the same surface. The striking feature of this surface is that there is evidence for a high degree of mobility in the chains. In fact, there are several regions in the image that imply that the chains are sweeping out an arch (anchored at one end) on a time scale faster than can be resolved on the basis of STM or moving laterally. This is evidenced by a sort of “ghosting”

where the same chain is imaged multiple times, perhaps on one image line. The herringbone reconstruction is very clearly resolved in the image in the spaces between the chains, as are the features along the straight sections. It is unlikely that this degree of resolution would be possible with a faulty tip. As was the case with CO, there appears to be far less order on the surface (of the Au-PDI oligomers) after the exposure to *cis*-2-butene than before.

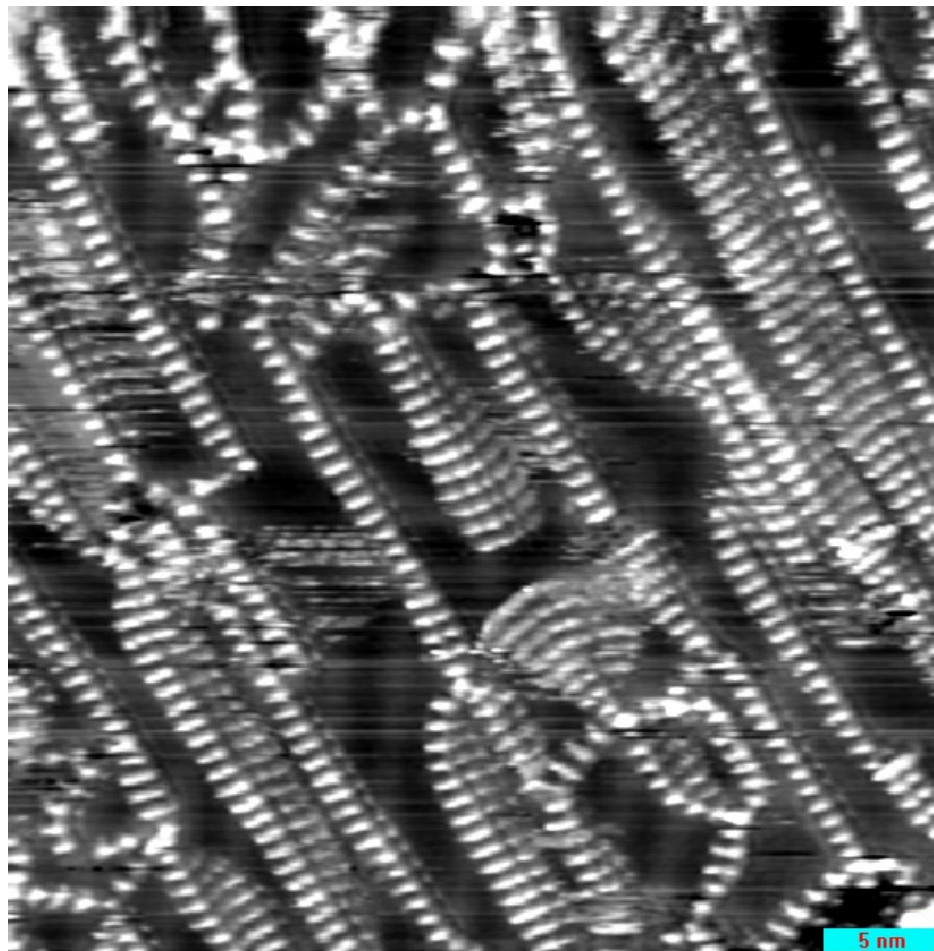


Figure 12: 110K STM image of *cis*-2-butene exposed $-(\text{Au}-\text{PDI})_n$ - surface. There is a high degree of mobility in the chains, as evidenced by arch-like structures. The chains appear anchored on one end, and free to move on the other. Some of the straight segments show similar behavior—evidence of hopping laterally, and imaging as kind of “ghost” image.

Conclusions:

In this chapter, adsorption of gases on $-(\text{Au}-\text{PDI})_n$ - oligomers was described, as investigated by RAIRS, STM, and electrical measurements. The prediction was that this would be an interesting

system in that it has been demonstrated that even for clean Au(111) surfaces, gold atoms occupying low-coordination number sites are significantly more reactive than those occupying terraces. This observation was made on Au(111) roughened with argon ion bombardment [11], and also the observation that CO forms stable $(\text{CO})_n$ ($n= 2-5$) clusters on Au(111) [19].

As evidenced in Figure 1, CO adsorption does occur on a Au/1,4-PDI oligomers on a Au(111) crystal, and the carbon monoxide peak was shown to be stable up to a temperature of ~ 150 K. Another striking feature of this data is that in addition to a pair of CO peaks at ~ 2003 and 2027 cm^{-1} , the -NC mode was shown to undergo a disruption. The -NC mode for the flat-lying 1,4-PDI state is symmetric and falls at an energy of 2153 cm^{-1} . However, after exposure to CO the 2153 cm^{-1} appears greatly reduced in intensity, and two new peaks at 2166 and 2128 cm^{-1} appear in its place. These peaks are attributed to an “anchored” and “free” mode of upright, η^1 PDI respectively [14]. The anchored mode falling at higher energy can be understood by considering that the lone-pairs of electrons on -NC are formally anti-bonding in character, and donating them to a metal atom serves to strengthen the -NC bond.

Heating of the CO saturated surface demonstrated that the molecule is stable on the surface to a temperature of ~ 150 K. However it is seen in Figure 1 that the -NC mode remains split after the CO has desorbed. Heating to slightly above room temperature is required to collapse the peaks back into a single (2153 cm^{-1}) peak. This suggests that the formation of the flat-lying state from the upright state is a (weakly) activated process.

Figure 4 showed a low-temperature STM image of a CO exposed, 1,4-PDI saturated Au(111) crystal. Recall from Chapter 3 that 1,4-PDI self-assembles structures that tended to be long (hundreds of nanometers) and largely straight. In Figure 4, this is clearly no longer the case. The structure of the chains has been greatly modified by the CO exposure, and now they are bent and curved, and it appears

as though much of the original 1,4-PDI present on the surface has desorbed. Also present on the surface are features on the order of 2-5 nm in size that appear to be (presumably gold) nanoparticles. Recall from Chapter 4 that the mechanism for chain formation involved mobile, 1,4-PDI/Au_{adatom} complexes diffusing on the surface and “clicking” into place on the growing oligomers. The DFT results presented in Chapter 4 imply that these adatom complexes are slightly repulsive, which is what prevents the adatoms from simply diffusing together and agglomerating into larger particles. The nanoparticle formation observed here is likely the result of an opposite process—the *decoordination* of PDI, followed by desorption of some fraction of the molecules, would leave the surface covered in some number of mobile, free, adatoms. The results are interesting in that gold nanoparticles are most reactive (and so far, offer the most utility) when in the 2-5 nm range [20], and STM images acquired over the course of this work indicate that 1,4-PDI dosing followed by PDI decoordination by an adsorbate such as CO might provide another route to the preparation of nanoparticles on surfaces.

Figure 5 shows a close-up image of CO exposed oligomers, acquired at ~110K. Recall from Chapter 3 that the oligomers (as assembled) show a periodicity of 1.13nm, and that the adatoms and phenyl rings of PDI image with the same apparent height. Clearly in Figure 5 this is no longer the case, with the chains now imaging as a series of alternating circular and oval features, with heights of 50 and 80 pm respectively. This could represent direct microscopic evidence for 1,4-PDI linking molecules becoming decoordinated from adjacent gold adatoms.

As an extension of the electrical measurements presented in Chapter 5, granular films were prepared and dosed with 1,4-PDI, and these films were exposed to increasing pressures of CO (at room temperature). As shown in Figure 6, the device did show an increase in sheet resistance as a function of CO pressure, with the maximum increase being ~16% at 700 Torr. The experiment was carried out by back-filling the chamber with CO and for the high-pressure experiment, equipment constraints

precluded taking measurements while the chamber was evacuated again. A reversibility study was included in Figure 6, showing good, reversible behavior at least out to 5 Torr CO pressure. The increase in sheet resistance with CO pressure is in accord with 1,4-PDI linker molecules becoming decoordinates as a result of gas adsorption. Chapter 5 described the ability of $-(\text{Au}-\text{PDI})_n-$ oligomers to bridge gold nanoparticles. The increase in conductivity through the films was described as resulting in a decrease in the tunneling barrier between the particles. If CO is indeed decoordinates linker molecules, exposure to this gas would be expected to cause an increase in resistance across the film as the oligomers would go from largely fully conjugated, to disrupted. This would certainly serve to increase the tunneling barrier between particles. One needs to use caution when interpreting this data, however, as it is likely that disruption (decoordinates) of the oligomeric chains between particles is not the only process involved. It is likely that in fact the nanoparticles themselves are participating in CO adsorption as they are presumably riddled with defect and low-coordination sites. Still, the magnitude of the resistance change gives some support to the idea that the degree of conjugation between particles can be modified with CO exposure.

To further investigate the utility of adatom templated structures, and in particular their (potential) role in the field of catalysis, two simple alkenes were investigated. *Cis*-2-butene and *trans*-2-butene were selected for the studies reported here. CO, coordinating a metal on atop or adatom sites, would present a small steric footprint. Figure 7 depicts a cartoon of the 2 butene isomers impinging on a (gold) atom. The molecules depicted as van der Waals spheres to give some idea of the steric demands of the two isomers. Formation of metal-alkene bonds typically results from the direct overlap of alkene π orbitals with the metal center d-orbitals. Considering the metal atoms in question reside on a surface, the steric demands of the adsorbate (the butenes) is even more stringent. It is likely, based on steric arguments, that the *cis*-isomer would coordinate the gold adatoms more tenaciously.

Figure 8 shows the result of a low-temperature RAIRS uptake study of *cis*-2-butene on 1,4-PDI saturated Au(111). The spectra shows a disruption in the -NC mode which is strikingly similar to the splitting observed upon CO exposure. Figure 9 was acquired for *trans*-2-butene, and this -NC mode does not show evidence of alteration upon gas exposure. For direct comparison, Figure 10 shows the results of a sequential butene dosing study. The *trans* isomer was examined first, then the *cis* isomer (with the same back ground). Clearly, the *trans* isomer is not shown to disrupt the -NC mode, while the *cis* isomer results in a -NC peak shape that is strikingly similar to that observed in the CO study. It seems clear that the *cis* isomer, with its two terminal methyl groups pointed in the same direction, has an exposed π -bond which can attack the metal atom head-on. In *trans*-2-butene, such overlap would be hindered by the bulky methyl groups—one of which would be pointing at the surface as the molecule impinges. While considering CO and the butene isomers, it is interesting that gas adsorption on -(Au—PDI)_n - oligomers seems to be a general phenomenon, the system is selective in terms of steric bulk. Indeed, the system undergoes decoordination on exposure to CO. Not shown is similar data indicating this process also occurs on exposure to H₂, O₂, and NO.

The STM data presented in Figures 11 and 12 offer direct evidence for *cis*-2-butene adsorption on PDI oligomers. The resolution of Figure 11 (a current map of the surface) is such that features appearing to be the molecules are present. They image as oval features (presumably a C=C bond), with small ball-like features on either end (methyl groups). These molecules are lined up laterally in a long chain and are most likely occupying gold adatoms which were generated and stabilized by 1,4-PDI.

Figure 12 is interesting as the image show evidence of a high degree of mobility in the chains upon *cis*-2-butene exposure. There are two locations where clearly the chain has been broken in the middle, but the un-broken segments of chain are sweeping out an arc on the surface. There are also long segments of chain that show evidence for hopping between adjacent sites. This behavior was never

observed for the un-exposed $-(\text{Au}-\text{PDI})_n$ - oligomers in our studies. This high degree of mobility is especially unexpected as the measurement was carried out at 110K. What is also evident (as was also observed for the CO studies discussed earlier) is that the surface was initially saturated with 1,4-PDI (data not shown), with oligomeric chains packed closely together. Clearly after butene exposure this is no longer the case—the coverage after exposure has decreased an estimated 50% which strongly suggests that 1,4-PDI is displaced upon gas adsorption.

It was mentioned in the introduction to this chapter that the ultimate goal of this research is with respect to *catalysis*—to do useful chemistry with the systems described herein. Adsorbing gasses on adatoms is an important step towards mastery of this subject. The other aspect that was discussed was the potential to tune the electronic structure of the atoms, and thus their reactivity.

There is an increasing volume of literature regarding gold-based *bimetallic alloys*, often found in the form of nanoparticles. The literature suggests that bimetallic alloys of Au-Pt [21], Au-Pd [22], Au-Ag [23], and Au-Cu [24] offer much higher activity than (pure) gold nanoparticles, but are quite selective, particularly with regards to oxidation chemistry (i.e. conversion of alcohols to ketones or aldehydes, not carboxylic acids). The unique properties of the bimetallic alloys is largely a result of the bridge sites created when two dissimilar metals are found adjacent to each other.

Surface alloys are routinely produced in our laboratory by thermally evaporating one metal on top of another, then annealing the surface to drive in the ad-metal. In our case, the alloys are typically produced by evaporating a few monolayers of gold on top of palladium, then annealing the palladium for specified periods of time, resulting in a surface with some well defined number of gold atoms.

Using the oligomerization chemistry presented here, it would be interesting to forgo the high temperature annealing step, and instead produce a surface (palladium, for example) with a coverage of loose gold adatoms, then expose this surface to 1,4-PDI. If the oligomerization chemistry proceeds on

a dissimilar metal surface (i.e. gold on palladium, copper, silver, etc.), it should be possible to template a well ordered array of bi-metallic bridge-sites.

The chemistry of bimetallic alloys is fascinating as it seems one atom (palladium, for example) is used to perform the dissociation part of the reaction—generating two atomic hydrogens from H₂, or two atomic oxygens from O₂, while the other atom works to stabilize the other reactant.

References:

- 1) 2003 July 21, The Times (UK), Section: Business, “Demand for Global Listing Helps to put New Gloss on Gold”
- 2) Häkkinen, H.; The gold-sulfur interface at the nanoscale; *Nature Chemistry*. **2012**, (4), 443-455.
- 3) Haruta, M.; Kobayashi, T.; Sano, H.; Yamada, N.; Novel gold catalyst for the oxidation of carbon monoxide at temperatures far below 0°C. *Chem. Lett.* **1987**, 405. 405-408.
- 4) Hutchings, G.J.; Vapor phase hydrochlorination of acetylene: Correlation of catalytic activity of supported metal chloride catalysts. *J. Catal.* **1985**, 96, 292-295.
- 5) Haruta, M.; in “Catalysis and Electrocatalysis at Nanoparticle Surfaces.”. ed. Wieckowski, A.; Saviova, E.R., Vayenas, C.; Dekker, M.; **2003**, New York, USA. 645.
- 6) Haruta, M.; *J. New Mat. Electrochem. Systems*. **2004**, 163-172.
- 7) Prati, L.; Villa, A.; The Art of Manufacturing Gold Catalysts. *Catalysts* **2012**, 2, 24-37
- 8) Bond, G.; Thompson, D.; Gold-Catalysed Oxidation of Carbon Monoxide. *Gold Bulletin*. **2000**. 33 (2) 41-51.
- 9) Janssens, T.; et. al.; Insights into the reactivity of supported Au nanoparticles: combining theory and experiments. *Topics in Catalysis*. **2007**. 44. (1-2). 15-26.
- 10) Barmparis, G.; Remediakis, I.; Dependence on CO adsorption of the shapes of multifaceted gold nanoparticles: A density functional theory. *Physical Review B*. **2012**. 86. 085457-(1-7)
- 11) Piccolo L.; Loffreda D; Cadete S. A.; Deranlot C.;Jugnet Y.; Bertolini J.C.; *Surf. Sci.* **2004**. 566–568:995
- 12) Meyer, R.; Lemire, S.; Shaikhutdinov, S.; Freund, H.; *Gold Bulletin*. **2009** 37. 72
- 13) Gottfried, J.; Schmidt, K.; Schroeder, S.; Christman, K.; *Surf. Sci.* **2003** 536 206.
- 14) Swanson, S.; et. al.; *Langmuir*. **2005**, 21 (11). 5034-9.
- 15) Boscoboinik, J.A.; et. al. *Top. Cat.* **2011**. 54 (1) 20-25.
- 16) Bradley, M.; Curve Fitting in Raman and IR Spectroscopy: Basic Theory of Line Shapes and Applications. Application Note: 50733. Thermo Fisher Scientific, Madison, WI.
- 17) Arenz, M.; Landman, U.; Heiz, U.; *Chem. Phys. Chem.*. **2006**. 1871-9.
- 18) Piccolo, L.; et. al.; *Surface Science*. **2004**. 995, 566-568.
- 19) Maksymovych, P.; Yates, J.; *Chem. Phys. Lett.* **2006**. 421. 473.

- 20) Meyer, R.; Lemire, C.; Shaikhutdinov, Sh.; Freund, H.; *Gold Bulletin*. **2004**. 37. 72-124.
- 21) Shen, Y.; Zhang, S.; Li, H.; Ren, Y.; Liu, H.; *Chem. Eur. J.* **2010**. 16. 7368-7371.
- 22) Kaizuka, K.; Miyamura, H.; Kobayashi, S.; *JACS*. **2010** 132. 15096-98.
- 23) Chaki, N.; Tsunoyama, H.; Negishi, Y.; Sakurai, H.; Tsukuda, T.; *J. Phys. Chem. C*. **2008**.

Chapter 7

Adsorption of 1,3-Phenylene Diisocyanide on Au(111)

Introduction

It has been shown previously that 1,4-phenylene diisocyanobenzene (1,4-PDI) on Au(111) react to form one-dimensional oligomer chains comprising alternating gold and 1,4-PDI units on the Au(111) surface [1-3]. This was also the focus of previous chapters. The oligomers form by extracting gold atoms from low-coordination sites on the gold surface. Since 1,4-PDI maintains its π -conjugation throughout the molecule and has two functional groups it has been proposed as a prototypical molecule for nanoelectronic applications [4-9]. It has also been recently demonstrated that it is possible to link between gold nanoparticles using a similar chemistry in which the 1,4-PDI extracts gold atoms from the gold nanoparticles to form an oligomeric bridge between them (Chapter 5). In the case of 1,4-PDI, the spacing between the gold atoms in the $-(\text{Au}-1,4\text{-PDI})_n-$ repeat unit is close to four times the gold-gold nearest-neighbor distance along the close packed directions on Au(111). However, DFT calculations suggest that there is some strain that distorts the plane of the 1,4-PDI molecule [1]. In order to explore whether the oligomerization found for 1,4-PDI is a general phenomenon and to ultimately explore the effect of molecular geometry on electron transport, the following explores the surface chemistry of 1,3-PDI on Au(111) surfaces using a range of surface-sensitive techniques.

Experimental Methods

1,3-PDI was prepared from 1,3-phenylenediamine *via* the “Phase Transfer” method (Wagner, PhD) and purified by vacuum sublimation at $\sim 80^\circ\text{C}$. Au(111) cleaning, annealing, and reconstruction was carried out according to the Chapter 2.

Results

The uptake and removal of 1,3-PDI on Au(111) at 300 K, monitored using Auger spectroscopy,

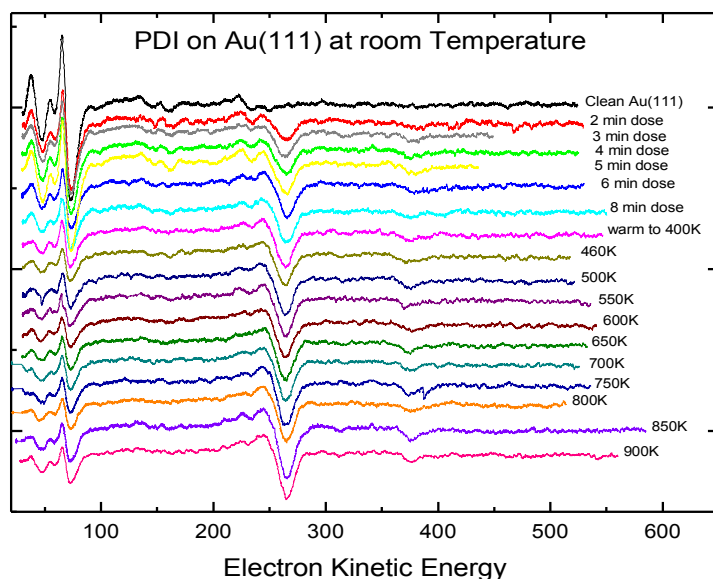


Figure 1: A series of Auger spectra after dosing 1,3-PDI on Au(111) at 300 K for up to 8 minutes and the effect of subsequent heating to 900 K.

is shown in Figure 1. The initial uptake is shown in the top spectra where the growth of a feature at ~ 270 eV is due to the carbon KLL feature. This is mirrored by the growth of a much less intense feature at ~ 380 eV due nitrogen (assigned to the N KLL signal). This indicates that both carbon and nitrogen adsorbs onto the surface, and is accompanied by a decrease in intensity of the gold signal (at ~ 70 eV) due to the low mean-free path of electrons at this kinetic energy. The variation in C KLL Auger signal with 1,3-PDI exposure is shown in Fig. 2 showing a smooth uptake of 1,3-PDI with increasing exposure. However, C KLL and N KLL signals show very little variation in intensity as the

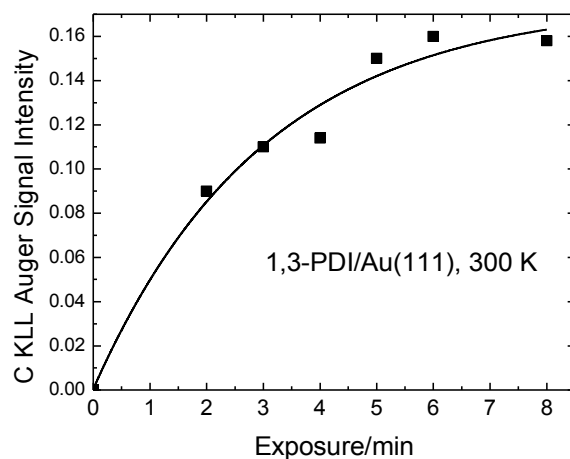


Figure 2: Uptake of 1,3-PDI on Au(111) at 300 K from the peak-to-peak intensity of the carbon KLL Auger features in the spectra shown in Fig.1.

sample is heated to ~ 900 K indicating that the majority of the adsorbed 1,3-PDI is very stably adsorbed on the surface.

Figure 4A) shows an STM image of 1,3-PDI dosed (1 minute, 0°C) onto a Au(111) surface at 300 K and imaged at 120 K to minimize thermal effects. This clearly shows a zig-zag motif that might be expected of a bent molecule. In some cases, the patterns close in on themselves to form hexagonal units. There are brighter spots in some regions of the images, which may be associated with 1,3-PDI adsorbing into a second layer. Figure 4B) shows a closeup of these “zigzag chain” structures.

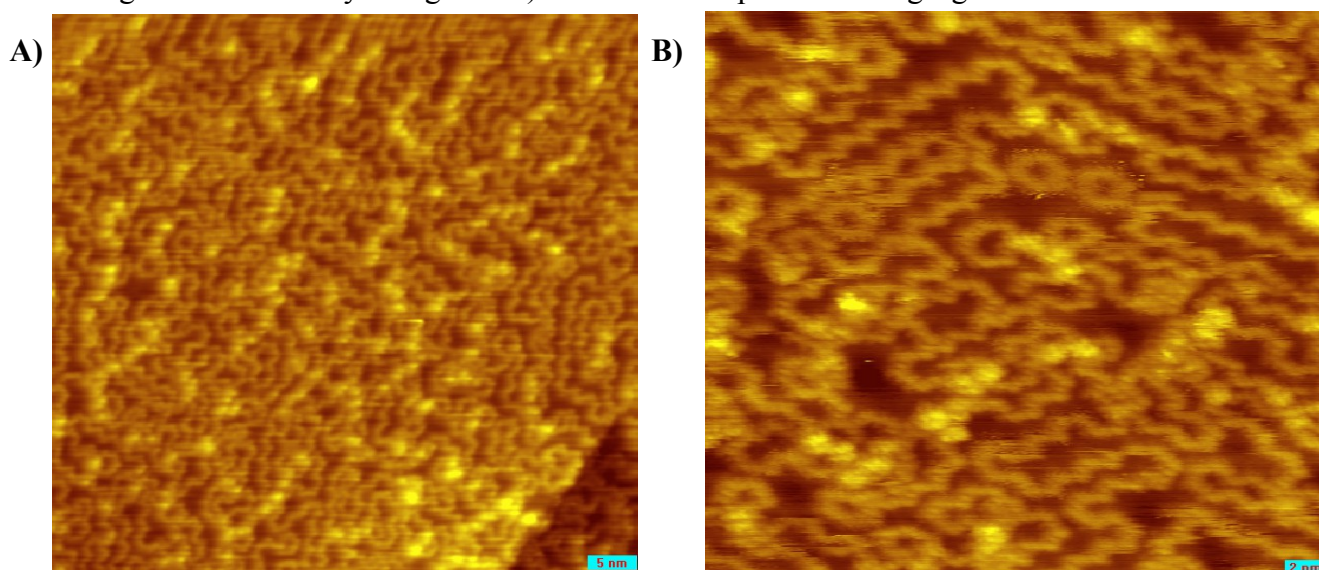


Figure 4: A) An STM image of a saturated overlayer of 1,3-PDI adsorbed on Au(111) at 300 K ($I_t = 132$ pA, $V_b = -0.5$ V). B) Shows long, straight segments of “zigzag chains” in addition to closed and hair-pin structures.

Infrared spectra were collected of PDI dosed onto Au(111) at 300 K for various times and the results are displayed in Fig. 5. The spectrum exhibits the strongest intensity after initial dosing at room temperature exhibiting an intense feature at ~ 2153 cm^{-1} , with weaker features at 849 and 772 cm^{-1} . While these assignments will be discussed in greater detail below, the ~ 2153 cm^{-1} mode is clearly assigned to an isocyanide stretching mode and confirms the adsorption of 1,3-PDI on the surface. As the exposure increases, the intensities of all of these features decreases, while heating to ~ 373 K, a temperature at which any second-layer 1,3-PDI desorbs, has essentially no effect on the spectrum.

Finally, density functional theory calculations were performed to establish possible geometries of 1,3-PDI on the surface. Based on the structure found for 1,4-PDI, a structure was generated with

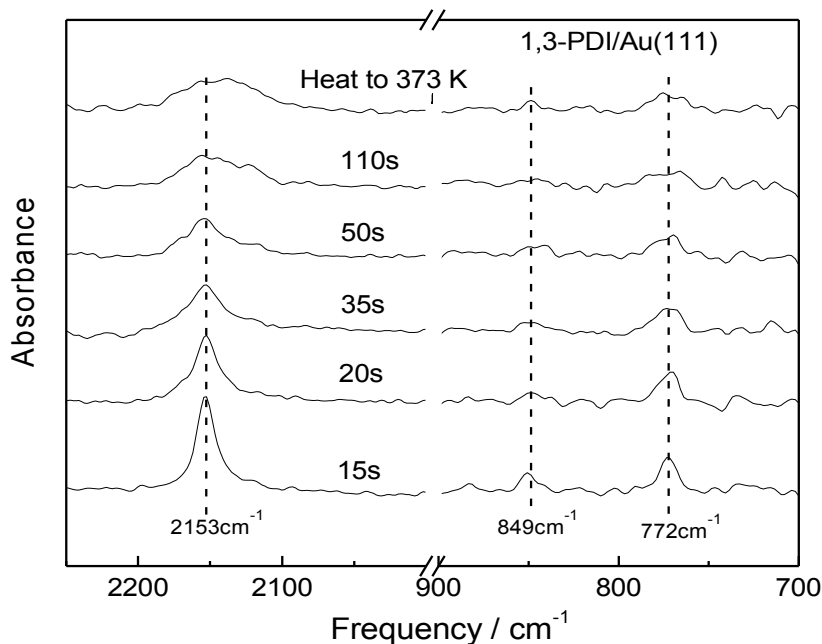


Figure 5: Reflection-adsorption infrared spectra of 1,3-PDI adsorbed on Au(111) at 300 K as a function of exposure. The top spectrum shows the effect of heating the sample to 373 K.

gold adatoms on the Au(111) surface and the initial structures were set with the plane of 1,3-PDI set at various angles (30° , 60° and 90°) with respect to the surface and the geometries allowed to relax. The most stable structure is depicted in Fig. 6, where the plane is tilted at $\sim 30^\circ$ to the surface with a binding energy of ~ 220 kJ/mol and is much larger than the energies of 1,3-PDI bonded directly to the gold surface (~ 60 kJ/mol, data not shown). The large energy difference accounts for the 1,3- and 1,4-PDI being able to extract gold atoms from the substrate to form the oligomer chains. However, the energy to tilt the plane is rather small varying by only ~ 16 kJ/mol as the angle changes from perpendicular to the most stable structure (Fig. 6).

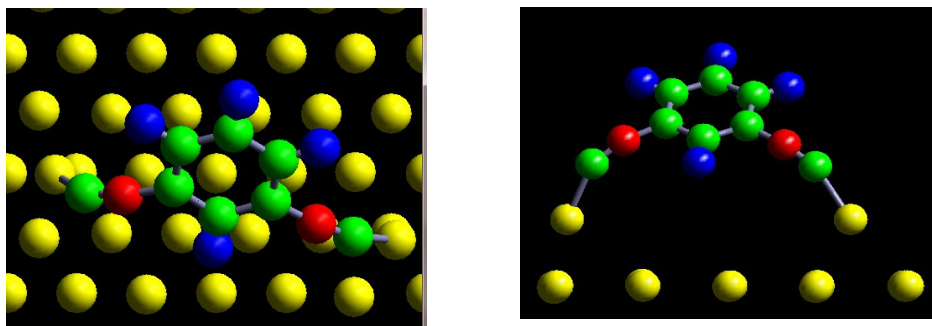


Figure 6: A depiction of the top and side views of 1,3-PDI adsorbed on gold adatoms on a Au(111) substrate calculated using density functional theory.

Discussion

1,3-PDI adsorbs strongly on Au(111) at 300 K and thermally decomposes to evolve hydrogen at ~ 700 K (Fig. 3(b)) and leave carbon and nitrogen on the surface (Fig. 1). Adsorption at ~ 90 K (Fig. 3A)) results in 1,3-PDI desorption at ~ 230 K, close to the desorption temperature of 1,4-PDI from the surface. This indicates that the chemistry of 1,3-PDI on Au(111) is similar to that found for 1,4-PDI, [1-3] which forms one-dimensional oligomer chains on the surface comprising repeat $-(\text{Au-PDI})-$ units by extracting gold atoms from low-coordination sites on the Au(111) substrate. The low-temperature (~ 230 K) desorption state is due to 1,3-PDI bonded to the surface by a single isocyanide group and may be due to a precursor to the one-dimensional chain or to 1,3-PDI adsorbed on top of a saturated layer of the oligomer chain. This assignment is supported by the observation that no 1,3-PDI desorbs from the surface at the lowest exposures since the initial 1,3-PDI oligomerizes on the surface.

The formation of stable species following 1,3-PDI adsorption is explored using density functional theory where the most stable adsorption geometry for a single 1,3-PDI molecule is shown in Fig. 6. The stability of this species (~ 220 kJ/mol binding energy) is in accord with its stability found on heating (Figs 1 and 3(b)). The calculations suggest that the most stable structure has a molecular plane is tilted at $\sim 30^\circ$ to the surface. It should be noted, however, that calculations for 1,4-PDI bonding to gold suggest that there is a strong preference for the isocyanide groups to bond to gold adatoms in a trans geometry [2]. This would suggest that the oligomer chains formed from 1,3-PDI should have a tendency to form zig-zag structures with the plane of the molecule close to parallel to the surface to accommodate this trans geometry. This conjecture is borne out by the STM images of 1,3-PDI on Au(111) (Fig. 4), where a large number of such structures are identified. However, there are clearly also regions in which this zig-zag structure is not maintained and in several cases, hexagonal structures can be discerned. This is likely to be a result of steric constraints that prevent the zig-zag chains from forming. There are a number of brighter regions that may arise from 1,3-PDI adsorbed into a second layer on top of the oligomer chains.

Further information on the nature of the molecular species comes from the infrared data (Fig. 5). While no work has been carried out previously on 1,3-PDI on metal surfaces, a significant amount

of work has been carried using 1,4-PDI. Early work on self-assembled monolayers (SAMs) of 1,4-PDI on gold films [16] suggested that it adsorbed perpendicularly to the surface with the free isocyanide group having a vibrational frequency of 2120 cm^{-1} and the surface-bound group shifted to 2181 cm^{-1} . More recent work [17] showed similar frequencies of 2121 (free) and 2172 (surface-bound) cm^{-1} . Sum-frequency generation (SFG) results [4], found corresponding vibrational frequencies of 2122 and 2195 cm^{-1} . An average of the literature of isocyanide SAM's on gold (summarized in reference [4]) results in values of $2123 \pm 1\text{ cm}^{-1}$ for a free isocyanide group and $2181 \pm 4\text{ cm}^{-1}$ for the surface-bound species.

Thus, the mode at 2153 cm^{-1} is clearly due to an isocyanide vibration but is not due to the surface-bound mode found for 1,4-PDI SAMs on gold (at $\sim 2181\text{ cm}^{-1}$). The vibrational spectrum of 1,4-PDI alone, with D_{2h} symmetry, has been assigned with the aid of quantum calculations [18] and the strongest modes are at 850 (B_{1g} symmetry), 1505 (B_{1u}), 2127 (A_g) and 2132 cm^{-1} (B_{1u}). The first two modes are aryl ring modes while the last two are the symmetric and asymmetric $C\equiv N$ stretching modes respectively. This confirms that the 2153 cm^{-1} feature is due to a bonded isocyanide stretching mode and the presence of a single mode suggests that they are symmetrically equivalent in accord with the calculated structure (Fig. 6). The $\sim 849\text{ cm}^{-1}$ and 772 cm^{-1} modes are in the out-of-plane C-H wagging modes. They depend strongly on the presence of substitutional groups on the benzene ring which affect the coupling between them [19]. Thus, the three hydrogen atoms in a 1,3-disubstituted molecule have in-phase, out-of-plane vibrations between 770 and 795 cm^{-1} , so that the mode at 772 cm^{-1} is assigned to this mode. An isolated hydrogen atom has an out-of-plane mode between 835 and 890 cm^{-1} , allowing the 849 cm^{-1} mode to be assigned to this frequency. This confirms that molecular 1,3-PDI is present on the surface.

Thus, the vibrational spectrum at low coverages is in accord with the geometry predicted using density functional theory (Fig. 6) since both the $C\equiv N$ stretching ($\sim 2153\text{ cm}^{-1}$) and out-of-plane C-H wagging (~ 772 and 849 cm^{-1}) are both evident. If the plane of the molecule were to lay flat on the surface, the $C\equiv N$ stretching modes would be forbidden by the surface selections rules [20,21].

In the case of 1,4-PDI on Au(111), the intensities of the vibrational modes increases with 1,4-PDI coverage, [1] while for 1,3-PDI on Au(111), the both the $C\equiv N$ stretching and C-H wagging modes

decrease in intensity with increasing exposure (Fig. 5). While part of this effect may be due to a change in orientation of the plane of the 1,3-PDI molecule discussed above, and this would have the effect of decreasing the intensity of the C≡N stretching mode (at 2153 cm⁻¹), but it should then increase the intensity of the out-of-plane C-H wagging modes (at ~772 and 849 cm⁻¹), while they also decrease. The vibrational model of the oligomer chain can be analyzed using factor groups [22,23] by assigning a point group to the repeat unit, which, in the case of 1,4-PDI is the Au-PDI-Au monomer unit. However, in the case of 1,3-PDI, an ideal zig-zag chain consists of two monomer units where the isocyanide groups bonded to a gold atom are *trans* to each other. Thus, for example, for an isolated 1,3-PDI molecule with an adsorption geometry shown in Fig. 6, with point group symmetry C_s, the irreducible representations of the C≡N stretching modes are A' + A''. Only the in-phase stretching mode is infrared allowed giving rise to a single isocyanide stretching mode as observed experimentally (Fig. 6). However, as the oligomer chain grows, the ideal zig-zag structure if the two opposite 1,3-PDI molecules has a factor group symmetry of C₂. In this case, the irreducible representations of the C≡N stretching modes are A + 3B, where only the A mode is infrared allowed. This indicates that the intensities of the isocyanide modes will not scale linearly with coverage and may partly account for the decrease in intensity of the spectral features with increasing coverage seen in Fig. 6.

Conclusions

The adsorption of 1,3-PDI on Au(111) at 300 K forms predominantly zig-zag chains on the surface consistent with the structures found previously for 1,-PDI on Au(111). They are therefore proposed to bind to gold atoms extracted from defect sites on the surface. However, other motifs are also observed, for example hexagonal units that are proposed to form due to spatial constraints on the surface. The proposed surface structure is consistent with the infrared spectra, which shows the presence of a single isocyanide mode and out-of-plane C-H modes that are consistent with the presence of molecular 1,3-PDI on the surface. The intensities of the infrared modes decrease at higher coverages and this effect can be ascribed to either a change in orientation as the polymer chains grow and to the change in symmetry between the isolated molecule and the factor group of the oligomer. The chains are extremely stable on the surface and thermally decompose only on heating above 600 K. A low-

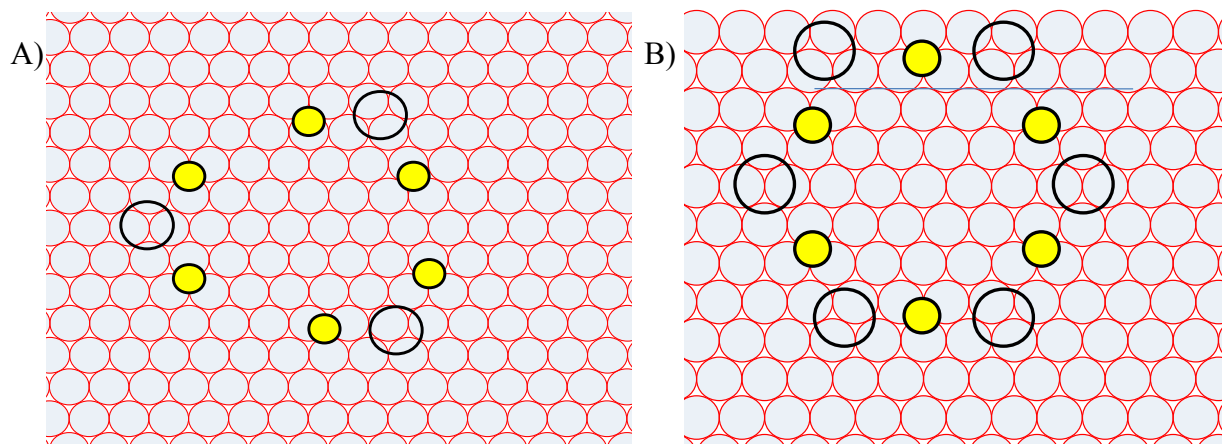


Figure 6: A) Represents 3 1,3-PDI monomers on a (111) surface. Note that the monomeric units are mediated by gold adatoms, as supported by DFT and STM studies. B) Represents a model for the commonly found hexagonal structures on the surface.

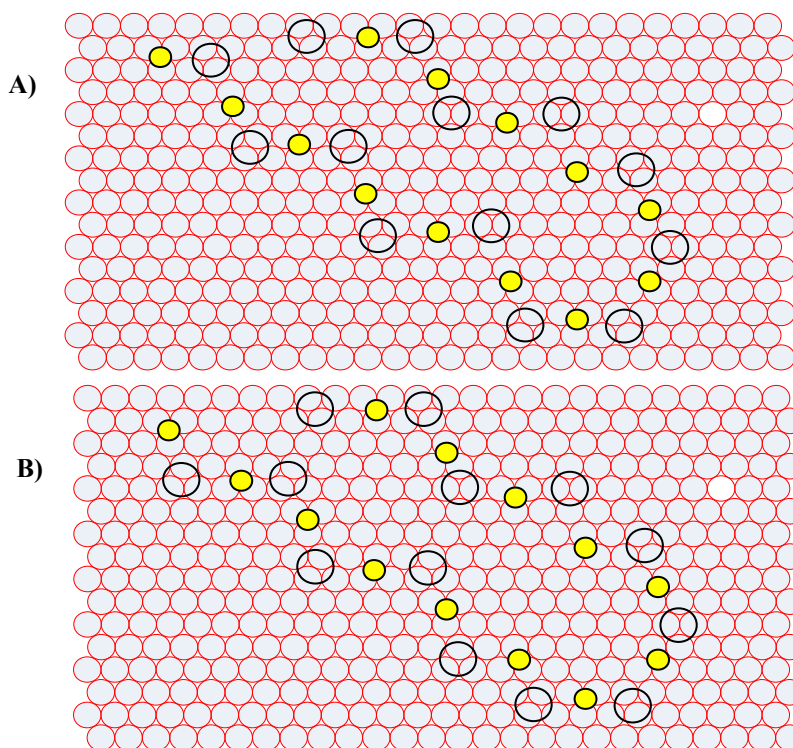


Figure 7: STM images indicate chains are often found with their long axis parallel with each other. A) is a representation of an “in phase” pair of chains while B) represents an “out of phase” pair.

temperature (~ 230 K) desorption state is detected when 1,3-PDI is adsorbed at ~ 90 K, due either to 1,3-PDI bonded to the gold surface via a single isocyanide group or bonded to gold atoms in the oligomer chain.

References

- 1) Boscoboinik, J.; Kestell, J.; Garvey, M.; Weinert, M.; Tysoe, W. *Top. Catal.* **2011**, *54*, 20.
- 2) Boscoboinik, J. A.; Calaza, F.; Habeeb, Z.; Bennett, D. W.; Stacchiola, D. J.; Purino, M. A.; Tysoe, W. T. *Physical Chemistry Chemical Physics* **2010**, *12*, 11624.
- 3) Zhou, J.; Acharya, D.; Camillone, N.; Sutter, P.; White, M. G. *The Journal of Physical Chemistry C* **2011**, *115*, 21151.
- 4) Ito, M.; Noguchi, H.; Ikeda, K.; Uosaki, K. *Phys. Chem. Chem. Phys.* **2010**, *12*, 3156.
- 5) Kim; Beebe, J. M.; Jun, Y.; Zhu, X. Y.; Frisbie, C. D. *Journal of the American Chemical Society* **2006**, *128*, 4970.
- 6) Li, Y.; Lu, D.; Swanson, S. A.; Scott, J. C.; Galli, G. *The Journal of Physical Chemistry C* **2008**, *112*, 6413.
- 7) Murphy, K. L.; Tysoe, W. T.; Bennett, D. W. *Langmuir* **2004**, *20*, 1732.
- 8) Robertson, M. J.; Angelici, R. J. *Langmuir* **1994**, *10*, 1488.
- 9) Shih, K.-C.; Angelici, R. J. *Langmuir* **1995**, *11*, 2539.
- 10) Kresse, G.; Joubert, D. *Phys. Rev. B* **1999**, *59*, 1758.
- 11) Blöchl, P. E. *Phys. Rev. B* **1994**, *50*, 17953.
- 12) Kresse, G.; Hafner, J. *Phys. Rev. B* **1993**, *47*, 558.
- 13) Kresse, G.; Furthmüller, J. *Phys. Rev. B* **1996**, *54*, 11169.
- 14) Kresse, G.; Furthmüller, J. *Computational Materials Science* **1996**, *6*, 15.
- 15) Perdew, J. P.; Burke, K.; Ernzerhof, M. *Phys. Rev. Lett.* **1996**, *77*, 3865.
- 16) Henderson, J. I.; Feng, S.; Bein, T.; Kubiak, C. P. *Langmuir* **2000**, *16*, 6183.
- 17) Swanson, S. A.; McClain, R.; Lovejoy, K. S.; Alamdari, N. B.; Hamilton, J. S.; Scott, J. C. *Langmuir* **2005**, *21*, 5034.
- 18) Han, H. S.; Han, S. W.; Joo, S. W.; Kim, K. *Langmuir* **1999**, *15*, 6868.
- 19) Colthup, N. B.; Daly, L. H.; Wiberley, S. E. *Introduction to infrared and raman spectroscopy. 2.ed*; Academic Press: New York, N.Y., **1975**.
- 20) Greenler, R. G. *The Journal of Chemical Physics* **1966**, *44*, 310.
- 21) Greenler, R. G. *The Journal of Chemical Physics* **1969**, *50*, 1963.
- 22) Liang, C. Y. *Journal of Molecular Spectroscopy* **1957**, *1*, 61.
- 23) Tobin, M. C. *The Journal of Chemical Physics* **1955**, *23*, 891.

Chapter 8

Self-assembled Structures of 1,4-Benzenedithiol on Au(111) and Formation of Conductive Oligomers Between Gold Nanoparticles on Mica

Introduction

It has been shown previously that 1,4-phenylene diisocyanobenzene (PDI) reacts following adsorption on a Au(111) surface to form one-dimensional, oligomeric chains comprising alternating gold and 1,4-PDI units [1-3]. This chain oligomerizes by extracting gold atoms from low-coordination sites on the gold surface. It has also been shown that gold nanoparticles can be electrically interconnected by the $-(\text{Au}-\text{PDI})_n-$ oligomers (Chapter 5) where, in this case, the 1,4-PDI extracts gold atoms from the gold nanoparticles to form the oligomeric bridge between them. This work was motivated by experiments on alkyl and aryl thiols on gold surfaces, where they form the anchoring chemistry for the formation of self-assembled monolayers, where it was clearly demonstrated that, rather than the thiolate group adsorbing on the gold surface (in a hollow or bridge site), it bonded to a gold adatom extracted from the substrate. Two thiolate groups could be accommodated by a gold adatom and could adopt either *cis* or *trans* configurations [6]. For the sake of electron counting, this coordination motif is something analogous to that found in an organo-gold RS-Au(I)-SR complex [7]. The thermodynamic driving force for this unusual surface structure arises since the additional energy gained by binding to a low-coordination atom outweighs the energy to extract the atom from the substrates. In fact gold-thiol bonds are typically stronger than gold-gold bonds. This suggested that

bifunctional molecules with functional groups that could bind in a similar manner to the substrate could form two linkages to gold atoms and potentially form oligomeric chains as found experimentally. It was also shown that the capability to form self-assembling oligomeric chains could be exploited to construct electrical linkages between gold nanoparticles on mica. Potential applications in forming two-dimensional metal organic framework structures on insulating substrates could also be envisaged.

While this self-assembly was first demonstrated using isocyanide-functionalized molecules, the results described above for aryl isocyanides imply that similar structures could occur with aryl dithiols, and the following explores the structures and properties of 1,4-benzenedithiol (1,4-BDT) on a Au(111) surface. 1,4-BDT has been used as a prototypical linker molecule for nanoelectronic applications either bridged between gold electrodes in a break junction or by using an STM tip as the counter electrode [8-10]. Surprisingly, given its importance in such applications, its structure following adsorption on a gold surface has not been explored in any detail. In view of this, and since analogous PDI bridges between gold nanoparticles in a nanoparticle array, similar experiments have been carried out to explore the surface morphology of 1,4-BDT on Au(111), and investigate its ability to bridge gold nanoparticles thermally evaporated on mica.

Experimental Methods

Scanning tunneling microscopy (STM) and reflection-absorption infrared measurements were made in separate ultrahigh vacuum (UHV), and electrical measurements were carried out as described in Chapter 2. 1,4-benzenedithiol (1,4-BDT) was obtained commercially (Sigma-Aldrich, 99% purity) and stored at -4°C until immediately before use. 1,4-BDT solutions in benzene were prepared in small quantities, stored frozen, and replaced frequently to minimize interference from oxidation/decomposition products.

Results:

STM:

Based on previous results for alkane and aryl monothiols [6,7] on gold surfaces, deprotonation to form thiolate species is expected to occur following adsorption at room temperature. STM images of benzene thiol on Au(111) indicate that it adsorbs by extracting gold atoms from the substrate where the resulting thiolate can adsorb in either *cis* or *trans* configurations about the gold adatom. Analogous chemistry for a bifunctionalized molecule, 1,4-PDI, where the isocyanide group binds to gold by extracting gold adatoms, forms linear, one-dimensional oligomers where two isocyanide groups binds to a gold adatom to form $-(\text{Au}-\text{PDI})_n-$ chains. In this case, the linear geometry of PDI results in the formation of linear chains. Based on the *cis* and *trans* geometries found for the bonding of benzene thiolates to gold adatoms, the formation of analogous chains from 1,4-BDT is expected to result in the formation of oligomers with either *cis* or *trans* configurations about the gold adatom. This conjecture is partially borne out by the experimental STM images at relatively low 1,4-BDT coverages shown in Fig. 1(A). This reveals islands of chains that can be observed close to the center of the image. The herringbone reconstruction of the underlying Au(111) lattice can be observed at the left of this image indicating the 1,4-BDT molecules bind strongly to each other, as expected if they form one-dimensional Au-1,4-BDT chains. The left edge of the islands formed following 1,4-BDT adsorption align along the ridges in the herringbone reconstruction suggesting that the precursors to the formation of the putative oligomer chains adsorb preferentially in the grooves of the herringbone reconstruction as observed previously. This domain has been shown to be *fcc* in nature, and so this preferential growth might suggest enhanced stability of adatoms located on these sites.

Images obtained at 1,4-BDT coverages close to saturation are displayed in Fig. 2(A). Now the one-dimensional motifs are more clearly seen and the zig-zag structures proposed to derive from thiolates bonded to gold in a *trans* configuration is indicated, and bends in the chain resulting from the *cis* configuration is also shown. For clarity only one sulfhydryl group is shown in Fig. 2(C), but it should be noted that the other group (in the *para* position to the one shown) can bond *cis* or *trans*

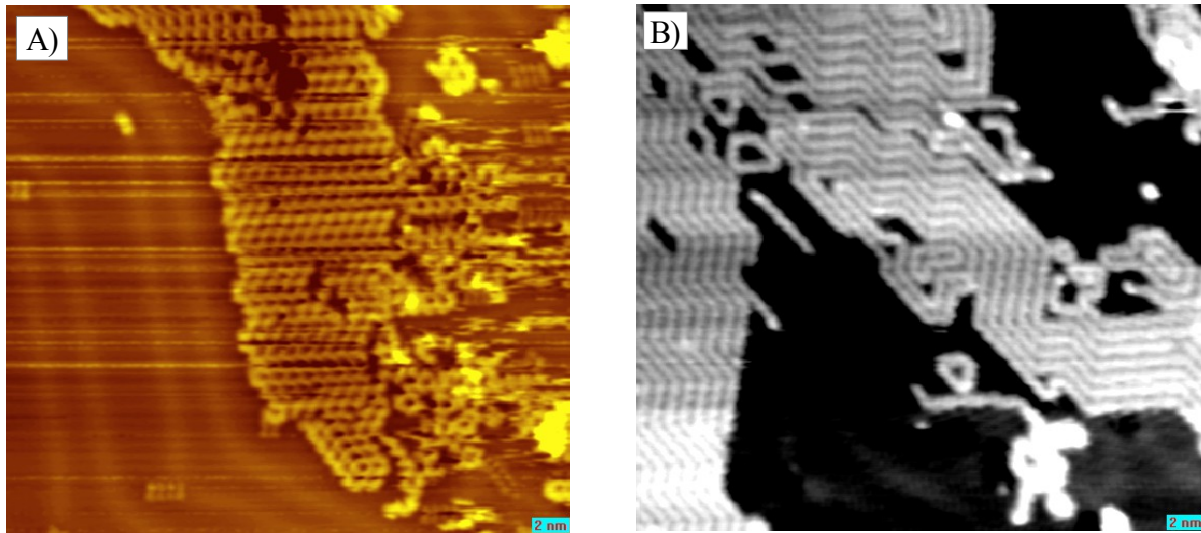


Figure 1: A) Intermediate coverage of 1,4-BDT on Au(111) at room temperature ($V = -0.5$ V, $I = 102$ pA) B) Intermediate coverage, 1,4-BDT dosed at room temperature, image acquired at ~ 110 K. ($V = -0.5$ V, $I = 112$ pA)

independently of the first. The chains show a clear tendency to grow parallel to each other. This presumably arises since the formation of one chain constrains the growth of subsequent chains since the chain structures clearly are not able to cross. Note that there are dark regions between the chains that will be discussed in greater detail below.

Figure 2B) displays an image of a saturated overlayer of 1,4-BDT on Au(111) under slightly different tunneling conditions that displays alternating bright and dark regions along the chain. This is emphasized by the line profile shown to the right of Fig. 2B) which clearly displays the high and low regions seen in the image. The repeat distance between the bright regions is ~ 680 pm. Imaging at a slightly different potential produced the image shown in Fig. 2(C), where circular regions separated by ~ 0.7 nm can be discerned. The diameter of these circular regions is ~ 0.45 nm, in good agreement with the diameter of images on benzene on Rh(111) [4]. The dark regions seen between the images in Fig. 2A) are shown more clearly in the wide-scan image in Fig. 4 for a saturated layer on 1,4-BDT on Au(111). This shows the one-dimensional structures seen in previous images and highlights the formation of dark patches between these structures. A profile across one of these dark regions is shown below the image suggesting that they are ~ 1 Å deep in the image. These features are presumably *etch*

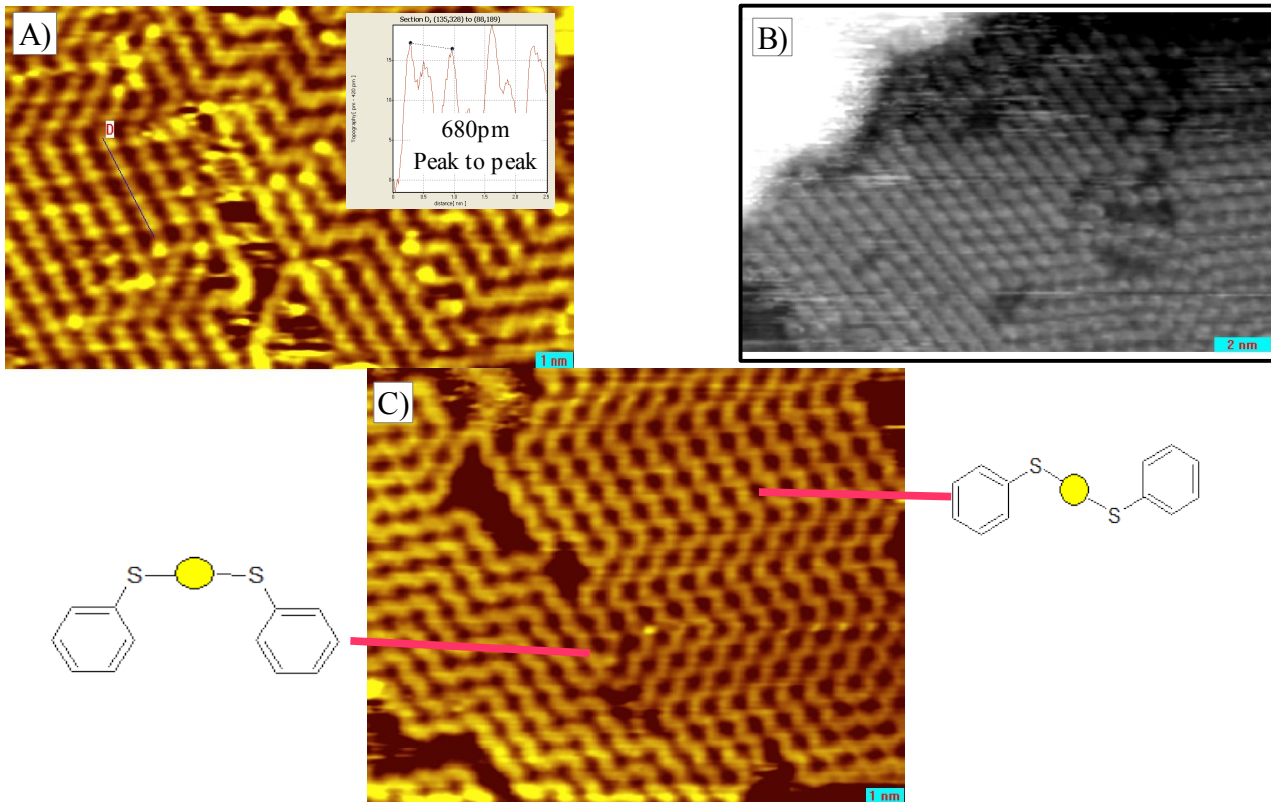


Figure 2: A) Line profile of 1,4-BDT chains shows pronounced bright/dim structure and differences in apparent height. This appears to be a direct observation of gold adatoms between 1,4-BDT phenyl rings. ($V = -0.4\text{V}$ $I = 96\text{pA}$) B) Higher resolution image showing lateral packing and resolution of the phenyl rings themselves. C) Illustrates straight segments of “all-*trans*” S-Au-S “zig-zag” bonding, and 120° *cis*-bends (the second S- on the ring omitted for clarity). *pits* generated by 1,4-BDT and are the most likely source for the Au adatoms found in the oligomers.

Time resolved images for 1,4-PDI oligomers on Au(111) indicated that these chains are quite mobile at room temperature [1, 11] and were shown to rapidly make and break connections between nanoparticles on a Au(111) surface. Careful analysis of ~several sets of sequential STM images of 1,4-BDT indicate that the oligomeric units, once formed, are rigidly locked in place. In fact, in none of the images was any evidence for mobility observed. R-NC-Au-CN-R involves exclusively the sigma-donation of electrons from the terminal carbon of the isocyanide into the gold orbitals of appropriate symmetry. Very little direct interaction between the isocyanide and substrate would be expected. In contrast, a currently widely accepted model for adatom templated thiolate bonding has the thiolate occupying an $\text{Au}_{\text{adatom}}\text{-Au}_{\text{atop}}$ site as in Figure 5. This direct interaction with the substrate would

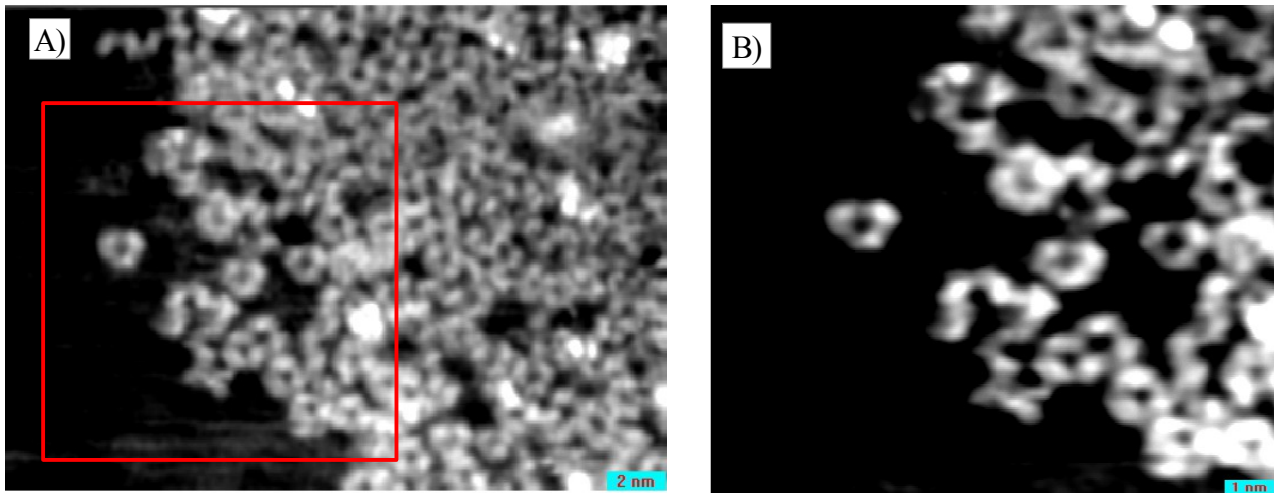


Figure 3: STM images of 1,4-BDT adsorbed on Au(111) at a temperature of $\sim 110\text{K}$. The crystal was warmed briefly to $\sim 250\text{K}$, and cooled back to 110K for imaging. B) was cropped from A) (indicated in red). The structures show three bright lobes and appear to be a 1,4-BDT trimer. ($V = -0.5\text{V}$, $I = 114\text{pA}$)

presumably serve to immobilize the oligomers once formed.

Figure 3 shows an STM image of 1,4-BDT dosed onto Au(111) at a temperature of $\sim 110\text{K}$, flashed briefly to $\sim 250\text{K}$, and cooled back to 110K for imaging. The surface shows a large number of hexagonal features (with three long sides and three short sides), with the short sides imaging as bright lobes. The length of the long sides is $\sim 1.45\text{nm}$ and the structures are presumably 1,4-BDT trimers. Examination of the trimers, and the segment of the chain-like structure (center, Fig. 3B) does not show signs of adatom templated growth. For thiophenol, deprotonation / adatom sequestration was shown to occur at a temperature of $\sim 15\text{K}$, [8] so a temperature of 250K should be ample to drive this (weakly activated) process. The formation of the trimers and the lack of order in the broken chain structure indicate that either the temperature (250K) was not high enough, or was not sustained long enough to facilitate the formation of well ordered $-(\text{Au-BDT})_n-$ oligomers.

Electrical Studies:

It has been shown previously that the $-(\text{Au-PDI})_n-$ oligomer chains for on Au(111) surface are capable of bridging between gold nanoparticles deposited onto a mica surface. In this case, it was proposed that the PDI molecules were able to extract gold atoms from low-coordination sites on the

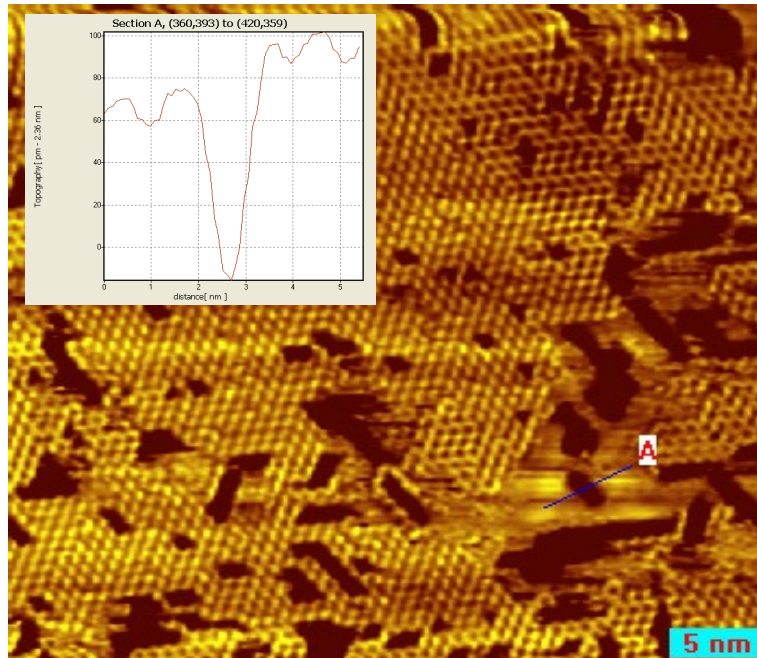


Figure 4: Wide area STM image of 1,4-BDT on Au(111) (room temperature) . Dark regions between chains image at $\sim 1 \text{ \AA}$ deep (inset) and are presumably one source for the gold adatoms required for oligomer growth, with step edges being the other. ($V = -0.5\text{V}$, $I = 142\text{pA}$)

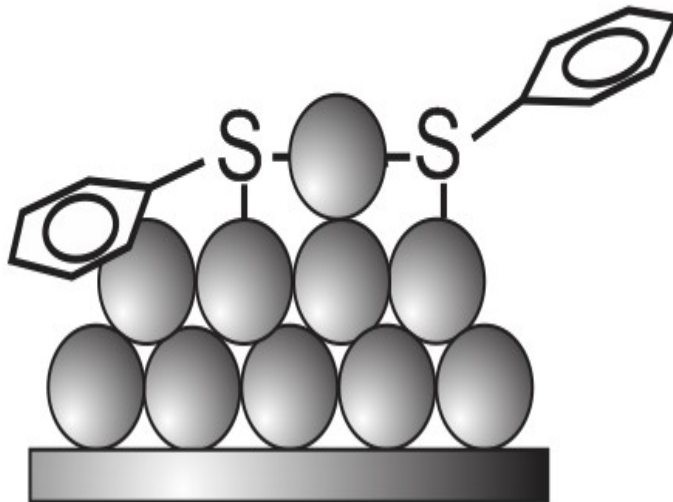


Figure 5: A reasonable model for a gold-dithiol unit. In this model the sulfur occupies a $\text{Au}_{\text{adatom}}\text{-Au}_{\text{atop}}$ bridge site. The direct interaction with the substrate might explain the total lack of mobility observed for Au/1,4-BDT oligomers. This type of bonding is in contrast to the so called “standard model” where the sulfur occupies a bridge or hollow site on the surface. [7].

Electrical Studies:

It has been shown previously that the $-(\text{Au-PDI})_n-$ oligomer chains for on Au(111) surface are capable of bridging between gold nanoparticles deposited onto a mica surface. In this case, it was

proposed that the PDI molecules were able to extract gold atoms from low-coordination sites on the gold nanoclusters and propagate to form one-dimensional oligomeric chains that were capable of forming molecular electronic linkages between the nanoparticles. The observation of a similar effect when dosing a gold-nanoparticle covered mica surface with 1,4-BDT would provide corroborative evidence for the formation of similar one-dimensional chains as found for PDI. Note that the STM images presented above indicate that one-dimensional chains do form from 1,4-BDT on Au(111).

The temperature variation in conductivity for gold-nanoparticle covered mica samples with varying initial gold loading, indicated by changes in $\ln(R_0)$, are shown in Fig. 6. In this case, the temperature variations are plotted as $\ln(R)$ vs. $T^{1/2}$ rather than an Arrhenius form (where they would vary as T^{-1}) since the resulting plots were linear, while the Arrhenius forms were curved. Similar behavior has been found for PDI-linked gold nanoparticles (Chapter 5) and provides corroborative evidence that 1,4-BDT

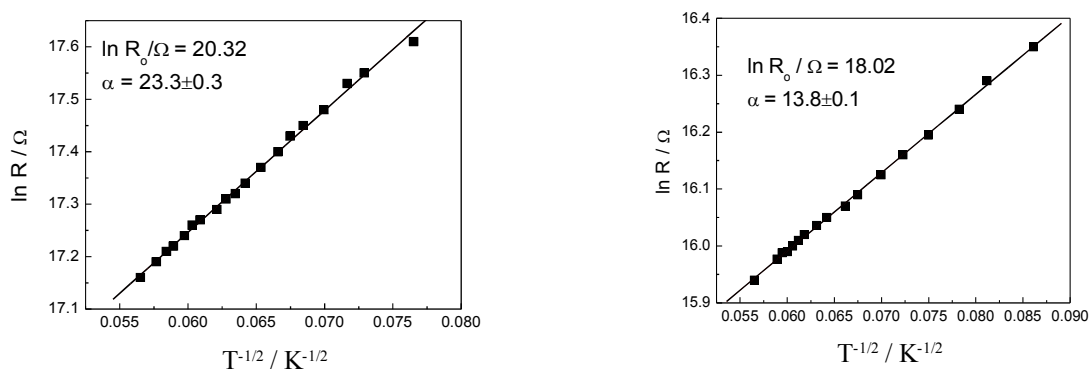


Figure 6: As was the case for 1,4-PDI on granular gold (Chapter 5), 1,4-BDT on similarly prepared films shows a linear $\ln(R)$ vs. $T^{1/2}$ dependence, a behavior which is predicted by the model of Abeles and Sheng. R_0 sheet resistance of the film prior to dosing, and scales with gold coverage. The slope the plot (α) provides insights into the height of the tunneling barrier between the particles.

forms similar oligomeric linkages. It has been shown previously that this behavior can be adequately reproduced by the Abeles model for thermally assisted tunneling through an array of nanoparticles. The salient point is demonstrated in Figure 7, where the value of α (derived from the $\ln(R)$ vs. $T^{1/2}$ plots) is shown to vary linearly with $\ln(R_0)$. This provides, in light of Abeles theory, strong

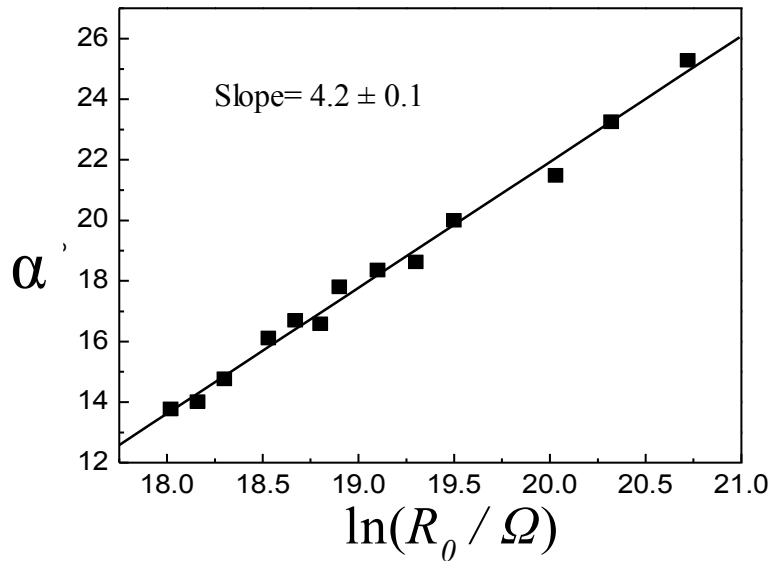


Figure 7: Indicative of the formation of Au-BDT oligomers between nanoparticles, the values of α scale linearly with $\ln(R_0)$. The slope of the plot for 1,4-BDT is 4.2 ± 0.1 vs. 3.7 ± 0.2 as was found for the 1,4-PDI system.

corroborative evidence for the formation of oligomeric bridges between particles as was demonstrated in Chapter 5 for the $-(\text{Au}-\text{PDI})_n-$ system on similarly prepared mica substrates [5,12,13].

Finally, for none of the samples studied did the temperature dependence of resistance on temperature change sign (i.e., for every sample resistance *increased* with *decreasing* temperature). A sign change might suggest that the enhancements in conductivity are a result of morphological changes in the nanoparticles themselves.

Discussion:

The surface chemistry of 1,4-BDT on Au(111) was investigated via STM and RAIRS. The molecule was conclusively shown to self-assemble long, oligomeric units at room temperature. Consistent with recent STM measurements of thiophenol, STM data for 1,4-BDT has demonstrated quite clearly that the assembly of these units is adatom templated. This type coordination motif can be formally described in terms of linear RS-Au(I)-SR subunits described in Chapter 2. The individual gold-dithiol bonds are strikingly similar to the recent report on thiophenol. The obvious difference in 1,4-BDT is that the *para*-substitution of two sulfhydryl groups allows for oligomerization and growth of linear chains, rather than the dimeric species observed in monothiols.

1,4-BDT has been the archetypal *molecular wire* since the very beginning of the field and as such it

has been subjected to a wide range of elegant electrical measurements. Many of these experiments were based on the mechanically controlled break junction (MCBJ) technique where a thin gold wire is carefully stretched to its breaking point leaving a pair of very sharp electrodes in opposition and between which a small number of molecules are installed. The gold point-contacts are then moved in and out of contact and conductance histograms collected, some of which corresponding to the conductance of single molecules. The findings presented in this chapter suggest that, at least on Au(111) surfaces in UHV, adatom mediated molecular wires form. It seems one source of considerable confusion when measuring the the conductance through thiolate molecules is that, while the most stable bonding between the thiolate and gold is *via* a gold adatom, it *can* occupy a hollow site directly on the surface. The quantum conductance between the adatom and the 3-fold hollow bonding differ by approximately 2 orders of magnitude (with the adatom bonding providing a much better quantum point contact). The situation is complicated further as the molecule is anchored to two electrodes which can bond in either configuration (giving rise to three possible states). The modulation of the tunneling barrier described in the electrical measurements presumably does not suffer from this issue as the molecules are not placed under tension to perform the measurement, and the overall bonding is dominated by S-Au-S, adatom templated species (although the “connection” to the nanoparticles themselves could potentially be different).

Our finding that 1,4-BDT self-assembles long oligomers combined with the already amply demonstrated conductivity of the molecule led to the final research presented in this chapter. Utilizing very similar methodology as presented in Chapter 5, a series of granular gold films were prepared on mica substrates and much like in the case of 1,4-PDI, 1,4-BDT produced profound reductions in sheet resistance across the films. It was our hypothesis that the dramatic enhancement in conductivity was a consequence of the gold nanoparticles becoming bridged by the (presumably) highly conductive Au-BDT molecular wires rather than a morphological change in the particles themselves. Indeed, fits of $\ln(R)$ vs. $T^{-1/2}$ showed the linear response predicted by the Abeles model for activated tunneling in granular materials.

Conclusions:

In this chapter the self assembly of 1,4-benzenedithiol oligomers on Au(111) was investigated.

While the conductivity of this molecule has been studied exhaustively both experimentally and computationally, these studies focused exclusively on the properties of *single molecules*. We report here the finding that 1,4-BDT shows a strong propensity for the generation of extended chains on Au(111). Our model for the generation of these structures is in excellent agreement with recent STM studies on thiophenol, specifically that the units are held together through adatom templated dithiol moieties of the form RS-Au(I)-SR as described in Chapter 2. In contrast to that research, we have selected a para-substituted dithiol which opened up the obvious possibility of forming extended chains. The conductivity of single 1,4-BDT molecules was already well established in the literature. By extending the granular thin-film methodology laid out for 1,4-PDI we have provided compelling evidence for the self-assembly of highly conductive 1,4-BDT/Au oligomers effectively bridging the gap between the nanoparticles making up the film.

Additionally, thiolates are a synthetically accessible class of molecules. With appropriate functionalization, one should be able to significantly shift the energies of the HOMO and LUMO orbitals, for example. Also, as the STM demonstrated a high degree of lateral packing between adjacent chains—and this might cause technical problems (i.e., electrons “hopping” between chains), it might become necessary to functionalize the ring with sterically bulky groups to prevent significant coupling between them. This should diminish conduction perpendicular to the chains without compromising that axial conduction. In fact, alkylating the ring might improve conductivity as a result of electron induction, as has been demonstrated for 1,4-tetramethyl diisocyanide [14].

References

- 1) Boscoboinik, J.; Kestell, J.; Garvey, M.; Weinert, M.; Tysoe, W. *Top. Catal.* **2011**, *54*, 20.
- 2) Boscoboinik, J. A.; Calaza, F. C.; Habeeb, Z.; Bennett, D. W.; Stacchiola, D. J.; Purino, M. A.; Tysoe, W. T. *Physical Chemistry Chemical Physics* **2010**, *12*, 11624.
- 3) Zhou, J.; Acharya, D.; Camillone, N.; Sutter, P.; White, M. G. *The Journal of Physical Chemistry C* **2011**, *115*, 21151.
- 4) Yoon, H. A.; Salmeron, M.; Somorjai, G. A. *Surf. Sci.* **1997**, *373*, 300.
- 5) Abeles, B.; Sheng, P.; Coutts, M. D.; Arie, Y. *Advances in Physics* **1975**, *24*, 407.
- 6) Maksymovych, P.; Yates, J.; *JACS*, **2008**, *130*, (24), 7518-9.
- 7) Häkkinen, H.; *Nature Chemistry*, **2008**, *4*, 443-55.
- 8) Bruot, C.; Hihath, J.; Tao, N.; *Nature Nanotechnology*, **2011**, *7*, 35-40.
- 9) Fujii, S.; Akiba, U.; Masamichi, F.; *Chemistry Letters*, **2008**, *4*, 408-9.
- 10) Li, C.; Pobelov, I.; Wandlowski, T.; Bagrets, A.; Arnold, A.; Evers, F.; *JACS*, **2008**, *130*, 318-26.

- 11) Boscoboinik, J.A.; **2010**, Ph.D. dissertation, University of Wisconsin-Milwaukee
- 12) Sheng, P.; Abeles, B.; Arie, Y.; *Phys. Rev. Lett.* **1973**, *31*, 44-7.
- 13) Kestell, J.; Abuflaha, R.; Boscoboinik, J.; Bai, Y.; Bennett, D.; Tysoe, W.T.; *Chem. Comm.* **2012**, *49*, 1422-4.
- 14) Habib, Z.; **2010**, Ph.D. dissertation, University of Wisconsin-Milwaukee

Chapter 9

The Surface Chemistry of 1,3-Benzene Dithiol on Au(111)

Introduction:

In the previous chapters and also in Chapter 10, a series of bi or tri-functional isocyanides and thiols were dosed onto Au(111) and the resulting surfaces were interrogated *via* STM, RAIRS, DFT and electrical conductivity measurements. In each case, long, oligomeric species were found to self-assemble, and in the case of 1,4-PDI and 1,4-BDT, pronounced enhancement of sheet conductivity in granular gold films was observed when the films were exposed to these molecules. In each case, STM data of sufficient resolution was acquired to directly observe a key feature of these systems—that the oligomers are adatom templated, of the form RS-Au-SR or -NC-Au-CN- (for 1,4-BDT, and the isocyanides respectively). Adatom bonding of thiolates on gold appears to be a general phenomenon.

In an effort to investigate benzene dithiol chemistry on gold, 1,3-benzene dithiol was interrogated similarly to the previous molecules. Interestingly, this molecule was among those reported fraudulently by Schön, et. al. [1]. However, in the initial report contesting the original publication, 1,3-benzene dithiol (1,3-BDT) was found to have a legitimate *gate effect*, although only 3 out of 256 samples exhibited this behavior [2].

The findings reported in this chapter strongly suggest that 1,3-BDT does indeed participate in gold adatom bonding. However, in stark contrast to the rest of the molecules in this volume, 1,3-BDT molecules were exclusively observed as monomeric species, as imaged by STM, regardless of coverage. Attempts to image gold adatoms directly were unsuccessful. However, time resolved STM

studies indicate that at room temperature the monomers are fairly mobile. While it is thermodynamically feasible, as demonstrated by DFT calculations found later in this chapter, for a thiolate to occupy a bridge or 3-fold hollow site on the surface, one would expect species coordinated in this fashion to be quite immobile [3]. The other alternative—a thiolate on Au_{adatom} motif, would presumably offer significant mobility. The mobility of thiol-adatom complexes is largely supported by the formation of the oligomeric species self-assembled with 1,4-BDT, if one considers that the long chains are assembled unit by unit (“clicking” into place). Very frequently the chains were observed to be a considerable distance from signs of adatom sequestration. The most likely scenario is that they arrived *via* surface diffusion of a precursor adatom complex. The mobility of adatom thiolate species on surfaces is one that seems general and has been borne out for a range of molecules. It has been implicated, for example, in the ordering of thiolate SAMs on Au(111).

In this section, DFT data will be presented that demonstrates that while 1,3-BDT is thermodynamically stable bonded directly to the surface of Au(111) (on two surface atop sites), it is in fact more stable in a di-adatom configuration by ~ 100 kJ / mol (-342 and -444 kJ / mol respectively). RAIRS data will be examined that is consistent with the formation of a self-limiting monolayer at room temperature. The data also suggests that 1,3-BDT exists on the surface with the phenyl ring parallel with the surface. Finally, the most compelling evidence for 1,3-BDT surface monomer species can be found in the evaluation of high-resolution STM images which clearly resolve the “pore” in the phenyl rings, a result that strongly implies that the rings are parallel with the surface. Even at high coverages, no evidence for dimer or oligomer growth was observed—a finding that will be addressed at length.

Results:

DFT calculations were carried out for various 1,3-BDT species on a Au(111) slab, as diagrammed in Figure 1. First, an η^1 , upright species was calculated, with the thiolate coordinating a gold adatom, and

the adatom occupying a 3-fold site on the surface (with the thiolate in the 3-position uncoordinated). An adsorption energy of -180 kJ/mol was calculated, which became more favorable by 25 kJ/mol upon applying van der Waals corrections to the system (-205 kJ/mol). The calculated structure is interesting in that a similar coordination motif was calculated for 1,4-PDI in its “Au_{adatom}” pendant (upright) state. However, a -NC group is formally triply bonded and it is not surprising that the molecule would adopt a geometry that is rigidly perpendicular to the surface. In the case of the η^1 thiolate complex, the bonding is formally sp^3 in character, and this is reflected in the Au_{adatom}-S-phenyl ring bond angle. It is interesting in that the calculate structure indicates that the most stable state is found when the ring is just a few degrees from perpendicular to the surface, as is the -SH group in the #3 position.

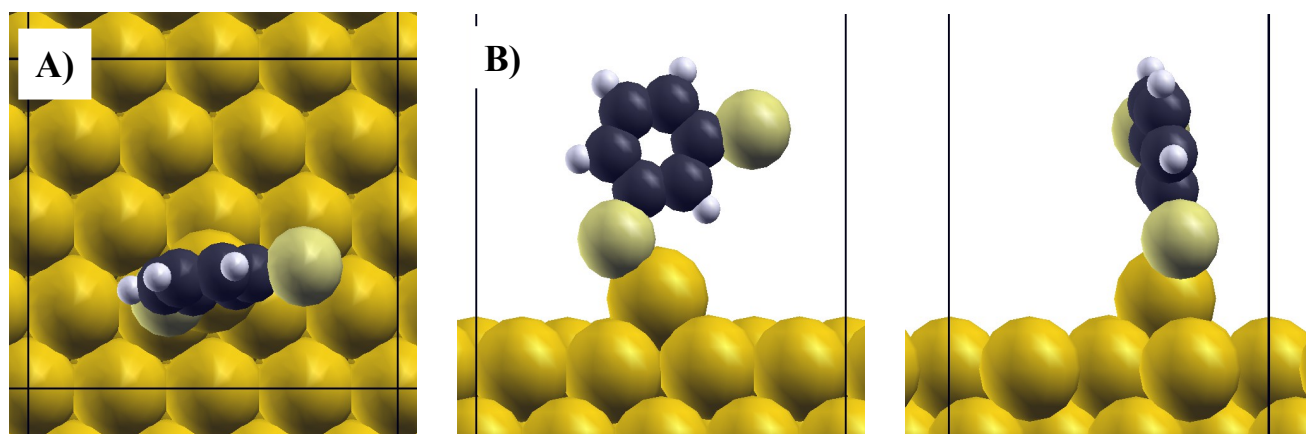


Figure 1: A) top view of η^1 adatom complex of 1,3-benzene dithiol (1,3-BDT) without consideration for van der Waals forces. $E_{\text{ads}} = -180$ kJ/mol. B) When van der Waals forces are considered, $E_{\text{ads}} = -205$ kJ/mol. This η^1 state was not observed experimentally, but may represent a short-lived precursor state in the formation of the monomeric 1,3-BDT species imaged *via* STM studies.

As was briefly mentioned, DFT calculations were carried out predominately because attempts at directly imaging Au_{adatoms} *via* STM proved unsuccessful. However, the mobility of 1,3-BDT molecules on Au(111) combined with evidence for a large number of *etch pits* (as imaged in STM, data to follow) suggest that indeed, adatom mediated bonding of the species on gold is the most likely state of these

molecules. To further investigate this, three coordination motifs were computationally investigated and the results summarized in Figure 2. First, an η^2 1,3-BDT surface complex was calculated with the thiolates occupying surface atoms in “atop” configurations. Secondly, an η^2 1,3-BDT surface complex was calculated where the thiolates occupied surface hollow sites. Thirdly, the 1,3-BDT “di-adatom”

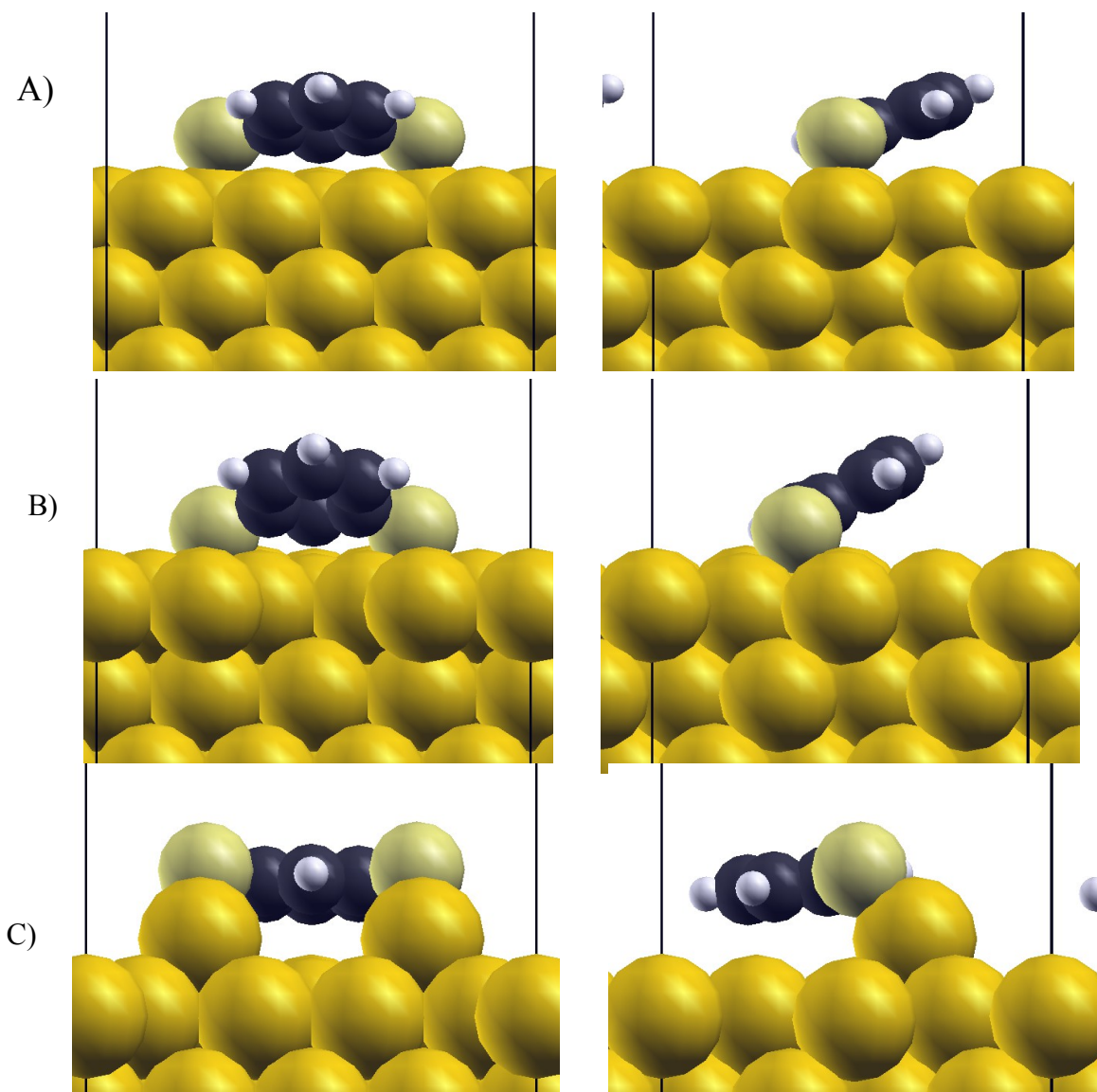


Figure 2: Structures of three η^2 1,3-BDT monomers on Au(111), corrected for van der Waals forces. A) is a “di-atop” complex with a calculated heat of adsorption of $E_{\text{ads}} = -342$ kJ/mol. B) is a “di-bridge” complex, with a heat of adsorption of $E_{\text{ads}} = -351$ kJ/mol. C) is a “di-adatom” complex with a heat of adsorption of $E_{\text{ads}} = -444$ kJ/mol. While bonding directly to the surface is stable, the di-adatom complex is more stable by ~ 100 kJ/mol.

complex was calculated. Interestingly, all three structures showed a substantial heat of adsorption. However, when comparing these structures to the η^1 complex in Figure 1, it must be remembered that the energies for the complexes in Figure 2 are largely accounted for by coordinating *two* functional groups, rather than one as was the case in Figure 1. It is also interesting to note that for the di-atom and di-bridge structures (Figure 2, A) and B)), the phenyl ring of 1,3-BDT resides at a considerable angle with respect to the surface ($\sim 30^\circ$), for the di-atom complex the ring is largely parallel with, and substantially away from the surface.

STM data was collected for 1,3-BDT at various exposures and temperatures. The most striking feature is that unlike 1,4-BDT, 1,3-BDT does not show any evidence for the creation of oligomers, or even dimers on the surface.

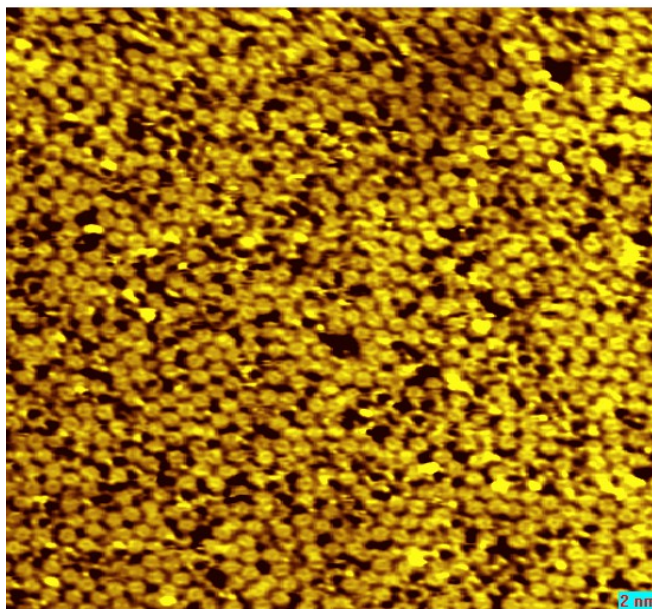


Figure 3: Saturation dose of 1,3-BDT on Au(111). The crystal was dosed and imaged at room temperature. No sign of ordered structures were observed under these conditions. Another striking feature is that the phenyl rings are clearly resolved including the central “pore” in the ring.

Figure 3 shows an STM image collected after a 20s exposure to 1,3-BDT (source at 0°C). The surface is clearly saturated but does not show any indication that oligomeric species exist. Figure 4 A) shows an incompletely annealed (clean) Au(111) crystal. In this image, clearly rows of atoms are

missing from the lattice. The image was included for comparison with Figure 4 B) which is a properly annealed and reconstructed Au(111) crystal which has been exposed to a 3 second (0°C) 1,3-BDT dose. The features imaging as black stripes and spots on the surface are measured to be on the order of 35 pm deep. This is significantly less than the 270 pm which might be expected (the *empirical radius* of gold is 135 pm [4]). However, even an excellent STM tip might have a radius of curvature of ~ 15 nm, so this under-estimate of the depth of the features is not inconsistent.

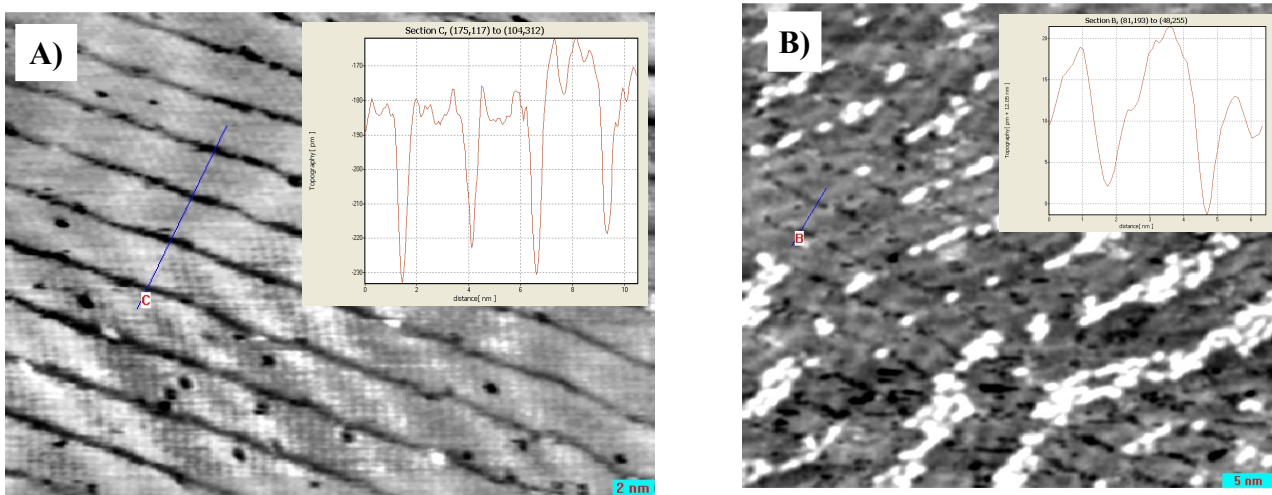


Figure 4: A) A clean but incompletely reconstructed Au(111) crystal. “Missing rows” of gold atoms, and black spots (missing surface atoms) image at ~ 50 pm deep. B) Properly annealed Au(111) crystal exposed to 3s 1,3-BDT dose. Adsorbates image as white features while black features suggest that significant *etch pitting* has occurred.

An interesting feature of the 1,3-BDT system on Au(111), as shown in Figure 4B), is that the molecules appear constrained in the space between the solitons in the herringbone reconstruction. Figure 5 shows a low-coverage image taken at $\sim 110\text{K}$ (dosed at room temperature). The image shows the formation of what appears to be a “missing row” reconstruction or super-lattice, and step edge decoration. The origin of the reconstruction is unknown, but the image has resolved what appear to be individual gold adatoms between the structures which might speak to the rate at which gold adatoms are sequestered from the surface atoms.

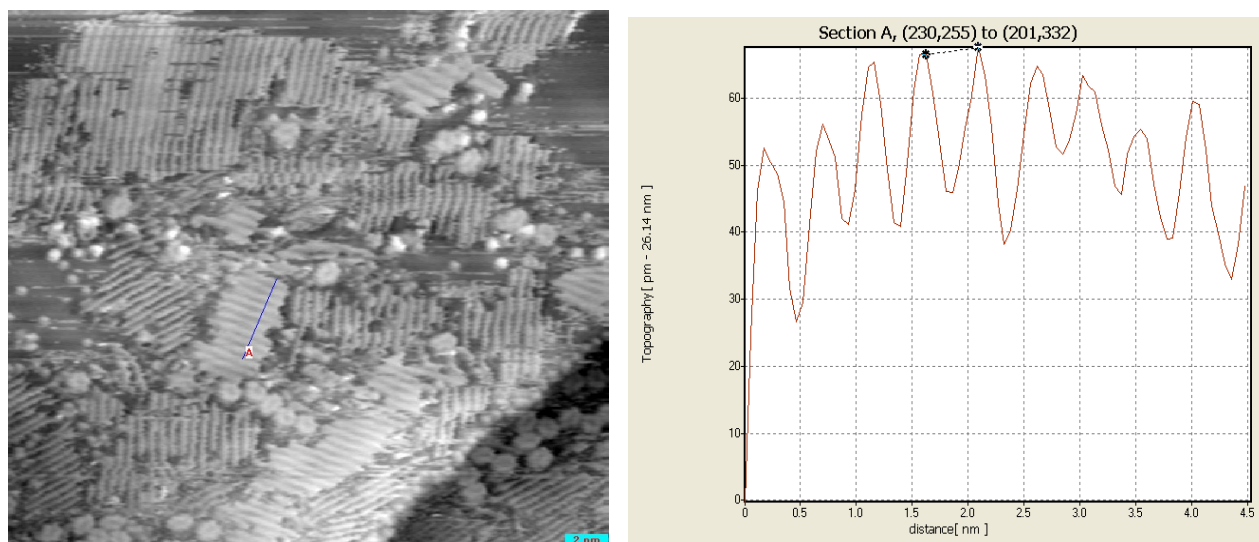


Figure 5: High resolution STM image of step edge and terraces. Clearly resolved are hexagonal phenyl ring (lower terrace especially clear) and an interesting super-lattice structure. The structure appears to be a “missing row” reconstruction. The origins of this structure are unknown, but was observed reproducibly with 1,3-BDT on Au(111)

Conclusions:

In this chapter the surface chemistry of 1,3-benzene dithiol on Au(111) was explored. In stark contrast to 1,4-BDT (or the isocyanide systems), monomeric species were observed exclusively, although the molecule appears to undergo the general phenomenon of deprotonation/adatom sequestration which is observed commonly in aromatic and alkyl thiols [5]. STM images acquired at low and intermediate coverages show evidence of extensive abstraction of gold atoms from the (previously atomically flat) terraces. Interestingly, large, extended etch pits are not observed—rather the abstraction seems to largely be *single* gold atoms being removed from the bulk. In an effort to understand why 1,3-BDT is found as a monomeric entity (exclusively), the following mechanism will be proposed. In the case of 1,4-BDT, it is likely that the precursor moiety is an η^1 adatom complex (i.e., one sulfydryl bonded to a gold adatom, one not coordinated). This entity would need to be long-lived enough to oligomerize, perhaps in a manner analogous to that described for 1,4-PDI. Likely due to steric constraints placed on system by the *meta* substitution of 1,3-BDT, the kinetics of the adatom

sequestration could be quite different. If, for example, the molecule impinges on the surface, it is unlikely that *both* -SH groups would deprotonate and sequester adatoms simultaneously. However, it is not unlikely that the formation of the di-adatom complex could happen in two rapid steps. The formation of the first R-S-Au_{adatom} group would anchor the molecule in place, and with just minor rocking and twisting about the S-phenyl ring bond, the second -SH group would be in proper orientation (i.e. impinging on the surface) to deprotonate and abstract a gold atom. It is possible that the di-adatom complex is not particularly stable, but that it is formed with such rapidity that the S-Au-S moiety does not have time to form. Generating a dimer or oligomer from the di-adatom 1,3-BDT species would require -S-Au_{adatom} bond scission at some stage. Gold-thiol bonds are tenacious and have an energy on the order of 100 kJ/mol. Thus dimers or oligomers would not be observed, even if the resultant S-Au-S bonding were more stable. If *all* of the thiolates on the surface were coordinated to adatoms, the system would be trapped in this state as the barrier to forming an S-Au-S *via* S-Au bond scission is too great—an example for *kinetic trapping* of the 1,3-BDT monomer species.

The observed diffusional anisotropy of the di-adatom monomers (their “confinement” to the spaces between the soliton walls of the Au(111) reconstruction [6,7]) can perhaps be understood in terms of site-determination of adatoms on single crystal surfaces. Recall from Chapter 2 that the herringbone reconstruction of Au(111) is a result of uniaxial tensile forces acting on the surface. By undergoing a slight contraction along the close-packed direction, the surface is able to contain ~4% more gold atoms than would be possible in the un-reconstructed surface. A consequence is that on Au(111), two sites are available to receive the adatom. *Fcc* sites are present in the domains between the soliton walls (where the dithiol monomers are constrained), while *hcp* sites are found on top of the solitons themselves. The two domains are separated by a stacking fault (the actual solitons, which image taller than the surrounding surface). Determination *fcc/hcp* site preferences is a difficult task, and at this writing only

two studies have been published [9]. For Pt_{adatom} / Pt(111) a clear *fcc* site preference was observed [10]. Theoretical studies on site preference for gold (and copper and silver) adatoms do not, in fact, indicate that such a preference exists at all [11]. Clearly, subtle contributions from both the electronic structure and the local relaxation have to be taken in to account. A recent account of adatom diffusion of Cu_{adatom} on Cu(111) (determined from counting “hopping frequency” from sequential STM images) indicated a diffusion barrier for an adatom $E_B = 37 \pm 5$ meV, and that the *hcp*→*fcc* hopping rate is ~75 times greater than the *fcc*→*hcp* hopping rate [hyldgaard phys rev b]. Taking experimental uncertainty into account, and assuming the frequency factor for the two processes is the same ($\nu_0 = 10^{12}$ s⁻¹), this places an upper bound of the Cu_{adatom} on *fcc* site being more stable, but only by ~8 meV.

The above discussion involved metal atoms on metal surfaces—a system which is significantly different from 1,3-BDT monomers on gold adatoms. First, in thiolate systems, the adatoms are coordinated to at least one sulfur. One would expect this to significantly alter the electronic structure of the adatom. This presumably enhances the mobility of the adatom on the surface. However, in the case of a di-adatom complex, as found in 1,3-BDT on Au(111), there is not one but two individual adatoms anchoring the molecule to the surface. If the molecule moves *via* concerted hopping of both adatoms simultaneously, assuming the two adatoms do not interact with each other, the overall hopping barrier would be twice that of individual RS-Au_{adatom} species. This would serve to lower the hopping frequency. The two effects should be somewhat compensatory. The series of images investigated for this discussion consisted of approximately 60 frames, with perhaps 100 molecules observed per frame. In only 2 of the images was a molecule observed to occupy an *hcp* site (i.e., trying to “hop over” the soliton wall). So, while the forces driving site selection are subtle, they are indeed significant enough that 1,3-BDT selects *fcc* sites, until surface crowding forces them to occupy the meta-stable *hcp* sites as

well. For a surface such as Au(111), which has two domains on which an adatom can reside (close, but different in energy), this represents a classic *double-potential well* problem. This behavior has been seen in (infunctionalized) aromatics on Au(111) [6,7,8].

Preliminary data (not shown) on granular gold films dosed with 1,3-BDT indicated that there is a measurable drop in sheet resistance, but to a far lesser degree than was observed for any of the other molecules. In fact the current work (STM studies in particular) was an attempt to understand why it performed so poorly as a molecular wire. To first order, the lack of oligomerization is clearly an issue. In the system presented here, through-bond tunneling of charge carriers would not be possible, and so conduction would proceed, presumably, through a *hopping* mechanism. Electrons, in a sense, jump from one π -system to the next. However, while 1,3-BDT has been demonstrated here to not oligomerize, it has indeed been installed in other electrode configurations and molecular conductance measurements performed. A deep seated assumption in the field of molecular electronics is that charge transport through organic (aromatic) molecular wires is dominated by the properties of the π -system. Indeed, theoretical studies on several systems indicate that the σ -framework may be neglected with little consequence [12,13]. Recent work, however, has indicated that in some cases quantum interference effects dominate transmission characteristics [14-17]. In particular, *para* (1,4) and *meta* (1,3)-substituted systems have been studied using both Hückel and DFT based methods, and the general conclusion is that (experimentally observed) low transmission through the 1,3-substituted system results from destructive quantum interference near the Fermi level. 1,4-substituted systems show relatively high transmission as a consequence of constructive interference through this same region.

To test the hypothesis that 1,3-BDT does not oligomerize under the conditions presented because of rapid sequestration of *both* adatoms (which effectively traps 1,3-BDT in the form of di-adatom monomeric species). It has already been demonstrated that sulfhydryl groups (R-SH) readily

deprotonate on gold and generate species of the form $\text{RS-Au}_{\text{adatom}}\text{-SR}$ or $\text{RS-Au}_{\text{adatom}}$. A lesser utilized reaction involves the generation of these adatom species from a thioether rather than the thiophenol. This being the case, it maybe be possible to induce oligomerization of 1,3-BDT by exposing the Au(111) surface not to the di-thiol, but to a thiophenol/thioether derivative. Potentially, this would allow for the rapid formation of the mobile, η^1 adatom templated moiety (Figure 8), which should be longer lived than 1,3-BDT, as the thioether functionality is less reactive. Figure 6 shows a methylthioether, but if the steric bulk (indicated by the concentric cones) proves insufficient to slow the reaction of the second sulfur, a larger group could be utilized.

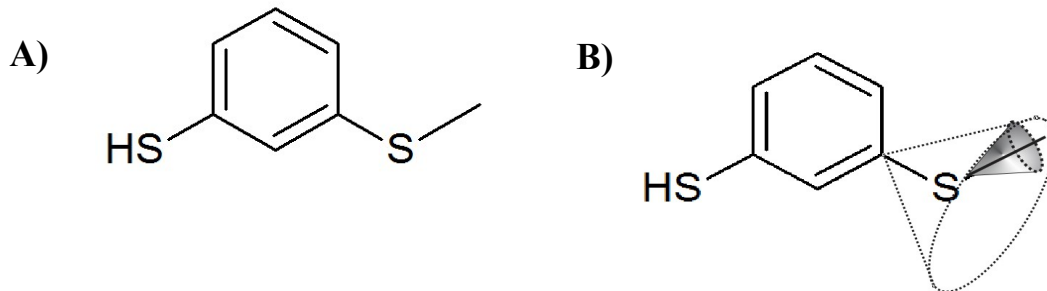


Figure 6: A) 3-sulphydrylphenyl-methylthioether B) The steric bulk (dotted cone) can be modulated by the identity of of the alkyl group (shaded cone), and this should tune the kinetics of dealkylation upon adsorption onto a metal surface. In theory, the sulphydryl group should react much more readily than the the thioether functionality.

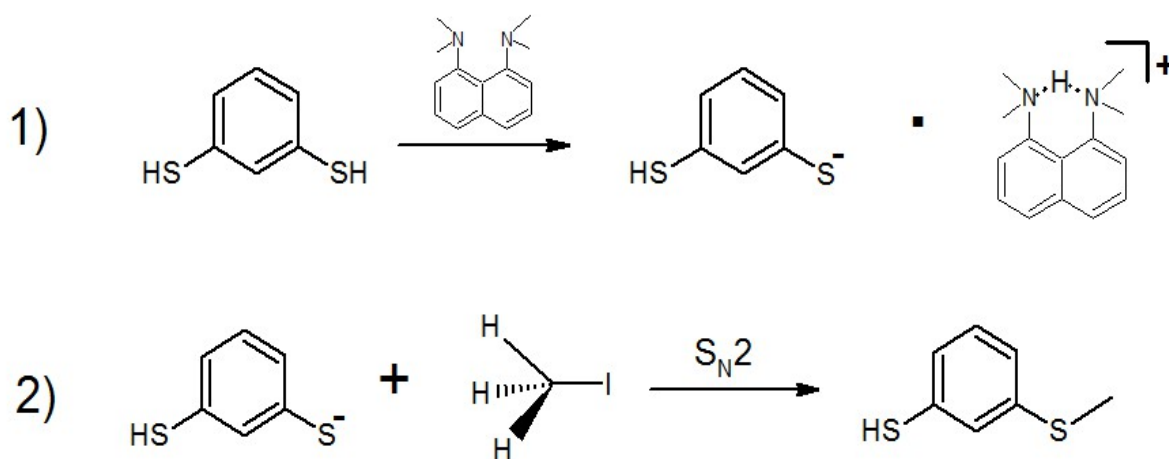


Figure 7: A proposed synthesis of 3-sulphydrylphenyl-methylthioether. In step 1, 1,3-BDT is deprotonated with 1 equivalent of Proton Sponge™ to generate the monothiolate. In step 2, the RS^- group is the nucleophile in an $\text{S}_{\text{N}}2$ reaction to generate the mono-thioether.

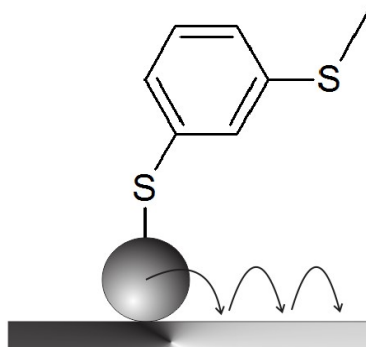


Figure 8: A postulated, mobile η^1 complex. Alkylating the second sulfur group (to generate a thioether) should significantly slow adatom sequestration for this group. For the methylthioether, methane should be produced *via* reductive elimination.

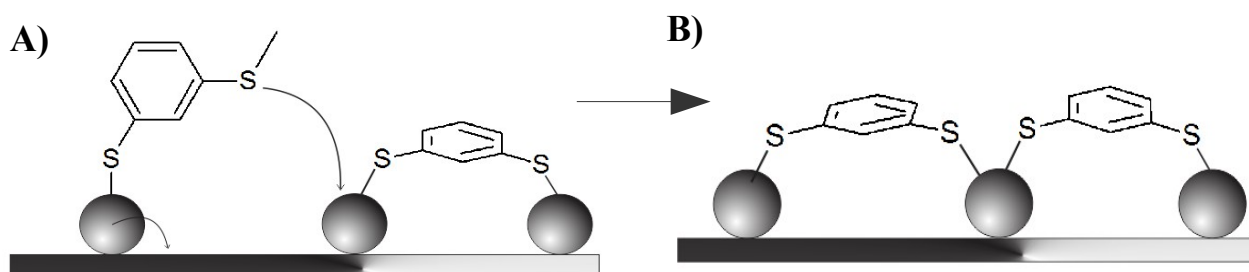


Figure 9: Proposed mechanism for growth of “zigzag chains” of the 1,3-dithiol. A) The mobile η^1 thioether diffuses into range of a (previously formed) di-adatom complex. B) The η^1 complex has simply to lean over and eliminate the alkyl group.

References:

- 1) Schön, J. H.; Meng, H.; Bao, Z. *Nature* (London). **2001**, *413*, 713.
- 2) Lee, J.; Lienstchnig, G.; Wiertz, F.; Janssen, R.; Egberink, R.; Reinhoudt, D.; Hadley, P.; Dekker, C.; *Nano Letters*. **2003**. (3). 2. 113-117.
- 3) Häkkinen, H.; *Nature Chemistry*, **2008**, *4*, 443-55.
- 4) http://en.wikipedia.org/wiki/Atomic_radii_of_the_elements_%28data_page%29
- 5) Maksymovych, P.; Yates, J.; *JACS*, **2008**, *130*, (24), 7518-9.
- 6) Sykes, C.; Mantooth, B.; Han, P.; Donhauser, Z.; Weiss, P.; *JACS*. **2005**, *127*, 7255-60.
- 7) Baber, A.; Jensen, S.; Sykes, C.; *JACS*, **2007**, *129*, 6368-69.
- 8) Carabineiro, S.; Nieuwenhuys, B.; *Gold Bulletin*, **2009**, *42*, (4), 288-301.
- 9) Repp, G.; Meyer, G.; Rieder, K.; Hyldgaard, P.; *Phys. Rev. B*. **2003**. Available at: <http://arxiv.org/pdf/cond-mat/0309288.pdf>
- 10) Wang, S.; Kurpick, G.; Ehrlich, G.; *Phys. Rev. Lett. B*, **1992**, *46*, 7121-6.
- 11) Kurpick, U.; *Phys. Rev. B*. **2001**, *63*, 45409-1 – 5.

- 12) Solomon, G.; Herrman, C.; Ratner, M.; *Topics in Current Chemistry*, **2012**, 313, 1-38.
- 13) Solomon, G.; Bergfield, J.; Stafford, M.; *Beilstein Journal of Nanotechnology*, **2011**, 2, 862-71.
- 14) Solomon, G.; Andrews, D.; Hansen, J.; Goldsmith, R.; Wasielewski, M.; van Duyne, R.; Ratner, M.; *J. Chem. Phys.* **2008**, 129, (5).
- 15) Walczak, K.; *Importance of quantum interference in molecular scale devices*. Available for download at: <http://arxiv.org/ftp/cond-mat/papers/0401/0401019.pdf>
- 16) Markussen, T.; Stadler, R., Thygesen, K.; *JACS*, **2010**, 10, (10) 4260-65.
- 17) Arroyo C.; Tarkuc, S.; Frisenda, R.; Seldenthuis, J.; Woerde, C.; Eelkema, R.; Grozema, F.; van der Zandt, H.; *Angewandte Chemie* **2013**, 52, 3152-55.

Chapter 10

Synthesis and Surface Characterization of 1,3,5-Phenylene Triisocyanide on Au(111)

Introduction:

STM interrogation of 1,4-PDI and 1,3-PDI on Au(111) led to the conclusion that two things direct the self assembly of the resultant nanostructures when these molecules are exposed to Au(111). First, NC-Au-CN bonding is observed almost always in a 180° coordination motif. The other important feature is the substitution pattern of the ring itself. A para-substituted diisocyanide forms linear chains, while a meta-substituted ring produces “zigzag” structures that turn at 120° . This is a trivial consequence geometry of the isocyanide groups with respect to each other (120° vs. 180° for 1,4-PDI). STM images of 1,3-PDI indicated that in some cases, the molecules form closed, hexagonal structures. This being the case, the hypothesis was put forth that 1,3,5-phenylene triisocyanide (with its 3-fold symmetry) should show a propensity to assemble a kind of honeycomb structure on Au(111). With three isocyanide functional groups oriented in a rigid 120° configuration, a 2-dimensional surface structure could be created, rather than the 1-dimensional $-(\text{Au}-\text{PDI})_n-$ linear oligomers described in Chapters 3-5.

The hexagonal self-assembly chemistry described in the following shows potential for generating highly ordered *nanopores* on Au(111) which could potentially be extended to template more complicated metal-organic framework (MOF) structures. With regards to the field of molecular electronics, two avenues for gating molecules have been employed. A typical method is to install the molecule on top of a dielectric grown on a conductor (i.e. SiO_2 on doped silicon). Another philosophy

involves covalently linking the gate to the molecule. While molecular level transistors can be synthesized, “but don't yet have a way to make the three-point connections to three electrodes on a nanoscale” [1]. 1,3,5-PTI might serve as a prototype 3-terminal molecule and a means of “wiring” functionalities into a nano-circuit as presumably the phenyl ring would provide a high degree of electronic coupling between isocyanide termini.

In this chapter, the synthesis of 1,3,5-phenylene triisocyanide (1,3,5-PTI) be described, along with STM and RAIRS characterization of this molecule upon adsorption onto Au(111). It will be shown that indeed, 1,3,5-PTI undergoes adatom templated self-assembly similar in many way to 1,4-PDI and 1,3-PDI systems already discussed. In fact, the 1,3,5-PTI hexagonal structures are very similar in morphology to the closed hexagonal structures occasionally found in the 1,3-PDI on Au(111) system described in Chapter 6.

Experimental:

STM and RAIRS studies were carried out as described in Chapter 2 and Appendix A. Reagents for the synthesis of 1,3,5-phenylene triisocyanide were purchased from Sigma-Aldrich and used as received. Standard inert atmosphere/Schlenk techniques were utilized.

Research on this molecule was hindered and complicated by stability problems. While the compound could be isolated, it proved to be rather unstable in it's dry, crystalline form even when stored under nitrogen in a freezer. To carry out STM and RAIRS studies, it was therefore necessary to prepare the compound immediately prior to use and carry out the final drying/degassing step on the Knudsen source installed on the chamber. The compound underwent decomposition upon room temperature storage for 2-3 days. Fortunately, the stability of the compound seems to be greatly enhanced upon adsorption onto Au(111) under UHV conditions. Surfaces thus prepared were analyzed over the course of days without noting decomposition as evidenced by STM.

Synthesis of 1,3,5-triisocyanobenzene from phloroglucinol

The other isocyanides discussed in this volume were prepared from the corresponding (commercially available) diamines. The two standard synthetic routes to isocyanides are the Hoffman carbylamine reaction (the “phase transfer reaction” [2]) and the Ugi method, where an amine is converted to a formamide which is then dehydrated with an equivalent of phosgene (or other agent) to yield the isocyanide [2,3]. Unfortunately, 1,3,5-benzenetriamine is not commercially available in gram quantities and is normally synthesized through the reduction of 1,3,5-trinitrobenzene (a high brisance explosive). The methodology described here relies on an alternative route to the formamide—the reduction of a readily synthesized trioxime. The synthetic methodology is summarized in Figure 1. All reagent were purchased from Sigma-Aldrich and used as received.

Step 1) The conversion of phloroglucinol to 1,3,5-cyclohexanone trioxime This reaction is based on the work of Baeyer who first determined that 1,3,5-benzenetriol exists predominately in it's *keto* tautomeric form, and that this triketone can be converted directly to the trioxime upon treatment with hydroxylamine hydrochloride and potassium carbonate [4].

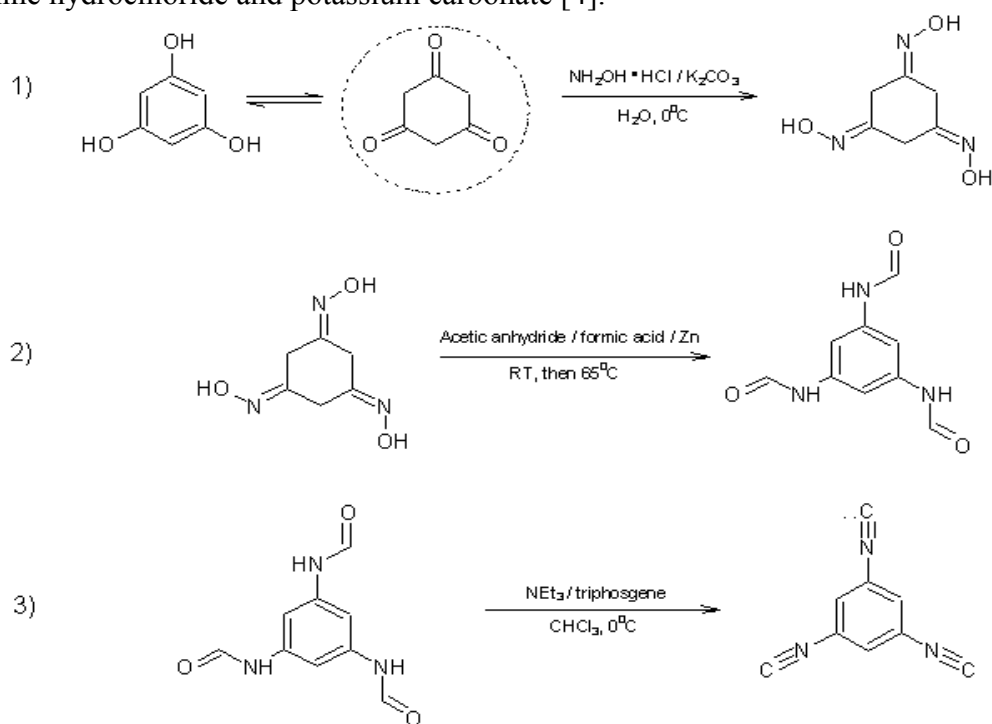


Figure 1: A 3-step route to 1,3,5-phenylenetriisocyanide

The original reference was used as reported (as translated by Prof. A. Arnold)[4]. To 1 part of phloroglucinol dihydrate (5 g) in 100 mL of deionized water was added 1.5 parts of hydroxylamine hydrochloride (7.5 g) followed by addition of 1.5 parts of (7.5g) of potassium carbonate in small portions with vigorous stirring. The pH of resultant solution was between 6 and 7. The solution was bubble degassed with nitrogen, capped with a septa, and stored at 0° C for 5-6 days. The slushy, partly frozen solution was thawed and filtered under vacuum to yield a cream/sand colored solid. This precipitate was rinsed with a small portion of ice cold water, a small portion of ice cold acetone, and a small portion of ether, then dried under vacuum for 2 days to yield 2.45g of a light tan solid. Another crop of product was collected upon placing the supernatant in the freezer for another 3 days. Similar treatment resulted in an additional 1.21g of a slightly darker colored solid, which darkened significantly upon storage in a freezer. The product was used without further purification or characterization.

Step 2) The conversion of 1,3,5-cyclohexanone trioxime to 1,3,5-trisformamidobenzene

This reaction was adapted from Arai, I. *et. al.* [2]. To a mixture of 0.56 g of phloroglucinol trioxime (0.005 mol) and 1.9 mL of acetic anhydride (0.03 mol) in 10 mL of 95% formic acid was added with stirring 1.65 g of zinc dust. The suspension was stirred vigorously under nitrogen. After 0.5 h another 1.65g of zinc dust was added and the reaction was heated to 60-70 °C (on a water bath) for an hour. This was followed by addition of next batch of (1.65 g) of zinc dust and mixture was stirred overnight at room temperature. The resulting brown solution was vacuum filtered through a Celite plug to remove excess zinc . Drop-wise addition of this solution to 25 ml of anhydrous ether (with vigorous stirring) afforded greyish-white precipitate. The precipitate was allowed to stir in anhydrous ether for 1-2 h, vacuum filtered through a glass frit, washed with ethanol and then with ether and dried in vacuo.

Step 3) Dehydration of 1,3,5-trisformamidobenzene to 1,3,5-phenylenetriisocyanide

The procedure was adapted from the “triphosgene method” of Wagner and Bennett [3,4]. To a

stirring mixture of 1,3,5-trisformamidobenzene (0.42 g) and triethylamine (3.3 mL) in 25 mL of anhydrous chloroform (on a salt/ice bath) was introduced 1.1836 g of triphosgene in 15ml dry chloroform via a pressure-equalizing addition funnel. The addition was carried out over the course of about 30 minutes. 2-3 drops at a time, after which the mixture was allowed to stir an additional 15 minutes. The mixture was brought to room temperature and stirred for 30 minutes, then brought to 40 °C and stirred another hour. The solvent was removed under vacuum. The solid obtained was dissolved in a minimum volume of dry toluene (5-10 mL). A small quantity of hexane was added to the toluene solution and the solution was bubble-degassed with nitrogen and placed in a freezer. After 24 hours a small quantity of yellowish-white solid was evident in the vial. The solvent was carefully decanted away and the crude 1,3,5-phenylenetriisocyanide dried in vacuo. The compound was characterized by electrospray mass spectrometry. FW=153.14. m/Z = 128.11, 102.12, and 76.13 corresponding to 1,3,5-PTI minus 1, 2, and 3 isocyno groups respectively.

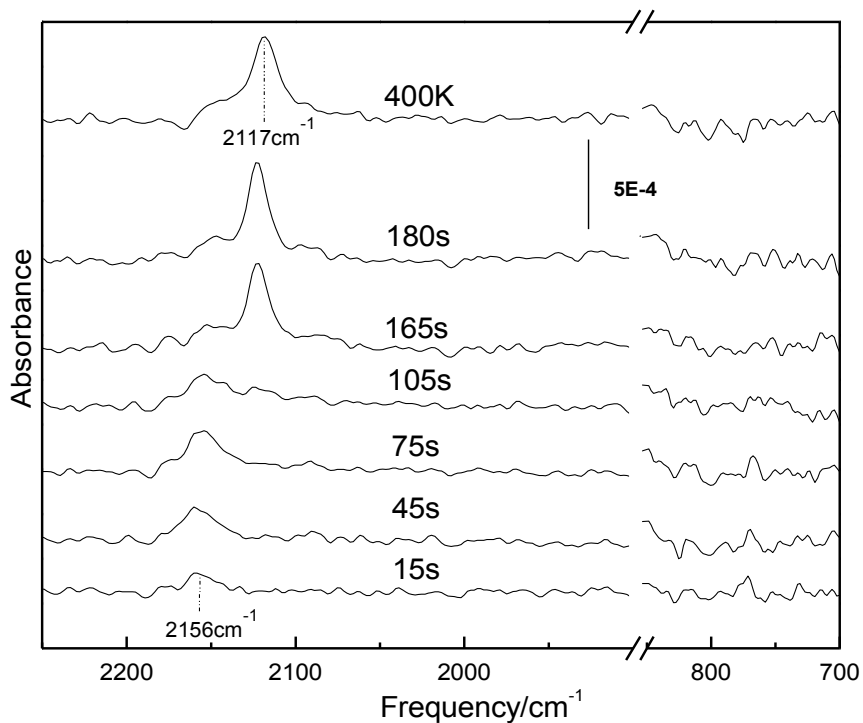


Figure 2: Room temperature 1,3,5-PTI uptake on Au(111). Note single peak corresponding to CN stretching mode. Also note red-shift in this frequency with increasing exposure.

Similar to 1,4-PDI (with a CN mode at 2136 cm^{-1}), 1,3,5-PTI shows a single peak that red-shifts from 2117 cm^{-1} to 2156 cm^{-1} with increased exposure. Presumably this is an effect of the isocyanide functional groups being somewhat coupled to each other *via* the gold adatom. Only one CN mode is observed which is consistent with the model presented below—that 1,3,5-PTI adopts a flat-lying η^3 orientation on Au(111) at all coverages.

Figure 3 shows an STM image of 1,3,5-PTI dosed onto room temperature Au(111). The image exhibits some scanning noise, but clearly shows a well defined, extended, hexagonal structure. The structure of the “honeycomb network” was elucidated through comparison with 1,4-PDI. Recall that the repeat distance of the gold adatoms (or phenyl rings) for the 1,4-PDI system was measured at 1.13 nm which is in excellent agreement with the calculated value of 1.14nm. For the 1,3,5-PTI system, the vertex to vertex spacing (averaged over 8 measurements) was found to be 1.17nm. Figure 4 presents a plausible model based on simple geometric arguments. 1,3,5-PTI was modeled in Avagadro and the

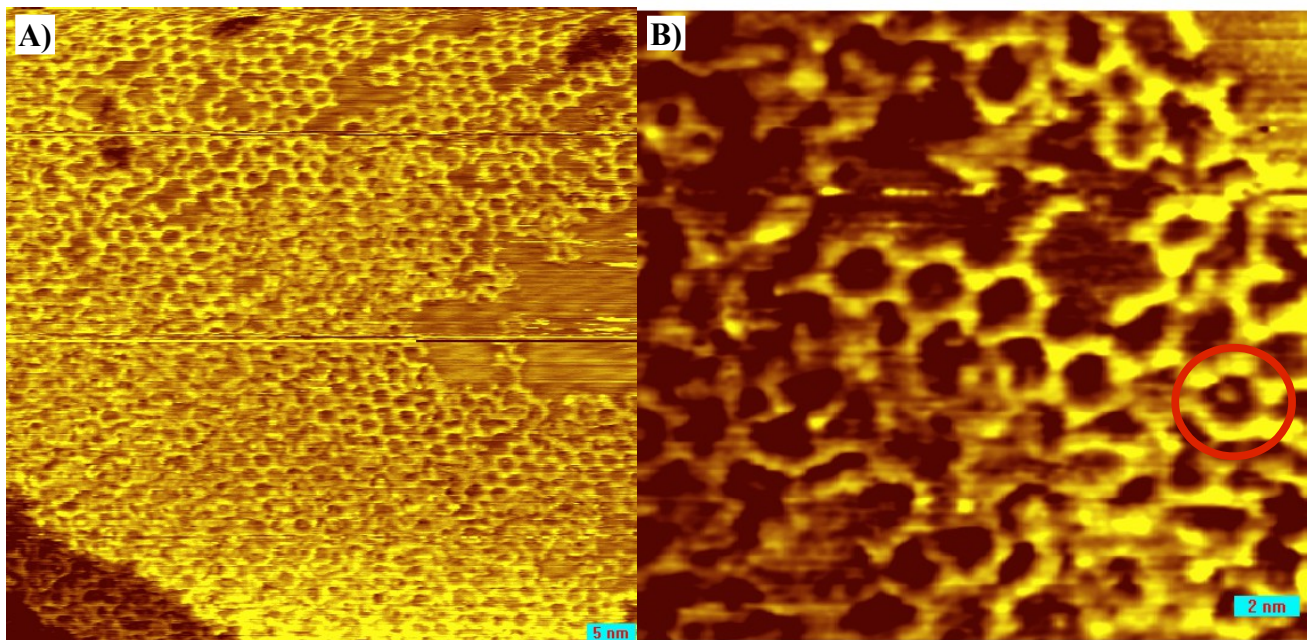


Figure 3: 1 minute 1,3,5-phenylenediisocyanide dose on Au(111). Note 2 dimensional, hexagonal lattice and eroded step edge. $V=-1.0\text{ V}$, $I=103\text{ pA}$. B) Some well formed hexagonal structures. Some, like the one circled show a protrusion inside the “nanopore” which could correspond to a low-coordination gold atom slightly proud of the surface.

geometry minimized at the MMFF94 level of theory. The distance from the centroid of the ring to the terminal carbon of the isocyanide group is 0.790 nm. If the diameter of a gold atom is taken to be ~ 0.350 nm, a ring to ring distance of 1.15 nm can be easily calculated. This is in excellent agreement with the experimentally observed value of 1.17 nm (Figure 5A) and B)). It also appears in Figure 5

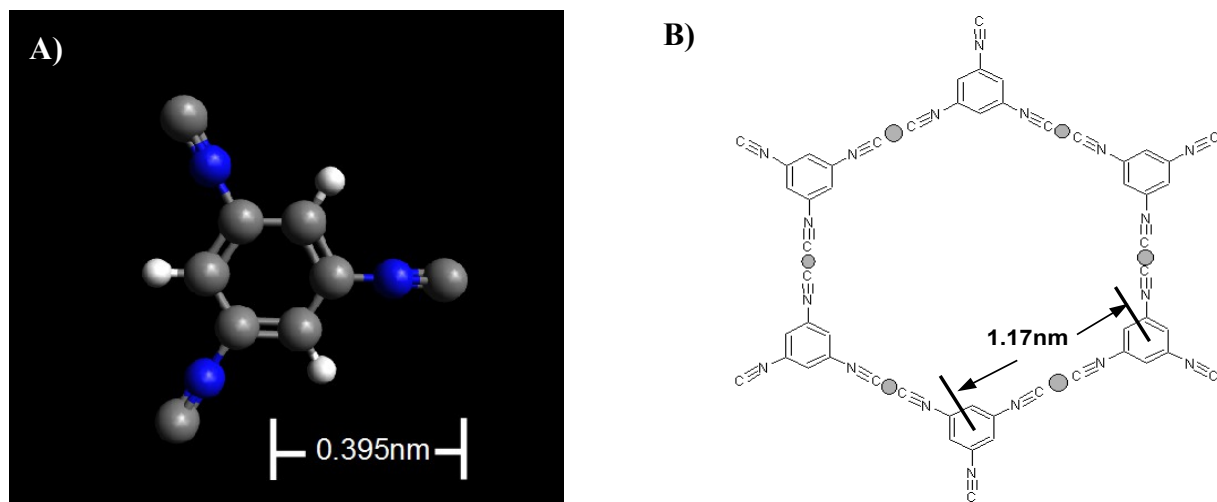


Figure 4: Structural model of 1,3,5-phenylenetriisocyanide “honeycomb” network. The structure is in accordance with simple geometric arguments—the 3-fold symmetry of the molecule and 180° NC-Au-CN bonding.

that gold adatoms are directly observable.

In Chapter 4, a model for the formation of 1,4-PDI/Au adatom oligomers was put forth. In the case of 1,4-PDI, it seems as though the preliminary steps in the reaction involve 1,4-PDI forming η^1 at step edges, which then lean over to coordinate another η^1 PDI /Au adatom moiety. The STM images did not show evidence of *etch pits* on terraces but rather a roughening of the step edge which suggests that the adatoms are sequestered from the step edges themselves. Figure 6 shows an intermediate coverage of 1,3,5-PTI on Au(111). In this case, there are regions which have been severely altered by the exposure. Apparently this particular isocyanide is capable of literally plucking gold atoms out of the bulk, and though some process of surface diffusion, move them to a distant location.

1,3,5-PTI Uptake on Au(111) at Room Temperature

Up to this point the discussion has focused on 1,3,5-PTI on Au(111) at fairly high coverages

(~50%). At these coverages it is clear that the organic molecules are directing the formation of discrete, closed, adatom mediated hexagonal structures. At very low coverages, 1,3,5-PTI induces

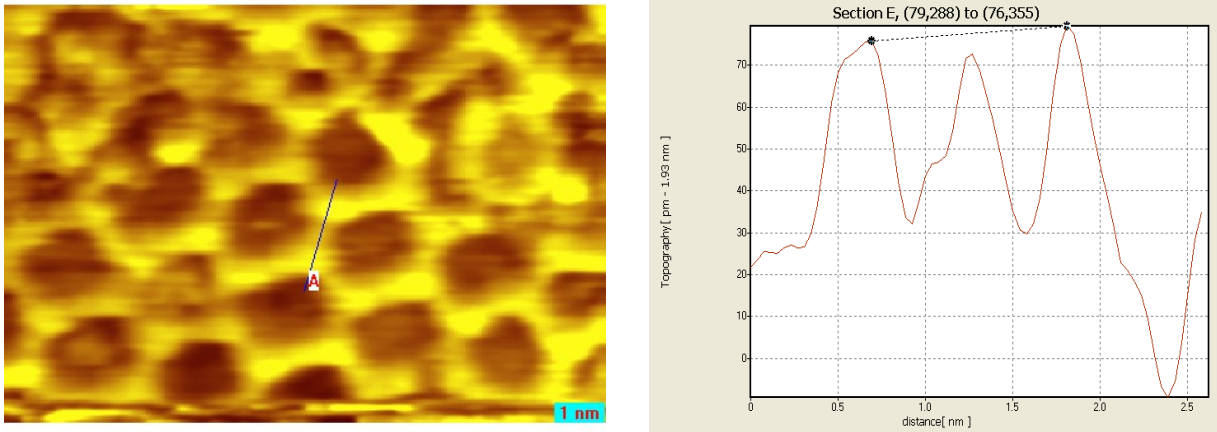


Figure 5: Small scan area image of well formed honeycomb and typical line scan along edge. All line scans show a protrusion in the center of the edge which is completely consistent with a gold adatom. Similar results were obtained in the Au(111)/1,4-PDI system. The vertex to vertex distance (averaged over 6 edges) was found to be 1.17 nm. $V = -1.0$ V, $I = 121$ pA.

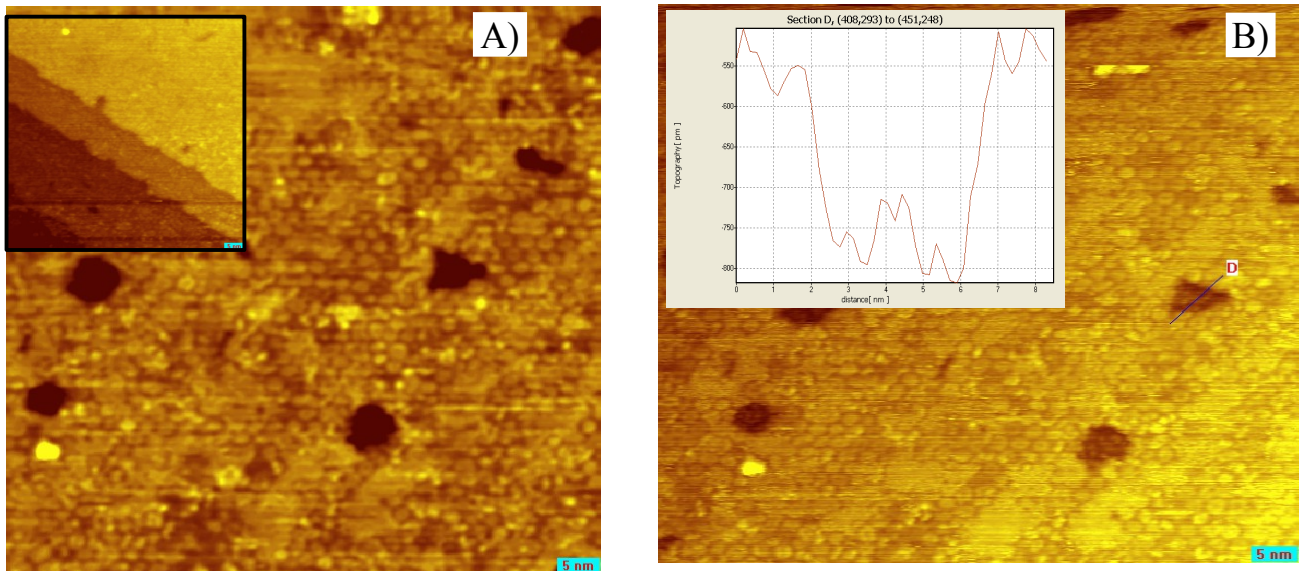


Figure 6: A) Etch pits and step edge erosion imply that 1,3,5-PTI is abstracting gold atoms from the bulk. B) Shows pits imaging at ~550pm which is slightly less than would be expected for an atomic step of gold. Closer examination, however, shows that more honeycomb structures exist in the bottom of the pit and could easily account for the discrepancy.

long range distortions in the herringbone reconstruction. Figure 7 is an image of a 3s dose 1,3,5-PTI. The images show that at these exposures, molecules can be found at the “elbows” of the herringbone

reconstruction. This atom protrudes the furthest, and has been shown to be more reactive. [6] The solitons themselves show a waviness which was confirmed by scanning 90° to the images in Figure 7 (data not shown).

As the dose of 1,3,5-PTI was increased to 30 seconds, the herringbone reconstruction becomes severely distorted. Figure 8 shows the solitons are beginning to form hairpin turns connected by triangular features. Interestingly, these features are extremely large with respect to the size of the molecules themselves.

With 90 seconds total PTI dosing time (Figure 8), the herringbone reconstruction has been completely lifted and replaced by large, 3-fold symmetric features. These features are ~ 20 nm wide, and image as a regular hexagon within an equilateral triangle. These psuedo-3-fold symmetric structures are located corner to corner, and in Figure 9B), these features are shown to propagate

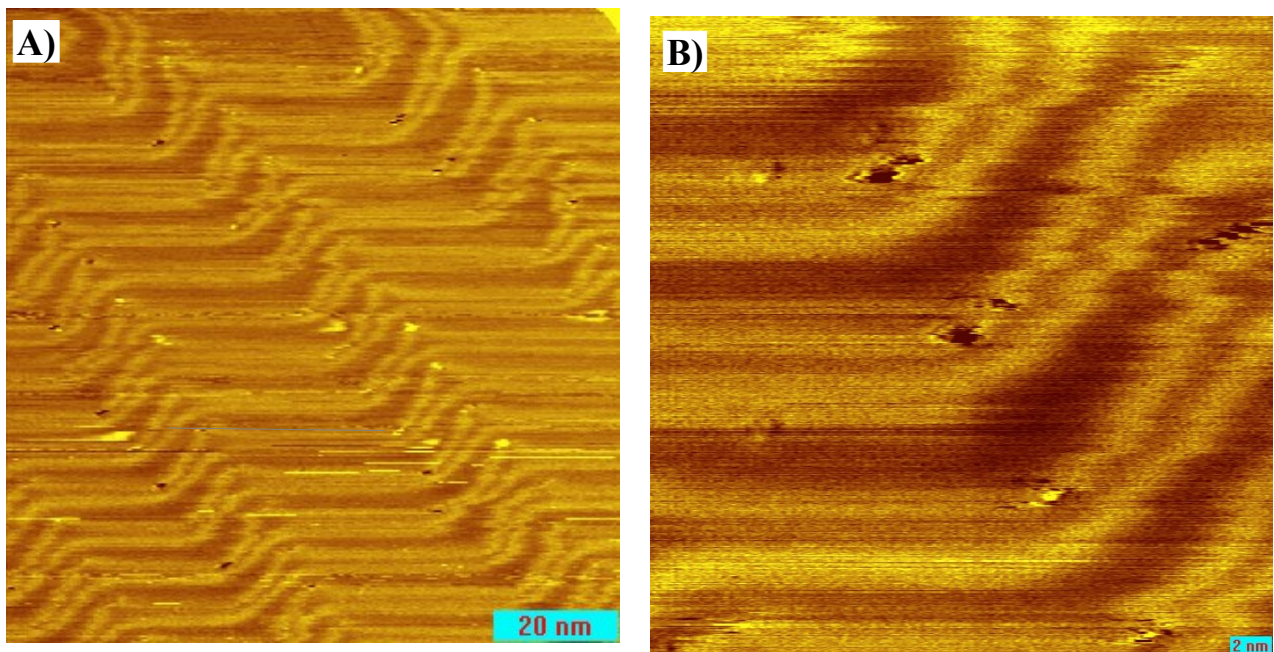


Figure 7: 3s 1,3,5-PTI dose on Au(111). The molecules are reacting first with the “pinched out” elbows of the herringbone reconstruction. B) Closeup of elbows, and “waviness” in the solitons of the reconstruction. $V = -0.5$ V, $I = 95$ pA

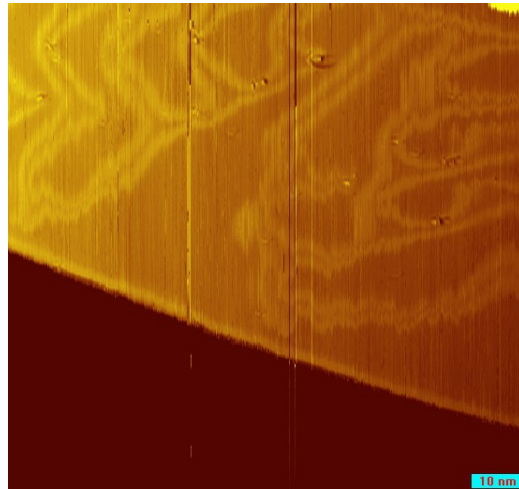


Figure 8: 30 second 1,3,5-PTI dose on Au(111). The herringbone reconstruction is lifted, and replaced with extended hairpin turn features. $V = -0.5\text{V}$, $I = 102\text{ pA}$.

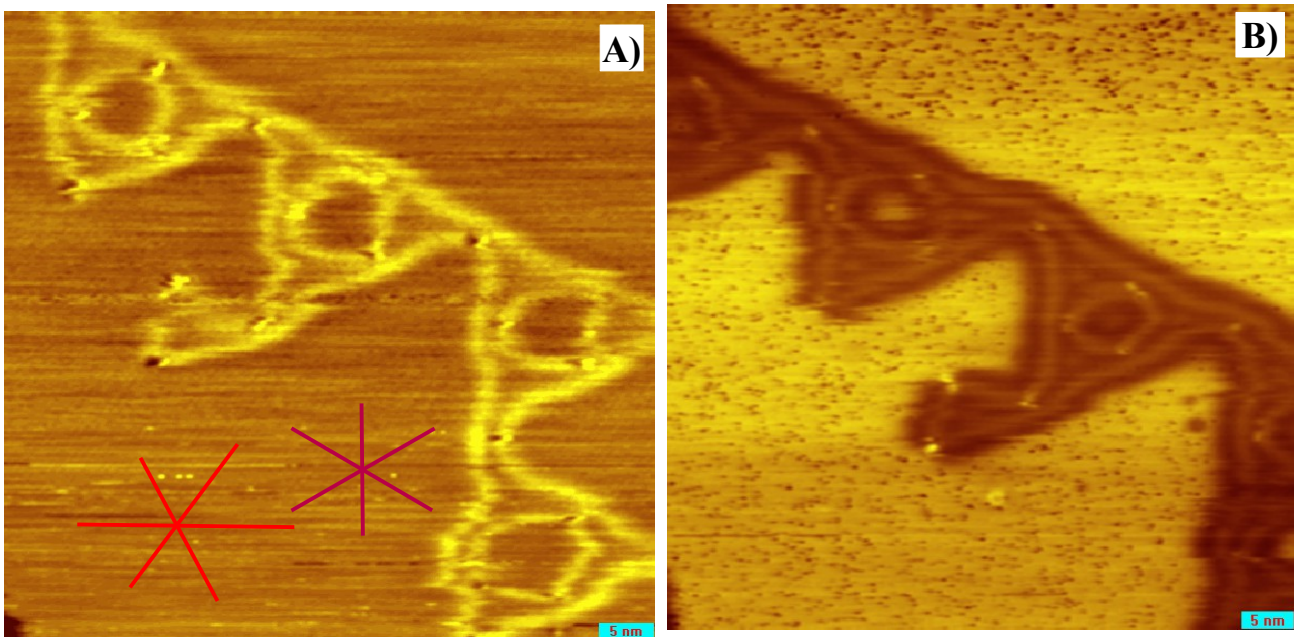


Figure 9: A and B show signs of long range structure induced by a low exposure of 1,3,5-PTI (2 minute dose). These features are $\sim 20\text{X}$ larger than the molecules themselves and appear to be a distortion of the herringbone reconstruction (rather than the adatom templated structures described above). In A) the directions of the original herringbone are given in red, and the directions of the long segments of the new reconstruction are given in purple. The new reconstruction is rotated 60° from the original.

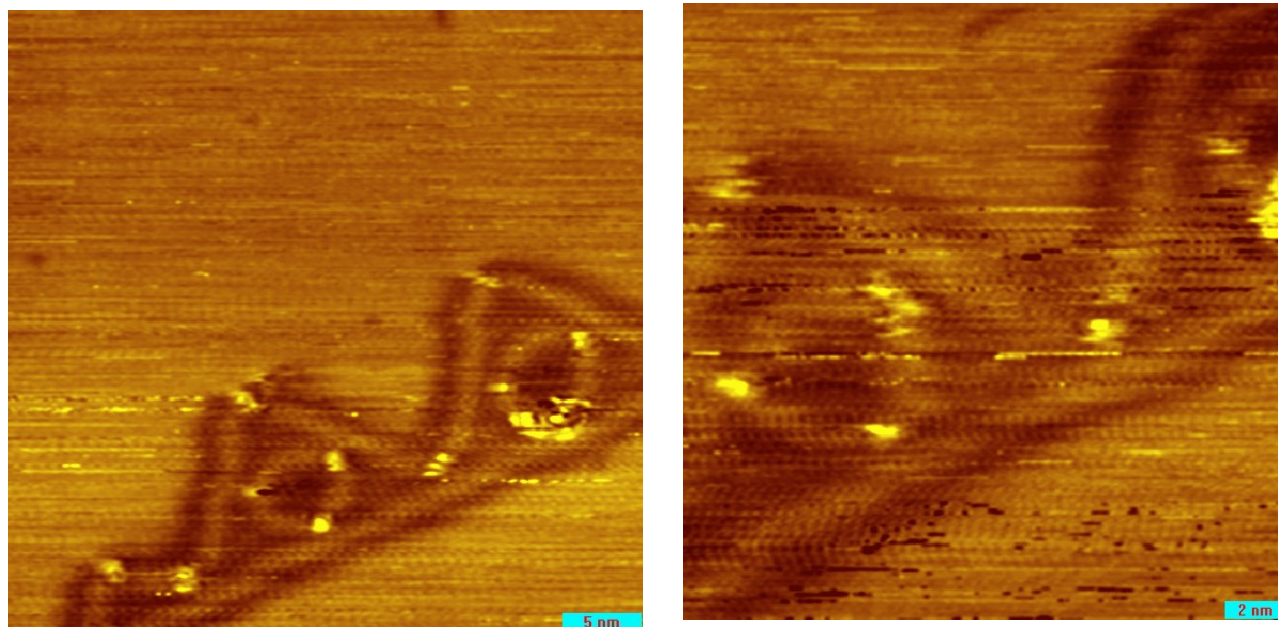


Figure 10: High resolution images of low-coverage 1,3,5-PTI on Au(111). Both images show corrugation of the substrate gold atoms. The herringbone reconstruction has been lifted and curious hexagon inside of a triangle structures are found in it's place.

Conclusions:

In this section the synthesis and characterization of 1,3,5-phenylenetriisocyanide was described. The molecule was investigated for several reasons. First, it was our goal to investigate whether the adatom mediated NC-Au-CN chemistry of 1,4-PDI and 1,3-PDI could be extended to a tri-functional molecule. The approach presented here is interesting in that it demonstrates the ability to template a 2-dimensional array of nano-pores (with a pore size of ~ 2 nm) which could have exciting potential for use in gold-based catalysis [7]. Another potential application for a tri-functional molecule such as 1,3,5-PTI is in the field of molecular electronics. One strategy toward “gating” a molecular device is would be to covalently link the molecule into a true 3-terminal device (analogous to a traditional transistor) [1].

With suitable modifications, it should be possible to functionalize the 2,4, and 6 positions. For example, chiral groups on the ring should produce a 6-fold symmetric chiral pore. For molecular

electronics or photonic applications, perhaps it could be functionalized with some type of antenna complex or photoredox active unit.

It was demonstrated that the most likely surface structure for higher coverages is the predicted extended “honeycomb” network. Obviously this is driven by the 180° coordination geometry of NC-Au-CN bonding, and the 3-fold symmetry of the molecule itself. The STM data is completely consistent with RAIRS spectra which show only 1 CN mode. This finding rules out 1,3,5-PTI adsorbing on a Au(111) surface in an η^1 or η^2 (which should show 2 CN modes based on symmetry arguments). The uptake of 1,3,5-PTI is also shown to be self-limiting at room temperature.

The repeat distance (vertex to vertex) of the 1,3,5-PTI hexagons is 1.18 nm—quite close to the 1.13 nm found in 1,4-PDI. With 1,4-PDI, evidence for a gold adatom with more than two isocyanides has not been found. These two findings suggest that the structure in Figure 4B—with 1,3,5-PTI at the vertices and NC-Au-CN structures making up the edges is correct.

STM images of 1,4-PDI on Au(111) did not show evidence for the formation of etch pits on terraces. Eroded step edges suggest that the step edges are the sink from which the adatoms sequestered. In the 1,3,5-PTI on Au(111) system, step edges also show signs of erosion. However, the terraces (which were atomically smooth prior to dosing) show signs of heavy pitting. 1,3,5-PTI is capable of “plucking” atoms out of the surface.

Finally, a curious discovery was made during STM interrogation of this system. When Au(111) is exposed to 1,4-PDI, straight oligomeric chains are observed exclusively and regardless of exposure. In the case of 1,3,5-PTI, low-coverage images show no evidence of adatom templated structures. Rather the molecule induces severe distortions in the herringbone reconstruction until pseudo-three fold symmetric features emerge (as a hexagon inside of a triangle). Atomically resolved images indicate that these structures are not adatom mediated nanostructures. Instead they appear to be a distortion of herringbone reconstruction itself. It appears from the images that as few as 6 properly placed 1,3,5-PTI

molecules can create a feature larger than 20nm, presumably by disrupting the surface energy of the gold in a highly directional manner.

References:

- 1) Breslow, R. Private email correspondence.
- 2) Wagner, N.; Investigation of the Electronic and Structural Properties of Bidentate Phospine Tungsten Complexes Containing Aromatic Isocyanide Ligands. PhD dissertation, University of Wisconsin-Milwaukee, **1999**.
- 3) Wagner, N.; Murphy, K.; Haworth, D.; Bennett, D.W.; Para-substituted Aryl Isocyanides. *Inorganic Synthesis*. Vol. 34 **2004**. John Wiley and Sons, Inc. 25-29.
- 4) Bayer, A.; Ueber den Schmelzpunkt des Phloroglucins. *Berichte der Duetschen Chemischen Gesellschaft*. **1886**, 19, (2) 2186-2187.
- 5) Arai, I.; Sei, Y.; Muramatsu, I.; Preparation of 1,3,5-Triaminobenzene by Reduction of Phloroglucinol Trioxime. *Journal of Organic Chemistry*. **1981**, 46, (22) 4597-4599.
- 6) Gao, L. *et al.* Constructing an Array of Anchored Single-Molecule Rotors on Gold Surfaces. *Physical Review Letters*. **101**, 1-4 (2008).
- 7) Tekale, B. *et. al.*; Gold Nanoparticle (AuNPs) and Gold Nanopore (AuNPore) Catalysts in Organic Synthesis. *Org. Biomol. Chem.*, **2014**,12, 2005-2027

Chapter 11

Conclusions

The experimental results presented in this dissertation were focused largely on the “self-assembly” chemistry of di and tri-functional molecular wire materials on Au(111) or granular thin films of gold on muscovite mica. Two seminal works laid the early foundations of the fields of nanotechnology and molecular electronics. Nobel Laureate Richard Feynman, in his famous 1959 “There's Plenty of Room at the Bottom” lecture at Caltech, envisioned a future where direct manipulation of atoms could prove a powerful strategy in the miniaturization of various devices [1]. In this visionary work, Feynman touts Mother Nature as an example of what is possible. A DNA molecule, for example, can code all of the information required to create a wide range of functional and exceedingly complicated structures. In his lecture, he clearly understood the technical challenges of manipulating objects on the *atomic* scale. There is a definite “scaling problem” at play. Clearly, if one were attempting to build a device of atomic dimensions (perhaps 10 atoms), a device with extremely high lateral and z-resolution would be required (technology which did not exist at the time of Feynman's talk). Still, such a “weird possibility”, as Feynman saw it could be realized. There were clear challenges to overcome, but no physical reason why it should not work.

Later, in 1974, Avarim and Ratner proposed a radically new idea [2]. The silicon based transistor was invented by Bell Laboratories 1948. The device, much like the modern transistor, relied on an N-P-N junction to modulate current. The device (and modern devices) rely on a semiconductor with carefully controlled levels of “n” or “p” dopants—materials which move the band energies up or down. Avarim and Ratner proposed that there is no reason why an analogous device could not be built from discrete *molecules*. Functionalized properly, it should be able to modulate the levels of the

HOMO and LUMO orbitals in much the same way as the bands of the semiconductors used in traditional transistors. Thus, the field of “molecular electronics” was born.

To understand, on a quantum mechanical level, the mechanism of the transmission of charge carriers through single molecules or small ensembles of molecules, a variety of elegant and exceedingly telling experiments have been devised. Frequently based on a *mechanically-controlled break junction* [3], single molecules are installed between (typically gold) point contacts, and I-V characteristics collected upon modulating the distance between the electrodes. A current challenge towards miniaturization is how to actually “wire” devices as their physical dimensions vanish.

This dissertation pick up with the observation that when a Au(111) single crystal was exposed to 1,4-phenylene diisocyanide (1,4-PDI), long, oligomeric chains spontaneously formed. The chains were presumably conductive as single molecules of 1,4-PDI measured in break junction studies seemed to indicate. This dissertation then, is an extension of this early finding. In the first chapters, the structure and a proposed growth mechanism for the $-(\text{Au}-\text{PDI})_n-$ chains was examined. Then, extensive electrical studies were carried out in an effort to confirm that indeed, the oligomers are capable of bridging nanoparticles some distance apart, on an insulating substrate (mica). This is obviously important if the devices hope to be integrated with modern silicon based CMOS technologies.

The chemistry was extended by examining 1,3-PDI which was also shown to oligomerize. However, as a result of the *meta*-substitution, the chains form with a pronounced “zigzag” structure, and the rings $\sim 30^\circ$ from the surface.

Another prototypical molecular wire, 1,4-benzene dithiol (1,4-BDT) was investigated, and was shown to oligomerize into long chains. Dithiols can participate in *cis* or *trans* bonding through the RS-Au-SR unit, and this gives rise to chains that are mostly straight, but bend occasionally due to the *cis*

units. The structure of this molecular wire was described, along with electrical properties.

1,3-benzene dithiol was not shown to oligomerize. Rather, it forms a di-adatom complex that is fairly mobile on the surface. The origin of this effect appears to be kinetic—if the molecule can sequester two adatoms (much) more quickly than two of the molecules can diffuse together and generate an RS-Au-SR bond, the dithiol system will not form.

The Avarim and Ratner device, a rectifier, is a 2-terminal device. A typical transistor is a 3-terminal device (one of them acting as a gate). One strategy towards molecular transistors is to utilize some kind of back or top-gating (a “field effect” device). Another strategy might be to covalently link the gate into the molecule. To that end, the chemistry of a tri-functional isocyanide (1,3,5-phenylene triisocyanide) was explored [4]. This molecule produced well ordered arrays of hexagonal nanopores, and once again participated in adatom templated bonding. This self-assembly is interesting as it demonstrates a new gold-adatom based approach to generating 2-dimensional metal-organic coordination frameworks.

The salient conclusions of this research are that the structure of metal-organic hybrid nanostructures on surfaces can be largely directed by trivial modifications to the coordination geometry of the molecules. STM data suggests that the oligomerization chemistry is a rather general phenomenon, and linear chains of 4,4'-biphenyl diisocyanide were shown to form spontaneously, as were oligomers of 1,4-diisocyano-2,5-dimethoxy benzene. This suggests that more complicated motifs could be constructed with appropriate synthetic modification. This ability would be critical if truly functional, “smart” materials were to be prepared *via* the self-assembly chemistry described in this dissertation.

The common thread running through the 5 molecules studied during the course of the research presented in this work is the role of the adatom in driving the assembly of oligomeric (or monomeric as

the case might be) species. Bonding between -NC or -SH “anchor groups” and low-coordination atoms (as would be found on step edges or defect sites) results in adatom species that are quite mobile on the surface, yet apparently they are repulsive with respect to each other. This allows for the formation of extended chains rather than the other alternative—the adatoms agglomerating into nanoparticles.

The adatom chemistry is interesting in its own right, as the literature amply shows that low-coordination sites are largely responsible for the more “interesting” chemistry gold can participate in. The strategies presented in this work offer a glimpse into previously unexplored self-assembly of potential molecular wire materials, with potential utility in the field of gold-based catalysts.

High level DFT calculations were used in conjunction with STM, RAIRS, and temperature dependent I-V measurements in an effort to elucidate both the structure and the growth mechanism for the oligomeric systems. Insights into the growth process would prove critical if functional devices were to be assembled. These molecules would have the requirement of structural asymmetry (a donor half, and an acceptor half, for example) and to function in a circuit it would be critical that they be installed with the proper directionality.

The future of this research is promising as there are a range of molecules which would prove fascinating to study. One is 4-isocyanothiophenol [7] which would be the obvious candidate to examine if the oligomerization chemistry works with mixed functional groups. Another totally unexplored class of molecules are the isocyano-heteroaromatics. The synthetic chemistry of these molecules is well understood (isocyanides are commonly used in benzodiazapine synthesis), and a pyridine-type functional group would allow for examination of Hush's “molecular alligator clip”—the Au-Py bond being strong, but not *too* strong [5,6]. Robust but modifiable—in theory at least. Heteroaromatics would also allow for dramatic changes in the energy of the HOMO and LUMO

orbitals of the ring system which could have profound implications on the transport properties. The first stage of this research would be to prepare and image these molecules, and determine if the self-assembly chemistry works for mixed functional groups.

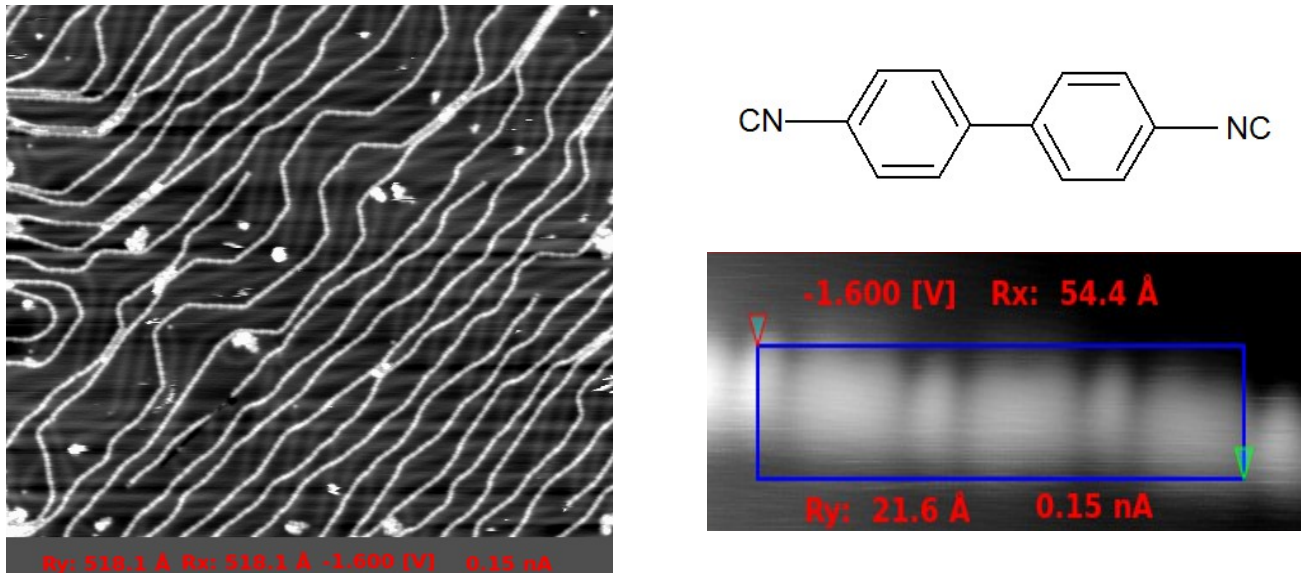


Figure 1: A 4.2K image of 4,4'-BPDI on Au(111). B) shows a high resolution image of 4 of the units. The image clearly shows the same NC-Au-CN bonding as was observed in the 1,4-PDI system.

(Images by D. Stacciola, BNL)

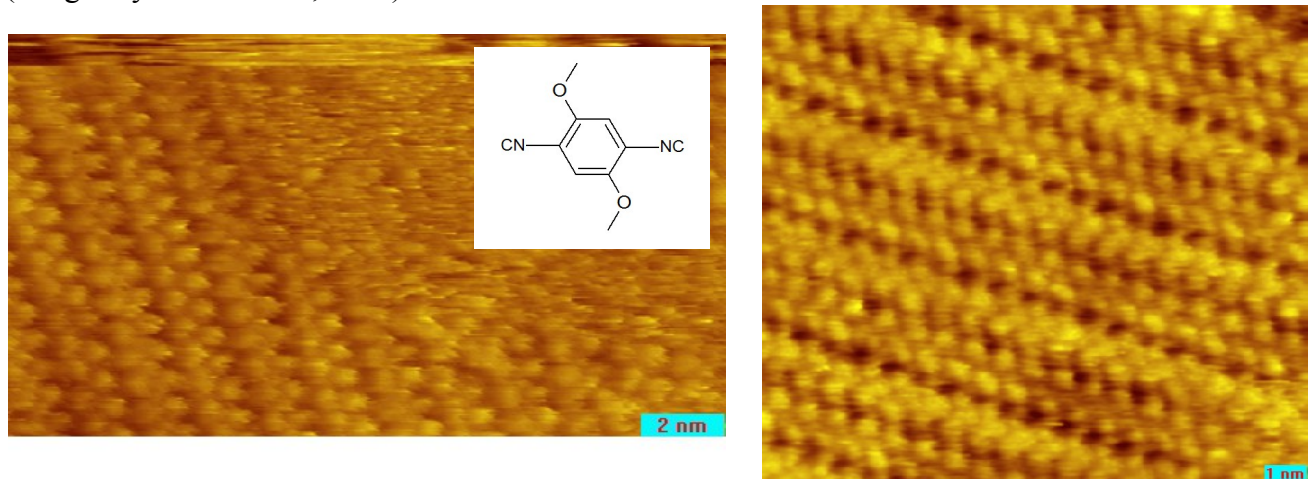


Figure 2: An STM image of 1,4-diisocyno-2,5-dimethoxy benzene. The oligomerization chemistry of 1,4-PDI appears to be a rather general phenomenon. This data suggests that 1,4-PDI can be functionalized, and the self-assembly chemistry and adatom mediation can still be harnessed.

References:

- 1) Feynman, R.; Transcript of 1959 American Physical Society talk available at www.zyvex.com/nanotech/feynman.html
- 2) Avarim, A.; Ratner, M.; *Chem. Phys. Lett.* **1974**, *29*, 277-83.
- 3) Reed, M.; Zhou, C.; Muller, T.; Burgin, T.; Tour, J.M.; *Science*, **1997**, *132*, 252-4.
- 4) Breslow, R.; private email correspondence.
- 5) Solomon, G.; Reimers, J.; Hush, N.; *J. Chem. Phys.* **2005**, *122*, 224502
- 6) Reuter, M.; Seideman, J.; Ratner, M.; *J. Chem. Phys.* **2011**, *134*, 154708.
- 7) Wagner, N.; **1996** Ph.D. Dissertation, University of Wisconsin-Milwaukee.

Appendix A

Tungsten Scanning Tunneling Microscope

Tip Fabrication and Conditioning

Introduction:

While in scanning tunneling microscopy (STM) one typically considers the mechanics of the technique in terms of a probe (typically a very sharp metal tip) scanning a surface, it is important to not lose sight of the reality that the images acquired by a scanning-tunneling microscope are in fact a convolution of the surface and tip states. While the tip essentially images the density of electronic states near the Fermi level of the sample, the sample is in fact doing the same to the tip. To further complicate the matter, the exact structure and integrity of the STM tip is rarely well understood. When scanning-probe microscopist refer to *sharp* tips, they are generally talking about *atomically* sharp tips—tips where a single atom at the apex is responsible for the vast majority of the tunneling current the experimental technique relies on [1]. The lateral resolution ultimately depends on how localized the tip-state is, and obviously for a metal tip this would ideally correspond to exactly 1 orbital protruding from the tip apex.

While this is not a trivial undertaking, it is actually not as difficult to achieve as one might think. Several methods of conditioning and sharpening tips are given in the second half of this appendix, but the problem begins with fabricating a tip of extremely small radius of curvature (RoC). A dedicated and thorough appendix on the subject was included in this volume since regardless of how well the STM is functioning or how clean the samples are, if a stable and clean tunneling junction between the tip and sample cannot be generated imaging is doomed to failure. Presented here are techniques and strategies that been implemented in the course of this research and have shown considerable utility.

While not exhaustive, this Appendix is meant as an initial point from which a microscopist can learn to fabricate, clean, sharpen and test tungsten probes.

Fabrication of STM Probes:

To date nobody has mastered STM tip fabrication and cleaning to the point where it is a completely straightforward process although some recent reports claim success rates in the 90% range [1]. It has been said that there are as many methods of fabrication as there are microscopist and a quick internet search for “tungsten STM probe fabrication” immediately yielded no less than 5 masters theses and a dozen journal articles focused entirely on the subject.

STM tips have been made of a wide range of materials over the years. Tungsten has been used since the earliest days of STM and the fabrication techniques were largely borrowed from the field-emission and field-ion microscope community. Gold has been used but while it is chemically inert, it is also exceedingly soft and fabrication requires the use of toxic reagents such as cyanide salts. Platinum-iridium is sometimes chosen for its chemical inertness and the ease with which tips can be fabricated. Most often the wire is simply cut (under tension) with a sharp pair of wire cutters. The tension and cutting can yield (with practice and luck) a tip with an atomically sharp asperity [2]. The fabrication of STM tips from drawn tungsten wire will be the focus of the discussion. It is a very hard metal which allows one to fabricate tips which are very stiff and mechanically stable, and rugged enough to withstand a certain level of abuse. The other factor is that tungsten is readily etched through anodic dissolution in a relatively innocuous NaOH or KOH solution.

Tungsten Wire for STM tips:

There are three options for the fabrication of STM tips from tungsten wire. The first and cheapest option is to simply use polycrystalline wire of the appropriate diameter (0.25mm for our RHK instrument). The resulting tips can work well, however they can also suffer from some instability due to the less than perfectly crystalline structure at the apex. Polycrystalline wire has a fibrous, thread

like structure which is a consequence of the manufacturing process (discussed below). Sometimes a tip made from this material is perfectly suitable. Unfortunately it is quite common that the tips suffer from instability while scanning (perhaps from unstable grain boundaries near the apex) and so our group virtually never uses this option.

By far the most expensive option is to use wire drawn from tungsten single crystals. It can cost in the range of hundreds of dollars per centimeter, and the literature suggests that the potential improvements in performance are hardly worth the staggering cost. This option is most frequently used by the field-ion microscope researchers who are studying crystallinity.

Our group has settled on a method of *recrystallizing* the polycrystalline tungsten wire described above. The literature suggests that when a metal in the body-centered cubic group is drawn into wire, the (110) plane preferentially oriented perpendicular to the drawing axis. The fibrous structure of polycrystalline wire is probably the result of long crystals aligning themselves along the axis [3], as a result of being hammered and pulled through diamond and tungsten carbide dies. While the recrystallized wire is probably not perfectly crystalline (as single-crystal wire should be), it is certainly *more* crystalline than the starting material. This is easily observed when one tries to cut or bend the recrystallized material. It is noticeably more brittle and much stiffer than the starting material.

The bulk properties of the wire are a consequence of its production [4]. Tungsten oxide is produced from its parent mineral *wolframite* and it purified by precipitation. The oxide is then roasted at high temperature in a hydrogen atmosphere to yield metallic tungsten powder and water. Tungsten powder is mixed with binders and pressed into bars under great pressure and fired to give a *pre-sintered*, rather porous material that is just beginning to consolidate. After this step, the bar has a large voltage placed across it and an enormous current is allowed to flow. The individual grains of powder begin to flow and crystallize together under the very high heat which the electrical current generates. The resulting bar undergoes *swaging* operations where a large hammer which strikes it at ~10,000 blows per minute.

Finally, this consolidated, polycrystalline but very dense mass is drawn through dies to produce the final wire. The hammering, drawing, and annealing operations do much to align large, long fibers along the axis of the wire. The recrystallization step described next does much to improve the mechanical properties of the wire (making it considerably stiffer), and presumably also helps to further refine the grain boundaries between crystals. As long as any remaining grain boundaries do not fall close to the apex of the tip, they can be neglected—with a bit of luck the etching will result in a single crystal being cut through to give the final scanning protrusion for the probe.

Tungsten Wire Recrystallization:

To accomplish the task, a piece of polycrystalline tungsten wire (~2' in length) is looped through a 2 kg weight. Either end of the wire is wrapped around a copper current feedthrough and placed in a vacuum chamber [5].



Figure A-1: Photo taken through view-port of tungsten wire recrystallization. The circular object in the center is a 2 kg weight which keeps the wire under considerable tension. (image used with permission Boscoboinik)

After ensuring that neither the wire nor the weight are shorted to the chamber, the flange is bolted down and the chamber is pumped down with a turbomolecular pump. A Variac transformer is used to apply an AC voltage across the electrical feedthroughs, heating the wire. The wire is first heated until it glows dull red (a temperature estimated to be 1000 K). It is maintained at this temperature for about

an hour to degas the wire and begin the recrystallization process. Then the voltage is stepped up a few volts at a time until a temperature of $\sim 1500\text{K}$ (bright yellow—Figure 1) is reached. The temperature is maintained at this temperature for about an hour. In the final step, the voltage is ramped up at about $2\text{V} / \text{minute}$ until the wire is sufficiently hot that it snaps under the tension of the 2 kg weight which opens the circuit and causes rapid cooling of the wire. After being allowed to cool the wire is removed from the chamber and the ends and middle section (which was in contact with the weight) are discarded and the wire is ready for use as starting material for STM tips. The end and middle sections will have not been heated sufficiently to recrystallize, but these cooler zones should be compared against the hotter zones by cutting them with sharp flush-cutters. The sections between the feedthroughs and weight should be resistant to cutting and springy. They also should have a nice, metallic sheen vs. the dirty gray of the cooler zones.

While the process is simple and straight forward, a few words are in order. The first regards safety while using the recrystallization device. The procedure we have adopted requires that the voltage be ramped up until the wire gets hot enough to snap under tension of a suspended weight. The snapping normally happens near the bottom of the wire (I.e., near the weight) but this not always the case. In one instance the wire snapped near the feedthrough, the weight fell, and allowed current to pass from one feedthrough to the pump body. Observation through the view port showed the wire glowing white hot and passing considerable current. For the sake of safety, care should be taken while ramping the final current and after the weight drops. After the wire snaps, simply ramp the voltage back down and turn off the transformer before touching the chamber.

The second point is of more practical concern. We desire mechanically stiff and highly crystalline wire to fabricate STM tips from. However, using the recrystallization technique above there is a chance of producing a recrystallized material that is unsuitable for STM probe fabrication. If the wire is heated for several hours (or longer) at a bright yellow (or hotter) temperature, the resultant wire

becomes extremely stiff (and presumably very crystalline). Unfortunately the wire is also so brittle that it often shatters while attempting to cut it and can typically be snapped with the fingers. This is unsuitable as the RHK tip holder requires that the tip wire have a small bend in it so that it will friction-fit snugly into the 0.3 mm barrel of the tip holder. There is no need to proceed beyond bright yellow for (Figure 1) for ~1 hour followed by a fairly fast ramping of the voltage to the breaking point of the wire. Polycrystalline tungsten wire prepared in this way is vastly superior in performance to un-treated wire and orders of magnitude cheaper than single-crystal wire.

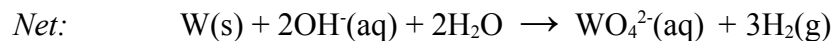
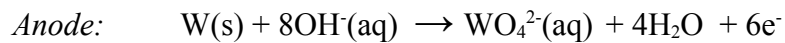
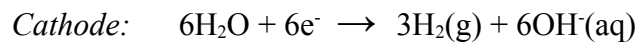
Wet Etching STM tips from tungsten wire:

Traditionally the etching process has been implemented by applying a positive DC voltage to the tungsten wire, and submerging the wire a few millimeters into an etching solution which contains a counter electrode. This configuration is usually called the *drop off technique* [6]. The kinetics of anodic dissolution are most vigorous just below the air/etchant interface and this results in a strong *necking action* where the tungsten wire is thinned to the point where it eventually snaps under tension from the lower section pulling on it under the influence of gravity [7]. The technique works extremely well and has been honed by several groups. The one complicating factor is that the voltage/current source must be shut off immediately after the lower section falls away lest the etching action continue after the drop off and blunt the tip. It seems the power supply must be shut off much faster than one can do by hand and so it is typically implemented with some type of feedback electronics that monitor current passing through the circuit and switch off the power supply on the order of 100ns after the drop off.

Another technique is available that circumvents the need for feedback electronics and is based in an approach called the *double lamellae drop-off technique*. While in the traditional drop-off technique there is one air/etchant interface, in the double lamellae technique the tungsten wire is etched by placing it in such a way that a thin film of sodium or potassium hydroxide necks the wire down from 2

air/etchant interfaces simultaneously. The most clever feature of this system is that the tungsten wire acts as its own feedback switch. As the current passing through the system decreases with time (at constant voltage), the surface area decreases (the tungsten wire is getting thinner). At the very moment the wire snaps under tension and drops off, the electrical circuit is broken and the electrochemical etching immediately stops.

With some practice it is possible to produce perfectly acceptable STM tips with this method. As will be demonstrated, a fairly high level of control over the final shape (the all important *aspect ratio*) can be had by altering a few parameters such as the thickness of the hydroxide thin film and the position of the air/etchant interface on the wire. When tungsten is exposed to a hydroxide solution, the following electrochemistry occurs at a bias of approximately +3.5 VDC:



During the course of the reaction, water is reduced to molecular hydrogen and tungsten (wire in this case) is oxidized to soluble tungstate ions (WO_4^{2-}). In the double-lamellae method of tip etching, the electrochemical reactions described above are constrained to a thin film of a strong hydroxide solution and this allows the etching to result in a strong necking effect which thins the wire until the gravitational force exerted upon the lower portion of the wire overcomes the tensile strength of the remaining tungsten cross section. At that moment the wire snaps under the tension tip of extremely small radius can be produced. A proper STM tip, however, requires more than a very small radius of curvature at the apex, or *apogee* as field-emission literature sometimes calls this asperity. The STM tip also requires the shank behind the apex to be rigid (ie, thick) enough to move the natural vibrational frequency of the tip outside of the scanning frequency of the instrument. Long, spindly tips, while

quite sharp and of very high aspect ratio, can mechanically couple to the scanning and this can produce strange “ghosting” in the resulting images. These tips are also mechanically extremely fragile.

Fortunately there are a few parameters the control things such as aspect ratio, and a great many of the pitfalls in tip fabricating can be avoided through simply keeping etching station and wire clean and vibration free. Even if each step is performed flawlessly, and after much practice, success rates are perhaps in the 70% range. This figure is in line with reports in the literature--STM tip fabrication is tricky and resides in a gray area between Art and Science.

The setup for tip etching is diagrammed in Figure A-1. Etching is accomplished by using a ring-shaped electrode with an inner diameter of ~3 mm. The diameter is small enough that a single drop of NaOH or KOH solution can fill it, and surface tension alone can easily hold it in place. As etching proceeds, a strong necking effect is observed as dissolution can only occur between the upper and lower interfaces. Additionally, the necking is more pronounced in the upper half of the film than the lower half. This effect has been attributed to a hydroxide ion gradient that forms as a result of formation of very dense and viscous tungsten oxide(s). As etching progresses, the tungsten oxides sink to the bottom of the film and displace the less dense hydroxide solution sits on top of it. As etching rate

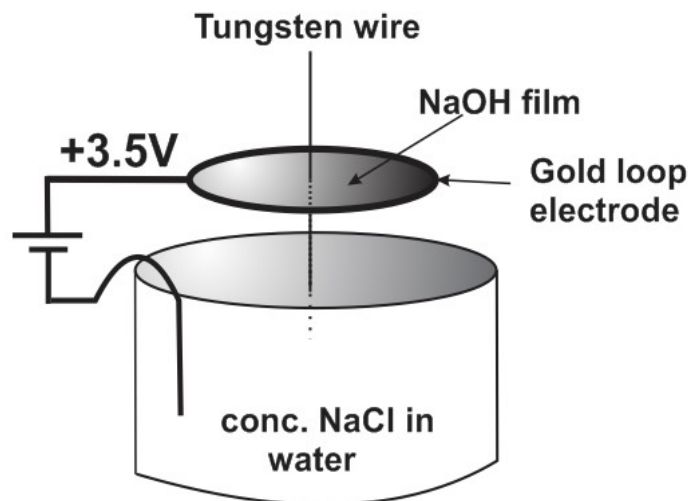


Figure A-2: Double lamellae tip-etching setup. Unlike the traditional drop-off method, in the setup pictured the tungsten wire serves as its own switch. Once the lower portion drops free, the circuit is broken and etching is halted.

Is a function of OH^- concentration, the wire thins more quickly near the top interface. This uneven etching can be used to great advantage when attempting to control the resulting aspect ratio of a tip.

If etching is allowed to proceed to completion in one step, where the hydroxide thin film etches through the wire uninterrupted, the results are typically unsatisfactory. Most often the tungsten wire thins over a long section and this often results in a tip that may be sharp, but the long, needle like tip is very prone to mechanical and acoustic noise, and is exceedingly fragile. Sometimes the long wire that connects the upper and lower portions of the tip seems to literally blow apart during the drop off leaving a tip that looks (under interrogation with an SEM) to have a hair or paintbrush like structure. Either case is obviously completely unsuited for STM.

Fortunately this can be remedied very simply by etching the tip in two steps. The first step we refer to as *necking down* the tungsten wire. In this step, a rather thick film of hydroxide solution is placed in the gold loop electrode and the tungsten wire is placed through it so that it comes in contact with the sodium chloride solution beneath. Then the voltage is pulsed several times to $\sim +7$ V in an effort to clean and smooth the wire. We call this step *electropolishing*—at high voltage asperities are etched more strongly than smooth areas and removes any loose tungsten fibers in the etch zone. Finally, a voltage is applied such that the hydrogen evolution at the gold/solution interface is vigorous, but not so vigorous that it disturbs the tungsten/solution interface. This is important as the asymmetric cutting action relies on gravity to set up a hydroxide ion gradient. The tungsten is observed periodically with a magnifying glass, and when the wire is thinned to approximately 1/3 of its original thickness the power supply is turned off. The thin film is removed by soaking it up into a Kimwipe. Then the film is replaced with fresh hydroxide solution. This time however, the thickness of the film is reduced (adjusting it by soaking some of it up or adding more as needed) to about half of what it originally was. The position of the tungsten wire is then adjusted so that it is slightly deeper in the film. In step 2, the lamellae should fall about 1/3 of the way down on the etch zone created in step 1. Finally, the voltage

is reapplied, and increased to a slightly higher value. It has been observed that a high etching rate (brought on by a full-strength hydroxide solution and higher voltage) results in tips with the etched portion emerging from etching mirror polished as opposed to the frosted or even porous finishes sometimes observed at lower voltages (~5 V is a good starting value). The voltage is increased as high as possible before the hydrogen gas evolution at the gold electrode begins to interfere with the tungsten/etchant interface. Depending on the exact voltages used, this entire process does not take longer than 20 minutes to complete, at which time the wire will have etched all the way through and the lower portion will have fallen into the sodium chloride solution thus breaking the circuit that drives the etching process.

Notice also from Figure A-3 that two types of tip cross sections are most often encountered. Commercial tips and the cross section most often shown in the literature is exemplified in B1. These tips go from full diameter to the apex in a single smooth curve. These are mechanically excellent as there is a large amount of material behind the apex. These are often fabricated by using a relatively thin film in “step 1” of the etching and cutting ~2/3 of the way through the wire. The thinnest possible film is used in “step 2” for very localized cutting just above the thinnest point from “step 1”.

Figure 3B shows another common cross section—a roughly conical cross section topped by a sharper cone. These can occur accidentally from the lamella shifting during etching. They can also be fabricated intentionally as follows. A relatively thick lamella is employed in “step 1”, and the tungsten wire is cut to about ½ it's original thickness. A thin lamella is then employed in “step 2”, positioned just above the thinnest point from “step 1”.

The cross section of the tip can largely be controlled by the exact placement of the lamella with respect to the tungsten wire during etching. The etching progress can be readily checked by momentarily turning off the power supply and examining (with a 2X lens) the wire/etchant. Note that the cutting action of the hydroxide solution is more aggressive at the top air/etchant interface. If a tip is

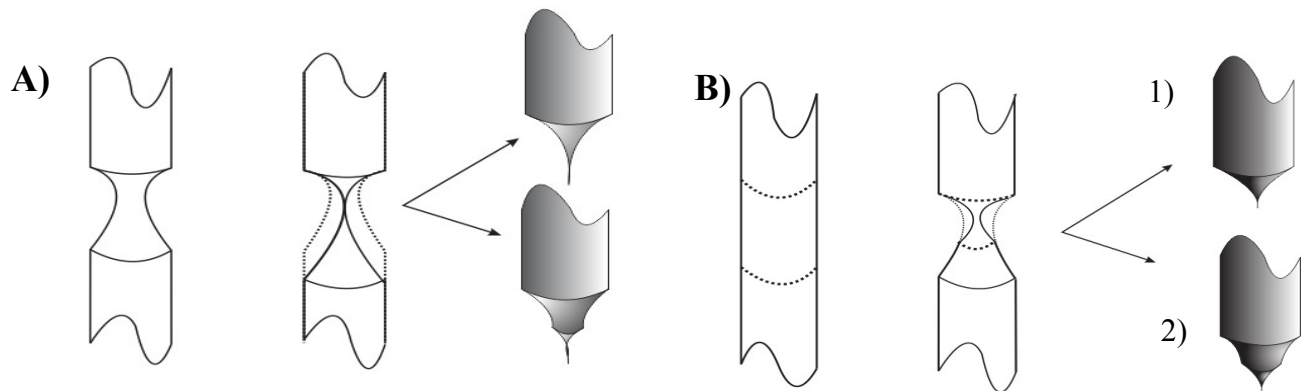


Figure A-3: One-step (A) and two-step (B) wet etching of tungsten STM tips. In the one-step process, resulting tips are frequently mechanically weak and wiry. In a 2-step process the wire is first *necked down* to about $\frac{1}{2}$ its original diameter, then carefully cut through. The aspect ratio of the tip is controlled by lamella thickness and placement.

showing signs of becoming too thin and wiry, it is normally possible to carefully push the tungsten slightly deeper into the solution and/or thin the lamella. This should help localize the cutting action and move it higher on the shank of the tip.

After the drop-off, the tip is withdrawn carefully (*atomically* sharp objects are incredibly fragile), dipped in DI water, then isopropanol, and finally allowed to dry. Observation under an optical microscope will normally suffice to determine if the tip looks suitable for further treatment and shows promise for use as an STM probe. The optical microscope can only resolve down to microns. However, it has been our experience that if a tip appears shiny, symmetric, and defect free, it indicates the etching process went properly. If it is riddled with defects or porosity, has a long wiry apex, or a strange or severely deformed cross section, it is better to start over.

As the success rate of tip fabrication is not terribly high, it is common to prepare them in batches of 5 or 6 and immediately discard any that are unsuitable. The tips emerge from the etching solution covered in a thick oxide/hydroxide coating. Metallic tungsten is quite reactive, so for long term storage outside of the microscope the tips are typically left covered with the oxide coating until just before use. The tips are stored until needed in a hard plastic box fitted with a block of Styrofoam in the bottom.

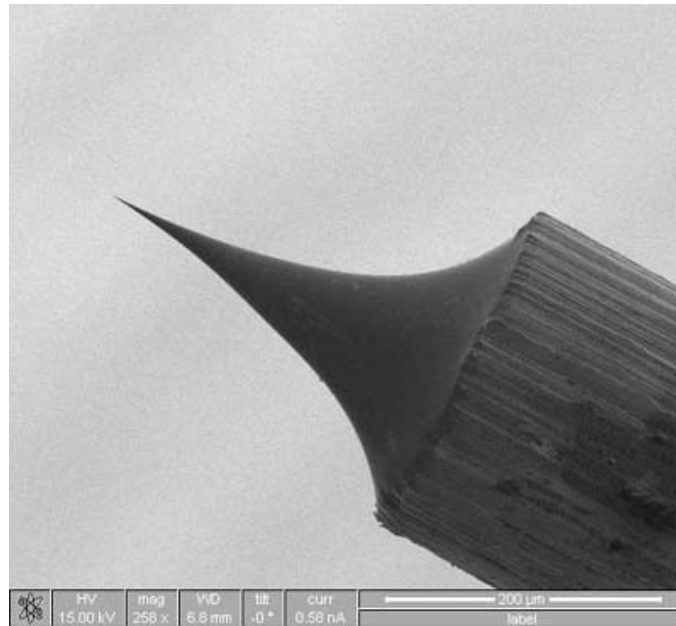


Figure A-4; SEM image of electrochemically etched tungsten probe at 258X magnification. Note flawless, perfectly symmetric etch zone. The tip is extremely sharp but mechanically rugged. (Image used with permission Joanna Millunchick, University of Michigan).

The wires are simply pushed into the block base first, making certain to not touch the apex in the process.

Tip Cleaning and Conditioning:

In this section, techniques for creating and maintaining *atomically sharp* STM probes will be discussed. In the first half of this Appendix the fabrication of tungsten STM probes was discussed, with a focus on creating a profile that a small *radius of curvature* but also had enough material behind the apex so that it was not prone to mechanical or acoustic vibrations. Another issue is that the wet-etched tungsten tip emerges from fabrication covered with a few hundred nanometer thick oxide/hydroxide coating. The coating is highly insulative and electrically unstable. In this section we will discuss transforming the as-fabricated tip into an atomically sharp one in addition to strategies for routine cleaning.

A tip might be considered *good* if it has a RoC of less than 50nm, and excellent if it's 10 or 15nm.

While this is exceedingly small and sharp, to achieve atomically resolved images it is at least 2 orders of magnitude too large. The theoretical work largely put forth by Chen [13] and others frames the issue in terms of *localized* tip states tunneling electrons into and out of localized states of the surface and adsorbates. In fact, in 1982 Binnig and Rohrer commented that an STM image is not simply a map of the corrugation of a surface, but rather “they reflect the corrugation of the electron wave functions near the Fermi level” (Fig. A-5) [8]. Baratoff who was on the original team of developers of the STM was perhaps the first to note that atomically resolved images could only result from tip with *single, localized state or dangling bond* [10]. If one keeps in mind that during a typical STM experiment the distance between the tip and sample is a mere 1-4 Å from crashing in to the surface, the problem becomes more clear. Here the vacuum gap between the tip and surface is smaller than the de Broglie wavelength of the electron. If the tip is sharp enough—maybe a single metal orbital, it can tunnel in to exactly one state and give rise to images of stunning resolution.

It has been said by many researchers, but perhaps most succinctly by Chen [9]: “every experimentalist knows that atomic resolution in STM is infrequent. Even if the most careful preparation of a tip is made, for example, by electrochemical etching or mechanical means, atomic resolution is not guaranteed”. In this section, several techniques for cleaning, conditioning, and sharpening STM tips will be presented with commentary on when they might be used to greatest effect. The exact nature of the tunneling junction is never well understood and it is very common to have abrupt changes in image resolution (sometimes for the better, sometimes not). However, the chances of acquiring quality images improve with the sharpness and cleanliness of the apex of the tip.

The predominate contamination on the as-etched tip has been shown to be tungsten trioxide, WO_3 , but probably also contains hydroxides left over from the etching process. In addition, the as-etched tip apex, while exceedingly sharp, might not be thermodynamically stable. Tips are often thought of and modeled as hemispheres of some radius. Keep in mind that this is a crude approximation—the actual

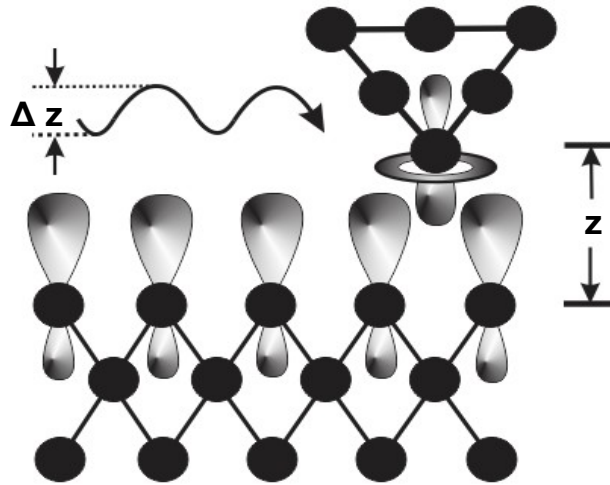


Figure A-5: A highly localized *tip-state* investigating the atomic corrugation of localized *surface-states*. For a tungsten tip, perhaps the tip-state is dz^2 in character. For a silicon surface, the states might be sp^3 . The key to good imaging is a stable and clean tunneling junction between the two.

apex is most certainly formed of facets generated by intersecting crystallographic planes. “Loose” low coordination atoms on the surface of the tip are somewhat free to move and this is particularly true under the influence of an electric field (such as a tunneling junction in an STM experiment). The following describes several common methods to both clean (remove oxides) and condition (stabilize and sharpen) new tips or give new life to old ones.

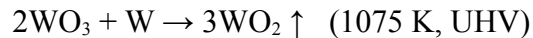
HF dipping:

Tungsten oxides are readily removed with mineral acids. Unfortunately metallic tungsten is also readily soluble and so using hydrochloric or nitric acid as suggested by some is probably not a good method. An exception is hydrofluoric acid (48% in water) which reacts readily with tungsten oxides to generate soluble tungsten fluoride, but not with metallic tungsten. Dipping the tips for 10 seconds in HF, then water followed by an isopropanol rinse results in very clean tungsten and is frequently used to bulk clean tips after fabrication. As a safety warning, reader is advised that HF is an extremely toxic and insidious reagent and care should be taken regarding its use and disposal.

Field-Emission Tip Conditioning:

An in depth theoretical discussion of field-emission (Fowler-Nordheim tunneling) can be found in Appendix B. Here its implementation as a tool for STM tip cleaning, conditioning and testing will be discussed. As already stated, an as-etched STM tip is covered in a thick oxide layer. The problem is obvious—how does one clean an object that is atomically sharp without destroying it?

At a temperature of 1075 K, WO₂ sublimes under UHV conditions [11]. This temperature is readily achieved using resistive heating. The other oxide found in abundance on an un-cleaned STM tip is WO₃ which fortunately undergoes the following reaction under the same conditions:



We can see immediately that by heating we can thermally sublime tungsten dioxide, and tungsten trioxide is decomposed to tungsten dioxide which then sublimes. The melting point of tungsten is 3700 K, so there is a large safety factor between cleaning the metal, and slumping the delicate apex of the tip which would have a slightly lower melting point than the bulk.

One can think of tungsten atoms in the bulk of the tip as being positive nuclei surrounded by a sea of negative charge. If a positive bias is placed on the tip (vs. a negative counter electrode), these positive nuclei experience a force aligned with the electric field vector. However the electron cloud exerts a force of equal magnitude but opposite direction (often called the *electron wind force*) and as a result the bulk atoms do not experience net movement as a result of the applied field. For surface atoms, and particularly for low-coordination atoms on the surface, this is no longer the case. Having a more localized electronic structure (I.e. not “diluted” in a sea of electrons) they will become somewhat desheilded and will experience a net force drawing them in the direction of the electric field vector. This can be used to great effect for tip conditioning as it has been suggested that the mobility of the atoms can literally “heal” defects created during fabrication. Also, it is our desire to take a tip of small radius, and grow an atomically sharp and thermodynamically stable asperity on top of it—something quite possible as demonstrated by field-ion microscopy [3].

While heating an STM tip to high temperature as a cleaning step is commonly employed, and field emission is frequently used as a test of STM tip sharpness, using them together as a hybrid

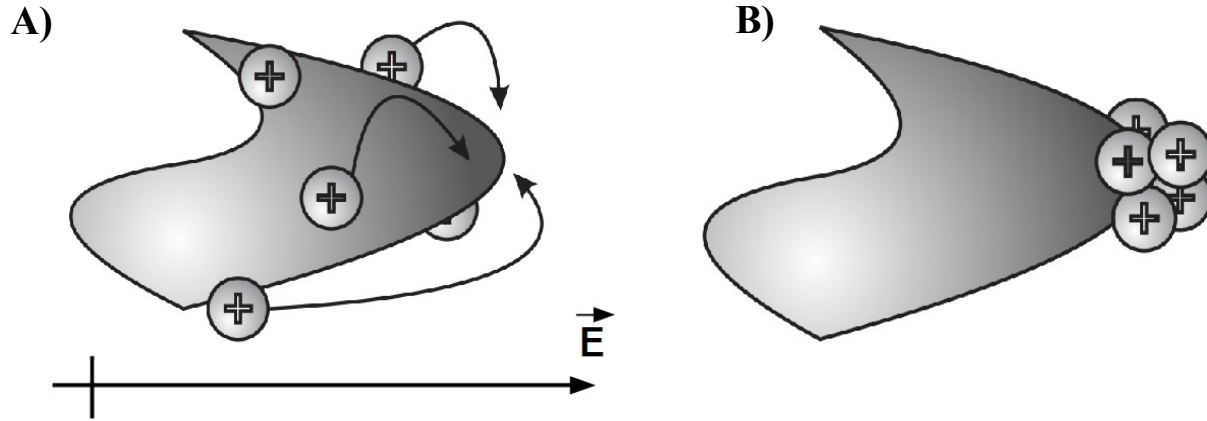


Figure A-6: An *electron wind-force* can be used to draw low-coordination atoms (A) to a sharp and stable tip (B).
cleaning/sharpening technique was first specifically reported by Grütter et. Al [7].

An STM tip preparation system was built according to Figure A-7. Briefly, a 6-way cross was installed atop a small ion pump. One current/thermocouple feedthrough was installed in opposition to a high voltage feedthrough. The length of the copper rods was reduced such that the final separation between them while they were installed in the 6 way cross (including heating filament and tip mounting tube) was ~ 2.5 cm. The current feedthrough was used to pass a current of $\sim 3-4$ A through a 60/40 Nichrome heating filament, to which a stainless steel capillary was spot welded. This allowed the STM tip to be installed by simply friction fitting it in place within the capillary. Measuring an accurate temperature at the extreme end of the STM tip would be extremely difficult, and so we used the method of Lucier [3] which relies on blackbody radiation. At a temperature of 1000 K tungsten just barely begins to glow in a darkened room, so taking it to a temperature where the tip is glowing a dull red is assumed to be approximately 1200 K. This should be ample to sublime tungsten oxides but still ~ 2000 K below the melting point.

The protocol typically used for field-emission tip cleaning and conditioning involved installing the tip in the field-emission chamber such that the apex of the tip was approximately 2.5 cm from the

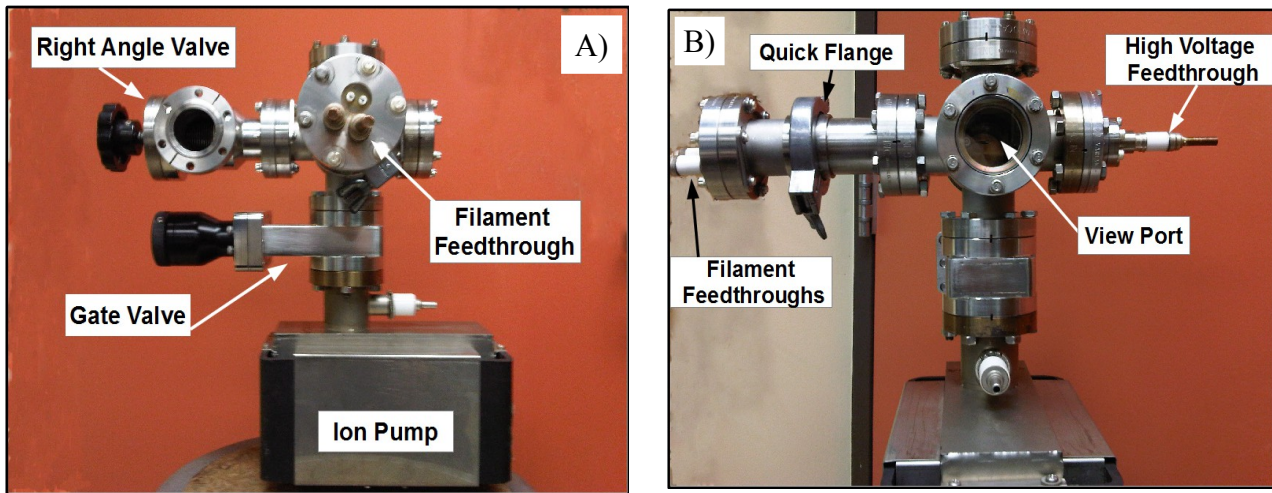


Figure A-7: A) Side and B) front view of Fowler-Nordheim tip conditioning system. Tips are mounted to nichrome filament. Tip conditioning and testing is performed by cycles of heating and field emission.

copper disc collector and pointed directly along the axis of it. The chamber was evacuated with a turbomolecular pump which was then valved off while the ion pump was brought up to power. The ion pump was able to achieve a base pressure $\sim 5 \times 10^{-8}$ Torr without bakeout. While this is not true UHV, this pressure still allows a mean free path of about 7 m which is more than adequate for this type of study.

Figure A-9 shows the results of a typical “Fowler Nordheim Run”. The tip was pumped down, flashed to dull red by applying $\sim 3-4$ VDC and 2-3 A to the Nichrome heating filament.

Then the DC voltage was slowly increased until a field emission current was detected. The voltage was increased stepwise until a final emission current of several nanoamps was detected (typically ~ 10 nA in arbitrary steps). The voltage and current were recorded at each point, and the results plotted to arrive at the a Fowler-Nordheim plot. It is clear that the slope of the lines decreases dramatically from run 1 to run 5 and also shifts to the right (to lower voltage). This is indicative of either a decrease in the radius of the tip and/or the removal of insulative tungsten oxides and other contaminants. In practice, there is also a dramatic enhancement of the stability in the measured field emission current. Typically in the first run current can jump erratically by $\pm 5 \mu\text{A}$. By the final run, current response is

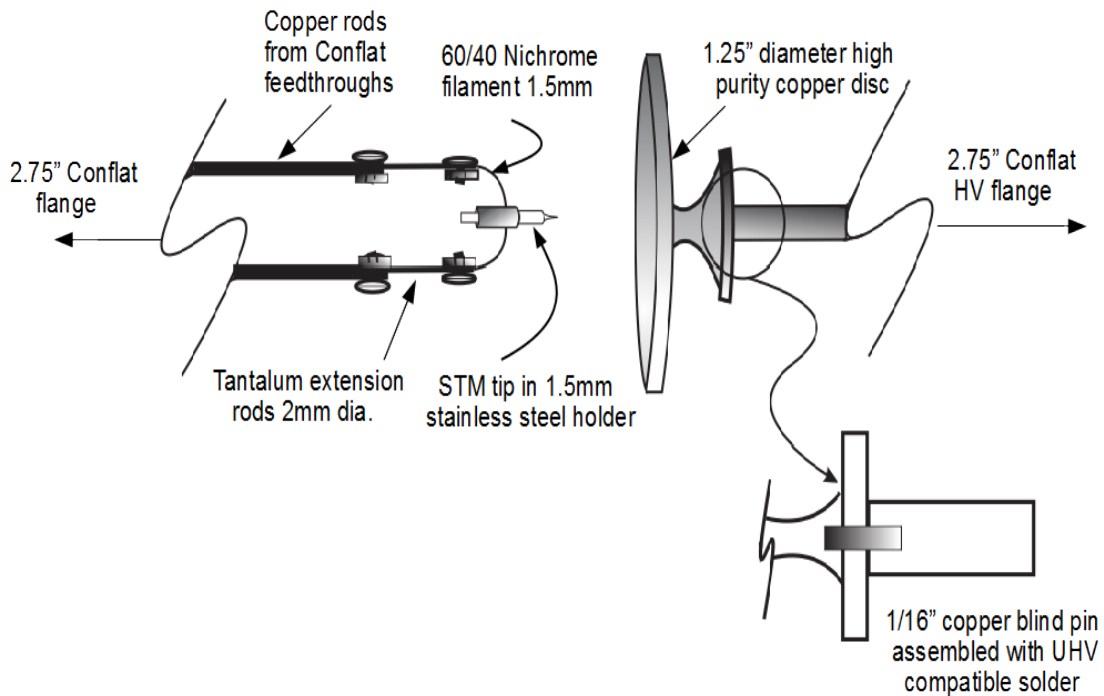


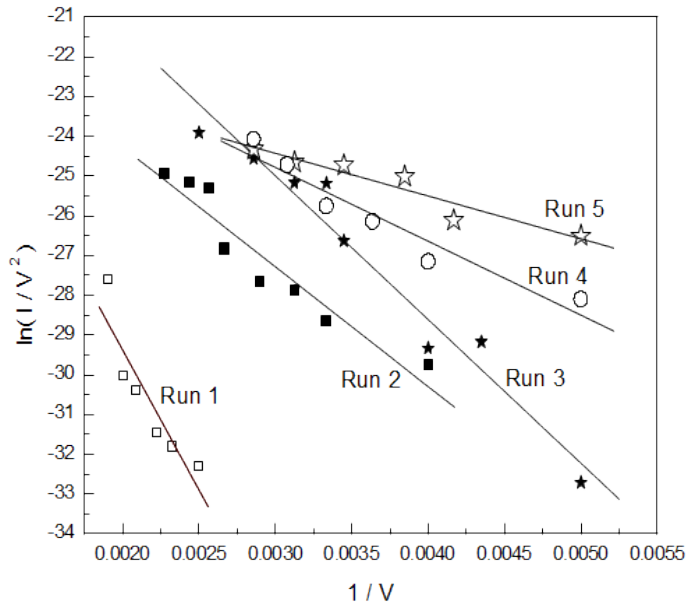
Figure A-8: Construction detail of the tip mounting system and copper disk. Heating is accomplished by passing a current through the nichrome filament. Field emission is carried out by placing a large bias between the tip and the copper disk. A Keithley picoammeter is placed in series to measure field-emission current as a function of applied voltage. extremely stable with voltage.

Recall from the Appendix B that the slope of a Fowler-Nordheim plot can be used to calculate the radius of an emitting tip according to Equation 1:

$$\text{Slope} = -6.8 \times 10^7 \phi^{3/2} \alpha k R \quad 1)$$

Where k is the field reduction parameter, α is the image correction term, and ϕ is the work function.

As discussed in the section on Fowler-Nordheim tunneling, metals do exhibit crystallographic anisotropy with regard to work function, and lacking intimate knowledge of the material requires the use of an estimate. The tungsten wire used for the fabrication of the tips is produced by forging, annealing, and drawing the bulk metal through various diamond and tungsten carbide sizing dies. This has been shown to result (for body-centered cubic metals such as tungsten) in a preferred grain orientation along the axis of the wire [3,7]. It has also been reported that the preferred and most often



Run	Slope	R
1	-7045	-0.91
2	-3011	-0.95
3	-3614	-0.97
4	-1858	-0.96
5	-1075	-0.95

Figure A-9: Typical results of a field-emission tip conditioning. The tip was flashed to dull red (~1200 K) prior to each field-emission run. Then a high-voltage supply was placed between the tip and the copper collector with a picoammeter in series. Bias was increased in arbitrary steps until a final current of ~10nA was arrived at, then brought back down. Notice dramatic reduction in slope and shift to lower voltage with run number.

observed face perpendicular to the drawn axis is the (110) plane [3]. This has been observed in polycrystalline wire, and is most certainly more accurate in the recrystallized wire used by our group. As the tip is taken to be hemispherical, we should consider the work function to be an average of the (1XX) work functions, weighted in favor of (110). (the tip is not hemispherical but composed of intersecting facets or planes). As $\phi_{110}=5.25$ eV, $\phi_{100}=4.63$ eV, $\phi_{111}=4.47$ eV, a reasonable estimate of the work function of the tip would be $\phi_{\text{effective}}=4.90$ eV. The value of image correction factor α is difficult to know, but by FIM it has been reported to typically be close to 1. Also, the value of k , the field reduction term resulting from the exact geometry of the tip, is not precisely known but is a factor of ~5 and does not vary greatly until the radius becomes extremely small (a few nanometers). Using these estimates in Equation 1, and ignoring the possibility that some of the reduction in the slope of the

F-N plot is a result of oxide removal and not geometric improvements, we estimate with some confidence that the tip radius has dropped from $\sim 190\text{nm}$ to $\sim 30\text{nm}$. The latter number is probably more valid as it presumably represents the cleanest of all the runs.

In summary, field-emission provide a to be a valuable tool for tip cleaning and sharpening. Pumping tips in to the tiny dedicated chamber takes minutes, and within an hour the tip can be either thoroughly sharpened and stabilized, or in the worst case scenario the tip will not emit even if a very large voltage is applied (600 or even 1000 V). While field emission will not guarantee a high-performance tip, poorly performing ones can be discovered readily.

Ion Bombardment:

Another method used to clean STM tips, and perhaps to sharpen them, is to subject them to argon ion bombardment. The tips are pointed directly down the axis of the ion gun. In our configuration the tip is held at ground potential and the ion gun is floated to a large positive bias. The bombardment is a direct response of accelerating the ions across this potential, with the energy delivered by the ion proportional to the accelerating voltage. It is a rather violent process as it has been reported that at an accelerating voltage of 1 kV, the ions have enough kinetic energy to ablate tungsten atoms. For this reason, ion bombardment is typically used cautiously, ramping up the the accelerating voltage (and resultant kinetic energy of the impacting ions) as needed. Two approaches seemed to be favored in the literature. The one suggested by Behm and Hofer [12] suggests that bombarding the tip with very high energy ions (1 or 1.5 kV accelerating potential), but for a very brief period of time is the proper method to remove oxides and other contamination without damaging the delicate apex of the tip. The other method commonly used is a more gentle accelerating voltage (we commonly use 500V) for a longer period of time. The “hard and short” technique using 1kV ions for perhaps 5 or 6 seconds works well for tips that are pumped in to the microscope without any pre-treatment. The heavy oxide coating on the tips seems to respond well. However, when pre-cleaned tips (either field emitted or HF dipped)

were subjected to the same treatment, in 3 out of 4 cases the tip was unsuitable for imaging. It is a small population to draw a hard conclusion on, but considering the ions have enough KE to ablate tungsten and there is no oxide coating to cushion it, this treatment seems too aggressive for pre-cleaned tips. The less aggressive treatment of bombarding the tips at 500V for perhaps 20 seconds (or less for routine cleaning) seems to work well for new, uncleaned tips. In the literature, times up to a minute are commonly encountered. The author has settle on a technique of splitting the difference between the two approaches. On new, un-cleaned tips, 1s at 1kV and 10s at 0.5kV has proven itself to do minimal damage to the tips. For a maintenance cleaning, 8 or 10s at 500V seems to be vigorous enough to remove contaminants without altering the tip geometry.

Controlled Crashing or “Dipping”:

While tip crashes (when the STM tip literally crashes in to metal-metal contact with the crystal) are the bane of STM microscopy and they can do great harm to the tip, it is possible to use a controlled crash as a cleaning or passivation step. Metallic tungsten is extremely reactive and it is doubtful that a tip which has been cleaned by ion-bombardment (which should yield a pristine metallic surface) will remain in that state for long. It is extremely likely that once the tip is brought in to tunneling range and bias is applied, species on the surface will be picked up by the tip. This is commonly encountered when a freshly cleaned tip is employed—they tend to be very unstable can require hours to get them into service. To get around this problem, it is common to drive the STM tip into the surface of the crystal (in a carefully controlled way) using a *force-distance curve*. If the crystal is much softer than the tip, and if the tip is driven in a small distance, there is little chance of causing serious damage to it. Our group commonly “dips” the tungsten tip 3-6 nm into a gold crystal. Imaging over one of the crash sites generally shows a *mound* of gold rather than the crater one might expect. The gold seems surprisingly plastic and crashing is an effort to pick up a small number of gold atoms and/or leave debris and contamination behind. Having a mechanically hard tip like tungsten with a chemically inert

material like gold in the role of the tunneling atom at the apex should provide an ideal combination. Indeed the first ever atomic resolution images of gold were collected by treating the tip in this way. According to Behm et. al.[12], dipping the tip in gold followed by biasing the tip to -7.5 V for four scan- lines was the key to generating a tip stable and sharp enough to perform the experiment. The claim is that the high negative bias *electromigrates* the gold atoms to form of stable tip on the end of the tungsten apex (perhaps a stable gold crystallite). Dipping in to gold followed by electromigration is a technique used very commonly by our group and frequently it works very well.

An alternative and most ill advised method is found in the manuals of at least two commercial STM instruments. In this case the crashing is literally that—turning off the voltage to the Z-piezo and letting it hammer into the surface. The user manuals suggest retracting the tip slightly by applying a voltage to the Z-piezo (ie, pulling the tip back from the surface) then hitting the “reset” button which basically cuts power to it. With no restoring voltage, the Z-piezo springs back to full extension driving the tip in to the surface. It has been attempted twice with our instrument, and in both cases the subsequent image lines showed obvious signs of a snapped off apex—the slope of the scan lines jumping erratically to the right and left, and the amplitude jumping into the 10's of nanometers. This seems like a very poor method considering the tip can be dialed in to the surface slowly and to a known distance by simply using the force-distance function.

Other “tricks”:

Good imaging requires a stable tunneling gap. However, it is exceedingly rare that the tips will function properly when starting an experiment, or that once they are performing correctly, they behavior will not abruptly change. Perhaps some atoms rearranged on the tip, or maybe the tip has picked up contamination. If a tip stops performing properly and will not spontaneously improve, one has a few tricks to try and gently bring the performance back. It is not really a matter of making the tip better. It's more of an evolutionary process in which you make the tip *different* and *sometimes* it's

better. A very commonly used technique is called *pulsing*. Our experiments are frequently carried out in the 1V scale. If, for example, a voltage of -0.5 V is the bias, rapidly moving the voltage range selector to the 10V scale will make the voltage jump to -5 V. The pulse lasts for perhaps a few seconds and it is common that a rather large (by STM standards) fragment is “dropped” from the tip—these objects can frequently be imaged and are sometimes surprisingly. Even when nothing “drops” from the tip, pulsing almost always results in a change in the image quality. Occasionally a really outstanding image can be achieved in this way and it's a simple, non-contact thing to try with little chance of damage. Increasing the voltage at a given set point moves the tip *away* from the surface, not towards it, which makes an inadvertent tip-crash unlikely.

Another commonly used method of conditioning and cleaning tips is to perform an *I-V curve*. Here, a voltage between about -5 to +5 V is ramped between the tip and sample. A nice continuous curve of current (on the y-axis) vs. voltage (on the x-axis) which goes through zero and is nearly vertical through the origin indicates a stable and clean tunneling junction is present, while a curve that is ragged, asymmetric, or perhaps is so bad it won't pass a current at all indicates the tip requires cleaning/conditioning. Often times several curves can be performed in succession and the response can improve dramatically.

Conclusions:

In this Appendix the fundamentals of STM probe fabrication and several strategies for cleaning, conditioning, and stabilizing the tips have been described. While preparing and maintaining a sharp tip is not a completely straight forward process, it is not outside the abilities of a typical researcher and requires the most basic of tools equipment (a DC power supply, an NaOH solution, and a few lengths of wire). As with most things in science, *luck* scales with *effort*. It is extremely common to spend vast amounts of time attempting to collect images to no avail, and then for unclear reasons the tip begins to behave as if by magic. After the basics of tip fabrication and conditioning are covered, the only other

“trick” is dedication and perseverance.

References:

- 1) Boscoboinik, J.A.; **2010**, Ph.D. dissertation, University of Wisconsin-Milwaukee
- 2) Revenikiotis, A.; Masters thesis, Royal Institute of Technology, Stockholm, Sweden.
- 3) Paul, W.; Miyahara, Y.; Grütter, P.; *Nanotechnology*, **2012**, 23, 335702.
- 4) For an excellent overview of the process, see <http://www.tungsten.com/>
- 5) Greiner, M.; Kruse, P.; *Rev. Sci. Instr.*, **2007**, 78, (2), 026104-3
- 6) Melmed, A.; *J. Vac. Sci. Tech. B.* **1991**, (2), 601-8.
- 7) Lucier, A.; Masters thesis, **2004**, McGill University, Montreal, Quebec.
- 8) Binnig, G.; Rohrer, H.; Scanning tunneling microscopy. *IBM Journal of Research and Development* **1986**. 30: 4.
- 9) Chen, C.; *J. Vac. Sci. A* **1990**, 9, (1), 44-8.
- 10) Baratoff, A.; *Physica*, **1984**, 127B, 143.
- 11) Hockett, L.; Creager, S.; *Rev. Sci. Instr.* **1993**, 64, (1), 263-4.
- 12) Winterlin, J.; Wiechers, J.; Höfer, H.; Behm, R.; *Phys. Rev. Lett.* **1989**, 62, (1), 59-63.

Appendix B

Work Functions, Field Emission and Fowler-Nordheim Tunneling

In an electrostatically neutral metal, electrons exist in a potential well which is often (crudely) represented as an abrupt step that the electrons in the bulk metal need to surmount. The barrier can be thought of as resulting from the electrostatic interaction of the electrons with the positive ions making up the lattice of the metal. When using the band theory of solids, energies are typically defined with respect to the Fermi level (μ) of the solid [1]. The Fermi level arises as a consequence of Fermi-Dirac statistics. The Pauli exclusion principle states that no two identical Fermions (particles with half-integer spin) can simultaneously occupy the same quantum state [2]. At absolute zero (0 K), the electrons would occupy first the lowest energy states, then the second lowest, and so forth until all of them had achieved their most thermodynamically stable states. At absolute zero, the Fermi level is then the highest energy level that is occupied and is analogous to a *highest occupied molecular orbital* (HOMO) in a molecule.

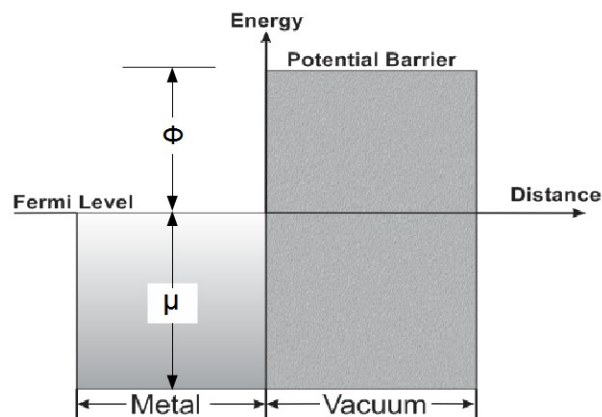


Figure B-1: A representation a metal/vacuum interface. μ is the Fermi level and ϕ is the work function. Both quantities are typically expressed in units of electron-volts (eV).

This can be more clearly explained by looking at the Fermi-Dirac distribution function directly (Equation B-1). At finite temperatures, some electrons have sufficient energy to occupy states above the Fermi level [1,3].

$$f(E) = \frac{1}{e^{(E-E_F/kT)} + 1} \quad \text{B-1}$$

The work function (ϕ) of the metal is the energy required for an electron to overcome the step and is defined as the minimum energy required for an electron at the Fermi level to escape into the free space immediately beyond the metal/vacuum interface. There are two main contributors to the magnitude of the work function. The first is the *inner potential* and is the difference in energy between the electron in the bulk metal, and the electron far away in a field-free vacuum. The inner potential is a property of the metal and is path independent –therefore it does not display crystallographic anisotropies. The second contributor to the work function is a result of the actual removal of an electron from a metal. While traversing the metal/vacuum interface, the electron experiences an extremely inhomogeneous environment. The termination of the metal results in a strong dipole layer. Moreover, the electron will always experience its corresponding image charge in the bulk of the metal [1]. The interaction of the electron with the surface is Coloumbic in nature and the magnitude of the effect is dependent on the surface structure. Therefore it is this second contribution which gives rise to the variance of work function with crystallographic orientation of the metal.

The above discussion focused on electrons associated with metals in the absence of an applied electric field. Under the influence of a strong electrostatic field ($\sim 10^7$ V/cm) however, electrons can overcome the potential barrier and tunnel into vacuum. This purely quantum mechanical effect is called *field emission* and will be the focus of this section. While the field emission effect had been known since the late 1800's, it was not until the late 1920's (shortly after the earliest years of quantum mechanics) that it had been described in terms of quantum tunneling. This seminal work was carried

out by Ralph Fowler and Lothar Nordheim and the set of approximate solutions to the Schrödinger equation with a barrier modified by an external field are frequently referred to as the *Fowler-Nordheim equations* [4]. It is important to clarify the difference between Fowler-Nordheim (field) emission and two other types of emission, those being *thermionic emission* and *photoemission*. In thermionic emission, an object such as a filament is heated to the point where the electrons gain enough thermal kinetic energy to surmount the barrier. Photoemission is a fundamentally different process in a metal which is irradiated with photons having an energy greater than the work function. The number of electrons being ejected from the surface increases with increasing photon flux. It was this principle for which Albert Einstein was awarded the 1921 Nobel Prize in physics [5]. What is important to note is that for both processes the electrons *overcome* the barrier kinetically. They are ejected from the surface thermally or photonically.

Fowler-Nordheim tunneling, as the name might imply, refers to electrons escaping a metal surface by going *through* the barrier. In the presence of a strong external field (on the order of 10^7 V/m), it is the barrier itself that becomes distorted away from the rectangular one described above. A schematic representation of the tunneling system is shown in Figure B-2. The original barrier, which is about equal to the image potential, is distorted by presence of an applied field [1].

The image potential has the form:
$$U_{img}(z) = \frac{-e^2}{4z} \quad \text{B-2}$$

And the applied potential has the form:
$$U_{field}(z) = -Fz \quad \text{B-3}$$

The tunneling barrier can then be represented according to Equation B-4 which is the sum of the image and applied potentials and the work function.

$$U_{eff}(z) = \phi_0 - \frac{-e^2}{4z} - Fz \quad \text{B-4}$$

The consequences of the deformation of the potential barrier will now be discussed. The salient point of the above discussion is that the application of an external electrostatic field is that both the *width* and the *height* of a the potential barrier decrease as a function of the strength of the applied field.

Heisenberg's uncertainty principle tells us that if the uncertainty in an electron's position is on the order of the width of a potential barrier, there exists a finite probability of finding it on the other side of the

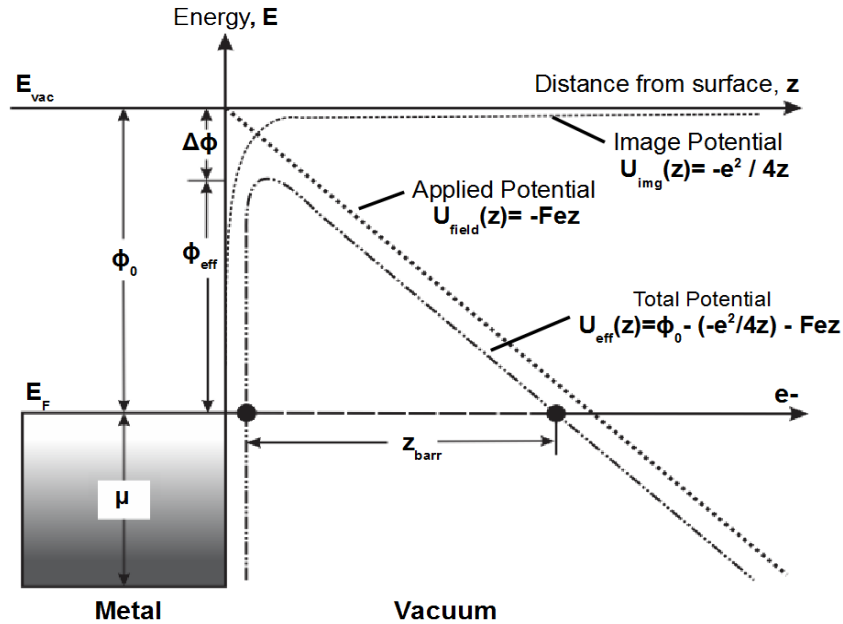


Figure B-2: Distortion of a barrier at a metal/vacuum interface as the result of an applied external field. The effective width and height decrease with field strength making tunneling through it more probable.

barrier (or more correctly, the electron exists on both sides of the barrier simultaneously). While semantically difficult, if we find the electron on the other side of the barrier we can say that the electron has *tunneled through it* (as opposed to being ejected or promoted over it).

Another way to formulate the effect is Wentzel-Kramers-Brillouin (WKB) theory which defines a quantum parameter typically referred to as a *transmission probability*, T [6]. As shown in Equation B-5, the transmission probability, which is a measure of finding an electron to the left of a barrier vs. to the right of it, scales both with the energy difference and with the width of the barrier, as would be expected for a classically forbidden event such as tunneling.

$$T(z) \approx 16 \frac{E}{U} \left(1 - \frac{E}{U}\right) e^{-2(z_2 - z_1) \sqrt{\frac{2m}{\hbar^2}(U - E)}} \quad \text{B-5}$$

For an unperturbed system, $U = \phi_0$ and electron faces the full width of the tunneling barrier (Δz). For the system perturbed by an applied field, $U = U_{eff}$ and $z = z_{eff}$. Obviously the transmission probability

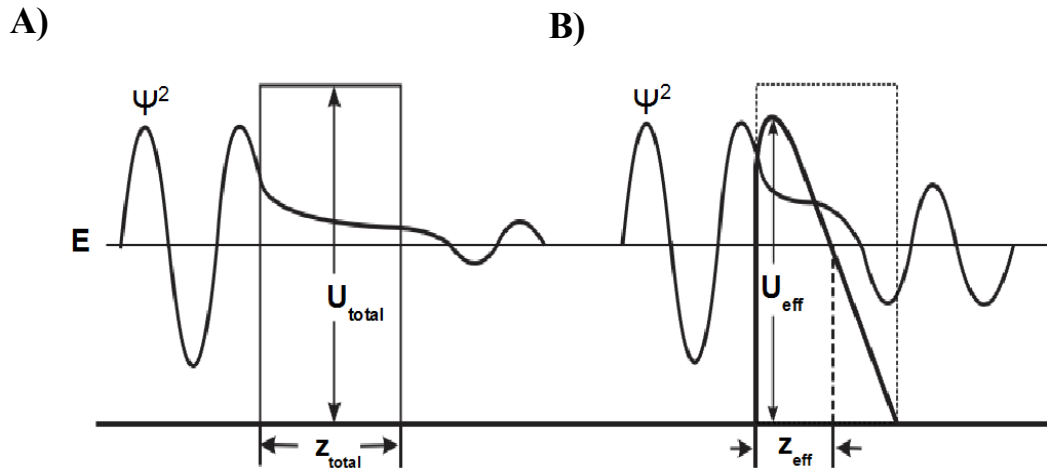


Figure B-3: Probability densities for A) an un-perturbed and B) a system perturbed by an external electric field.

increases with decreasing height and decreasing width of the barrier. This can be seen graphically by examination of the amplitude of the square of the electron wave function (Ψ^2) in Figure B-3.

Emission from Sharp Tips:

Field emission had been known for some time, but was put into a rigorous mathematical framework by Fowler and Nordheim in 1928 when they were able to describe the current density of an emitter (i) in terms of a metal's work function Φ , and the strength of the applied field F [1,2]. They used an elegant and straightforward approach to the problem which consisted of computing the penetration probability of electrons into the barrier, multiplying this by the arrival rate of electrons at the barrier, and integrating over all electrons with an energy less than or equal to the Fermi level, μ . The resulting *Fowler-Nordheim Equation* (Equation B-6) was an astonishing success and with minor upgrades, remains valid nearly 100 years later.

Equation B-6 describes the current density of an emitter without regarding the image potential.

$$i = \frac{e^3}{2\pi h} \frac{\sqrt{(\mu/\Phi)}}{\mu + \Phi} F^2 e^{\left(\frac{-4\pi\sqrt{8m}\Phi^{3/2}}{3ehF}\right)} \quad \text{B-6}$$

where e is the elementary charge, h is Planck's constant, m is the mass of an electron, μ is the Fermi

level, Φ is the work function, and F is the applied field strength. After substituting in accepted constants Equation B-7 results:

$$i = 6.2 * 10^{-6} \left(\frac{\sqrt{\mu/\Phi}}{\alpha^2(\mu + \Phi)} \right) F^2 e^{(-6.8 * 10^7 \frac{\Phi^{3/2}}{F} \alpha)} \quad \text{B-7}$$

where i is in A/cm², Φ and μ are in eV, and the field strength F is in V/cm.

If the image potential is included, α is included as the *image correction parameter* whose value falls between 1 and 0.

$$i = 6.2 * 10^{-6} \left(\frac{\sqrt{\mu/\Phi}}{\mu + \Phi} \right) F^2 e^{(-6.8 * 10^7 \frac{\Phi^{3/2}}{F})} \quad \text{B-8}$$

More corrections to the original F-N equation have been proposed. However, for our purposes the above discussion of the matter is more than adequate. As will be described, while field emission is very interesting in its own right, our interest in it has focuses on field emission of *sharp* and three-dimensional emitters as opposed to the 1-dimensional ones described above. In this context F-N theory provides both a basis for testing sharpness of STM probes prior to installation in UHV, and also provides a method for taking *sharp* tips and making them *atomically sharp* through a series of annealing and field emission cycles.

As was discussed in the section on STM tip preparation, the ultimate goal in fabrication is to arrive at a tip possessing a radius as small as possible. STM tips are frequently imaged using a scanning-electron microscope (SEM). However, it has been reported that the technique can damage the STM probe beyond repair. Measurement based on F-N tunneling, however, are ideally suited for estimating the radius of an STM tip, and provide a method for cleaning and in-situ sharpening as was discussed in Appendix A.

If a voltage V is applied to a sphere of radius R , the resulting field experienced by the sphere can be represented by Equation B-9.

$$F = \frac{V}{R} \quad \text{B-9}$$

However, an STM tip is not spherical, but in fact should be thought of as a hemispherical end atop a

conical shank. The shank reduces the field to some extent and Equation B-9 is then corrected by multiplying the radius by a *field reduction term*, k .

$$F = \frac{V}{kR} \quad \text{B-10}$$

From these equations it can be seen that for a given applied voltage, a smaller tip radius results in a larger electrostatic field. As was shown above, according to Fowler-Nordheim theory, a larger field results in higher current densities. Finding the exact value of k is difficult but fortunately this is of no consequence here. We are using F-N theory as a diagnostic tool and tip-sharpening/cleaning method as described in section Appendix A.

We can relate the tip radius to the current density by substituting Equation B-10 (V/kR) into Equation B-8 and obtaining the following:

$$I = a 6.2 * 10^{-6} \left(\frac{\sqrt{\mu/\phi}}{\alpha^2(\mu + \phi)} \right) \frac{V^2}{(kR)^2} e^{(-6.8 * 10^7 \frac{\phi^{3/2} \alpha kR}{V})} \quad \text{B-11}$$

where I is the total field-emitted current in Amperes, and a is the total area of the emitter in cm^2 . This provides us with a direct relationship between the tip radius, and the two other variables—applied voltage and measured emission current.

Taking the natural logarithm of both sides of Equation B-11 yields the following expression:

$$\ln\left(\frac{I}{V^2}\right) = \ln\left(a 6.2 * 10^{-6} \left(\frac{\sqrt{\mu/\phi}}{\alpha^2(\mu + \phi)}\right) \frac{1}{(kR)^2}\right) - 6.8 * 10^7 \frac{\phi^{3/2} \alpha kR}{V} \quad \text{B-12}$$

It is clear from the above expression that a plot of $\ln(I/V^2)$ vs. $1/V$ should yield a straight line with a slope that can give information about the tip radius as a result of equation:

$$\text{Slope} = -6.8 * 10^7 \phi^{3/2} \alpha kR \quad \text{B-13}$$

And this is the basis of the *Fowler-Nordheim Plot* which provides a straight forward method for the estimation of the radius of a sharp tip (by monitoring the 2 easily accessible parameters, the bias voltage and the field-emission current).

It should be noted here that the difficulties in solving the expression exactly include the fact that polycrystalline wire was used for tip fabrication and as such the work function is not exactly known (as

stated above, it is highly dependent on crystallographic orientation). Also, the exact value of the shielding parameter k is difficult to know, even with intimate knowledge of the tip geometry, as is the image correction parameter, α . Fortunately the exact values are not required. The interesting and perhaps most pragmatically useful aspect of field emission measurements is the observation of how the slope of the plots *change* as one cycles a given STM tip through cycles of field emission and flashing as was discussed at length in Appendix A.

References:

- 1) Lucier, A.; Masters thesis, **2004**, McGill University, Montreal, Quebec.
- 2) <http://hyperphysics.phy-astr.gsu.edu/hbase/pauli.html>
- 3) http://en.wikipedia.org/wiki/Fermi%E2%80%93Dirac_statistics
- 4) Fowler, R.; Nordheim, L.; *Proceedings of the Royal Society A*. **119**, (781), 173-81.
- 5) http://www.nobelprize.org/nobel_prizes/physics/laureates/1921/
- 6) de Aguiar, M.; “The WKB Approximation” **2013**. Available for download at:
<http://www.ifi.unicamp.br/~aguiar/Cursos/FI001/wkb.pdf>

John D. Kestell

Education and Awards:

University of Wisconsin-Milwaukee

Fall 2010—Present *Graduate Student/PhD Candidate*

- Graduation expected Spring 2014

University of Alabama at Birmingham, Birmingham, AL

Spring 1998—Fall 2010 *Graduate student*

- Graduate Assistance in Areas of National Need (GAAN) grant 1998-2002
- Teaching assistanceship UAB 1997-2003
- 3.62/4.0 over PhD level courses (30 credits)—Inorganic, physical, and theoretical chemistry.

Los Alamos National Laboratories, Los Alamos, NM

March 2002—*Invited researcher*

- Experimentation in time resolved infrared spectroscopy
- Theoretical work on metal-ligand charge transfer processes
- Optical spectroscopy of organometallic and conducting polymers
- DOE energy research in optical energy transduction

University of Alabama at Birmingham, Birmingham, AL

12/1998—*Bachelor of Science in chemistry, physics minor*

- Recipient—National Science Foundation Research Experience for Undergraduate (REU) grant Summer 1998
- Undergraduate teaching assistant—organic, inorganic, physical chemistry

University of Wisconsin-Oshkosh, Oshkosh, WI

1993-1996—*Chemistry major, physics minor*

McCrone Institute, Chicago, IL

06/2005—Completed “PLM for Analysis of Asbestos Samples”

Work History:

UW- Milwaukee Dept. of Chemistry and Biochemistry

Fall 2010—Present—*Teaching Assistant and Research Assistant*

- Teaching undergraduate laboratories (physical and freshman chemistry)
- Teaching discussion sections, tutoring, and exam reviews
- Summer RA positions working in the field of “molecular electronics”

Hydrite Chemical Co., Oshkosh, WI

01/2008—7/2010—*Quality Control and Formulation Chemist*

- Assaying incoming and outgoing products and components
- Safety and environmental compliance
- Addressing customer concerns and complaints
- Work with QC department to resolve production issues and customer complaints

Sigma Aldrich Fine Chemicals, Sheboygan Falls, WI

09/2006-01/2007—*Contract R&D chemist*

- Organic and organometallic synthesis
- R&D of new compounds and materials
- Project selection based on current literature and trends
- Scale-up from bench to kilogram batch
- Work on “problemated preparations” and unresolved scale-up issues

Houghton Intl, New Holstein, WI

03/2005-09/2006—*Formulation chemist*

- Formulation of coolants and cutting fluids at Tecumseh Engines plant
- Development of corrosion removal/inhibitor formulations
- Waste water analysis/clearing chemistry according to state regulation
- Frequent monitoring of factory machines for concentration and coolant efficacy.

Publications:

Kestell, J.; Williams, Z.; Stultz, L., Claude, J.P.; *Medium Dependence of Intramolecular Vibrational Modes Coupled to MLCT Transitions in Metal Polypyridyl Complexes.* J. Phys. Chem. A 2002; 106 (24) 5768-5778

Boscoboinik, J.A.; Kestell, J.; Garvey, M.; Weinert, M.; Tysoe, W.T.; *Creation of Low-Coordination Gold Sites on Au(111) by 1,4-Phenylene Diisocyanide Adsorption.* Topics in Catalysis 2011; 54 (1): 20-25

Kestell, J.; Abuflaha, R.; Boscoboinik, J.A.; Bai, Y.; Bennett, D.; Tysoe, W.T.; *Linking Gold Nanoparticles with Conductive 1,4-Phenylene Diisocyanide—Gold Oligomers.* Chem. Comm., 2013, **49**, 1422-1424

Kestell, J.; Abuflaha, R.; Garvey, M.; Bennett, D.; Tysoe, W.T.; *Determination of Adsorbate Structures from 1,4-phenylene Diisocyanobenzene on Gold.* Submitted for publication in Surface Science 3/2014

Garvey, M.; Kestell, J.; Abuflaha, R.; Bennett, D.; Henkelman, G.; Tysoe, W.T.; *Understanding and Controlling the 1,4-Phenylene Diisocyanobenzene-Gold Oligomer Formation Pathways.* Manuscript in preparation.